SPT

UNIVERSITY OF ILLINOIS
URBANA

AERONOMY REPORT NO. 86

ION AND ELECTRON TEMPERATURES IN THE TOPSIDE IONOSPHERE

by
D. E. Munninghoff

April 1, 1979

Library of Congress ISSN 0568-0581

Aeronomy Laboratory
Department of Electrical Engineering
University of Illinois
Urbana, Illinois

Supported by
National Science Foundation

UILU Eng 79 2505

AERONOMY REPORT

NO. 86

ION AND ELECTRON TEMPERATURES IN THE TOPSIDE IONOSPHERE

by

D. E. Munninghoff

April 1, 1979

Supported by
National Science Foundation
Grants ATM 75-15523, ATM 77-06787, and ATM 78-15224

Aeronomy Laboratory
Department of Electrical Engineering
University of Illinois
Urbana, Illinois

ABSTRACT

Experimental and theoretical ion and electron temperatures in the topside ionosphere are investigated. Experimental results come from an analysis of incoherent-scatter data taken at Arecibo, Puerto Rico. Consideration of the energy balance equations gives the theoretical ion and electron temperatures.

Two ions, O^+ and H^+, are assumed to be the only ions present in the topside ionosphere. Experimental evidence shows that a third ion, He^+ is relatively unimportant compared to O^+ and H^+. Photoionization of neutral particles, charge transfer, and diffusion of these charged particles are the important physical processes which are used to calculate their number density profiles. O^+ and H^+ number densities are shown to affect the O^+, H^+, and electron temperatures.

Analysis of theoretical autocorrelation functions of the incoherent-scatter power spectra shows that number densities and temperatures of O^+, H^+, and electrons can be deduced from experimental autocorrelation functions. Experimental temperature results indicate that the maximum difference between H^+ and O^+ temperatures occurs at 550 km. This agrees with temperatures calculated from the energy balance equations. The experimental and theoretical H^+ and O^+ temperatures agree fairly closely from 200 to 1200 km while the electron temperatures agree from 400 to 1200 km.

TABLE OF CONTENTS

LIST OF TABLES

LIST OF FIGURES

LIST OF SYMBOLS

A	area of magnetic field tube
ACF	autocorrelation function
B	magnetic field strength
c_v	specific heat of a gas at constant volume
C_{ij}	heat transfer between ions i and j
D_e	electron Debye length
D_i	ion Debye length
E	electric field strength
E_r	energy of rth particle
$f(v)$	statistical velocity distribution
g	relative velocity
h	Planck's constant
I	magnetic field dip angle
k	Boltzmann's constant
K_e	electron thermal conductivity
K_i	ion thermal conductivity
L_{in}	heat loss of ion to neutrals
m_e	electronic mass
m_i	ionic mass
n	number density (cm^{-3})
P_{ei}	heat transfer from electrons to ions
p	pressure
Q	thermal electron heating rate
$\bar{Q}_D$	average momentum transfer collision cross section
r_e	classical electron radius

s	distance along magnetic field
S_ω	incoherent-scatter power spectrum
T_r	Maxwellian temperature of rth particle
t	time
u_r, v_r	velocity of rth particle
Z_r	atomic charge of rth particle

GREEK

α	$4\pi D_e/\lambda$
Λ	ratio of center of mass energy to Coulomb potential energy
∇	gradient
ϵ_o	permittivity of free space
λ	radio wavelength
λ_m	mean free path
ν	collision frequency of a single particle
$\bar{\nu}$	average momentum transfer collision frequency
σ	collisior cross section
τ	time delay
χ	zenith angle
Ω	gyrofrequency
ω	Doppler shift frequency

1. INTRODUCTION

1.1 *The Neutral Atmosphere*

The goal of aeronomy is the knowledge of all physical parameters of the upper atmosphere. This implies the formation of models to describe the neutral atmosphere since most physical phenomena deal with the upper atmosphere's neutral constituents. Two important physical parameters which are necessary in any reliable atmospheric model are the number density and temperature of the neutral species. A number of different neutral atmospheric models exist depending on different conditions in the upper atmosphere. The most commonly used models are the ones which specify a thermopause temperature (temperature at the upper boundary of the earth's atmosphere). These models are based on observations from a number of different experiments. *CIRA* [1972] gives a review of the atmospheric models in the region from 110 to 2000 km which is the region being studied in this work. *CIRA* [1972] atmospheric models are used in this work and are the models that are commonly used today. *CIRA* [1972] models are reproduced in Appendix A.

In the remaining sections in this chapter the ionospheric regions of the atmosphere of the earth will be discussed. Also, collision processes, transport of charged particles, and thermal processes of the upper atmosphere will be discussed. After incoherent-scatter radar is introduced, the statement of the problem will be given in section 1.9.

1.2 *Ionospheric Regions*

The atmosphere of the earth can be divided into several different regions. When studying charged particles in the earth's atmosphere, the *D*, *E*, and *F* regions are discussed. These regions are identified by layers or ledges in the electron concentration profiles.

The *D* region contains charged particles formed by radiation whose

absorption cross section is smaller than 10^{-19} cm^2. The *D* region is between 40 and 90 km. Radiation which produces ionization in the *D* region includes solar X-rays having wavelengths less than 10 Å and ultraviolet radiation of wavelengths greater than 1750 Å. Also important is the absorption of Lyman-α radiation. The gases O_2 and N_2 are ionized by solar X-rays while NO is ionized by Lyman-α.

The *E* region contains charged particles formed by radiation whose absorption cross section is less than 5×10^{-18} cm^2. The *E* region is between 90 and 160 km. Solar radiation in the range 100-31 Å and that greater than 800 Å are important while solar Lyman β line at 1025 Å and the C(III) line at 977 Å are important since they ionize O_2. Ionization of O is produced by Lyman continuum at wavelengths less than 910 Å.

The *F* region has charged particles produced by radiation whose absorption cross section is greater than 10^{-17} cm^2. The *F* region is above 160 km. Radiation whose wavelength is in the range 100 to 800 Å ionizes N_2, O_2 and O. The *F* region has two layers, the F_1 and F_2 layers. The F_1 layer is a layer controlled by ion interchange processes. The F_2 layer contains atomic molecules and charged particles; diffusion is important in determining the ion profiles. The F_1 layer is below the F_2 layer.

1.3 *Ionization in the* F_1 *Region*

In the F_1 region the major ions are NO^+, O^+, O_2^+ and N_2^+. NO^+ is the dominant ion at altitudes between 140 and 170 km. Above 170 km O^+ becomes the dominant ion due to the much lower loss rate for O^+. To calculate equilibrium number densities for NO^+ and O^+ one must consider all the important reactions that bring about formation or loss of NO^+ and O^+. Therefore, ion chemistry rate coefficients are important in determining which reactions must be used

and which reactions can be neglected. For NO^+ the important sources of ionization include charge transfer of NO with $O^+(^4S)$, N_2^+ and O_2^+. The most important sink of NO^+ is dissociative recombination. For O^+ the important source of ionization is photoionization while charge transfer with N_2 and O_2 act as the important sinks of ionization. In Figures 1.1 and 1.2 are shown some theoretical and experimental profiles of NO^+ and O^+ number densities. Both Figures 1.1 and 1.2 show that NO^+ and O^+ densities depend on the solar zenith angle. Therefore, a model of F_1 ionization must take into account variations that depend on the time of day.

1.4 *Ionization in the* F_2 *Region*

The discussion of the last section concerned the solution to the ion continuity equation where chemistry is the important process. The present section gives an introduction to the current theory of the F_2 region.

The ionospheric F_2 region is formed through the competition between ion transport and chemical process up past the electron density peak which is the beginning of the topside ionosphere. The F_2 region begins at about 225 km and the principal ion is $O^+(^4S)$. At high altitudes, around 1000 km, H^+ becomes the principal ion. The predominant neutral gas is O, although N_2 and O_2 are important in O^+ loss processes. The oxygen ion density in the F_2 region is determined both by plasma transport and chemical reactions. In the steady state and in the absence of diffusion or convection the ion density would be expected to increase with increasing altitude since the effective ion recombination coefficient decreases rapidly with increasing altitude. But at sufficiently high altitudes ion recombination is balanced by ion transport and a peak in the ion density is reached. So, ion transport is responsible for for a decreasing density distribution with increasing altitude in the topside ionosphere.

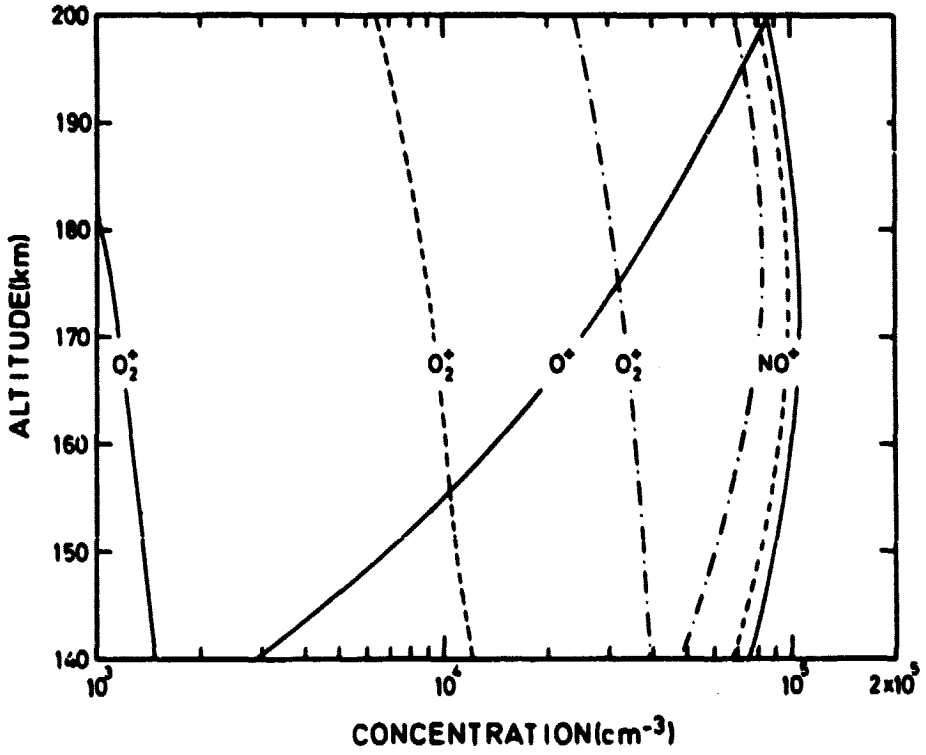

Figure 1.1 Theoretical profiles of NO^+, O_2^+, and O^+ [after *Banks and Kockarts*, 1973].

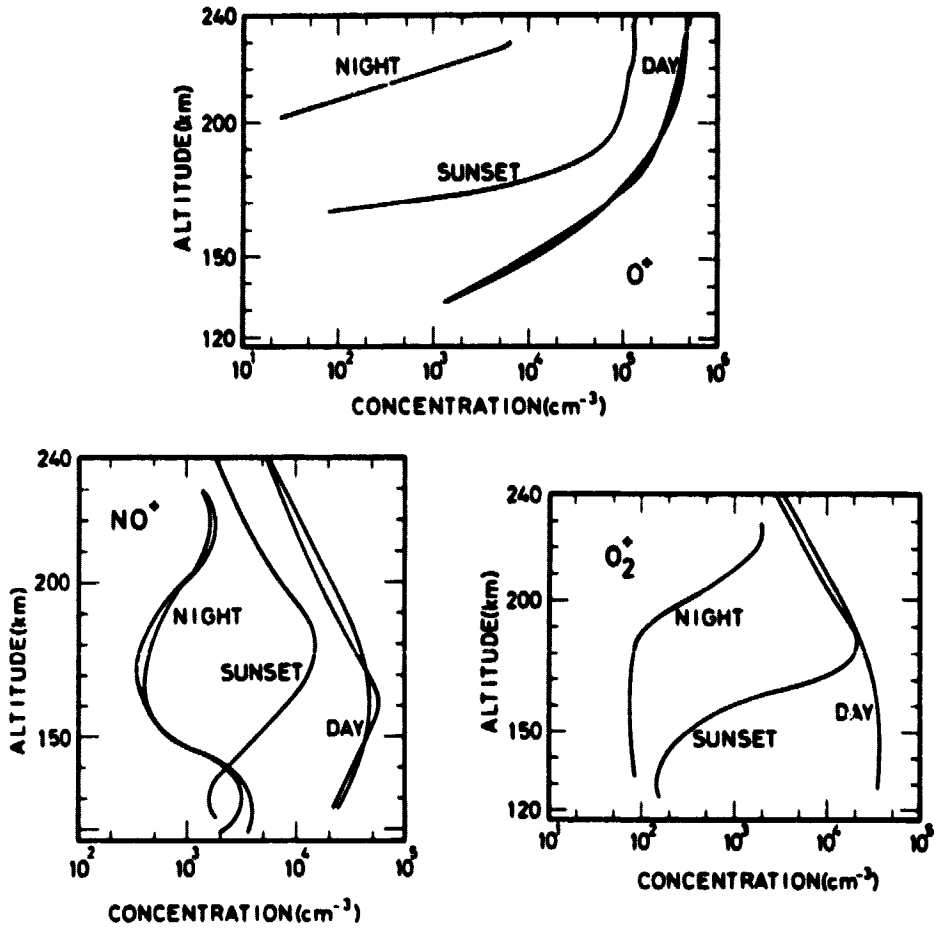

Figure 1.2 Experimental profiles of NO^+, O_2^+, and O^+ for daytime, sunset, and nighttime conditions [after *Banks and Kockarts*, 1973].

Atomic oxygen ions produced in the upper F_2 region diffuse downward with typical velocities in the range 10-20 m sec^{-1} [*Bowhill*, 1962]. A series of electron density profiles at Arecibo, Puerto Rico are shown in Figure 1.3.

The production of hydrogen ions in the F_2 region is brought about both through photoionization and through accidentally resonant charge exchange [*Hanson and Ortenburger*, 1961]

$$O^+(^4S) + H(^2S) \rightleftarrows O(^3P) + H^+ + \Delta E \qquad (1.1)$$

The energy defects of (1.3) are small relative to thermospheric energies ($kT \sim .1$ eV) so the reaction proceeds rapidly in both directions. Using rates of photoionization and charge exchange given by *Banks and Kockarts* [1973], one finds that photoionization is important only when the oxygen ion density is less than $10^2 - 10^3$ cm^{-3} which is far less than F_2-region oxygen ion densities. Calculations of hydrogen ion densities for chemical equilibrium (rate of increase in ions per unit volume per unit time = zero) show that the hydrogen-to-oxygen ion density ratio increases rapidly with altitude because atomic oxygen decreases more rapidly with altitude than atomic hydrogen does [*Banks and Kockarts*, 1973]. Thus, hydrogen ions eventually become the dominant ion species in the topside ionosphere.

1.5 *Collision Processes in the Topside Ionosphere*

The study of collisions is important in the study of electron and ion thermal balance. Ions, neutral particles, and electrons exchange energy through elastic, inelastic, and Coulomb collisions. In this section, collision processes of binary mixtures in thermal disequilibrium will be considered.

A gas of particles of type i is assumed to have a Maxwellian velocity distribution given by

$$f(v_i) = n_i(m_i/2\pi kT_i)^{3/2} \exp(-m_i v_i^2/2kT_i) \qquad (1.2)$$

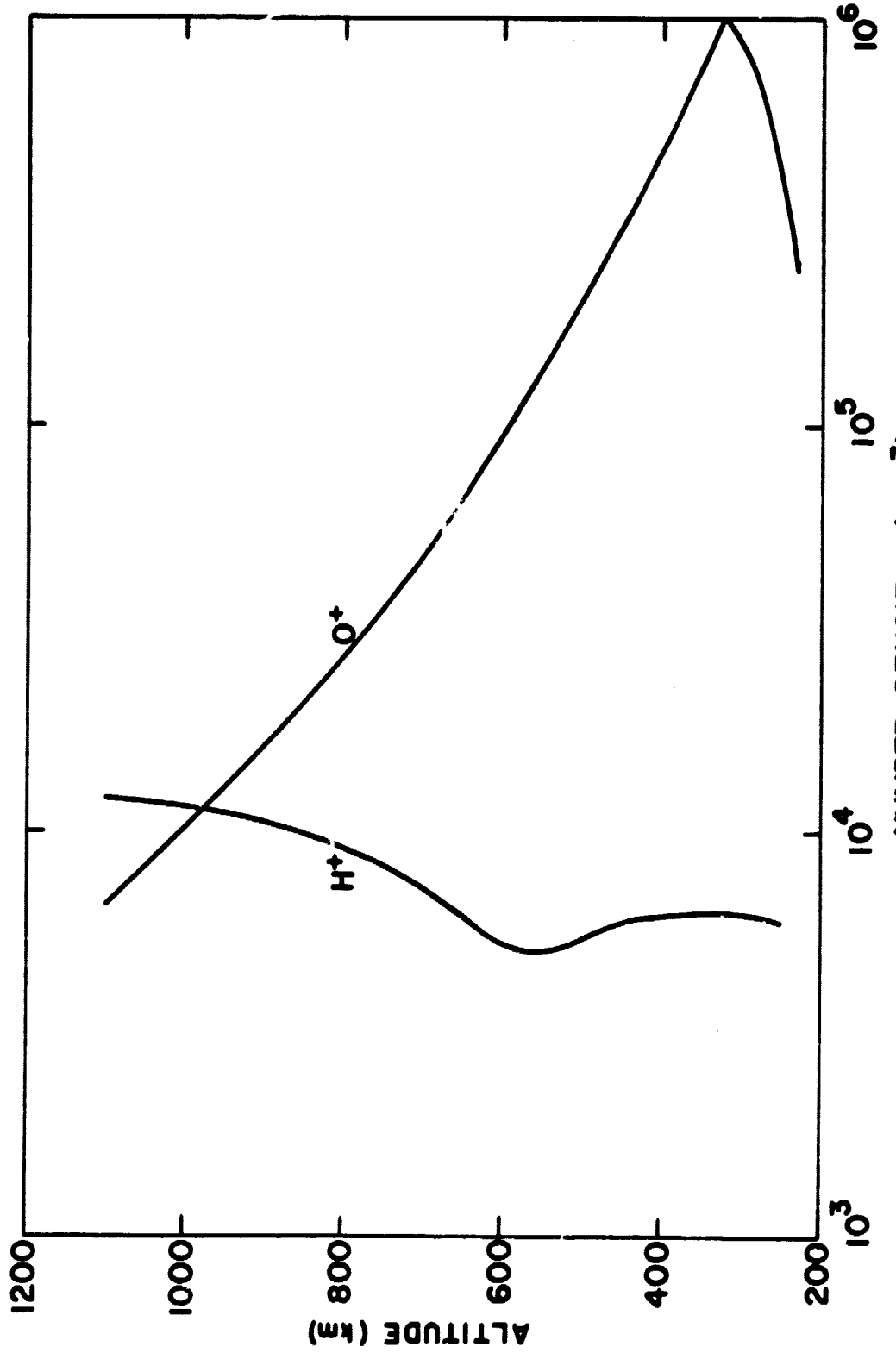

Figure 1.3 Daytime profiles of $n(O^+)$ and $n(H^+)$ for the F region over Arecibo, Puerto Rico.

where v_i is the velocity of the i-th species,

n_i is the number density,

m_i is the mass,

T_i is the temperature, and

k is Boltzmann's constant.

$f(v_i)$ is normalized so that

$$\int f(v_i)dv_i = n_i \tag{1.3}$$

One of the most important concepts of kinetic theory used in aeronomy is the concept of the average collision frequency between particle type 1 and particle type 2 given by

$$\bar{\nu}_{12} = \frac{1}{n_1} \int g\,\sigma(g) f(v_1) f(v_2) d\vec{v}_1 d\vec{v}_2 \tag{1.4}$$

where g is the relative speed between particles of type 1 and 2

$$g = \vec{v}_1 - \vec{v}_2 \tag{1.5}$$

$\sigma(g)$ is the velocity dependent collision cross section which depends on the nature of particle interaction, i.e. Coulomb force, induced dipole attraction, rotational and vibrational excitation, etc.

For example, the collision frequency of a particle with atomic oxygen with the hard sphere approximation of $\sigma_0 = 5 \times 10^{-15}$ cm^2, $m = 2.8 \times 10^{-23}$ gm, and $T = 300$K is:

$$\bar{\nu}_{i0} = 1.1 \times 10^{-10}\, n(0)\ \text{sec}^{-1} \tag{1.6}$$

Other types of collision processes will be discussed in more detail later.

1.6 *Transport of Charged Particles*

The ion composition is an important parameter in the study of ion conduction in the topside ionosphere. The ion composition is controlled by diffusion in the topside ionosphere. This diffusion is not ambipolar diffusion because in the topside ionosphere several ion species are involved and the scattering cross section for ambipolar diffusion is very small compared to the Coulomb scattering cross section of thermal protons with oxygen ions; [*Hanson and Ortenburger*, 1961].

The ion composition and ion number density profiles vary from night to day. Typical profiles of ion composition are shown in Figures 1.3 and 1.4 for nighttime and daytime data. The daytime data shows the case of outward plasma flow while the nighttime data shows the case of inward plasma flow. The maintenance of the large nighttime number density peak is due to this inward plasma flow. The transport of charged particles will be discussed in more detail later.

1.7 *Thermal Processes*

The transfer of heat between charged particles and neutral particles and other charged particles is important in the study of the topside ionosphere. While all particles have the same temperature in the *D* and *E* regions, in the *F* region ions, electrons, and neutrals each have separate temperatures. The neutral temperature increases rapidly with altitude above 120 due to the absorption of solar ultraviolet radiation by the neutral atmosphere. The increase of temperature gradually becomes small at altitudes above 500 km due to the decrease in absorption of solar ultraviolet radiation with altitude and a large neutral thermal conductivity. The ions and electrons have almost the same temperatures as the neutrals at altitudes below 200 km due to large thermal-electron heating rates by photoelectrons and large heat transfer

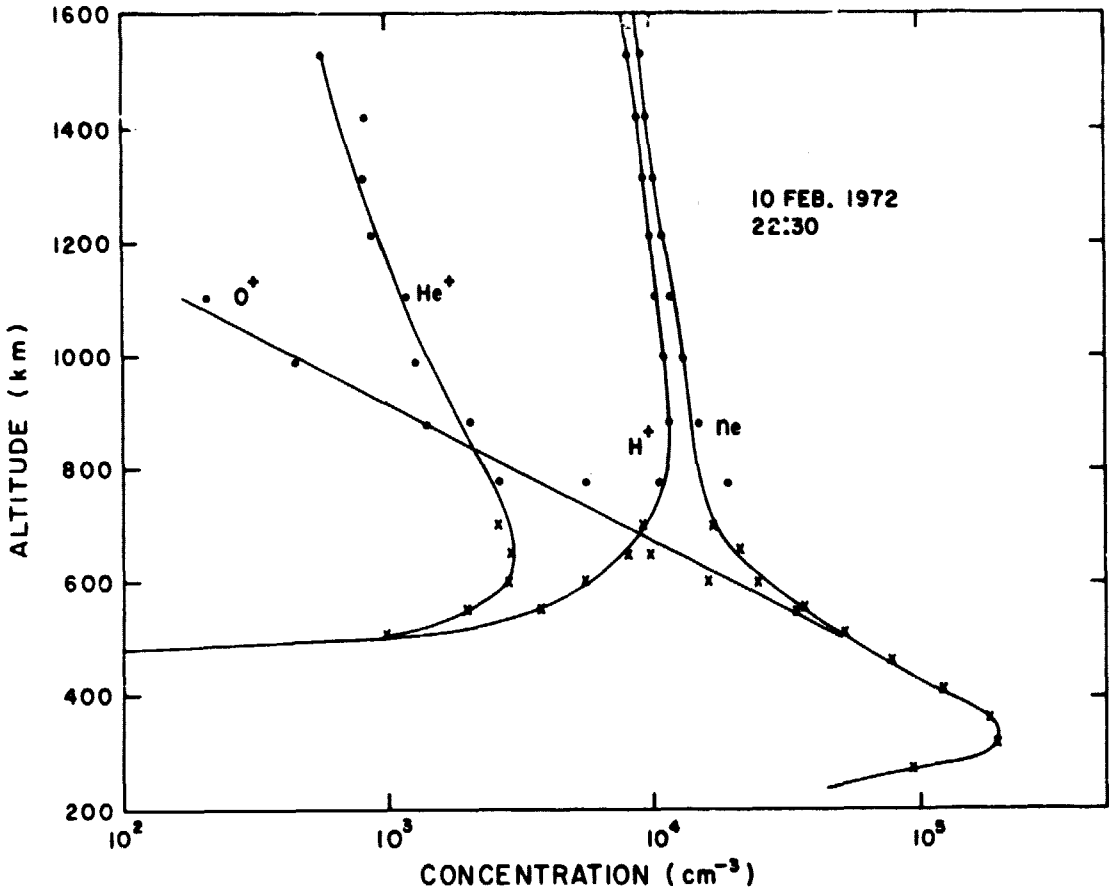

Figure 1.4 Nighttime profiles of n_e, $n(O^+)$, $n(H^+)$, and $n(He^+)$ for the F region over Arecibo, Puerto Rico [after *Hagen and Hau*, 1974].

rates between ions and neutrals, and electrons and neutrals, through elastic and nonelastic collisions. The electron temperature increases rapidly above the neutral temperatures with altitude above 200 km since heat transfer to neutrals and ions decreases with altitude. The ion temperature increases above the neutral temperature above 200 km but it is lower than the electron temperature due to larger ion-neutral heat transfer rates than electron-neutral heat transfer rates. At high altitudes the electron and ion temperatures are controlled by thermal conduction. Since the thermal conduction is different for electrons, positive oxygen ions, and positive hydrogen ions, these particles can all have separate temperatures. This will be discussed in more detail later.

1.8 *Incoherent-scatter Radar*

Incoherent scatter (Thomson scatter) is a process where incident electromagnetic radiation is reradiated by charged particles with random phase. When the exploring wavelength is large compared to the Debye length given in equation (1.7), the scattering of radiation can be thought as arising from density fluctuations caused by plasma waves. The principal component of the returned signal are scattered waves introduced by the presence of ion-acoustic waves and electron-induced waves at the gyrofrequency ($\omega_H = eB/cm_e$) and the plasma frequency ($p = (n_e e^2/m_e \epsilon_0)^{1/2}$) ($c$ is the speed of light, ϵ_0 is the permittivity of free space, B is the earth's magnetic field, e, m_e, n_e are the electronic charge, electronic mass, and electron number density, respectively).

Although it was first thought [*Gordon*, 1958] that the spectrum of reflected incoherent-scatter signals would be Gaussian in shape with a center to half power width of .71 times the Doppler shift of an electron approaching the radar at the mean thermal speed, later observations [*Bowles*, 1961] proved that the bandwidth was considerably less than the Doppler shift of the electron. Subsequent theoretical work [*Fejer*, 1960; *Dougherty and Farley*, 1960;

Salpeter, 1960a; and *Hagfors*, 1961] has shown that the influence of ions can effectively narrow the spectrum width when the exploring wavelength is much larger than the Debye length. The Debye length or Debye shielding distance is given by

$$D_p = (\epsilon_0 kT/n_e e^2)^{1/2} \text{ meters} \qquad (1.7)$$

where k is Boltzmann's constant, T_e is the electron temperature. D_e is of the order of 1 cm or less below altitude 1000 km and rises to about 6 cm at altitude 2000 km. Arecibo Ionospheric Observatory (see section 1.9) operates the radar at wavelength of 69.8 cm. This is the radar facility which will be used in this work.

Information about the temperature and number density of electrons, O^+, and H^+ can be deduced from incoherent-scatter returns. This is done by fitting theoretical generated spectra with experimental spectra. This will be discussed in more detail later.

1.9 *Statement of the Problem*

In this work both experimental observations and theoretical analysis of the thermal structure of the topside ionosphere will be studied. The experimental observations are in the form of incoherent-scatter returns from Arecibo, Puerto Rico which is located at a magnetic latitude of 30°N. The magnetic dip angle, I, is 50° at Arecibo. The antenna at Arecibo is a spherical disc with a radius of curvature of 245 meters and a diameter (viewed from above) of 305 meters. Details of the system have been described by *Gordon* [1964]. Parameters such as temperature, density, and composition of the charged particles can be deduced from incoherent-scatter returns by use of incoherent-scatter theory. Discussion of the theory and the analysis of the experimental data will be given later.

Theoretical analysis of the thermal structure of the topside ionosphere involves solving the appropriate energy balance equations for the charged particles in the topside ionosphere. In this work the major ions are assumed to be the positive charged oxygen ion, O^+, and the positive charged hydrogen ion, H^+. Together the number densities of O^+ and H^+ add up to be the electron number density or

$$n_e = n(O^+) + n(H^+)$$

where n_e is the electron number density, and $n(O^+)$ and $n(H^+)$ are the number densities of O^+ and H^+.

The electron, O^+ and H^+ energy balance equations are coupled nonlinear differential equations. Analytic solutions are impossible to obtain, so numerical methods are used to solve these equations. By using different atmospheric models theoretical profiles for the electron, O^+ and H^+ temperatures can be obtained and compared with those of corresponding atmospheric conditions.

Experimental analysis of incoherent-scatter radar returns can be performed to obtain O^+, H^+, and electron number densities and temperatures. This involves numerical methods of fitting experimental autocorrelation functions to theoretical autocorrelation functions.

The objective of this work is the investigate of thermal processes of electrons, O^+ and H^+ ions in the topside ionosphere. Through theoretical and experimental deduction of temperature profiles the importance of various heat transfer processes can be verified. Thus, comparison between experimental and theoretical results will indicate further refinements in the theory of heat transfer between charged particles and other charged particles or neutral particles.

2. IONS IN THE TOPSIDE IONOSPHERE

2.1 *Introduction*

Parameters which can easily be measured by existing experimental techniques are usually used in describing physical processes in the ionosphere. The observed values of these parameters are compared with the values calculated from theoretical models. These parameters include values of electron temperatures, ion temperatures, ion densities, electron density, and neutral densities, and velocities of neutrals and charged particles.

One of the most important parameters is the ion density distribution. *F* region ion densities have been measured or deduced from a number of experimental instruments, including incoherent scatter radars, ion mass spectrometers, Langmuir probes and retarding potential analyzers aboard rockets and satellites, and radio wave sounders or ionosondes. Recent experiments using these experimental techniques [*Hoffman*, 1967; *Hoffman et al.*, 1974; *Moorcroft*, 1964; *Knudsen and Sharp*, 1966; *Hagen and Hsu*, 1974] have indicated that O^+ and H^+ are major constituents in the topside ionosphere. In Figure 2.1 [*Hagen and Hsu*, 1974], one notices that O^+ is the major ion at F_2 maximum and H^+ is the major ion at altitudes above 1000 km. This is the case in all typical profiles of ion composition in the topside ionosphere. He^+ is usually a minor ion near the altitude where the transition between O^+ and H^+ as major ions takes place and is less than 10% the total ion concentration at all other altitudes.

In the topside ionosphere the neutral particle density becomes small so ion-neutral collisions lose their importance in the ion momentum equations at increasing altitudes above the F_2 maximum. Therefore, the ions move along the magnetic field lines when there are no perpendicular electric fields

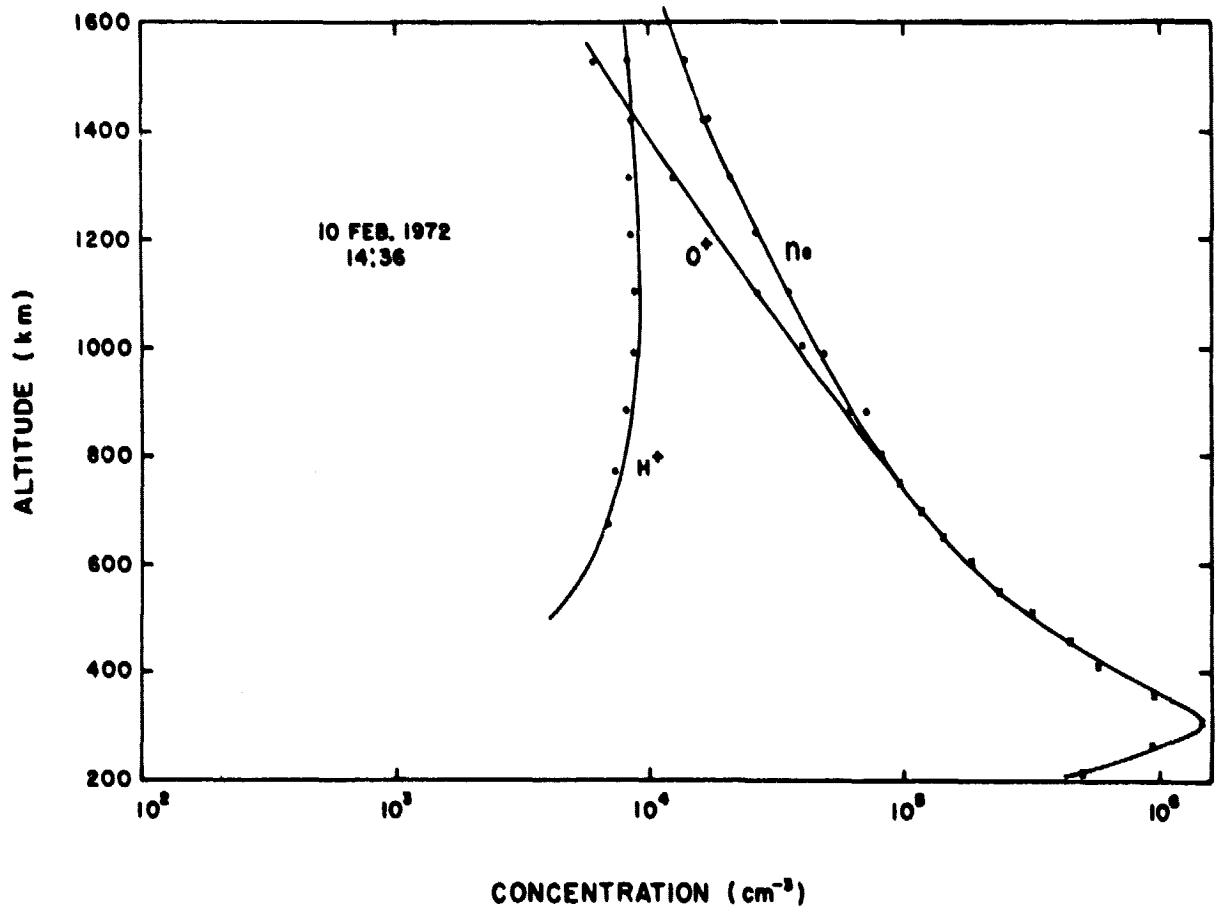

Figure 2.1 Daytime profiles of n_e, $n(O^+)$, $n(H^+)$, and $n(He^+)$ for the F region over Arecibo, Puerto Rico [after *Hagen and Hsu*, 1974].

present. The action of the charge separation electric field inhibits the movement of the ions even though ion-neutral collisions are no longer important. Ion-ion collisions are important since they also help in keeping the ions from moving quickly out of the earth's atmosphere.

2.2 *Hydrogen Ions*

Oxygen and hydrogen atoms have almost the same ionization potential. The oxygen ionization potential is slightly greater than the hydrogen ionization potential. This implies that charge transfer between oxygen atoms (O) and hydrogen ions (H^+) can proceed almost as rapidly as charge transfer between hydrogen atoms (H) and oxygen ions (O^+). This reaction can be expressed as

$$H^+ + O \rightleftarrows O^+ + H + \Delta E \tag{2.1}$$

where ΔE is small compared to thermospheric energies in the F region. In Table 2.1 are given some time constants for O^+ - H charge exchange. This table gives data for several atmospheric models. The time constant given in Table 2.1 is the time constant for changes in $n(H^+)$ when production is zero and when flux of H^+ is zero [*Banks and Kockarts*, 1973].

$$\tau(H^+) = \left(\frac{8}{9}\,\overline{Q_E}\, n(0)\,(8kT_i/\pi\, m(H))^{1/2}\right)^{-1} \tag{2.2}$$

where $\overline{Q_E} = (1.5 \pm 0.5) \times 10^{-15}$ cm^2 is the charge-exchange cross section for (O^+,H) collisions, $n(O)$ is atomic oxygen density, T_i is the ion temperature and $m(H)$ is the mass of hydrogen.

The continuity equation governing the H^+ number density is

$$\partial n(H^+)/\partial t + \nabla\cdot(n(H^+)\vec{C}(H^+)) = p(H^+) - \ell(H^+) \tag{2.3}$$

where $\vec{C}$ is transport velocity

$$p(H^+) = I(H)n(H) + \overline{Q_E}\, n(H)n(O^+)\,(8kT_n/\pi m(H))^{1/2} \tag{2.4}$$

TABLE 2.1

Time constants[a] for O^+-H charge exchange (after *Banks and Kockarts*, 1973).

Altitude (km)	Atmospheric model thermospheric temperatures					
	750 K	1000 K	1250 K	1500 K	1750 K	2000 K
200	2.3(−1)	2.3(−1)	1.9(−1)	1.6(−1)	1.1(−1)	8.2(−2)
250	8.0(−1)	6.2(−1)	4.4(−1)	3.5(−1)	2.4(−1)	1.6(−1)
300	2.6(0)	1.5(0)	9.4(−1)	6.6(−1)	4.3(−1)	2.8(−1)
350	9.1(0)	3.6(0)	1.9(0)	1.2(0)	7.3(−1)	4.5(−1)
400	2.5(1)	8.3(0)	3.7(0)	2.2(0)	1.2(0)	7.1(−1)
450	7.6(1)	1.9(1)	7.3(0)	3.8(0)	1.9(0)	1.1(0)
500	2.2(2)	4.3(1)	1.4(1)	6.5(0)	3.1(0)	1.7(0)

a Values are in sec.

b 2.3(−1) = 2.3×10^{-1}.

is the production of H^+

$$\ell(H^+) = \frac{8}{9} \bar{Q}_E \, n(O) n(H^+) (8kT(H^+)/\pi m(H))^{\frac{1}{2}} \tag{2.5}$$

is the loss of H^+. $I(H)n(H)$ is production from photoionization of H. T_n is the neutral gas temperature. $T(H^+)$ is the hydrogen ion temperature. The $e - H^+$ recombination rate is negligible compared to the charge transfer rate. When the conditions for chemical equilibrium ($\vec{C}(H^+) = 0$ and $\partial n(H^+)/\partial t = 0$) are used, the H^+ density can be derived from the continuity equation.

$$\frac{n(H^+)}{n(O^+)} = \frac{9}{8} \frac{n(H)}{n(O)} \left[\frac{T_n}{T(H^+)}\right]^{\frac{1}{2}} \left[1 + \frac{I(H)}{Q_E n(O^+) (8kT_n/\pi m(H))^{\frac{1}{2}}}\right] \tag{2.6}$$

Using $I(H) = (8.8 \pm 3.3) \times 10^{-8}$ sec^{-1} and $T_n = 1000$ K one finds that photoionization is not important when $n(O^+)$ is greater than 10^3 cm^{-3}. Since $n(O^+)$ is typically greater than 10^4 cm^{-3} in the topside ionosphere (2.6) can be reduced to

$$\frac{n(H^+)}{n(O^+)} = \frac{9}{8} \frac{n(H)}{n(O)} \, (T_n/T(H^+))^{\frac{1}{2}} \tag{2.7}$$

This implies the hydrogen to oxygen ion density ratio increases rapidly with altitude since atomic oxygen decreases more rapidly with altitude than atomic hydrogen does. In Table 2.2 are given some $n(H^+)/n(O^+)$ for several atmospheric models. Equation (2.7) shows that the hydrogen ion density for chemical equilibrium does not depend on the charge exchange rate even though charge exchange is the dominant source of protons in the topside ionosphere. $n(O)$ and $n(H)$ are the important parameters for determining $n(H^+)$.

Tables 2.1 and 2.2 show that $\tau(H^+)$ and $n(H^+)/n(O^+)$ increase with altitude. Eventually $\tau(H^+)$ and $n(H^+)/n(O^+)$ become large enough so that ionic diffusion becomes important and controls the distribution of number density. The

TABLE 2.2

Hydrogen to oxygen ion density ratios: chemical equilibrium (after *Banks and Kockarts*, 1973).

Altitude (km)	Thermospheric temperatures					
	750 K	1000 K	1250 K	1500 K	1750 K	2000 K
200	4.6(–4)	6.9(–5)	3.3(–5)	2.8(–5)	2.8(–5)	2.9(–5)
250	1.4(–3)	1.4(–4)	4.5(–5)	3.1(–5)	2.8(–5)	2.8(–5)
300	4.2(–3)	3.0(–4)	7.0(–5)	3.8(–5)	3.0(–5)	2.8(–5)
350	1.2(–3)	6.7(–4)	1.2(–4)	5.1(–5)	3.4(–5)	2.9(–5)
400	3.5(–2)	1.4(–3)	2.1(–4)	7.3(–5)	4.1(–5)	3.2(–5)
450	8.8(–2)	3.1(–3)	3.7(–4)	1.1(–4)	5.3(–5)	3.7(–5)
500	2.7(–1)	6.8(–3)	6.8(–4)	1.7(–4)	7.2(–5)	4.4(–5)

a 4.6(–4) = 4.6×10^{-4}

transition from chemical to diffusive equilibrium does not greatly affect the H^+ distribution because usually this occurs when $n(O^+) >> n(H^+)$. When $n(O^+) >> n(H^+)$ the chemical and diffusive equilibrium solutions for the hydrogen ion density are nearly the same.

2.3 *Helium Ions*

The source of helium ions in the topside ionosphere is the photoionization of atomic helium by solar radiation with wavelength, λ, less than 504 Å. This reaction is expressed as

$$I(\mathrm{He}): \quad \mathrm{He}(^1S) + h\nu(\lambda < 504\ \text{Å}) \rightarrow \mathrm{He}^+(^2S) + e \tag{2.8}$$

The important loss reactions involve charge transfer and dissociative charge transfer with O_2 and N_2 given by

$$(\gamma_{10}): \quad \mathrm{He}^+ + O_2 \rightarrow \mathrm{He} + O + O^+ + 5.85\ \mathrm{eV} \tag{2.9}$$

$$(\gamma_{10}^*): \quad \mathrm{He}^+ + O_2 \rightarrow \mathrm{He} + O_2^+ + 12.25\ \mathrm{eV} \tag{2.10}$$

$$(\gamma_6): \quad \mathrm{He}^+ + N_2 \rightarrow \mathrm{He} + N + N^+ + 0.28\ \mathrm{eV} \tag{2.11}$$

$$(\gamma_6^*): \quad \mathrm{He}^+ + N_2 \rightarrow \mathrm{He} + N_2^+ \tag{2.12}$$

See Appendix B for rate coefficients given above.

Thus the continuity of He^+ number density is

$$\partial n(\mathrm{He}^+)/\partial t = \nabla\cdot(n(\mathrm{He}^+)\vec{C}(\mathrm{He}^+)) =$$

$$I(\mathrm{He})n(\mathrm{He}) - n(\mathrm{He}^+)[(\gamma_{10} + \gamma_{10}^*)n(O_2) + (\gamma_6 + \gamma_6^*)n(N_2)] \tag{2.13}$$

If the conditions for chemical equilibrium are applied one gets

$$n(\mathrm{He}^+) = \frac{I(\mathrm{He})n(\mathrm{He})}{(\gamma_{10} + \gamma_{10}^*)n(O_2) + (\gamma_6 + \gamma_6^*)n(N_2)} \tag{2.14}$$

This equation implies that $n(He^+)$ increases with altitude since $n(N_2)$ and

$n(O_2)$ decrease much more rapidly with altitude than n(He) does. At high altitudes diffusion cannot be ignored and so therefore the $n(He^+)$ distribution will decrease with altitude.

He^+ never becomes the predominate species in the topside ionosphere. Its maximum density is 5×10^3 cm^{-3} [*Hoffman*, 1967]. *Hanson et al.* [1969] showed that even at 1068 km that only 0.14% He^+ existed in the topside ionosphere.

2.4 *Oxygen Ions*

Oxygen ion, O^+, is the principal ion of the F_2 region and the predominate neutral gas is O. The F_2 region is formed through the competition between ion transport and chemical process. Oxygen is ionized through solar ultraviolet radiation ($\lambda < 910$ Å). O^+ is lost through slow ion-molecule reactions with N_2 or O_2 to form NO^+, N_2^+, or O_2^+.

The altitude profile of the O^+ ion density is controlled both by ion transport and ionic reactions. Ion transport is important at higher altitudes because in the absence of ion transport the steady state O^+ ion density would continue to rise with altitude due to the decreasing ion recombination coefficient. However, at high altitudes chemical processes cannot compete with ion transport. Thus, a peak in the O^+ ion density is reached.

Short wavelength solar ultraviolet radiation ($\lambda < 910$ Å) ionizes atomic oxygen at the rate

$$q(O^+) = I(O)n(O)$$

where $I(O) = (3.2 \pm 1.3) \times 10^{-7}$ sec^{-1} and $n(O)$ is the density of atomic oxygen. The importance of the final state of O^+ is in this case significant due to the rapid reaction of $O^+(^2D)$ with N_2 in comparison with $O^+(^4S)$ with N_2. $O^+(^4P)$ and $O^+(^2P)$ can be neglected due to relatively small cross sections.

Thus, only $O^+(^4S)$ reactions and transport are important.

The important ionic reactions which O^+ is lost are

$$\gamma_1: \quad O^+ + N_2 \rightarrow NO^+ + N$$

$$\gamma_2: \quad O^+ + O_2 \rightarrow O_2^+ + O$$

where $\gamma_1 = (1.1 \pm 0.3) \times 10^{-12}$ cm^3 sec^{-1} and $\gamma_2 = (2 \pm 0.2) \times 10^{-11}$ cm^3 sec^{-1}.

The O^+ ion density is extremely variable in its maximum density and peak altitude. Changes in the neutral atmosphere such as temperature and density changes and neutral winds can affect the magnitude and height of the F_2 peak. The neutral winds raise or lower the peak altitude of the F_2 layer if the drift is upward or downward. Also north to south winds tend to move ionization up magnetic field lines. For increasing exospheric temperatures the peak density increases and the peak altitude shifts upward [*Rishbeth and Barron*, 1960].

Outward and inward flows of O^+ also affect the density profile. Shortly after dawn outward flow of O^+ from the F_2 region to high altitude magnetic field tubes replace ionization which was lost during the night as a result of recombination. In the evening and during the night inward flow of O^+ (created through H^+ to O^+ charge exchange) maintains large densities in the F_2 region.

Another factor which affects the F_2 peak is the magnetic dip angle I. The vertical component of ion diffusion is reduced for smaller values of I.

The effects of electric fields on F_2 region electron densities has been used to explain diurnal variations [*Stubbe and Chandra*, 1970]. But the magnitude of these fields (5 mV M^{-1}) appear to be much larger than experimental values [*Cauffman and Gurnett*, 1971]. Thus, the role of electric fields in the F_2 region is generally neglected.

2.5 *Ion Diffusive States*

The discussion in the previous sections dealt with chemical equilibrium states for H^+ and He^+ which exist at low altitudes in the F region. Above 500-700 km this is not the case. Diffusion and convection become the dominant processes. Mechanical forces such as gravity. electric and magnetic fields, pressure gradients and centrifugal forces also become important. The F_2 region can act as either a source or sink of ionization for the topside plasma since diffusion strongly couples the F_2 region to the topside ionosphere.

Magnetic fields are important since charged particles can move only along field lines if there are no electric fields. Therefore, when discussing motions of charged particles in the topside ionosphere one speaks of motions along the magnetic field lines.

In the topside ionosphere there are three diffusive states which are important in determining the ion density distributions. These states are diffusive equilibrium, inward plasma flow, and outward plasma flow (see Fig. 2.2). The first state, diffusive equilibrium, corresponds to a state where there is no net transport of ions along the magnetic field tubes. This state rarely occurs in the earth's atmosphere at mid and high latitudes. Only at low latitudes does the topside ionosphere have a chance to reach a state of diffusive equilibrium. Still, this state serves as an important basis for the understanding of inward and outward plasma flow.

Inward diffusive flow results when there is an excessive plasma pressure at high altitudes in the magnetic field tube. H^+ and He^+ diffuse downward to regions where ion-neutral reactions convert these into O^+ and N_2^+ thereby enhancing the ion density distribution in the F_2 region. Calculations of

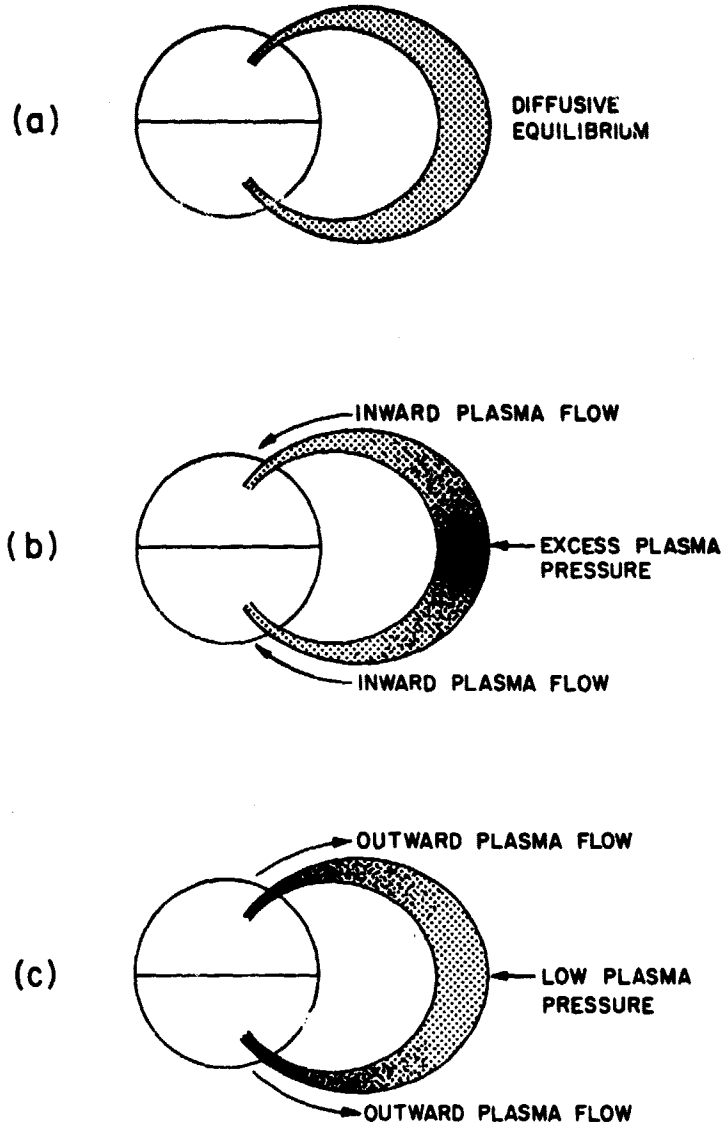

Figure 2.2 The three different diffusive states.

inward diffusive flow shown in Fig. 2.3 indicate that the ion density distribution are unchanged from diffusive equilibrium at low altitudes (below 500 km.) This is discussed in detail later. Outward diffusive flow of light ions results from low plasma pressure at high altitudes in the magnetic field tube. If there are no magnetospheric electric fields then the upward flow plasma replenishes the field tube and eventually diffusive equilibrium comes about. During magnetic storms magnetospheric convection and the plasmapause, a sharp latitudinal decrease in plasma density which normally occurs near 65° magnetic latitude, can move to magnetic shells as low as $L \gtrsim 2.5$ [*Ryoroft and Burnell*, 1970]. Following the storm the field tube is essentially empty because field tube convection moves to higher L shells [*Banks et al.*, 1971] and plasma flow must eventually fill the field tube.

2.6 *Continuity and Momentum Equations*

The basic equations for determining the ion density distribution are the continuity and momentum equations. The ion momentum equation for flow parallel to the magnetic field line is

$$\frac{\partial u_i}{\partial t} + u_i \frac{\partial u_i}{\partial s} + g_{||} + \frac{1}{n_i m_i} \frac{\partial p_i}{\partial s} - \frac{Z_i e}{m_i} E_{||} = \sum_k \nu_{ik}(u_i - u_k) \quad (2.15)$$

where u_i is the ion bulk transport velocity, u_k is the ion bulk transport velocities of other ions, $g_{||}$ is the acceleration of gravity (positive inwards) parallel to B (the magnetic field), s is a coordinate along B, A is the area of the field tube at point s, $Z_i e$ is the atomic charge of the ion, n_i is the ion density and m_i is the ion mass, $E_{||}$ is the electric field parallel to B and ν_{ik} is the momentum transfer ion diffusion collision frequency, p_i and p_e are the ion and electron gas pressures ($p_i = n_i k T_i$), the summation is over all neutral and other charged particles.

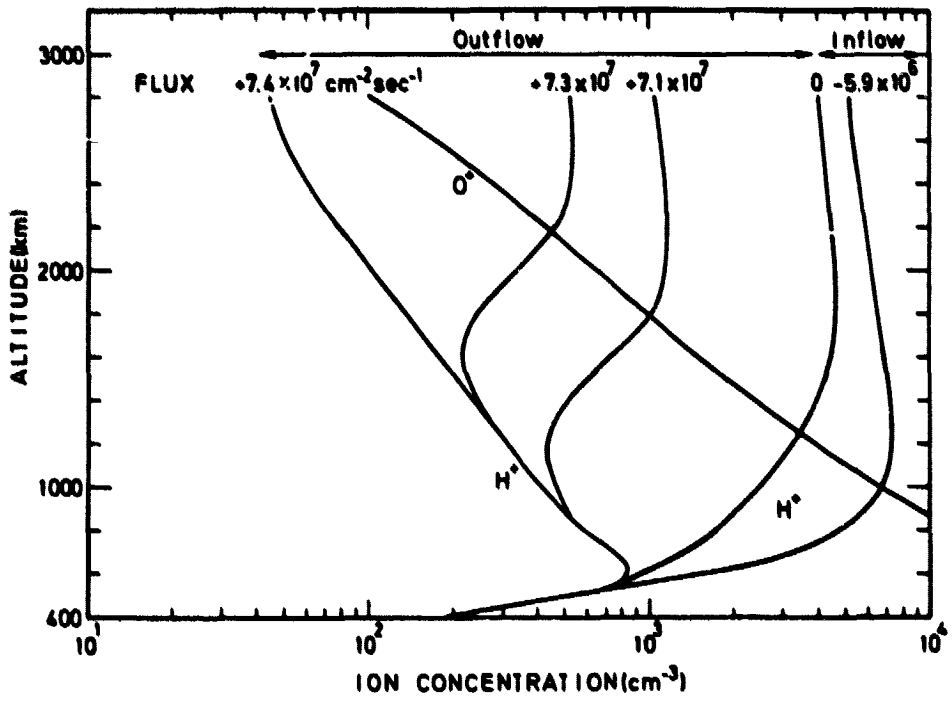

Figure 2.3 Profiles of $n(H^+)$ and $n(O^+)$ for a 1000 K model thermosphere and different escape fluxes. The $n(O^+)$ profile applies to the largest outflow. Also, $n(O^+)|_{400\ km} = 2 \times 10^5$ cm^{-3}, $T_e|_{400\ km} = 2500$ K, and the heat flux at 400 km is 5×10^9 eV cm^{-2} s^{-1} [after *Banks and Kockarts*, 1973].

The continuity equation for ions in general is

$$(\partial n_i/\partial t) + \nabla\cdot(n_i\vec{u}_i) = p_i - \ell_i \tag{2.16}$$

where n_i is the number density of the ion, p_i is the production rate of ions, ℓ_i is the loss rate of ions.

The ion continuity equation parallel to the magnetic field is

$$(\partial n_i/\partial t) + \frac{1}{A}\frac{\partial(n_i u_i A)}{\partial s} = p_i - \ell_i \tag{2.17}$$

where s is length along the field line and A is the area of the field tube at point s.

Since the ion mass is much greater than the electron mass, the electron momentum equation can be expressed simply as

$$\frac{1}{n_e}\frac{\partial p_e}{\partial s} + eE_{||} = 0 \tag{2.18}$$

Using (2.18), (2.17) can be expressed as

$$\frac{\partial u_i}{\partial t} + u_i\frac{\partial u_i}{\partial s} + g_{||} + \frac{1}{n_i m_i}\frac{\partial p_i}{\partial s} + \frac{Z_i}{n_e m_i}\frac{\partial p_e}{\partial s} = \sum_k \nu_{ik}(u_i - u_k) \tag{2.19}$$

where charge neutrality requires that

$$n_e = \sum_i Z_i n_i \tag{2.20}$$

Equations (2.17) and (2.19) are nonlinear differential equations and are difficult to solve analytically without making some initial approximations. Fortunately, the flow conditions of diffusive equilibrium and low speed flow permit explicit analytic results. At low latitudes these two conditions are enough to describe typical conditions in the topside ionosphere [*Nagy et al.*, 1968].

2.7 *Diffusive Equilibrium*

The complex problem of solving for ion density distributions is simplified in the case of diffusive equilibrium. When considering an ionosphere made up of several different ion species the assumption, $u_i = 0$, for all ion species makes explicit results possible. Ignoring centrifugal force and letting $u_i = 0$ equation (2.19) for steady state conditions can be expressed as

$$\frac{1}{n}\frac{\partial p_j}{\partial s} + m_i g_{||} - Z_i e E_{||} = 0 \tag{2.21}$$

The electron momentum equation becomes

$$\frac{1}{n_e}\frac{\partial p_e}{\partial s} + e E_{||} = 0 \tag{2.22}$$

Charge separation electric fields in the electron momentum equation are large enough so that inertial, gravitational and frictional effects can be ignored.

The effect of gravitation in equations (2.21) and (2.22) is that the light ions are displaced to regions of the weakest gravity. Parallel electric fields are also important in keeping the ions in layers at higher altitudes. The gradients of density with respect to s can be removed from equations (2.21)-(2.22) to give the parallel electric field.

$$eE_{||} = \frac{g_{||}\sum_j^i (Z_j n_j m_j / n_e) + kT_i(\partial/\partial s \ \ln(T_i/T_e))}{T_i/T_e + \sum_j^i (Z_j^2 \, n_j/n_e)} \tag{2.23}$$

For an example take the case where $n(O^+) >> n(H^+)$ and $n(O^+) >> n(He^+)$

$$eE_{||} = \frac{g_{||}\, m(O^+) + kT_i(\partial/\partial s \ \ln(T_i/T_e))}{T_i/T_e + 1} \tag{2.24}$$

Equation (2.24) shows the parallel electric field decreases the effect of gravity on ion distribution because if $eE_{||}$ is substituted into (2.16) the coefficient of the gravity term is less than one.

Now, since $eE_{||}$ is known the ion density distributions can be calculated from the equations below.

$$\frac{1}{n_e}\frac{\partial n_e}{\partial s} = -\frac{g_{||}\sum_j^i (Z_j n_j m_j/n_e) + kT_i(\partial/\partial s \ln(T_i/T_e)}{kT_i + kT_e \sum_j^i (Z_j^2 n_j/n_e)} - \frac{\partial \ln T_e}{\partial s} \tag{2.25}$$

$$\frac{1}{n_i}\frac{\partial n_i}{\partial s} = -\frac{m_i g_{||}}{kT_i} + Z_i \frac{T_e}{T_i}\frac{g_{||}\sum_j^i (Z_j n_j m_j/n_e) + kT_i(\partial/\partial s \ln(T_i/T_e))}{kT_i + kT_e \sum_j^i (Z_j^2 n_j/n_e)} - \frac{\partial \ln T_i}{\partial s} \tag{2.26}$$

For an example take the case where j is a minor species in a plasma dominated by a singly charged ion (H^+ in O^+ plasma). Also take $\partial T_i/\partial s = \partial T_e/\partial s = 0$ then

$$\frac{1}{n(H^+)}\frac{\partial n(H^+)}{\partial s} \simeq \frac{-m(H^+)g_{||}}{kT_i}\left[1 - \frac{m(O^+)/m(H^+)}{1 + T_i/T_e}\right] \tag{2.27}$$

This equation shows that $n(H^+)$ can decrease or increase with altitude depending on the sign of the term in the brackets. In the topside ionosphere T_i/T_e will be between 0.25 and 1.00; so $n(H^+)$ will increase with altitude.

$$n(H^+) = n(H^+)_a \exp \int_a^s \frac{m(H^+)g_{||}}{kT_i}\left[\frac{m(O^+)/m(H^+)}{1 + T_i/T_e} - 1\right] ds \tag{2.28}$$

$$= n(H^+)_a \exp\left[\int_a^s \frac{15\, m(H^+) g_{||}}{kT_i}\, ds\right] \tag{2.29}$$

Equations (2.25) and (2.26) can be simplified with the use of the mean ionic mass.

$$m^+ = n_j m_j / n_e \tag{2.30}$$

Also, the principal ions of the topside ionosphere are singly charged; so the expressions for the electron and ion density are

$$\frac{1}{n_e}\frac{\partial n_e}{\partial s} = -\frac{m^+ g_{||}}{k(T_e + T_i)} - \frac{\partial \ln(T_e + T_i)}{\partial s} \tag{2.31}$$

$$\frac{1}{n_i}\frac{\partial n_i}{\partial s} = -\frac{m_i g_{||}}{kT_i} + \frac{m^+ g_{||}}{k(T_e + T_i)}\,\frac{T_e}{T_i} - \frac{\partial \ln(T_e + T_i)}{\partial s} \tag{2.32}$$

If equations (2.31) and (2.32) are integrated along the magnetic field tube from a to s the coupled equations for the electron and ion density distributions become

$$n_e = n_{ea}\frac{(T_e + T_i)_a}{(T_e + T_i)} \exp\left[-\int_a^s \frac{g_{||}\, m^+}{k(T_e + T_i)}\, ds'\right] \tag{2.33}$$

$$n_j = n_{ja}\frac{(T_e + T_i)_a}{(T_e + T_i)} \exp\left[-\int_a^s \frac{g_{||}\, m_j}{kT_i}\, ds' + \int_a^s \frac{T_e}{T_i}\frac{m^+ g_{||}}{k(T_e + T_i)}\, ds'\right] \tag{2.34}$$

Equations (2.33) and 2.34) must be solved numerically to obtain electron and ion density distributions for arbitrary electron and ion temperature variations. An example of these calculations is shown in Figures 2.4-2.7. These profiles were obtained from (2.34) by numerically integrating upward from 500 km using different boundary conditions at 500 km. Equation (2.7) was used

as a boundary condition for $n(H^+)$ in one case. In all cases $n(O^+)$ was assumed to be 1×10^5 cm^{-3} at 500 km. Also, different temperature models were used for ion and electron temperature profiles. They are shown along with $n(H^+)$ and $n(O^+)$ on each figure. The boundary condition for H^+ in Figures 2.4 and 2.5 were applied at 200 km using equation (2.7). This was due to the large H^+ number densities which resulted from using equation (2.7) at 500 km. The H^+ number densities were too large to satisfy the assumptions used in equations (2.31) and (2.32). The O^+ boundary condition was still applied at 500 km. Below 500 km an experimental profile for the O^+ number density was used in all the cases.

Figures 2.4-2.7 show that H^+ dominates the ion distribution at high altitudes. The level where the composition transition between H^+ and O^+ takes place is at slightly higher altitudes for atmospheres having larger thermopause temperatures.

In Figure 2.6 H^+ and O^+ number density profiles are shown for the cases where H^+ at 500 km is 1×10^3 cm^{-3} and that found from equation (2.7). The O^+ profile decreases more rapidly in the first case. The calculations for the case of $n(H^+) = 1 \times 10^3$ cm^{-3} at 500 km are not shown in Figures 2.5 and 2.8 because the profiles are almost exactly the same and the temperature profiles are all about the same from 500 to 1200 km.

In Figure 2.8 the dependence of ion composition on electron temperature is shown. The composition transition level moves to higher altitudes as the heat flux and $T_e + T_i$ increase. This is due mainly to a slower decrease in O^+ densities as $T_e + T_i$ increases.

2.8 *Low Speed Plasma Flow*

Besides diffusive equilibrium the atmosphere of the low and mid latitudes can exist in a state of low speed plasma flow. Indeed, low speed plasma flow

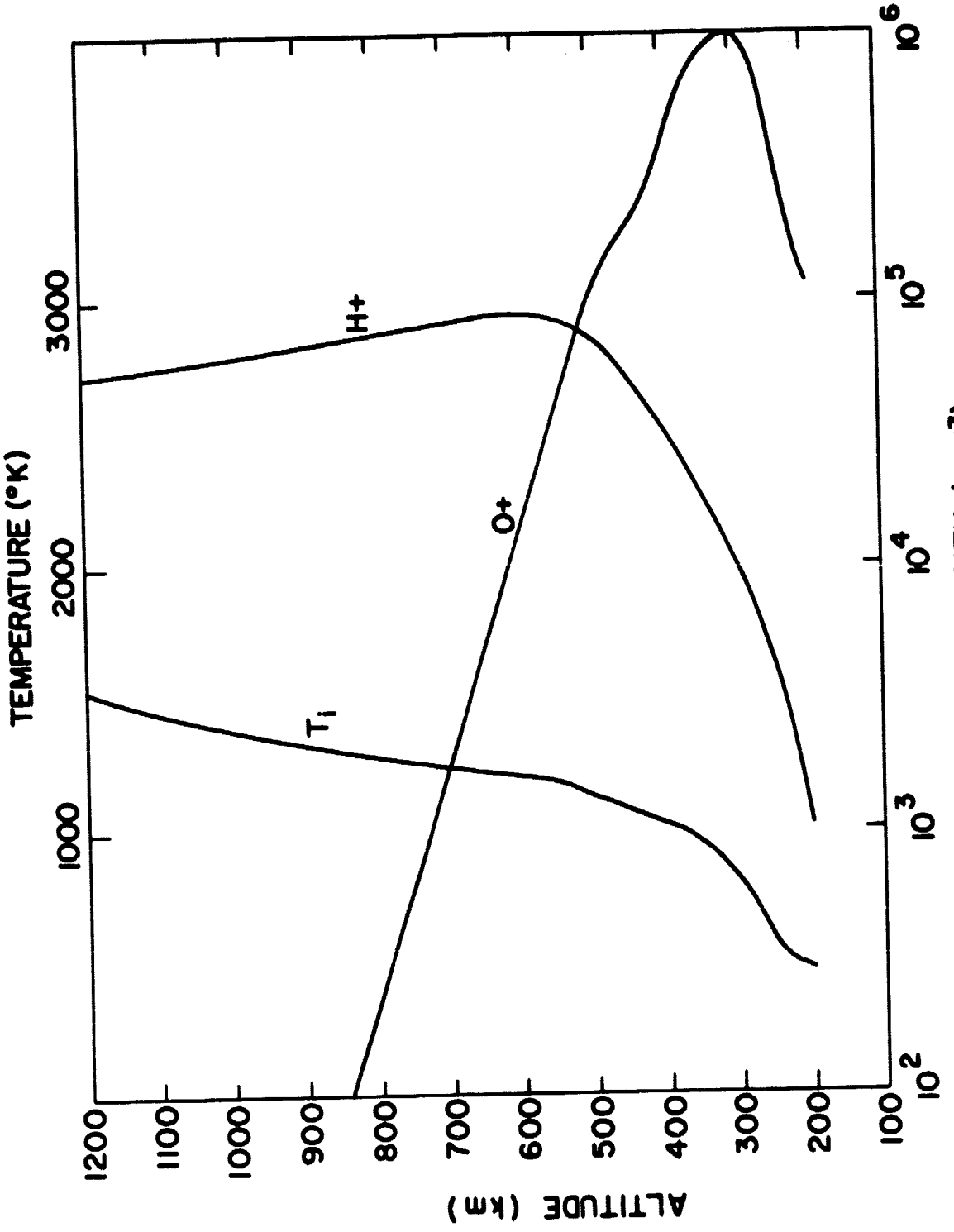

Figure 2.4 Profiles of $n(O^+)$ and $n(H^+)$ for a 500 K model thermosphere. The ion temperature profile is also shown.

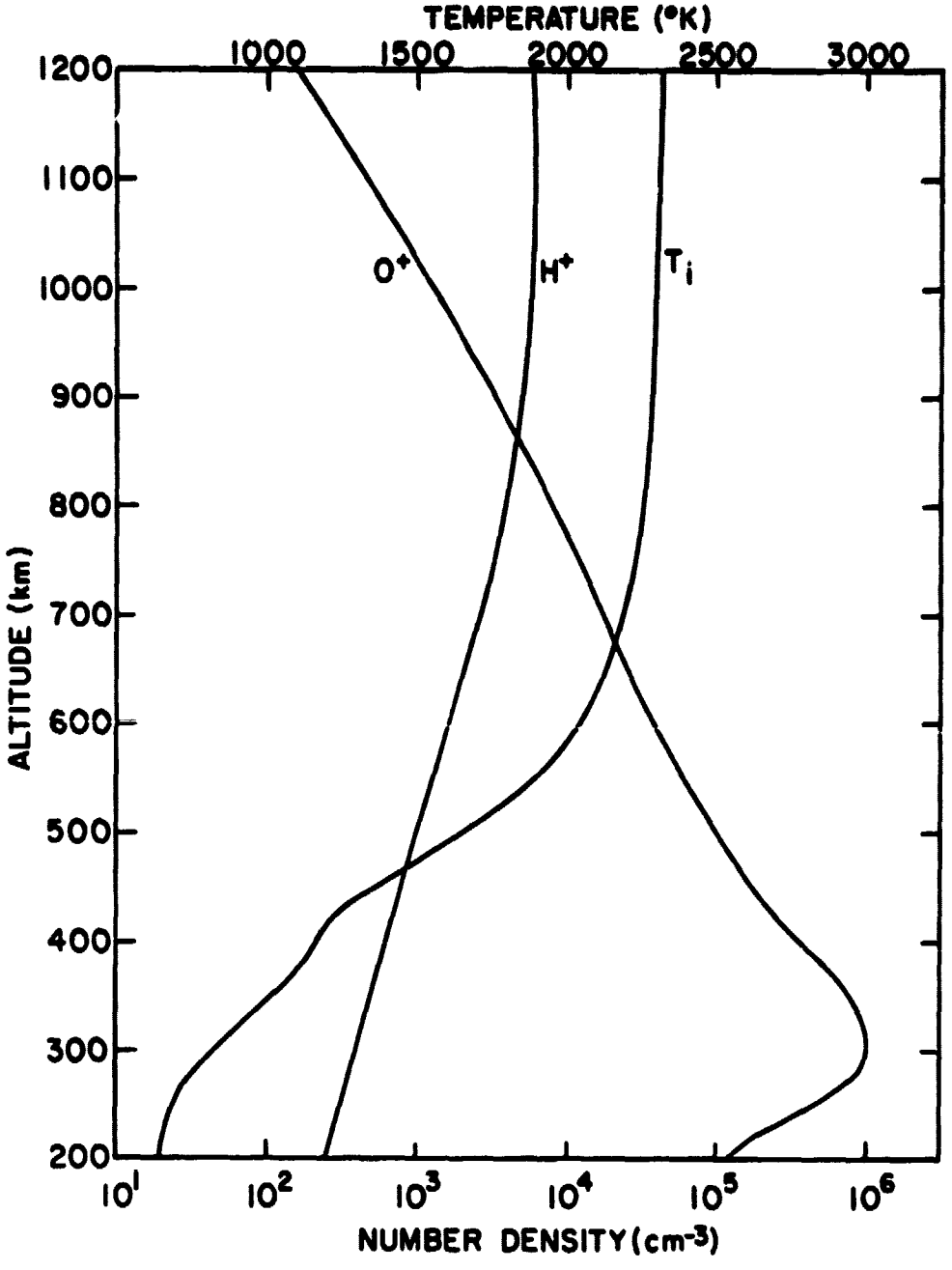

Figure 2.5 Profiles of $n(O^+)$ and $n(H^+)$, and T_i for a 700 K model thermosphere.

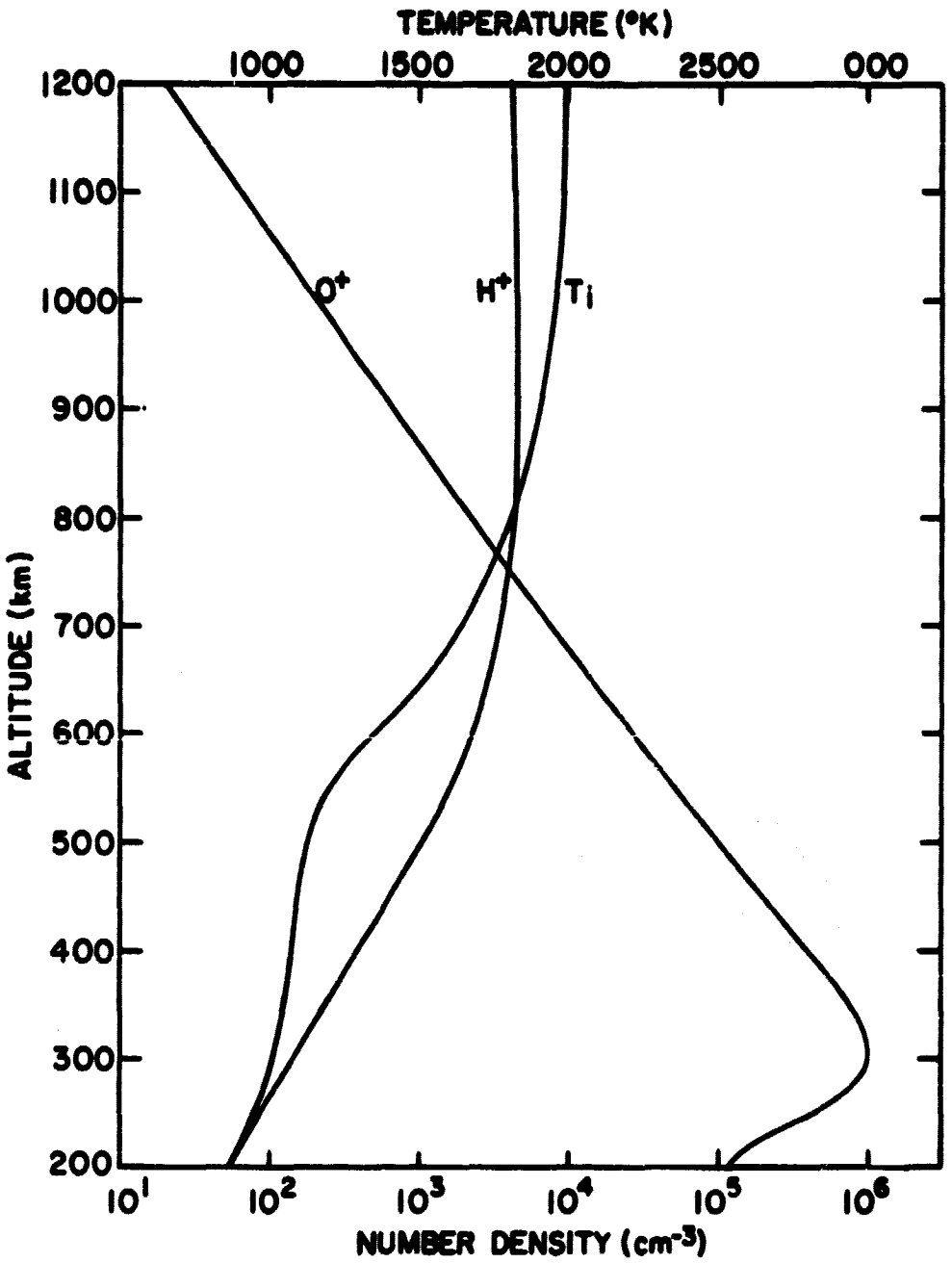

Figure 2.6 Profiles of $n(O^+)$, $n(H^+)$, and T_i for a 700 K model thermosphere.

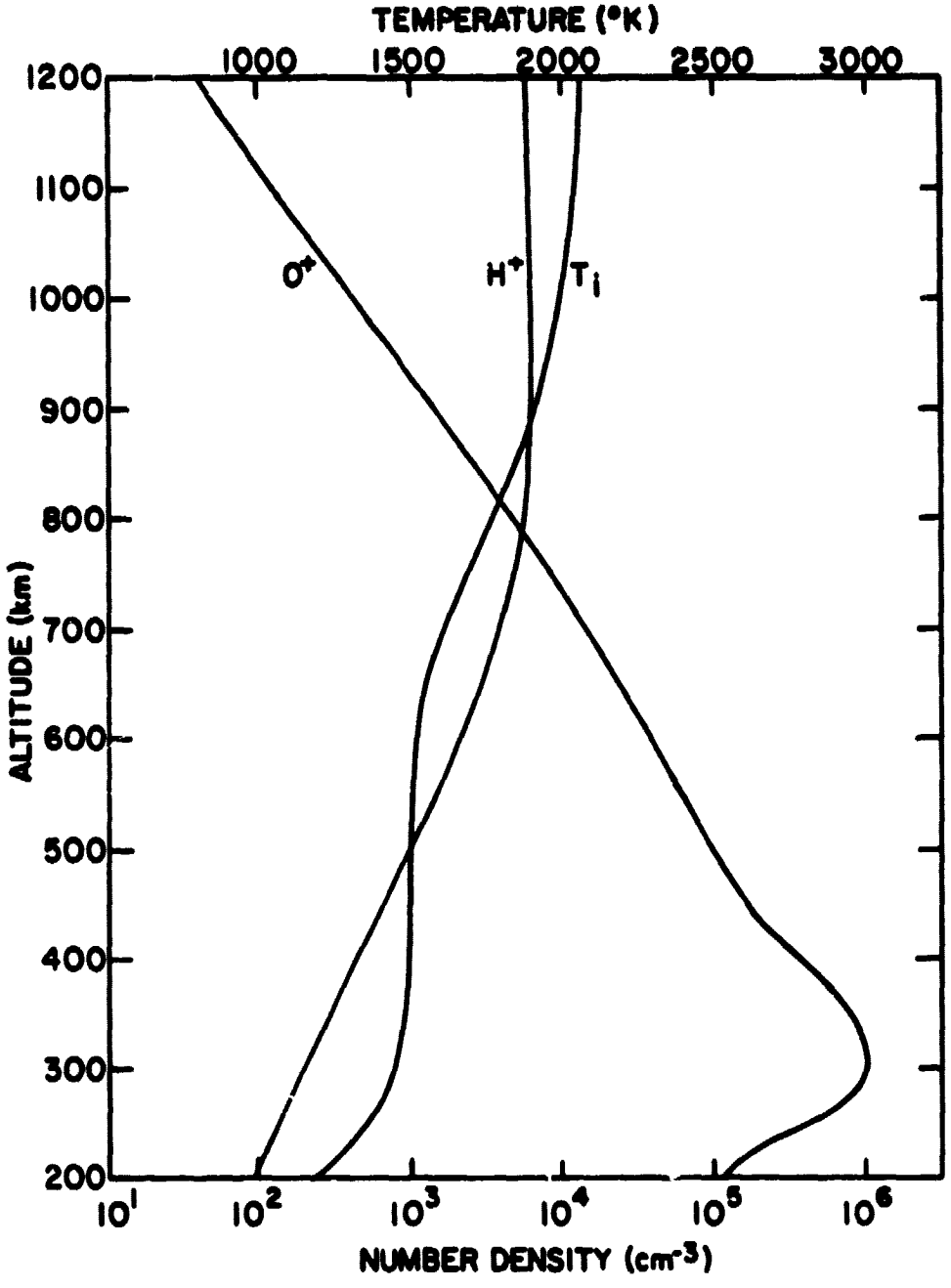

Figure 2.7 Profiles of $n(O^+)$, $n(H^+)$, and T_i for a 1500 K model thermosphere.

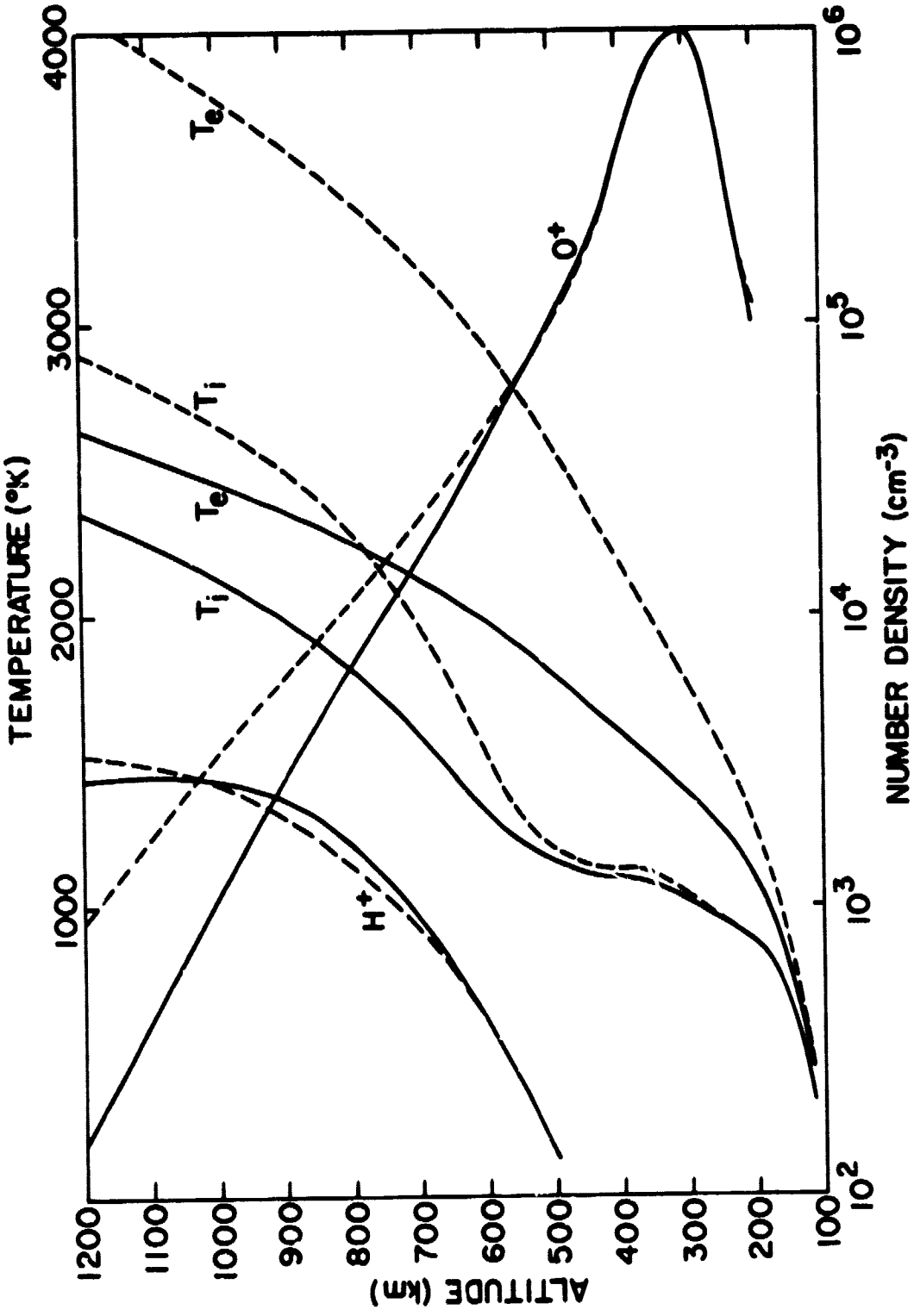

Figure 2.8 Profiles of $n(O^+)$ and $n(H^+)$ for a 1000 K model thermosphere and different electron temperature profiles.

is important because the coupling between the magnetosphere and the F_2 region results in almost continual ion transport.

The problem of ion flow in the topside ionosphere should not be confused with the ambipolar diffusion of O^+ in the F_2 region. In the topside ionosphere several ion species are involved in transport. Also, the scattering cross section for ambipolar diffusion is very small compared to the Coulomb scattering cross section of thermal protons with oxygen ions [*Hanson and Ortenburger*, 1961].

The low speed flow momentum follows from (2.19)

$$\frac{\partial u_i}{\partial t} + g_{||} + \frac{1}{n_i m_i}\frac{\partial p_i}{\partial s} + \frac{Z_i}{n_e m_i}\frac{\partial p_e}{\partial s} = \sum_k \nu_{ik}(u_i - u_k) \qquad (2.35)$$

where the inertial term is dropped since this case applies to low speed flow. (2.30) is valid as long as $u << (kT_i/m_i)^{\frac{1}{2}}$ i.e. subsonic flow.

Due to the nonlinear coupling between the ion equations of motion, analytic solutions for the ion densities have not been obtained. But in the regions below 1000 km H^+ and He^+ are usually minor constituents. Thus, the electron pressure gradient term (in equation (2.35)) becomes linear (in $n(O^+)$.) Using the assumptions: 1) a minor ion species, j, diffuses through a stationary background ion gas of density n_i with $n_j << n_i$; 2) steady state is used in the equation of motion for electrons and major ions; 3) the temperatures of the two ion species are the same, one can derive analytic expressions for the ion density and ion flux [*Banks and Kockarts*, 1973].

The equations of motion for electrons and ions are

$$\frac{1}{n_e}\frac{\partial p_e}{\partial s} + eE_{||} = 0 \qquad (2.36)$$

$$\frac{1}{m_i n_i}\frac{\partial p_i}{\partial s} + g_{||} - \frac{eE_{||}}{m_i} = \nu_{ij}\, u_j \tag{2.37}$$

$$\frac{1}{m_j n_j}\frac{\partial p_j}{\partial s} + g_{||} - \frac{eE_{||}}{m_j} = -\nu_{ji}\, u_j \tag{2.38}$$

where $u_i = 0$ and ν_{ji} is defined such that $n_i m_i \nu_{ij} = n_j m_j \nu_{ji}$.

Eliminating $eE_{||}$ from (2.38) with (2.36) one finds that

$$u_j = -D_{ji}\left[\frac{1}{n_j}\frac{\partial n_j}{\partial s} + \frac{m_i g_{||}}{kT_i} + \frac{T_e/T_i}{n_e}\frac{\partial n_e}{\partial s} + \frac{1}{T_i}\frac{\partial (T_e + T_i)}{\partial s}\right] \tag{2.39}$$

where $D_{ji} = (kT_i/m_j)/\nu_{ji}$.

In (2.39) $\frac{1}{n_e}\frac{\partial n_e}{\partial s}$ is unknown, but in most real cases the distribution of of electron is assumed to be equal to the O^+ density distribution. Also if it is assumed that the momentum transferred to O^+ from the minor constituents does not affect O^+ distributions, i.e. $m_j \nu_{ij} u_j = 0$, then (2.36) + (2.37) gives

$$\frac{1}{m_i n_e}\frac{\partial (p_i + p_e)}{\partial s} = -g_{||} \tag{2.40}$$

which gives

$$\frac{1}{n_e}\frac{\partial n_e}{\partial s} = -\frac{m_i g_{||}}{k(T_e + T_i)} - \frac{1}{(T_e + T_i)}\frac{\partial (T_e + T_i)}{\partial s} \tag{2.41}$$

Substituting this into (2.39) and using the definitions

$$H_p = k(T_e + T_i)/m_i g_{||} \tag{2.42}$$

and

$$H_j = kT_i/m_j g_{||} \tag{2.43}$$

one gets $u_j = -D_{ji}\left[\frac{1}{n_j}\frac{\partial n_j}{\partial s} + \frac{1}{H_j} - \frac{T_e/T_i}{H_p} - \frac{1}{T_e + T_i}\frac{\partial (T_e + T_i)}{\partial s}\right]$ (2.44)

Equation (2.44) in conjunction with the jth species continuity equation

$$\frac{1}{A}\frac{d(n_j u_j A)}{ds} = p_j - \ell_j \tag{2.45}$$

can be used to find a second-order differential equation in n_j which is

$$\frac{d^2 n_j}{ds} + X(s)\frac{a n_j}{ds} + Y(s) n_j = Z(s) \tag{2.46}$$

where p_i is the ion production rate, ℓ_i is the loss rate, $X(s)$, $Y(s)$, and $Z(s)$ are functions derived from quantities in equations (2.45) and (2.44).

To solve (2.46) numerical methods are required but analytic solutions can be found when the production, loss, thermal gradients and gravity variations are ignored. The two linear independent solutions are given as

$$n_j = n_{ja}\exp\left[\frac{T_e/T_i}{H_p} - \frac{1}{H_j}\right](s-a) \tag{2.47}$$

$$n_j = n_{ja}\exp\left[-(s-a)/H_p\right] \tag{2.48}$$

where a represents the lower reference point.

The first solution (2.47) is the solution for the condition $u_j = 0$, non-diffusing minor constituents. This solution gives a minor ion density which increases with altitude if $H_j < H_p\, T_i/T_e$. At high altitudes the condition $n_j << n_i$ is violated by this solution.

The second solution (2.48) gives a minor constituent which decreases in density with altitude. The diffusion velocity associated with this solution can be derived from (2.44) as

$$u_j = D_{ji}\left[\frac{1 + T_e/T_i}{H_p} - \frac{1}{H_j}\right] \tag{2.49}$$

The case of H^+ flowing through O^+ has a limiting flux of

$$\Phi_i = n_j u_j = 1.1 \times 10^4 [n(H)/n(O)]\, T_n^{\frac{1}{2}}\, T_i \tag{2.50}$$

TABLE 2.3

H^+ limiting fluxes.

T_n(K)	n(O) (cm^{-3})	n(H) (cm^{-3})	Flux($T_i = T_n$)	Flux (T_i = 2000 K)
750	4.3×10^3	7.7×10^6	4.1×10^9	1.1×10^{10}
1000	4.4×10^6	1.2×10^5	9.6×10^6	1.9×10^7
1250	1.7×10^7	3.3×10^4	9.5×10^5	1.5×10^6
1500	3.6×10^7	1.4×10^4	2.5×10^5	3.3×10^5

Geisler [1967] has found an analytic expression for the limiting flux of H^+ moving through O^+ for thermal equilibrium. Using a different approach his results predict H^+ limiting fluxes which are approximately the same as those presented in Table 2.3.

Typical limiting fluxes for different thermospheric models are shown in Table 2.3. Values in Table 2.3 are based on thermal equilibrium between electrons and ions and thus the limiting fluxes are underestimated. Numerical solutions give somewhat larger fluxes.

The previous discussion dealt with approximate solutions to the ion momentum and ion continuity equations. H^+ and He^+ are not minor constituents at high altitudes and therefore the solutions for the density distributions of H^+ and He^+ are not generally analytic. Equations (2.39) and (2.45) must be solved by numerical methods.

3. THERMAL PROCESSES IN THE TOPSIDE IONOSPHERE

3.1 *Introduction*

In this chapter all the various heat transfer processes in the topside ionosphere will be discussed. This includes heat transfer through electron-neutral elastic and nonelastic collisions, electron-ion Coulomb collisions, ion-ion Coulomb collisions, and ion-neutral elastic and nonelastic collisions. Also discussed is heat transfer through thermal diffusion, convection, and thermal conduction. Particular attention will be paid to the role of thermal conduction in determining electron and ion temperatures.

Electrons created in the photoionization of neutral gas particles was recognized as a source of electron gas heating in 1946 [*Drukarev*, 1946]. When a solar photon ionized a neutral gas particle the excess energy, the energy difference between the incident photon and final ion is given to the photoelectron. In fact, most of the energy goes to the photoelectron because the mass of the ion is much greater than the electron mass. This photoelectron loses its energy as it travels through the atmosphere. At energies near 15 eV the photoelectron exchanges its energy with neutral gases through nonelastic excitation collisions. At energies near 1.5 eV the photoelectron transfers its energy to the ambient electron gas.

The important sources of energy for the atmospheric gases all originate from ultraviolet radiation from the sun (see Figure 3.1). The ambient electron gas receives most of its energy through Coulomb collisions with the hotter photoelectrons. The thermal electrons, on the other hand, are an important source of heating of the ion gases. The neutral gas receives its energy through superelastic collisions with excited neutrals produced when ultraviolet radiation from the sun is absorbed.

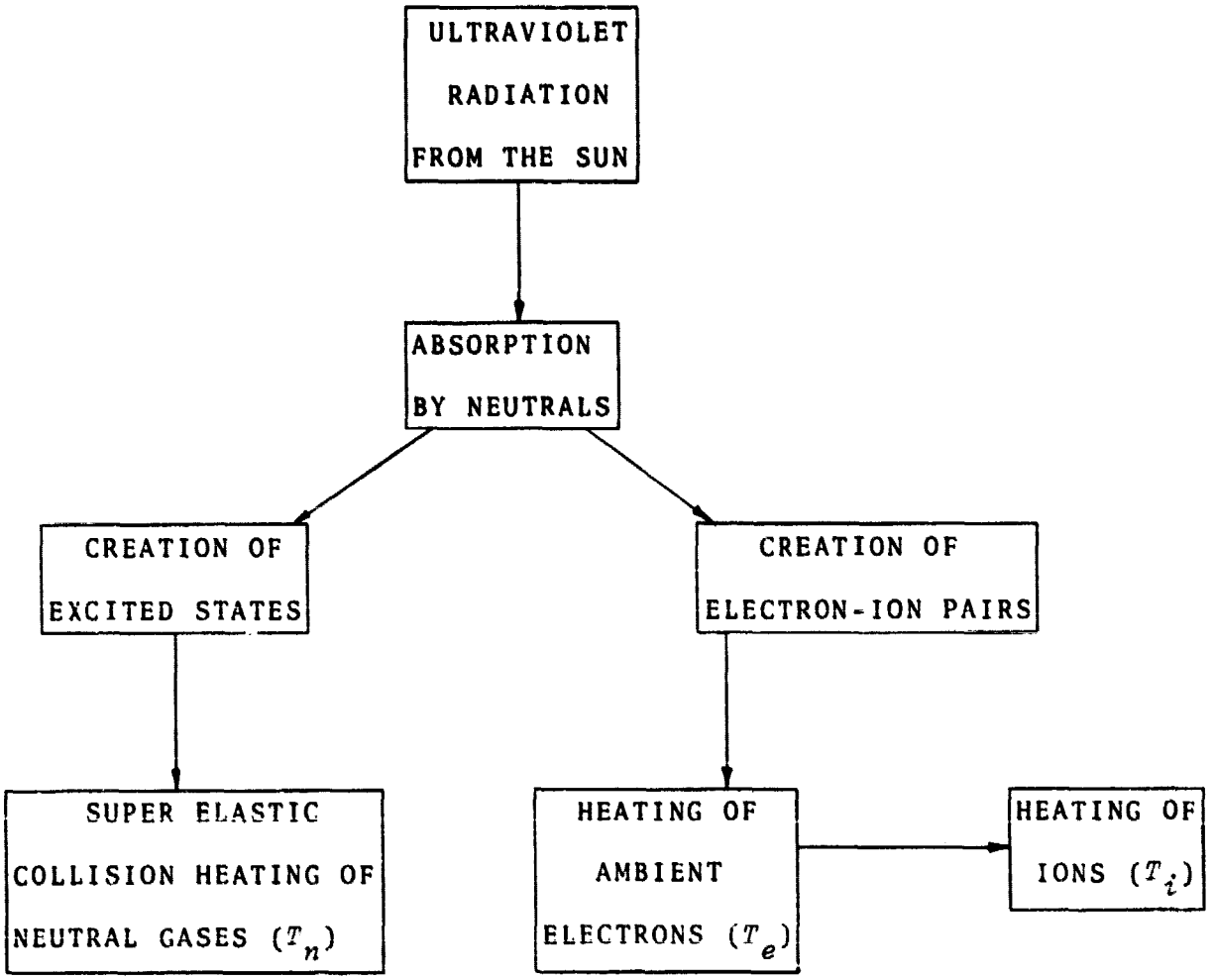

Figure 3.1 Sources of energy for particles in the F region.

The importance of heating of the ambient electron gas by photoelectrons was first discovered by *Hanson* [1963] who found that the electron temperature is substantially greater than the neutral temperature in the *F* region. This is due to the heating of ambient electrons by photoelectrons. Experimental data from a Langmuir probe on a Javelin rocket shows that the electron temperature is greater than the neutral temperature (see Figure 3.2) [*Hanson et al.*, 1969]. Incoherent scatter radar measurements [*Evans*, 1962; *Hagen and Hsu*, 1974], other rocket measurements [*Spencer et al.*, 1965, *Nagy et al.*, 1963], and satellite measurements [*Smith*, 1968, *McClure et al.*, 1973] show conclusively that the electrons are heated to higher temperatures than neutrals which is due to photoelectron heating.

The importance of electron heat conduction was also deduced by *Hanson* [1963] who found that heat conduction is responsible in keeping the electron temperature constant even at high altitudes. Photoelectrons produced at lower altitudes were found to contribute to non-local heating at higher altitudes [*Geisler and Bowhill*, 1965], which in turn is conducted back down to lower altitudes along the lines of magnetic force.

Photoelectrons which transfer most of their heat to the ambient electron gas do not heat the ion gases because of the mass of ions is much greater than the mass of electrons. The thermal electrons are sources of energy for the ion gases. Below 300 km neutral gases rapidly cool the ion gases and so $T_i \approx T_n$ [*Hanson*, 1963]. At high altitudes the energy given to ions by electrons cannot be dissipated by the ions to the neutrals. In fact, the ion temperature approaches the electron temperature at high altitudes [*Banks*, 1967a].

Thermal conduction for the ion gases is important in keeping the ion temperature substantially below the electron temperature [*Banks*, 1967b].

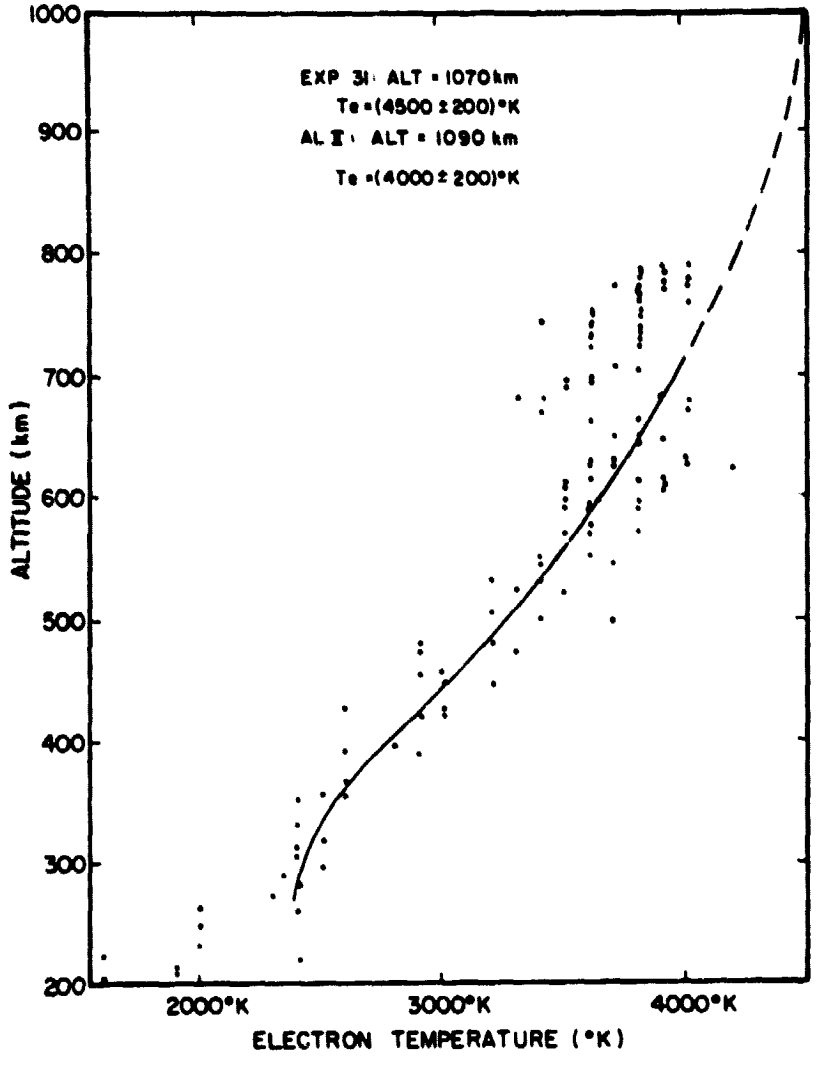

Figure 3.2 An electron temperature profile from a Javelin rocket experiment [after *Hanson et al.*, 1969].

Also important is the effect of heat transfer between individual ion species. This heat transfer is weak enough to permit significant temperature differences between O^+ and H^+ at altitudes near 400 km [*Banks*, 1967a].

In the following sections the important heat transfer processes of the ionosphere will be discussed in more detail.

3.2 *Energy Balance Equations*

The energy balance equation for a plasma composed of electrons, several ion species, and neutral gases can be derived from Boltzmann's equation as

$$n_r DE_r/Dt - \partial p_r/\partial t + \nabla\cdot\vec{K}_r = M_r + n_r\vec{F}_r\cdot\vec{u}_r \tag{3.1}$$

where n_r is the gas number density, $p_r = n_r kT_r$ is the gas partial pressure, T_r the gas temperature, u_r the rth species transport velocity, K_r the rth species heat flux vector, F_r the external forces. M_r is the kinetic energy moment of the collision term

$$M_r = \frac{1}{2}\int m_r\vec{v}_r\cdot\vec{v}_r(\partial f_r/\partial t)_c\, dv_r \tag{3.2}$$

$$E_r = \frac{5}{2}kT_r + \frac{1}{2}m_r u_r^2 \tag{3.3}$$

$$DE_r/Dt = \partial E_r/\partial t + \vec{u}_r\cdot\nabla E_r \tag{3.4}$$

The term $(\partial f_r/\partial t)_c$ is the change in the velocity distribution function per unit time for a collision, M_r is the mass of the rth particle, and k is Boltzmann's constant. The term M_r represents the formation of energy per unit volume minus the energy loss rates per unit volume due to interactions with other gases. M_r includes both transfer energy due to unequal mean flow velocities and unequal species temperatures. This is expressed in the general form $M_r = \sum_p M_{rp}$, where

$$M_{rp} = [2m_r m_p/(m_r + m_p)^2] n_r \bar{\nu}_{rp} \left[\tfrac{3}{2} k (T_p - T_r) f(v/\alpha) \right.$$

$$\left. + \tfrac{1}{2}(m_r \vec{u}_r + m_p \vec{u}_p)(\vec{u}_p \cdot \vec{u}_r) g(v/\alpha) \right] \tag{3.5}$$

for elastic collisions, with $\bar{\nu}_{rp}$ the momentum transfer collision frequency, $v = |\vec{u}_r - \vec{u}_p|$, $\alpha = 2k(T_r/m_r + T_p/m_p)$, and $f(v/\alpha)$ and $g(v/\alpha)$ are functions determined by the velocity dependence of the interaction cross section p is an index indicating a neutral or charged particle.

The effect of an external magnetic field is present in the flow vector $\vec{K}_r$, which becomes increasingly anisotropic as the ratio of the collision frequency to gyrofrequency becomes small. Then most of the heat flows parallel to the magnetic field. Another effect of the external magnetic field is the confinement of charged particle flow along the magnetic field lines.

The term M_r can be reduced to specific forms depending on the type of interactions used. For example, if one considers the hard sphere interaction then [*Banks and Kockarts*, 1973]

$$f(v/\alpha) = \frac{\pi^{1/2}}{2} \left(\frac{v}{\alpha} + \frac{\alpha}{2v}\right) \operatorname{erf}\left(\frac{v}{\alpha}\right) + \frac{1}{2} \exp\left(\frac{-v^2}{\alpha^2}\right) \tag{3.6}$$

$$g(v/\alpha) = \frac{3\pi^{1/2}}{8} \left(\frac{v}{\alpha} + \frac{\alpha}{v} - \frac{\alpha^3}{4v^3}\right) \operatorname{erf}\left(\frac{v}{\alpha}\right)$$

$$+ \frac{3}{8}\left(1 + \frac{\alpha^2}{2v^2}\right) \exp\left(\frac{-v^2}{\alpha^2}\right) \tag{3.7}$$

where $$\bar{\nu}_{rs} = \frac{4}{3} n_s \left(\frac{8k}{\pi}\right)^{1/2} (T_r/m_r + T_s/m_s)^{1/2} \pi\sigma^2 \tag{3.8}$$

erf is the error function, and σ is the collision cross section. For Coulomb interaction, one has [*Banks and Kockarts*, 1973]

$$f(v/\alpha) = \exp(-v^2/\alpha^2) \tag{3.9}$$

$$g(v/\alpha) = \frac{3\pi^{\frac{1}{2}}}{4}\left(\frac{\alpha}{v}\right)^3 \operatorname{erf}\left(\frac{v}{\alpha}\right) - \frac{3}{2}\left(\frac{\alpha}{v}\right)^2 \exp\left(\frac{-v^2}{\alpha^2}\right) \tag{3.10}$$

where $$\bar{\nu}_{rs} = \frac{16\pi^{\frac{1}{2}}}{3}\,\frac{n_s Z_r^2 Z_s^2 e^4 \ln \Lambda}{\mu\,\alpha^{3/2}} \tag{3.11}$$

μ is the reduced mass given by

$$\mu = m_r m_s/(m_r + m_s)$$

Z_r, Z_s are the atomic charge of the rth and sth particle, and $\ln \Lambda$ is the factor which depends on the minimum scattering angle (it will be discussed later). For inverse velocity dependent cross section

$$f(v/\alpha) = g(v/\alpha) = 1 \tag{3.12}$$

In this case the energy transfer term is

$$M_{rs} = [(2m_r m_s/(m_r + m_s)^2]n_r \bar{\nu}_{rs}\left[\frac{3}{2}k(T_s - T_s) + \frac{1}{2}(m_s\vec{u}_s + m_r\vec{u}_r)\cdot(\vec{u}_s - \vec{u}_r)\right] \tag{3.13}$$

Using this result equation (3.1) can be reduced to

$$n_r(DE_r/Dt) - \partial p_r/\partial t = n_r\vec{F}_r\cdot\vec{u}_r - \nabla\cdot\vec{K}_r + \sum_s \frac{2m_r m_s}{(m_r + m_s)^2}\, n_r\bar{\nu}_{rs}$$

$$\left[\frac{3}{2}k(T_s - T_r) + \frac{1}{2}(m_s\vec{u}_s + m_r\vec{u}_r)\cdot(\vec{u}_s - \vec{u}_r)\right] \tag{3.14}$$

Equation (3.14) can be further reduced if one uses the fact that the heat flow vector is essentially along the magnetic field line. A cylindrical coordinate system whose axis is parallel to $\vec{B}$ and where changes in the intensity of $\vec{B}$ are taken into account gives

$$\nabla\cdot\vec{K}_r = -\frac{1}{A}\frac{\partial}{\partial s}\, AK_r'\,\frac{\partial T_r}{\partial s} \tag{3.15}$$

where s is a coordinate parallel to $\vec{B}$, A is the area of magnetic field tube at point s, $A \propto B^{-1}$, and K_r' is the rth species thermal conductivity.

3.3 *Electron Energy*

The source of energy for electrons is the energy from photoelectrons. Since photoelectrons are created from photoionization of the neutral atmosphere, one must know the ultraviolet flux spectrum, the composition of the neutral atmosphere, and relevant absorption and ionization cross sections in order to determine the photoelectron energy spectrum. Photoelectrons are transported and can deposit their energy elsewhere in the atmosphere. Thus, the photoelectron flux is needed in order to solve the problem of photoelectron heating of the ambient electron gas. The solution of the photoelectron transport is a difficult problem and will be discussed later.

Usually when dealing with electrons one divides the energy distribution into two components. The first component deals with the ambient electron energy distribution. This component is assumed to have a Maxwellian distribution with a characteristic temperature T_e. This component also covers the low energy portion of the energy distribution (0.01 - 0.3 eV). The second component of the energy distribution is the so-called "tail" of the electron energy distribution. This tail contains photoelectrons with energies greater than 1.5 eV.

The ambient electrons gain energy from electron-electron Coulomb collisions with a rate given by [*Schunk and Hays*, 1971]

$$\frac{dE}{dt} = -2\sqrt{2}\,\pi\, n_e\, e^4/(m_e E)^{1/2} \ln C_1 \tag{3.16}$$

$$\frac{dE}{dt} = -7.7 \times 10^{-6}\, n_e/E^{1/2} \ln C_1 \tag{3.17}$$

where $$C_1 = \frac{m_e v_e^3}{\gamma e^2 \omega_p} \quad \text{(classical)} \quad kT_e << E < \frac{m_e e^4}{2h^2} \tag{3.18}$$

$$C_1 = \frac{m_e v_e^2}{h \omega_p} \quad \text{(quantum) } E > \frac{m_e e^4}{2h^2} \tag{3.19}$$

with $\ln \gamma = 0.5771$ = Euler's constant, h = Planck's constant and ω_p = plasma frequency.

The photoelectron energy loss per unit length is

$$\frac{dE}{ds} = -1.3 \times 10^{-13} \frac{n_e}{E} \ln C_1 \tag{3.20}$$

Equation (3.20) can be used to calculate local photoelectron heating rates.

The electron energy balance equation must include photoelectron heating and cooling through elastic and inelastic collisions with neutral particles. Inelastic collisions are especially important because cooling through elastic collisions is generally slow. This will be discussed in detail later. The electron energy balance equation is

$$n_e \frac{DE_e}{Dt} - \frac{\partial p_e}{\partial t} = n_e \vec{F}_e \cdot \vec{u}_e - \nabla \cdot \vec{K}_e + Q_e$$
$$- L_e + \sum_s m_e n_e \bar{\nu}_{es} (\vec{u}_s - \vec{u}_e)^2 \tag{3.21}$$

where Q_e is heat production due to photoelectrons and L_e is heat loss due to inelastic and elastic collisions with neutral particles, and Coulomb collisions with ions. $\sum_s m_e n_e \bar{\nu}_{es} (\vec{u}_s - \vec{u}_e)^2$ is the rate of energy production due to elastic thermal electron collision with ions and neutrals, i.e. Joule dissipation.

3.4 *Production of Photoelectrons and Local Heating*

The production of photoelectrons is a very complex problem due to variation of the incident flux of solar photons. There have been a number of measurements of the solar EUV flux by rocket and satellite-borne instruments with varying degrees of resolution and accuracy [*Hall et al.*, 1963, 1965, 1969; *Hinteregger*, 1965; *Hall and Hinteregger*, 1970; *Hinteregger*, 1970].

When considering the ionizing effect of solar ultraviolet photons of flux I_∞ at the outer boundary of the earth's atmosphere, one has

$$q_j = n_j(\sigma_i^j I_\infty)\, e^{-\tau} \tag{3.22}$$

where n_j is the j-th neutral particle number density, q_j is the production rate of ionization, σ_i^j is the ionization cross section and τ is the optical depth given by

$$\tau = \int_z^\infty n_j \sigma_a^j ds \tag{3.23}$$

where σ_a^j is the absorption cross section, and the integration is over the optical ray path.

Equation (3.22) gives the ionization rate for a particular neutral species. To find the total ionization rate one must sum over all the neutral particles. Thus

$$q = \sum_j q_j = \sum_j n_j(\sigma_i^j I_\infty)e^{-\tau}$$

The concept of the "heating efficiency" [*Hanson and Cohen*, 1968] can be be used to calculate the rate of heat input given locally to the thermal electron gas. Heating efficiency is defined as the energy input to the thermal electron gas per electron-ion pair produced by photoionization. The photoelectron-thermal electron heating rate is given by

$$P_e(z) = \varepsilon(z)\, q = \varepsilon(z) \sum_j n_j(\sigma_i^j I_\infty)\, e^{-\tau} \tag{3.24}$$

where $\varepsilon(z)$ is the heating efficiency.

As an example of equation (3.24) take the case of an isothermal hydrostatic neutral atmosphere of temperature T_n, and total density given by

$$\sum_i n_j = n(a)\, \exp(-(z-a)/H) \tag{3.25}$$

where $H = kT_n/mg$ is the scale height, $n(a)$ is density at altitude a, and z is the altitude. If σ_a is constant then the rate $P_e(z)$ is

$$P_e(z) = \varepsilon(z)\, n(a)\sigma_i\, I_\infty$$
$$\exp(-(z-a)/H - n(a)H\sigma_a \exp(-(z-a)/H)) \qquad (3.26)$$

This shows that the rate of heat input decreases exponentially with altitude if $\varepsilon(z)$ is constant. The heating efficiency, $\varepsilon(z)$, plays an important role in the solution of the electron temperature. The altitude dependence of $\varepsilon(z)$ should show the effectiveness of neutral particles in taking energy from the photoelectrons by inelastic collisions. At altitudes above 250-300 km at moderate to high magnetic latitudes the heating efficiency loses its physical significance because photoelectrons are transported and deposit their energy non-locally. Above the altitude (escape altitude) where transport is assumed to be non-negligible, the non-local contribution is added to the heating rate [*Geisler and Bowhill*, 1965; *Nagy et al.*, 1969; *Swartz and Nisbet*, 1972].

The theory of non-local heating of the topside ionosphere by photoelectrons as developed by *Geisler and Bowhill* [1965] is based on a number of assumptions. At altitudes above about 300 km collisions between photoelectrons and neutral constituents are ignored due to low neutral densities. The photoelectron pitch angle α is assumed to remain constant as the photoelectron is slowed to thermal energy and the photoelectron flux from the conjugate ionosphere is ignored. The rate of non-local heating is given by the product of the photoelectron flux and the absolute value of dE/ds, where dE/ds is the rate of energy loss per unit lengths along the magnetic field [see Eq. 3.20 $\ln C_1 = 15$]

$$\frac{dE}{ds} \sim -Kn/E, \qquad (3.27)$$

where $K = 1.95 \times 10^{-12}$ eV^2 cm^2, E is the energy of the photoelectron, n is

the ambient electron density.

This method of calculating the non-local photoelectron heating rate serves as a basis for further calculations by *Mantas* [1973]. In his method the electron gas heating rate is also calculated from the product of dE/ds and the photoelectron flux as

$$P_e(s) = \int (dE/ds)\ \phi^T(E,s)dE \tag{3.28}$$

where $\phi^T(E,s)$ is the photoelectron flux. But the quantity (dE/ds) depends on the energy of the photoelectrons in a more complex way than that given in (3.27) since collisions of photoelectrons with neutrals are not ignored. Also $\phi^T(E,s)$ depends on the photoelectron energy.

$$\frac{dE}{ds} = \frac{1}{v_e}\ \frac{dE}{dt} = -\frac{1}{v_e} \sum_k \sum_j \nu_{kj}\ \overline{W}_j \tag{3.29}$$

where ν_{kj} is the single collision frequency, v_e is the photoelectron velocity, and $\overline{W}_j$ is the mean energy lost per collision of the j type.

$$\nu_{kj} = n_k\ g\ \sigma_k^j(g) \tag{3.30}$$

where n_k is the density of the k-th particle, g is the relative velocity of of the colliding particles, $g = |\vec{v}_1 - \vec{v}_2|$, and $\sigma_k^j(g)$ is the velocity dependent cross section for the event j.

The photoelectron flux energy spectrum has been calculated by *Mantas* [1973]. In his calculations pitch angle distributions and the effect of the photoelectron flux from the conjugate ionosphere are taken into account. The lower limit of the heat input integral (3.28) is taken to be 1eV since electron temperatures at altitudes below 300 km have energies less than this value. In Figure 3.3 profiles of the electron heating rate are shown for solar zenith angle $\chi = 0°$ and $90°$.

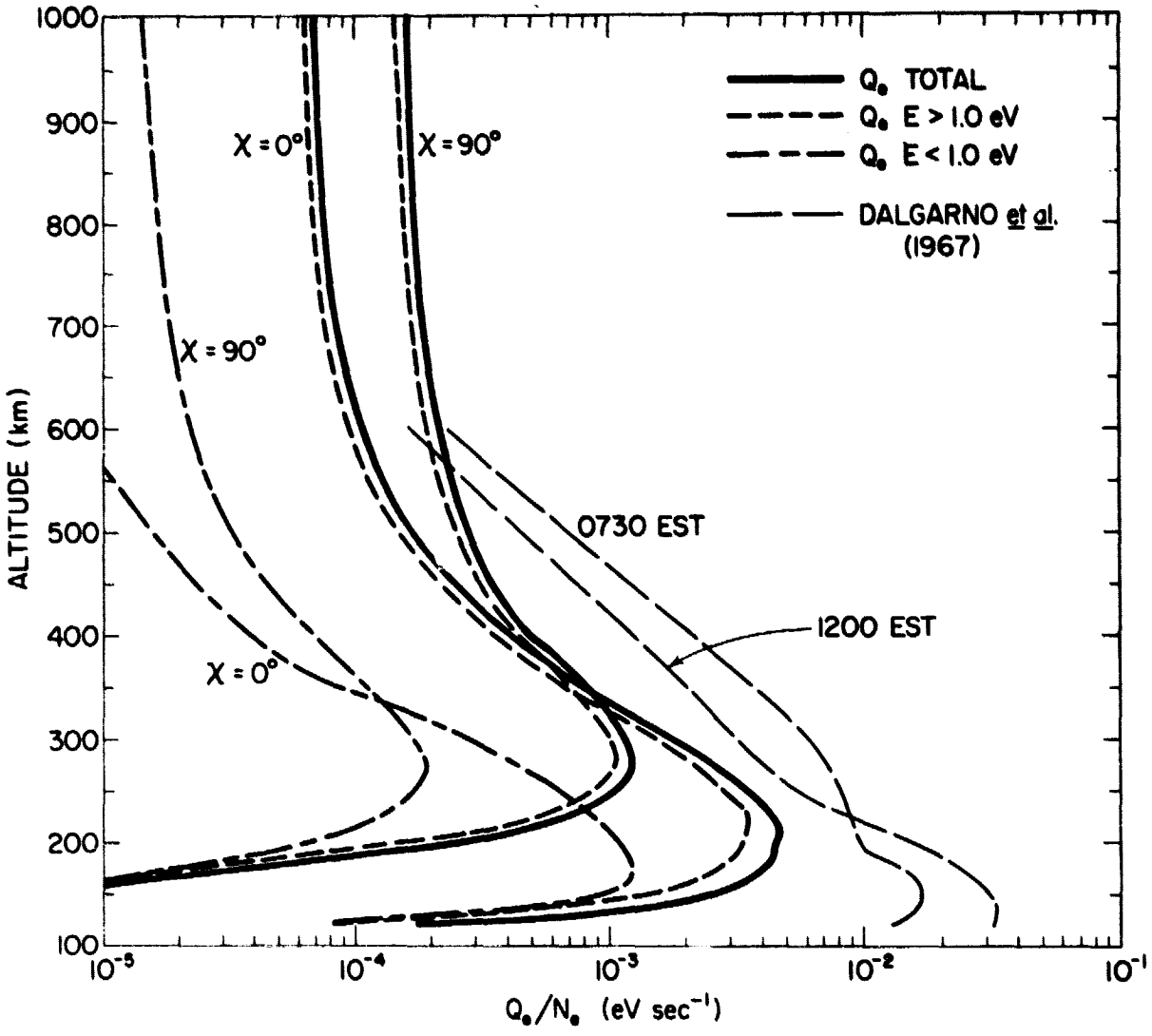

Figure 3.3 Thermal electron heating rates [after *Mantas*, 1973].

3.5 *Other Energy Sources for Electrons*

Although photoelectron heating is the major source of heating for the ambient thermal electrons, one cannot ignore other possible sources of heat for electrons. Electrons can gain heat through interactions with electric fields or Joule heating. Electrons can also be heated by hot neutrals.

Charge particles drift through the neutral gas when there is an electric field and a magnetic field applied to a region in the atmosphere. This drifting causes collisions between neutrals and charged particles which act to limit the final transport velocity of the charged particles. Now since the final transport velocity is lowered due to the neutral and charged particle collisions, motion is converted into random thermal energy. This energy is important in the auroral atmosphere [*Walker*, 1971]. The rate of energy transfer for electrons is small compared with that for ions. The electrons are not heated significantly by the electric fields because the mass factor is much greater for ions. This heating is only important in the auroral ionosphere because the field-aligned currents are a result of auroral electron precipitation. The heating can be ignored at lower latitudes where electron precipitation is not significant.

Joule heating can also be caused by collisions due to differing transport velocities of electrons and ions. Thus, electric currents flow and the electron heating rate follows from the M_n equation (3.5) and the Coulomb interaction equation (3.10). The Joule heating rate is given by

$$J_e = m_e \bar{\nu}_e \ (\vec{u}_e - \vec{u}_i)^2 \ g(v/\alpha) \tag{3.31}$$

where $$g(v/\alpha) = 3\pi^{\frac{1}{2}}/4(\alpha/v)^3 \ \mathrm{erf}(v/\alpha) - 3/2(\alpha/v)^2 \ \exp(-v^2/\alpha^2) \tag{3.32}$$

$$v = |\vec{u}_e - \vec{u}_i| \ , \qquad \alpha^2 = 2kT_e/m_e \tag{3.33}$$

and $\bar{\nu}_e$ is mean electron-ion collision frequency.

Electron heating by hot neutrals is possible because of the presence of significant numbers of hot neutrals. Energetic oxygen atoms with characteristic temperatures as high as 5400 K have been found to have a significant number density above 1000 km under quiet solar activity condition and above 1600 km under active conditions [*Rohrbaugh and Nisbet*, 1973]. Thermal electrons can be heated by these hot neutrals through elastic collisions. Calculations shown below indicate that this source of heat for electrons is much smaller than heating by photoelectrons.

If, $$n(0) \approx 10^4 \text{ cm}^{-3} \tag{3.34}$$

$$\langle E \rangle_0 \approx 0.7 \text{ eV} \approx 5400 \text{ K} \tag{3.35}$$

where $n(0)$ is the concentration of the energetic oxygen atoms and $\langle E \rangle_0$ is the average energy of these O atoms. In equation (3.35), a Maxwellian velocity distribution is assumed to exist, since the mean free path is very long and these energetic oxygen atoms have a collision frequency which allows a random distribution around the average squared velocity. The energy transfer rate for elastic collisions between electrons and O atoms is given by [*Banks*, 1966a].

$$L_{eo} = -3.74 \times 10^{-18} n_e n(0) T_e^{\frac{1}{2}} (T_e - T) \tag{3.36}$$

With $n_e = 1 \times 10^4 \text{ cm}^{-3}$, $T_e = 3000$ K, and $T = 5400$ K, one has

$$L_{eo} = 4.9 \times 10^{-5} \text{ ev cm}^{-3} \text{ s}^{-1}. \tag{3.37}$$

Now, for the photoelectron heating rate at 1000 km one has [*Mantas*, 1973]

$$\chi = 0^\circ \quad Q = 7 \times 10^{-1} \text{ ev cm}^{-3} \text{ s}^{-1}$$

$$\chi = 90^\circ \quad Q = 1.5 \text{ ev cm}^{-3} \text{ s}^{-1} \tag{3.38}$$

χ is solar zenith angle, Q is photoelectron heating rate. Comparison of L_{eo} with Q indicate that heating through energy transfer between electrons and energetic oxygen atoms can be neglected during the day.

Another source of electron heating is energy gained through de-excitation of the vibrational levels of nitrogen which have characteristic temperatures of about 3100 K [*Walker*, 1968]. This nitrogen vibrational energy is produced by the collisions with photoelectrons due to the large cross sections for vibrational excitation of molecular nitrogen by electrons. This source of electron heating is principally effective in the *E* region (100-140 km). It will be neglected in *F*-region electron heating.

3.6 *Energy Losses of Electrons for Elastic Collisions*

Elastic collisional energy transfer between mixed gases having separate Maxwellian velocity distributions is one of the physical processes by which electrons lose energy. A deeper physical insight into this process can be achieved by considering a simple model of energy transfer.

First, the average energy loss per collision of a single particle of mass m_1 and kinetic energy ε_1 traveling through a gas composed of particles of mass m_2 and average energy $\bar{\varepsilon}_2$ is [*Huxley and Crompton*, 1962]

$$\Delta\varepsilon_1 = -[2m_1m_2/(m_1 + m_2)^2]\ (\varepsilon_1 - \bar{\varepsilon}_2) \tag{3.39}$$

The rate at which the single particle loses energy per unit time is given by the single particle collision frequency

$$\nu_{12} = n_2 g\ q_D \tag{3.40}$$

where n_2 is the ambient gas number density, g is the relative velocity given previously, q_D is the velocity dependent momentum transfer cross section,

$$q_D = 2\pi \int \sigma(g,\theta)(1 - \cos\theta)\ \sin\theta\ d\theta \tag{3.41}$$

and $\sigma(g,\theta)$ is the differential scattering cross section.

The average rate of energy transfer of a single particle follows from (3.39) and (3.40) as

$$\overline{\frac{\Delta E}{\Delta t}} = -\frac{2m_1m_2}{(m_1 + m_2)} (\varepsilon_1 - \bar{\varepsilon}_2)\nu_{12} \tag{3.42}$$

Now, the total average energy transfer exchange rate follows from combining the average rate of energy transfer of a single particle of Maxwellian gas mixed with the original gas as

$$\frac{dU_1}{dt} = -\frac{2m_1m_2}{(m_1 + m_2)^2} n_1(\bar{\varepsilon}_1 - \bar{\varepsilon}_2)\bar{\nu}_{12} \tag{3.43}$$

$$U_1 = \tfrac{1}{2}n_1m_1\overline{v_1^2} = n_1\bar{\varepsilon}_1 \tag{3.44}$$

where $\bar{\varepsilon}_1$ is now the average energy of particles with mass m_1, and $\bar{\nu}_{12}$ is the average collision frequency which takes into account the many different relative velocities between the various gas particles.

The result (3.43) shows that the energy exchange rate can be decomposed into three factors: mass ratio, a difference in average particle energy, and an energy transfer collision frequency. The first two quantities are independent of the mode of interaction between the two gas species. The collision frequency contains the factors which depend on interparticle forces.

The exact result for the total average energy exchange rate is given by [*Desloge*, 1962]

$$\frac{dU_1}{dt} = -4\pi n_1n_2\frac{(m_1m_2)^{7/2}(T_1 - T_2)}{(m_1 + m_2)^2(2\pi k)^{3/2}(m_2T_1 + m_1T_2)^{5/2}} \int_0^\infty g^5 q_D(g)\, \exp(-Kg^2)dg \tag{3.45}$$

where $$U_1 = \int \frac{1}{2} m_1 v_1^2 f_1 \, d^3 v_1 \tag{3.46}$$

$$K = (2kT_1/m_1 + 2kT_2/m_2)^{-1} \tag{3.47}$$

$$q_D(g) = 2\pi \int \sigma(g,\theta)(1 - \cos\theta) \sin\theta \, d\theta \tag{3.48}$$

U - gas total kinetic energy

n - particle number density

m - particle mass

T - Maxwellian temperature

k - Boltzmann's constant

g - relative velocity between particles

$q_D(g)$ - velocity dependent momentum transfer cross section

v - particle velocity in laboratory system

d^3v - velocity space volume element

θ - center of mass scattering angle

$\sigma(g,\theta)$ - differential scattering cross section

f - velocity distribution function

If one lets

$$\bar{Q}_D = K^3 \int g^5 \, q_D(g) \exp(-Kg^2) dg \tag{3.49}$$

and $$\bar{\nu}_{12} = \frac{4}{3} n_2 \, \bar{g} \, \bar{Q}_D \tag{3.50}$$

where

$$\bar{g} = \int \int f_1 f_2 |\vec{v}_1 - \vec{v}_2| d^3 v_1 d^3 v_2 \tag{3.51}$$

or if f_1 and f_2 are Maxwellian velocity distributions

$$\bar{g} = (8k/\pi)^{1/2} (T_1/m_1 + T_2/m_2)^{1/2} \tag{3.52}$$

and $\bar{\epsilon}_1 = \frac{3}{2} kT_1$ and $\bar{\epsilon}_2 = \frac{3}{2} kT_2$

then

$$\frac{dU_1}{dt} = - 3n_1 \frac{m_1 m_2}{(m_1 + m_2)^2} k(T_1 - T_2)\bar{\nu}_{12} \tag{3.53}$$

There is an arbitrary numerical factor of 4/3 which has been noted by *Nicolet* [1953] in an analysis of electron collision frequencies based upon an analysis of collision integrals and diffusion coefficients derived by the velocity distribution method. Since $m_e << m_2$, for electrons Q_D becomes

$$Q_D = \left(\frac{m_e}{2kT_e}\right)^3 \int_0^\infty v^5 \, q_D(v) \, \exp(-m_e v^2/2kT_e) dv_e \tag{3.54}$$

To apply this equation to electron-neutral collisions one must have analytical expressions for the momentum transfer cross sections. But unfortunately these results don't exist and one must use laboratory results. A description of the current methods used to measure elastic electron-neutral momentum transfer cross sections can be found in *McDaniel* [1964], and *Hasted* [1964]. Empirical expressions are found for q_D for the atmospheric gases and are presented in the following sections.

3.6.1 *Molecular nitrogen.* *Pack and Phelps* [1961] have measured the drift velocity of electrons under the influence of a constant electric field. Their data for the electron momentum transfer cross section for electron energies between 0.02eV and 0.1eV can be represented by the equation

$$q_D = 1.88 \times 10^{-15} E^{\frac{1}{2}} \text{ cm}^2 \tag{3.55}$$

where E is the electron energy measured in eV. For energies above 0.1eV there is a correction which has been found by *Englehardt et al.* [1964] who calculated q_D from measurements of electron mobilities and diffusion coefficients. The data gives

$$q_D = (1.83 - .73E^{\frac{1}{2}})E^{\frac{1}{2}} \times 10^{-15} \text{ cm}^2 \tag{3.56}$$

Substituting this equation into the $\bar{Q}_D$ equation gives

$$\bar{Q}_D(N_2) = (2.82 - 9.44 \times 10^{-3} T_e^{\frac{1}{2}})T_e^{\frac{1}{2}} \times 10^{-17} \text{ cm}^2 \tag{3.57}$$

which is valid over the range 100 K $\leq T_e \leq$ 4500 K.

3.6.2 *Molecular oxygen.* The Boltzmann equation can be used to evaluate the drift velocity, the diffusion coefficient, and the electron mobility in molecular oxygen if the cross sections are known. Measurements of electron mobility and diffusion coefficients can be compared with predicted values. Therefore, the momentum transfer cross sections can be adjusted so the predicted and measured values of electron mobility and diffusion coefficients agree within 20 percent. *Hake and Phelps* [1967] have done this analysis and their results are shown in Figure 3.4. As a first order approximation to this data one has

$$q_D = (2.2 + 5.1E^{\frac{1}{2}}) \times 10^{-16} \text{ cm}^2 \tag{3.58}$$

which applies over the range $0.02 \leq E \leq 1.0$ eV.

Substituting q_D into the $\bar{Q}_D$ equation gives

$$Q_D(O_2) = (2.2 + 7.86 \times 10^{-2} T_e^{\frac{1}{2}}) \times 10^{-16} \text{ cm}^2 \tag{3.59}$$

which applies over the range 150 K $\leq T_e \leq$ 5000 K.

3.6.3 *Atomic oxygen.* The experimental results for atomic oxygen give only total scattering cross sections due to the chemical activity of oxygen in any closed container. The momentum transfer scattering cross section can be calculated theoretically from quantum theory partial wave phase shifts as

$$q_D = \frac{4\pi}{k_1^2} \sum_{\ell=0}^{\infty} (\ell + 1) \sin^2 \eta_\ell \tag{3.60}$$

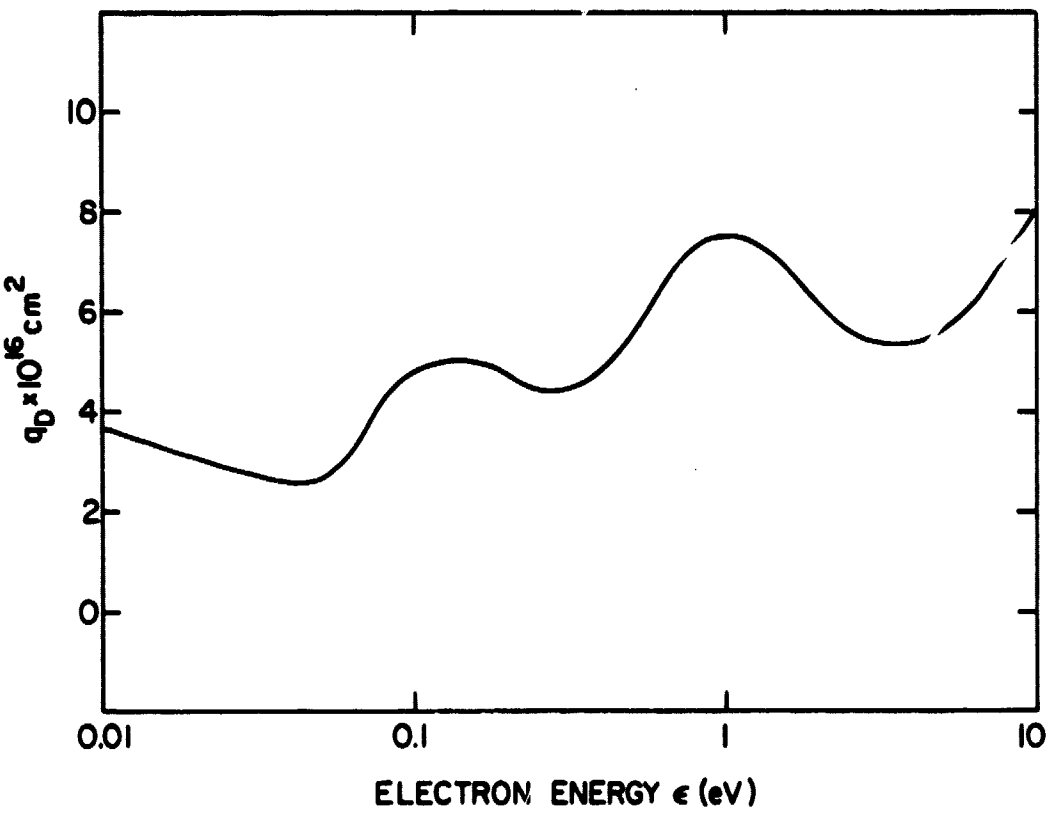

Figure 3.4 Momentum transfer cross sections for O_2 [adapted from *Hake and Phelps*, 1967].

where $k_1 = (2\pi m_e v_e/h)$ is wave number, h is Planck's constant, ℓ is the angular momentum quantum number, and η_ℓ is the partial wave phase shift due to the action of the scattering potential. The phase shifts can be calculated from measurements of photodetachment cross sections [*Cooper and Martin*, 1962]. If one accepts that the values for the scattering phase shifts are good for for determining the momentum transfer cross section for atomic oxygen then [*Banks*, 1966a]

$$q_D = (3.4 \pm 1.0) \times 10^{-16} \text{ cm}^2 \tag{3.61}$$

or $$\bar{Q}_D (O) = (3.4 \pm 1.0) \times 10^{-16} \text{ cm}^2 \tag{3.62}$$

independent of the electron temperature for $T_e < 4000$ K.

3.6.4 *Atomic hydrogen*. Like atomic oxygen, there are no experimental measurements for the electron-hydrogen momentum transfer cross section. Theoretical calculations of scattering phase shifts for electrons in hydrogen [*Smith et al.*, 1962] can be used to calculate both total cross sections and momentum transfer cross sections via equation (3.60). These predicted total cross sections agree with measurements of total cross sections by *Brackman et al.* [1958] and so errors in the calculation of the momentum transfer cross sections should not be too large. Using equation (3.60) and the results of *Smith et al.* [1962] and fitting a suitable analytic expression for the energy dependence gives

$$q_D = (54.7 - 28.7\ E) \times 10^{-16} \text{ cm}^2 \tag{3.63}$$

and $$\bar{Q}_D(H) = (54.7 - 7.42 \times 10^{-3} T_e) \times 10^{-16} \text{ cm}^2 \tag{3.64}$$

over the temperature range 150 K $\leq T_e \leq$ 5000 K.

3.6.5 *Helium*. The experimental data for electron-helium momentum transfer cross sections give a constant cross section of 5.6×10^{-16} cm^2

[*Pack and Phelps*, 1961] over the energy range 0.0 to 0.4 eV. Thus,

$$\bar{Q}_D(\text{He}) = 5.6 \times 10^{-16} \text{ cm}^2 \tag{3.65}$$

which is independent of the electron temperature over the range $0 \leq T_e \leq$ 6000 K. The error is within 10% because of the good agreement between experimental data.

The values of $\bar{Q}_D$ for the different atmospheric gases are shown in Figure 3.5 which are calculated from the analytic formulas given previously. The errors involved in using these expressions can be estimated by considering how close they agree with experimental data and by the accuracy of the experimental data. For molecular nitrogen and molecular oxygen the uncertainty in $\bar{Q}_D$ is approximately 20 percent or less [*Englehardt et al.*, 1964; *Hake and Phelps*, 1967]. $\bar{Q}_D$(He) is accurate to within 10 percent, but for atomic hydrogen and atomic oxygen $\bar{Q}_D$ should be less than 25 percent and 30 percent, respectively based on quantum calculations.

3.6.6 *Charged particles.* The momentum transfer cross section for charged particles can be calculated from equation (3.48) and the Rutherford differential scattering cross section

$$\sigma(\vartheta,g) = \left[\frac{z_1 z_2 e^2}{2\mu g^2}\right]^2 \text{cosec}^4(\theta/2) \tag{3.66}$$

where μ is the two particle reduced mass, $z_{1,2}$ are the respective atomic charges, e is the electron charge and θ is the center of mass scattering angle. Integrating $\sigma(\theta,g)$ over θ, one gets

$$q_D(g) = 8\pi \left[\frac{z_1 z_1 e^2}{2\mu g^2}\right]^2 \ln\left(\frac{2}{1 - \cos\theta_m}\right) \tag{3.67}$$

where θ_m is minimum scattering angle determined from the parameters of the charged particles. The relation between the impact parameter, b, the

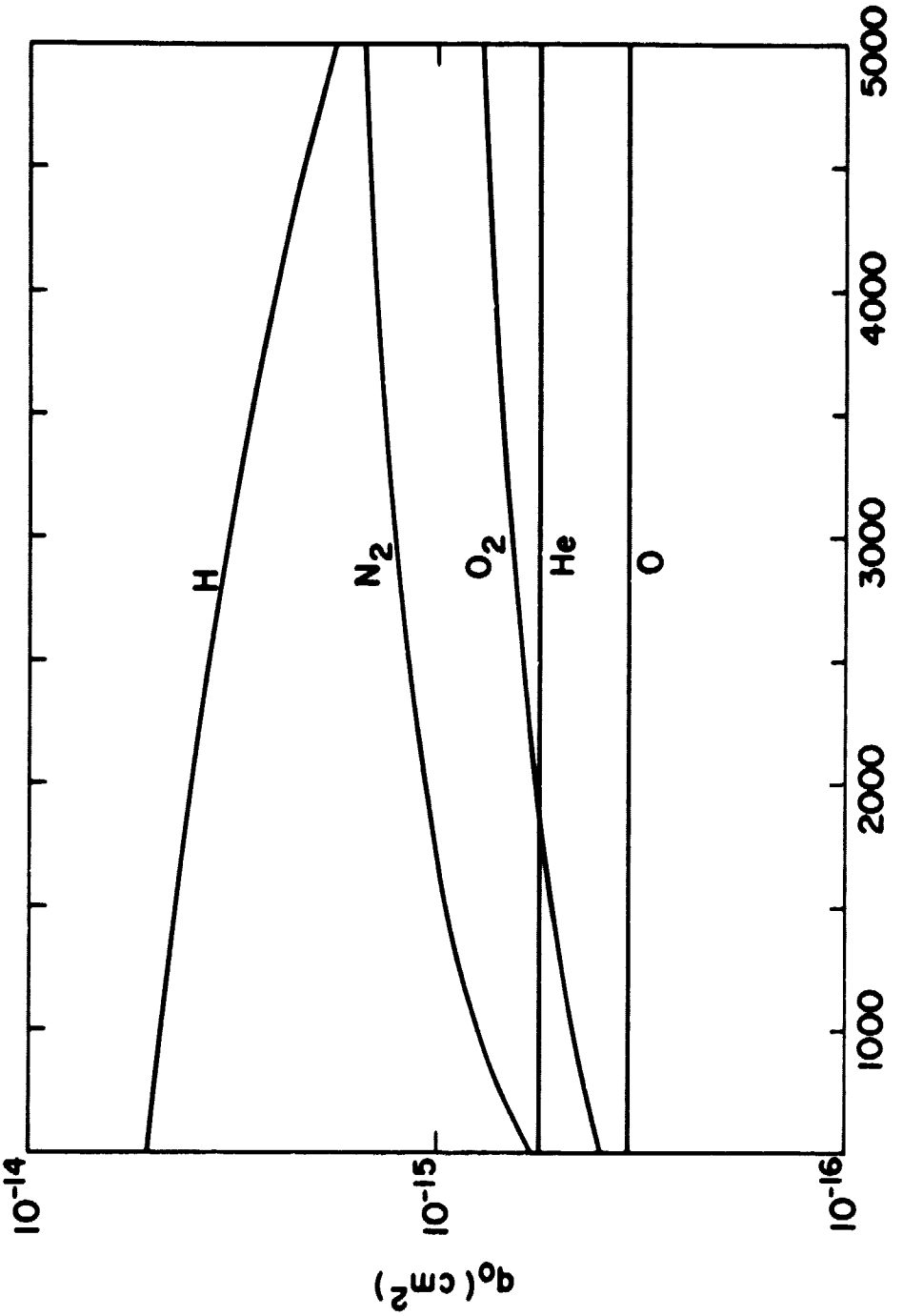

Figure 3.5 Average momentum transfer cross sections.

scattering angle, θ, and the relative velocity, g, is given by

$$(1 - \cos\theta) = \frac{2}{1 + (b/b_0)^2} \tag{3.68}$$

where $b_0 = z_1 z_2 e^2/\mu g^2$, other quantities defined previously. The minimum scattering angle θ_m can be calculated from this equation when b is a maximum, b_1. Calculation of the maximum impact parameter, b_1, follows from considering the shielding of charge due to electrostatic polarization effects [*Cohen et al.*, 1950]. The Debye length, D_e, which represents the maximum distance over which microscopic density fluctuations are correlated by random electric fields, can also be used as the effective range of the Coulomb interaction and so can be used in equation (3.68) as the maximum impact parameter. Since $D_e >> b_0$

$$q_D = 16\pi \left[\frac{z_1 z_2 e^2}{2\mu g^2}\right]^2 \ln\left[\frac{\mu g^2 D_e}{z_1 z_2 e^2}\right] \tag{3.69}$$

which is the momentum transfer cross section between two arbitrary charged particles.

The argument of the logarithm in equation (3.69) can be expressed in terms of the center of mass energy of the colliding particles, E, as

$$\Lambda = \frac{\mu g^2 D_e}{z_1 z_2 e^2} = \frac{2ED_e}{z_1 z_2 e^2} \tag{3.70}$$

Calculations of $\ln \Lambda$ for various particle energies and Debye lengths are shown in Table 3.1 where $z_1 = z_2 = 1$. For the earth's atmosphere particles energies and Debye lengths are such that the approximation $\ln \Lambda = 15$ can be used with an uncertainty of less than 10%.

Using (3.70), (3.69) and (3.49) for two gases with different Maxwellian

TABLE 3.1

Values of ln Λ for different electron energies (E) and Debye lengths (D_e)

E(ev)/D_e(cm)	.1	.3	.5	1.0	2.0	5.0	10.0	20.0	50.0	100.0
1.0E-02	9.54	10.64	11.33	11.84	12.54	13.45	14.15	14.84	15.75	16.45
5.0E-02	11.15	12.25	12.94	13.45	14.15	15.06	15.75	16.45	17.36	18.06
1.0E-01	11.84	12.94	13.63	14.15	14.84	15.75	16.45	17.14	18.06	18.75
2.0E-01	12.54	13.63	14.33	14.84	15.53	16.45	17.14	17.88	18.75	19.44
5.0E-01	13.45	14.55	15.24	15.75	16.45	17.36	18.06	18.75	19.67	20.36
1.0E+00	14.15	15.24	15.94	16.45	17.14	18.06	18.75	19.44	20.36	21.05
5.0E+00	15.75	16.85	17.55	18.06	18.75	19.67	20.36	21.05	21.97	22.66
1.0E+01	16.45	17.55	18.24	18.75	19.44	20.36	21.05	21.75	22.66	23.36
5.0E+01	18.06	19.16	19.85	20.36	21.05	21.97	22.66	23.36	24.27	24.97
1.0E+02	18.75	19.85	20.54	21.05	21.75	22.66	23.36	24.05	24.97	25.66

temperatures one gets

$$\bar{Q}_D = \frac{\pi}{2} \frac{z_1 z_2 e^2}{k \mu} \frac{\ln \Lambda}{(T_1/m_1 + T_2/m_2)^2} \tag{3.71}$$

which applied to charged particles of arbitrary mass and charge.

3.6.7 *Electron collision frequencies and energy transfer rates.* The momentum transfer cross section for electron-neutral elastic collisions derived in the previous sections can be used to calculate electron energy transfer collision frequencies and energy transfer rates via equations (3.50) and (3.53). The final results are given in Tables 3.2 and 3.3.

For charged particle the electron energy transfer collision frequency and energy transfer rate has been calculated by *Banks* [1966a]. With $\ln \Lambda \approx 15$, the collision frequency is

$$\bar{\nu}_e = (54 \pm 5)\, n_i / T_e^{3/2} \text{ sec}^{-1} \tag{3.72}$$

and the energy transfer rate is

$$\frac{dU_e}{dt} = -(7.7 \pm 0.8) \times 10^{-6} n_e n_i \frac{(T_e - T_i)}{A_i T_e^{3/2}} \text{ eV cm}^{-3}\text{sec}^{-1} \tag{3.73}$$

where A_i is the ion atomic mass in amu.

Note in equation (3.73) that for a fixed T_i there occurs a maximum energy transfer rate at $T_e = 3T_i$. If the temperature dependence of the term $\ln \Lambda$ where included in (3.73) one has instead $T_e = 3.5T_i$. Equation (3.73) is important since it expresses energy transfer between charged particles in a single equation.

3.7 *Energy Losses of Electrons Through Inelastic Collisions*

Besides elastic collisions, inelastic collisions are also important for electron cooling. Electrons can excite neutral particles and thereby transfer some of their energy to the neutral particles. Rotational, vibration,

TABLE 3.2

Electron energy transfer collision frequencies for elastic collisions with atmospheric neutral particles.

Neutral species	Collision frequency $\bar{\nu}_{en}/(4/3\ n_e(8k/\pi)^{\frac{1}{2}}(T_e/m_e)^{\frac{1}{2}})$
N_2	$(2.82 - 9.44 \times 10^{-3}\ T_e^{\frac{1}{2}})T_e^{\frac{1}{2}} \times 10^{-17}$
O_2	$(2.2 + 7.86 \times 10^{-2}\ T_e^{\frac{1}{2}}) \times 10^{-16}$
O	$(3.4 \pm 1.0) \times 10^{-16}$
H	$(54.7 - 7.42 \times 10^{-3}\ T_e) \times 10^{-16}$
H_e	5.6×10^{-16}

TABLE 3.3

Electron energy transfer rates for elastic collisions with atmospheric neutral particles.

Neutral Species	Energy transfer rate $-\frac{dU_e}{dt}$ ($eVs^{-1}\ cm^{-3}$)
N_2	$n(N_2)n_e(T_e - T_n)\ 1.77 \times 10^{-19}(1 - 3.35 \times 10^{-3}\ T_e^{\frac{1}{2}})T_e$
O_2	$n(O_2)n_e(T_e - T_n)\ 1.21 \times 10^{-18}(1 + 3.57 \times 10^{-2}\ T_e^{\frac{1}{2}})T_e^{\frac{1}{2}}$
O	$n(O)n_e(T_e - T_n)\ 3.74 \times 10^{-18}\ T_e^{\frac{1}{2}}$
H	$n(H)n_e(T_e - T_n)\ 9.63 \times 10^{-16}(1 - 1.35 \times 10^{-4}\ T_e)T_e^{\frac{1}{2}}$
H_e	$n(H_e)n_e(T_e - T_n)\ 2.46 \times 10^{-17}\ T_e^{\frac{1}{2}}$

electronic, and fine-structure excitations by thermal electrons are possible for the atmospheric neutral particles N_2, O_2, O, H, and He.

Electronic excitation of N_2 is not a significant energy loss process for electrons in the ionosphere due to the relatively large excitation potential of the first excited state (6.2 eV). The electronic excitation potentials of H and He are larger than for N_2 so energy loss through electronic excitations of N_2, H, and He can be neglected in the ionosphere. For O the first excited state, $O(^1D)$ lies 1.97 eV above the ground state $O(^3P)$. Thus, for electron temperatures greater than about 23000 K electron impact excitation of the ^1D state can be important. Since electron temperatures in the *F* region are much less than 23000 K, electronic excitation of O is also not important.

The excitation of the second excited state of atomic oxygen $O(^1S)$ is not a significant energy loss process for electrons since the excitation potential of 4.2 eV is too large for ionospheric electrons.

The electronic excitation potential for $O_2(a^1\Delta_g)$ lies only 0.96 eV above the ground state. But due to very small excitation cross section leading to $O_2(a^1\Delta_g)$ [*Schulz and Dowell*, 1962] this is not a significant sink of electron thermal energy.

Electron energy loss rates from electron-impact-induced transitions of the fine-structure levels of atomic oxygen are important because the $^3P_0$ and $^3P_1$ levels are 0.028 and 0.020 eV above the ground state $^3P_2$ level and must be included in the electron energy balance equation. This cooling is brought about by the collision process

$$e + O(^3P_J) \rightarrow e + O(^3P_{J'}) \tag{3.74}$$

The distribution of levels J follows from assuming that the reaction

(3.74) proceeds rapidly. The distribution is given by [*Dalgarno and Degges*, 1968]

$$n_J = \frac{n(2J + 1)\ \exp(-E_J/kT_n)}{\sum_{J=0}^{2} (2J + 1)\ \exp(-E_J/kT_n)} \tag{3.75}$$

where n is the number density of atomic oxygen, E_J is the energy of the state with total angular momentum J and T_n is the neutral particle gas temperature. The time rate of change of the electron energy E through excitation and de-excitation of the fine structure levels of atomic oxygen is given by

$$\frac{dE}{dt} = v \sum_{J=0}^{2} n_J \sum_{J' \neq J} (E_J - E_{J'})\ Q(J, J', E) \tag{3.76}$$

where v is the electron velocity, and $Q(J, J', E)$ is cross section for collision (3.74). The cross section $Q(J, J', E)$ can be calculated from theoretically derived collision strengths. *Breig and Lin* [1966] were the first to derive these collision strengths. More recently *Tambe and Henry* [1976] and *LeDourneuf and Nesbet* [1976] have recalculated these collision strengths. Cross sections calculated from these more recent data are shown in Table 3.4. The mean rate of change of E can be calculated from [*Dalgarno and Degges*, 1968]

$$\overline{\frac{dE}{dT}} = 2\pi\ (\pi k T_e)^{-3/2}\ (2/m_e)^{1/2} \sum_{J=0}^{2} n_J$$

$$\times \int_0^\infty E\ \exp(-E/kT_e) \sum_{J' \neq J} (E_J - E_{J'})\ Q(J, J', E)\ dE \tag{3.77}$$

where the electrons were assumed to have a Maxwellian velocity distribution with characteristic temperature T_e. The mean cooling rates are shown in Figure 3.6. To a first approximation the cooling rates of Figure 3.6 can be represented by

TABLE 3.4

Total cross sections for de-excitation of the spin-multiplet levels of OI by electron impact.

Transition ($J \rightarrow J'$)	Electron Energy (K)	Cross Section (πa_0^2)
1→2	20000	0.5435
	10000	0.5193
	5000	0.4988
	2000	0.4577
	1000	0.3999
	500	0.2841
0→2	20000	0.4230
	10000	0.4609
	5000	0.4672
	2000	0.4262
	1000	0.3472
	500	0.1894
0→1	20000	0.5469
	10000	0.4183
	5000	0.3536
	2000	0.3078
	1000	0.2841
	500	0.2525

$$Q(J \rightarrow J') = \frac{\pi}{(k')^2} \Omega(J', J) / (2J + 1)$$

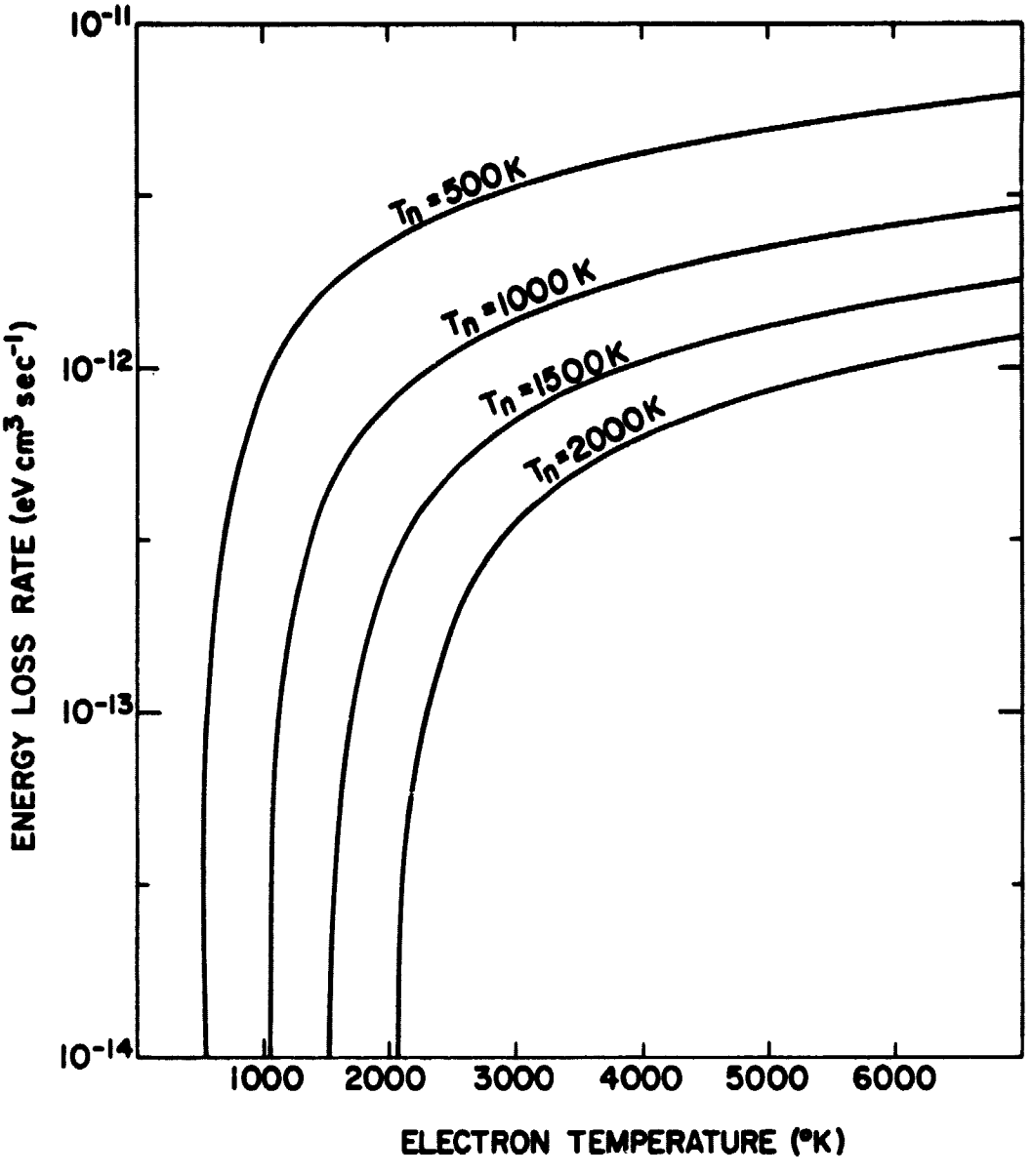

Figure 3.6 Mean cooling rates for electron impact induced fine-structure transitions in atomic oxygen.

$$\frac{dU_e}{dt} = -3.4 \times 10^{-11} n_e n(0) \left[5 + 3 \exp(-E_2/kT_n) + \exp(-E_3/kT_n)\right]^{-1}$$
$$\times T_e^{1/2} \{(.81 + 8.6 \times 10^{-5} T_e) E_2[\exp(-E_2/kT_e) - \exp(-E_2/kT_n)]$$
$$+ (.32 + 8.7 \times 10^{-5} T_e) E_3[\exp(-E_3/kT_e) - \exp(-E_3/kT_n)]$$
$$+ (.32 + 8.9 \times 10^{-5} T_e) E_1[\exp(-E_1/kT_e) - \exp(-E_1/kT_n)]\} \qquad (3.78)$$

where $E_1 = 0.00833$ eV, $E_2 = 0.01965$ eV, $E_3 = 0.02798$ eV, and $k = 8.62 \times 10^{-5}$ eV K^{-1}. The integrals in equation (3.77) are approximately equal to coefficients of the terms $[\exp(-E/kT_e) - \exp(-E/kT_n)]$ in equation (3.78). The cooling rate is proportional to $(T_e - T_n)$ as T_e approaches T_n.

Election cooling by vibrational excitation of O_2 has been calculated by *Lane and Dalgarno* [1969]. Their results are shown in Figure 3.7. Although the results show that the heat loss by vibrational excitation of O_2 is not a dominant heat loss process, it may contribute up to 20% of the total hea' loss in the *E* region. So, it must be included in any accurate quantitative study of the thermal balance in the *E* region. The electron cooling rate by vibrational excitation of O_2 can be represented by

$$\frac{dU_e}{dt} = -8 \times 10^{-16} n(O_2)\, n_e (T_e - T_n)\, T_e^{1/2} \text{ eV cm}^{-3} \text{ s}^{-1} \qquad (3.79)$$

The vibrational excitation of N_2 is a more efficient electron cooling process than rotational excitation of N_2 for electron temperatures above 1500 K [*Dalgarno and Henry*, 1965]. In Table 3.5 cooling rates due to vibrational excitation of N_2 from *Rees et al.* [1967] are presented.

Electron cooling through rotational excitation of O_2 has been calculated by *Dalgarno et al.* [1968]. They used the expression

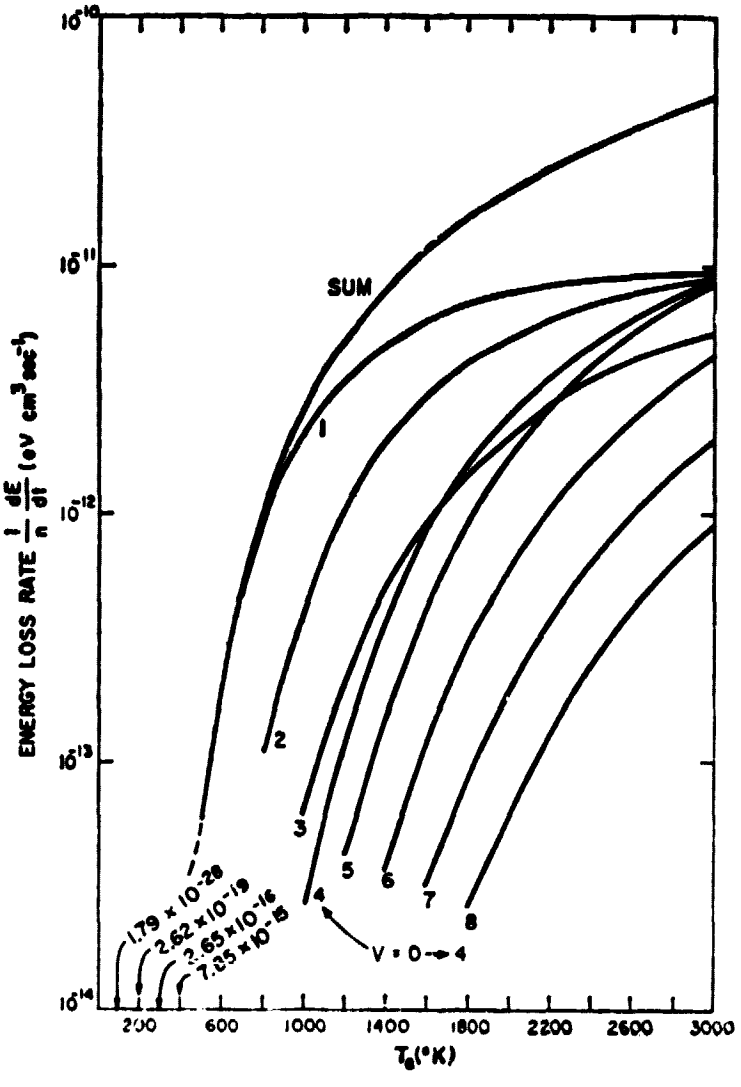

Figure 3.7 Electron cooling rates by vibrational excitation of O_2 [after *Lane and Dalgarno*, 1969].

TABLE 3.5

Cooling rates through vibrational excitation of N_2 (after *Dalgarno et al.* 1967).

$$\frac{dU_e}{dt} = -n_e\, n(N_2)\, R$$

T_e (k)	R	T_e (k)	R
200	3×10^{-19}	2500	1×10^{-11}
300	7×10^{-17}	3000	5×10^{-11}
500	7×10^{-15}	3500	1×10^{-10}
1000	2×10^{-13}	4000	3×10^{-10}
1500	8×10^{-13}	4500	2×10^{-9}
2000	2×10^{-12}	5000	7×10^{-9}

$$\frac{\overline{dE}}{dt} = -n_e n(O_2)\ 7 \times 10^{-14}\ \frac{(T_e - T_n)}{T_e^{1/2}}\ \text{eV cm}^{-3}\ \text{sec}^{-1} \qquad (3.80)$$

where $n(O_2)$ is the number density of O_2 and the other quantities have been given previously.

Rotational excitation of N_2 has been studied by *Dalgarno and Moffett* [1963]. The computed cross sections are in satisfactory agreement with the analysis of the experimental swarm experiments of *Engelhardt et al.* [1964]. They can be represented by the cooling rate

$$\frac{dU_e}{dt} = -n_e n(N_2)\ 2 \times 10^{-14}\ (T_e - T_n)/T_e^{1/2}\ \text{eV cm}^{-3}\ \text{s}^{-1} \qquad (3.81)$$

with a possible uncertainty of a factor of 2.

3.8 *Thermal Conduction*

Particle collisions determine the thermal conductivity. In ionized gases charge separation electric fields have the effect of limiting the flow of electrons. Thus, electric fields tend to reduce the effective thermal conductivity.

Owing to the dependence of the thermal conductivity of a gas of charged upon the inverse square root of the mass of the particle, the thermal conductivity of the electron gas is much larger than that for the ion gas [*Chapman and Cowling*, 1970; *Spitzer*, 1962]. Nevertheless, the ion thermal conductivity cannot be ignored completely since at high altitudes the rate of energy transfer from electrons to ions is slow. Thus, ion conduction will be important in determining ion temperature profiles.

3.8.1 *Electron thermal conduction.* The importance of the electron thermal conductivity in the electron energy balance equation was studied by *Geisler and Bowhill* [1965]. In their work three situations that probably

could be found within the ionosphere were investigated. The first case is that of an overheated electron gas at all altitudes. In this case the effect of thermal conduction is to conduct downward the excess heat through a strong electron temperature gradient to the heat sink in the lower thermosphere. The second case is that there is heat sink at high altitudes where heating of electrons is slow. In this case even a small temperature gradient will result in a heat flux that is sufficient to exceed the capacity of the heat sink and so the electron gas is not cooled by the heat sink. The third case is that the electron gas is only overheated in the region between 200 and 250 km. This case leads to a temperature maximum around 200 km and the temperature is controlled by neutral cooling rather than by thermal conduction at the maximum.

The calculation of the electron thermal conductivity is carried out by considering the mean free path within a weakly ionized gas. This permits the separation of the collision effects of neutral and charged particles collisions. The effective thermal conductivity can then be found from the individual conductivities of neutrals and electrons. This has been executed by *Banks* [1966c] who arrived at

$$K_e = \frac{7.7 \times 10^5 \, T_e^{5/2}}{1 + 3.22 \times 10^4 \, \frac{T_e^{.2}}{n_e} \, \Sigma \, n_n \bar{Q}_D} \quad \text{eV cm}^{-1} \text{ sec}^{-1} \text{ K}^{-1} \tag{3.82}$$

where K_e is the effective electron thermal conductivity, the summation is over all neutral gas species present, $\bar{Q}_D$ is the average momentum transfer cross section. For low neutral particle number densities this expression (3.82) reduces to

$$K_e = 7.7 \times 10^5 \, T_e^{5/2} \text{ eV cm}^{-1} \text{ sec}^{-1} \text{ K}^{-1} \tag{3.83}$$

which is the equation derived by *Spitzer* [1962] for a fully ionized gas. The effect of the neutral atmosphere on the electron thermal conductivity for several values of T_e is shown in Figure 3.8. The transition between the fully ionized case and the partially ionized case of (3.82) occurs when the curves depart from the horizontal.

The effect of the earth's magnetic field on the thermal conductivity is important since the thermal conductivity is anisotropic with different values parallel and perpendicular to the field lines [*Chapman and Cowling*, 1970]. The value of the thermal conductivity is unaffected when temperature gradients are parallel to the magnetic field. The perpendicular component is reduced by the factor $\nu_e/(\nu_e^2 + \Omega_e^2)$ [*Chapman and Cowling*, 1970] where ν_e is the mean collision frequency and Ω_e is the electron cyclotron frequency or gyrofrequency. In the earth's atmosphere $\nu_e/(\nu_e^2 + \Omega_e^2) << 1$ since $\nu_e \approx 10^{-9}\ n_n\ \text{sec}^{-1}$ and $\Omega_e \approx 10^6$ sec. Thus, only electron temperature gradients parallel to the field lines will be effective in transporting energy through the electron gas.

At high altitudes the electron temperature profile can be determined from thermal conduction alone. The heating and cooling terms in equation (3.14) can be neglected. If steady state is assumed and the effect of external forces is ignored, then the electron temperature can be calculated from

$$\frac{\partial}{\partial z} K_e \frac{\partial T_e}{\partial z} = 0$$

Integrating one gets

$$K_e \frac{\partial T_e}{\partial z} = K_e \frac{\partial T_e}{\partial z}\bigg|_a$$

or

$$T_e^{5/2} \frac{\partial T_e}{\partial z} = \left[T_e^{a}\right]^{5/2} \frac{\partial T_e}{\partial z}\bigg|_a \qquad (3.84)$$

where the subscript a refers to some reference altitude. Integrating again gives

C-2

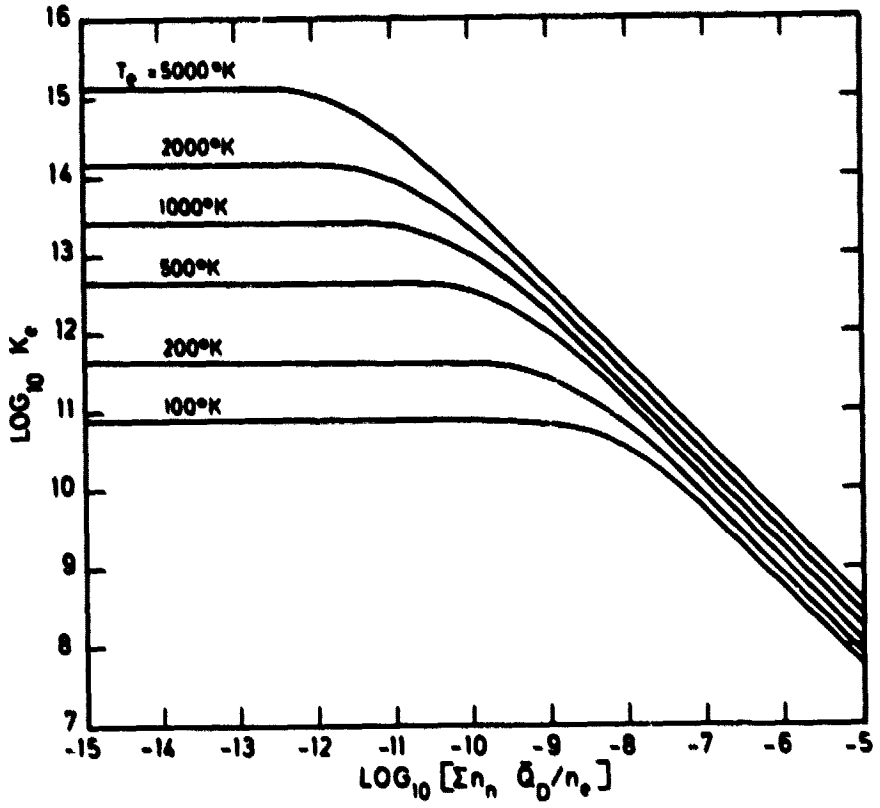

Figure 3.8 The effect of the neutral atmosphere on the electron thermal conductivity [after *Banks and Kockarts*, 1973].

$$T_e = \left[(T_e^a)^{7/2} + \frac{7}{2} \left[T_e^a \right]^{5/2} \frac{\partial T_e}{\partial z} \bigg|_a (z-a) \right]^{2/7}$$

or
$$T_e = T_e^a \left(1 + \frac{7}{2} \frac{\partial \ln T_e}{\partial z} \bigg|_a (z-a)\right)^{2/7} \tag{3.85}$$

showing that the electron temperature must continually rise with altitude. The presence of the heat flux can be inserted into (3.85) giving

$$T_e = \left[(T_e^a)^{7/2} + \frac{7}{2} \Phi_{||}^a (z-a) \right]^{2/7} \tag{3.86}$$

where $\Phi_{||}^a$ is the heat flux at some reference altitude.

3.8.2 *Ion thermal conduction*. Although ion thermal conductivity is not important at lower altitudes it can be effective in keeping the ion temperature significantly below the electron temperature at high altitudes [*Banks*, 1967b]. Thermal energy flows along the lines of magnetic field when there is a gradient in the ion temperature. Generally, heat flux for a single ion is given by

$$Q_i = - K_i \nabla T_i \tag{3.87}$$

but diffusion and thermal diffusion can alter this expression when the ion temperature is small and when ion densities are large. The importance of diffusion heating or cooling due to ion transport can be calculated by comparing the term

$$\left(\frac{3}{2} n_e k\right) \left(u \frac{\partial T_i}{\partial z} + \frac{2}{3} T_i \frac{\partial u}{\partial z}\right) \tag{3.88}$$

with $\frac{\partial Q_i}{\partial z}$

where u is the ion diffusion velocity, z is the vertical coordinate, and n_e is the electron concentration. In Table 3.6 are shown some calculations of diffusive heating and thermal flux from conduction where the ionization fluxes have been taken from Table 2.3.

TABLE 3.6

Comparison between diffusive heating and thermal flux from conduction for ions with $n_e = 1 \times 10^4$ cm^{-3} and $\frac{\partial^2 u}{\partial z^2} \ll 1$.

Ion Temperature (K)	Diffusion velocity	$\frac{\partial T}{\partial z}$	$\frac{\partial u}{\partial z}$	Diffusive heating (ev cm^{-3})	Thermal Flux (eV cm^{-3})
1000	1m/s	1 K	1×10^{-5}/s	1×10^{-2}	9×10^{-2}
2000	1m/s	1 K	1×10^{-5}/s	1.9×10^{-2}	2.6×10^{-1}
3000	1m/s	1 K	1×10^{-5}/s	2.8×10^{-2}	4.7×10^{-1}
1000	10m/s	10 K	1×10^{-5}/s	1.4×10^{-1}	9×10^{-1}
2000	10m/s	10 K	1×10^{-4}/s	3.0×10^{-1}	2.6
3000	10m/s	10 K	1×10^{-4}/s	3.9×10^{-1}	4.7

The calculation of the ion thermal conductivity K_i for a single ion gas of atomic mass A_i has been performed by *Chapman and Cowling* [1970] and is

$$K_i = 4.6 \times 10^4 (T_i^5/A_i)^{1/2} \text{ eV cm}^{-1} \text{ sec}^{-1} \text{ K}^{-1} \quad (3.89)$$

where the second approximation correction has been used. Below 500 km the ion conductivity is damped because of ion-neutral collisions, and is divided by $[1 + 3.22 \times 10^4 (T_i^2/n_i) \Sigma n_n \bar{Q}_D]$.

When there is a mixture of ions in the ionosphere and a single ion temperature is assumed, then the thermal conductivity must be adjusted to take into account the different values of the thermal conductivity for each individual ion. The exact expression is difficult to obtain but a density weighted thermal conductivity can be used as [*Banks*, 1967a]

$$K_i = 1.2 \times 10^4 [n(O^+) + 2n(H^+) + 4n(He^+)]/n_e \quad (3.90)$$

which is accurate to within several percent in binary mixtures. ($n(O^+)$ is the number density of O^+ ions, $n(H^+)$ is the number density of H^+ ions, and $n(He^+)$ is the number density of He^+ ions). When there is a mixture of ions and separate ion temperatures are calculated, then equation (3.89) is used for thermal conduction of each individual ion. The solution for the separate ion temperatures is discussed later in Chapter 6. The effects of ion-neutral collisions which is included in the electron thermal conductivity can be neglected above 300 km.

3.9 *Energy Sources for Ions*

The major source of heating of ions is energy transfer through Coulomb collisions with thermal electrons. The energy transfer rate has been calculated previously and is given in equation (3.73).

In addition to heating by the electron gas, ions can be heated through dissipation of wave energy, or through electric fields, chemical reactions, or inelastic collisions. But experimental observations indicate that the

electron gas is the primary source of ion heating altitudes above 300 km. Incoherent scatter measurements of *Evans* [1969] and *Hagen and Hsu* [1974] show that the ion temperatures are always equal to or less than the electron temperature. This implies that the electron gas is the major ion heat source.

Different ion species can have separate temperatures. H^+ ions are heated to higher temperatures than O^+ ions due to the larger collision frequency of electron with H^+ ions. Thus, H^+ ions can transfer energy to the cooler O^+ ions through Coulomb collisions, and H^+ ions are then an energy source for O^+ ions.

Below 300 km, the effects of neutral winds, electric fields, and electric currents can cause ion heating through conversion of bulk transport into random thermal motions. This is ion Joule heating. Also, since heat production and energy loss are governed by the same collisional processes, the ion temperature can be found from (3.14) when steady-state conditions apply as

$$T_i = T_n + m_n(\vec{u}_i - \vec{u}_n)^2/3k \tag{3.91}$$

Generally, electric fields and neutral winds are not large enough to have a significant effect in raising the ion temperature above the neutral temperature.

3.10 *Energy Losses for Ions*

There exist for ions three methods of energy loss: ion-neutral elastic collisions, ion-ion Coulomb collisions, and ion-neutral resonant charge exchange. The process of ion-neutral resonant charge exchange is fundamentally elastic in nature but it cannot be described by the equation of collisional energy transfer. This is discussed later in Section 3.10.2. The analysis of laboratory and theoretical cross section data are used to obtain the resonance ion-neutral energy transfer rates. In the following subsections the

collision frequency and energy transfer equations are discussed for elastic ion-neutral and ion-ion collisions.

3.10.1 *Ion-neutral collisions.* The energy transfer rate for two gases with Maxwellian velocity distributions characterized by the temperatures T_1 and T_2 and particle masses m_1 and m_2 is given by equation (3.53). Accurate expressions for both energy transfer rates and collision frequencies can easily be derived from equation (3.53) once the velocity dependent momentum transfer cross section is known. At low temperatures the induced dipole attraction with a potential of $Q = -\alpha e^2/2r^2$ is the most important ion-neutral interaction (α is the neutral atom polarizability, and r is the radial separation). Using this relation it is found that the average momentum transfer collision cross section is proportional to $(T_1 + T_2)^{-1/2}$ and that the collision frequency is independent of the temperature.

The induced dipole force of attraction is countered by a short-range quantum mechanical repulsion at temperatures greater than 300 K. The nature of this repulsive force is linked directly to the details of the ion and neutral orbital electron structures. This creates a problem since there are almost no data available for either the cross sections or collision frequencies for ion-neutral collisions at high temperatures. Thus, ion-neutral energy transfer rates are somewhat uncertain. The rates are estimated by using the low temperature polarization interaction with a suitable truncated repulsive potential to account for short range quantum effects.

Dalgarno et al. [1968] has evaluated the ion-neutral interaction potential by assuming the polarization potentials at distances greater than a small atomic radius and an elastic sphere repulsive potential at distances less than this atomic radius to simulate quantum repulsive effects. The

ion-neutral collision frequency for singly charged ions is given by

$$\bar{\nu}_{in} = 2.6 \times 10^{-9}\, n_n (\alpha_o/\mu_{in})^{1/2} \text{ sec}^{-1} \tag{3.92}$$

where α_o is the neutral gas atomic polarizability in units of 10^{-24} cm^3, and μ_{in} is the ion-neutral reduced mass in amu. The ion-neutral elastic energy transfer rate is calculated from equation (3.53) as

$$\frac{dU_i}{dt} = -\, 2.6 \times 10^{-4}\, \frac{A_i A_n\, n_i}{(A_i + A_n)^2}\, \bar{\nu}_{in}\, (T_i - T_n) \text{ eV cm}^{-3} \text{ sec}^{-1} \tag{3.93}$$

where A is the atomic mass of the indicated particle. In Table 3.7 are shown the ion energy loss rates to the atmospheric gases where the polarizabilities are from *Banks and Kockarts* [1973]. The differences in the rates are due mainly to changes in the mass factors rather than changes in the atomic polarizability.

3.10.2 *Ion-ion collisions.* In studies of ionospheric thermodynamics a single ion temperature is often used throughout the ionosphere. However, *Banks* [1967a] has shown that a temperature difference exists between H^+ and O^+ ions and between He^+ and O^+ ions. This difference is largest for H^+ and O^+ ions and has a maximum of 200 K in the region between 250 and 650 km. The important factor limiting the size of the temperature difference is the rapid ion-ion energy exchange rate. The Coulomb interaction determines the ion-ion energy transfer frequency which follows from equation (3.71). The ion-ion energy transfer rate is calculated from equation (3.53) using equation (3.71) as

$$\frac{dU_i}{dt} = -\, \frac{3.3 \times 10^{-4}\, n_1 n_2\, (T_1 - T_2)}{A_1 A_2 [(T_1/A_1) + (T_2/A_2)]^{3/2}} \text{ eV cm}^{-3} \text{ sec}^{-1} \tag{3.94}$$

TABLE 3.7

Ion energy loss rates for elastic collisions with atmospheric gases (after *Banks*, 1967b).

Neutral Species	Ion	Energy loss rates (10^{-14} eV cm^{-3} sec^{-1})
N_2	O^+	$6.5\, n(O^+)n(N_2)(T_i - T_n)$
O_2	O^+	$5.8\, n(O^+)n(O_2)(T_i - T_n)$
H_e	O^+	$2.8\, N(O^+)n(H_e)(T_i - T_n)$
N_2	H^+	$3.1\, n(N_2)n(H^+)(T_i - T_n)$
O_2	H^+	$2.8\, n(O_2)n(H^+)(T_i - T_n)$
H_e	H^+	$5.5\, n(H_e)n(H^+)(T_i - T_n)$

where the subscripts apply to the two ion species and A is the ion mass in amu.

The H^+ ions lose energy to O^+ ions and the O^+ ions in turn gain energy through O^+ - H^+ Coulomb collisions. This is because H^+ ions are heated 16 times faster by electrons as shown in equation (3.73).

3.10.3 *Resonant ion-neutral collisions.* The importance of charge exchange in the ion energy balance equation has been investigated by *Banks* [1966b]. In process of exchanging charge both of the original particles tend to retain its original kinetic energy. Thus, the reaction is fundamentally elastic in perserving the total kinetic energy even though the identity of the ion has changed. Thus, charge exchange provides energetic ions a rapid way in which to transfer energy to neutral particles. For many atmospheric ion-neutral pairs the probability of charge exchange collisions is much larger than that for normal elastic collisions.

The energy loss rate of an ion gas is derived from considering energy balance in ion production and loss. For Maxwellian velocity distributions with characteristic temperatures, T_i and T_n the ion-neutral energy loss rate is [*Banks*, 1966b]

$$\frac{dU_i}{dt} = -\frac{3}{2} n_i k \bar{\nu}_E (T_i - T_n) \tag{3.95}$$

where $\bar{\nu}_E$ is the ion-neutral charge exchange collision frequency. In Table 3.8 are given energy loss rates for ions of the topside ionosphere.

Besides resonant ion-neutral charge exchange collisions between atmospheric gases of the same species, there exists an accidentally resonant charge exchange between H^+ and O. This has been discussed previously in Section 2.2 with regard to hydrogen-ion production and loss. The energy loss rates for oxygen and hydrogen ions due to charge exchange are [*Banks*, 1967a]

TABLE 3.8

Resonance charge exchange energy loss rates.

Species	$\frac{1}{n_i\, n_n}\,\frac{1}{(T_i + T_n)^{\frac{1}{2}}}\,\frac{1}{(T_i - T_n)}\,\frac{dU_i}{dt}$
O^+, O	2.1
H^+, H	13.0
H_e^+, H_e	3.9

$$\left.\frac{dU_i}{dt}\right|_{O^+-H} = 3.8 \times 10^{-15} n(O^+) n(H) T_n^{1/2} [T(O^+) - \frac{8\, n(O) n(H^+)}{9\, n(O^+) n(H)} T_n^{1/2} T^{1/2}(H^+)] \text{ eV cm}^{-3} \text{ sec}^{-1} \quad (3.96)$$

$$\left.\frac{dU_i}{dt}\right|_{H^+-O} = 3.4 \times 10^{-15}\, n(H^+) n(O) T^{1/2}(H^+) \times [T(O^+) - \frac{9\, n(H) n(O^+)}{8\, n(H^+) n(O)} (T_n^3 / T(H^+))^{1/2}] \text{ eV cm}^{-3} \text{ sec}^{-1} \quad (3.97)$$

The resonant charge exchange energy loss rates are based on experimental results reported in [*Banks*, 1966b]. While the maximum error in He^+ - He charge exchange cross sections is less 15 percent, the maximum errors associated with O^+-O, O^+-H, H^+-O, and H^+-H charge exchange cross sections are less than 11, 10, 10, and 1 percent respectively.

4. INCOHERENT SCATTER THEORY

4.1 *Introduction*

Information about the temperatures of the ions and the electrons and about the mixture of ions can be obtained from observations of the scattering of electromagnetic waves from density fluctuations in the medium. *Gordon* [1958] was the first to predict that the width of the frequency spectrum would be determined by a Doppler spread caused by the thermal velocities of the electrons. Later observations by *Bowles* [1962] and *Pineo et al.*, [1960] showed the frequency spectrum to be much narrower than anticipated because the Doppler spread is determined by the thermal velocity of the ions. The theory of this phenomenon has been developed by a number of workers [*Fejer*, 1960, 1961; *Dougherty and Farley*, 1960; *Renau*, 1960; and *Salpeter*, 1960a, b] and all arrived at identical conclusions.

Fejer [1961] has developed a theory of scattering of radio waves by an ionized gas in thermal equilibrium in the presence of a uniform magnetic field. This is a generalized treatment in that the results would be used for several types of ions present and for unequal values of the individual ion temperatures and electron temperature.

Moorcroft [1964] has studied the effects of ionic composition on the nonmagnetic spectrum. From his work *Hagen and Hau* [1974] have deduced the structure of the protonosphere above Arecibo.

In this chapter attention will be paid to the effects of unequal ion temperatures on the spectrum where a magnetic field is not present which is relevant for all directions of propagation except those nearly perpendicular to the magnetic field lines. The ions, O^+ and H^+, will be treated and considered in detail. The ion, He^+, is not considered in this treatment because of its

of its relative unimportance with respect to H^+ and O^+. Experimental observation of He^+ indicate that its number density is less than ten percent of the H^+ number density [*Rees et al.*, 1971; *Gleeson and Axford*, 1967].

The effects of ionic composition, electron temperature, and Debye length on the nonmagnetic spectrum will also be considered. The H^+ number density plus the O^+ number density is assumed to equal the electron number density. Electron temperatures are assumed to be greater than or equal to the ion temperatures. This has been shown to exist by a number of experimental observations of the topside ionosphere [*Hagen and Hsu*, 1974]. Theoretical expressions for scattering from the thermal density fluctuations in an ionized gas have been taken from a paper by *Fejer* [1961]. Computations in this work were programmed on the H-P 9830, the CDC Cyber 1700, and the IBM 360 at the University of Illinois.

4.2 *Incoherent Scatter from a Thermal Unmagnetized Plasma*

The influence of ions on the scattering characteristics has been shown to be important when the exploring wavelength is very much larger than the Debye length [*Dougherty and Farley*, 1960; *Salpeter*, 1960a; *Hagfors*, 1961]. The Debye length or shielding distance D_e is

$$D_e = (\varepsilon_0 kT_e/n_e e^2)^{1/2} \quad \text{meters} \tag{4.1}$$

where ε_0 is the permittivity of free space, k is Boltzmann's constant, T_e is the electron temperature, n_e is the electron density, and e is the charge on the electron. The scattering can be thought of as arising from density fluctuations brought about by longitudinal oscillations in the plasma. Ion-acoustic waves and electron-induced waves at the plasma frequency and the electron gyrofrequency comprise a major part of these oscillations. In the absence of collisions the frequency spectrum of the scattered power from

randomly distributed electrons is

$$S(\omega) = \left| \frac{1 - \sum_{j=2}^{3} C_j}{1 - \sum_{j=1}^{3} C_j} \right|^2 \pi^{-1/2} \Omega_1^{-1} n_1 \sigma_e \exp(-\omega^2/\Omega_1^2)$$

$$+ \left| \frac{C_1}{1 - \sum_{j=1}^{3} C_j} \right|^2 \sum_{j=2}^{3} \pi^{-1/2} \Omega_j^{-1} n_j \sigma_e \exp(-\omega^2/\Omega_j^2) \tag{4.2}$$

where $$\Omega_j = k_\omega (2kT_j/m_j)^{1/2} \tag{4.3}$$

$$C_j = D_j^{-2} k_\omega^{-2} [-1 + 2(\omega/\Omega_j) \exp(-\omega^2/\Omega_j^2)$$

$$\times \int_0^{\omega/\Omega_j} \exp y^2 dy + i \pi^{1/2} (\omega/\Omega_j) \exp(-\omega^2/\Omega_j^2)] \tag{4.4}$$

$$D_j = (\epsilon_0 kT_j/n_j e^2)^{1/2} \tag{4.5}$$

and $$k_\omega = 4\pi/\lambda \tag{4.6}$$

where λ is the transmitted wavelength

Subscript 1 refers to electrons, 2 refers to O^+, and 3 refers to H^+. The Thomson scattering coefficient of an electron is

$$\sigma_e = (\mu_0 e^2 \sin\gamma/4\pi m_1)^2 \tag{4.7}$$

where μ_0 is the permeability of free space, γ is the angle between the electric field vector of the incident wave and direction of scattering, and the other quantities have been defined previously.

In equation (4.2) the first term is called the electronic term and second term is called the ionic term. For large values of the parameter $\alpha = 4\pi D_e/\lambda$ the spectrum function is very broad and most of the scattered power is in the electronic part of the spectrum [*Fejer*, 1961]. This spectrum

has a Gaussian shape. For small values of α the spectrum becomes narrow and the ionic part of the spectrum contains most of the scattered power. It is this feature which allows radar investigation of the ionosphere using apparatus of lower sensitivity. In the topside ionosphere α is generally quite small. At larger values of α the scattered power can be calculated by use of approximations.

The only term in equation (4.2) which is not analytic is the integral

$$\int_o^{\omega/\Omega_j} \exp y^2 dy \qquad (4.8)$$

This can be expressed as the power series

$$\frac{\omega}{\Omega} \exp(\omega^2/\Omega^2) \sum_{k=1}^{\infty} \frac{(k-1)!}{(2k-1)!} \left(\frac{-\omega^2}{\Omega^2}\right)^{k-1} \qquad (4.9)$$

(see Appendix B), or as an asymptotic expansion

$$\frac{\Omega}{2\omega} \exp(\omega^2/\Omega^2)$$

$$\times \left(1 + \frac{\Omega^2}{2\omega^2} + 3\left(\frac{\Omega^2}{2\omega^2}\right)^2 + 15\left(\frac{\Omega^2}{2\omega^2}\right)^3 + 105\left(\frac{\Omega^2}{2\omega^2}\right)^4 + \ldots\right)$$

Both the power series and the asymptotic expansion used in the calculation of the power spectrum depends on the magnitude of the quantity, ω^2/Ω^2. When ω^2/Ω^2 is small, the power series is very useful since it converges rapidly. When ω^2/Ω^2 becomes large and the power series fails to converge, the asymptotic expansion is used with very little error entering into power spectrum calculations.

Buneman [1962] has shown that the total cross section attributable to the ionic component when $T_e = T_i$ is given by

$$\sigma = \sigma_e/(1 + \alpha^2)(2 + \alpha^2) \qquad (4.10)$$

which approaches $\sigma_e/2$ as $\alpha \to 0$. In the topside ionosphere, T_e is often not equal to T_i. Generally T_e/T_i is in the range 1 to 4. When this is true the effect of varying T_e/T_i on the total echo power can be expressed as

$$\sigma = \sigma_e/(1 + \alpha^2)(1 + T_e/T_i + \alpha^2) \qquad (4.11)$$

The exact variation of the total cross section α as a function of T_e/T_i has been calculated by *Moorcroft* [1963] and is shown in Figure 4.1 for the case $\alpha \to 0$.

4.3 *Characteristics of Theoretical Spectra*

4.3.1 *Spectra for one type of ion.* In order to better understand the more complicated case of two ions, spectra for one type of ion will be reviewed and examined first. Power spectra are shown in Figure 4.2 for scatter from ionized gases where the ion present is either oxygen or hydrogen for electron-ion temperature ratios T_e/T_i of 1.0, 2.0, and 3.0. Only half of the spectrum is shown since the spectrum is symmetric about the transmitter frequency. The scale for the power scattered per unit incident power density (power spectral density) is normalized by the power spectral density at zero Doppler shift. The frequency scale is normalized by the factor $\lambda(m_e/8kT_e)^{1/2}$. This indicates that the position of the peak in the spectrum depends on $T_e^{1/2}$, since the peak position doesn't change significantly when the frequency scale is normalized by this factor. Figure 4.2 also shows that the width of the spectrum is nearly proportional to the square root of the ion mass. Thus, if the frequency scale is normalized by $m_i^{1/2}$ as is shown in Figure 4.3, then the peak of the spectrum appears at almost the same Doppler frequency shift for both O^+ and H^+.

The width of the spectrum also depends on the ion temperature. This is shown in Figure 4.4 for O^+ where T_e/T_i is assumed to be equal to 1. The

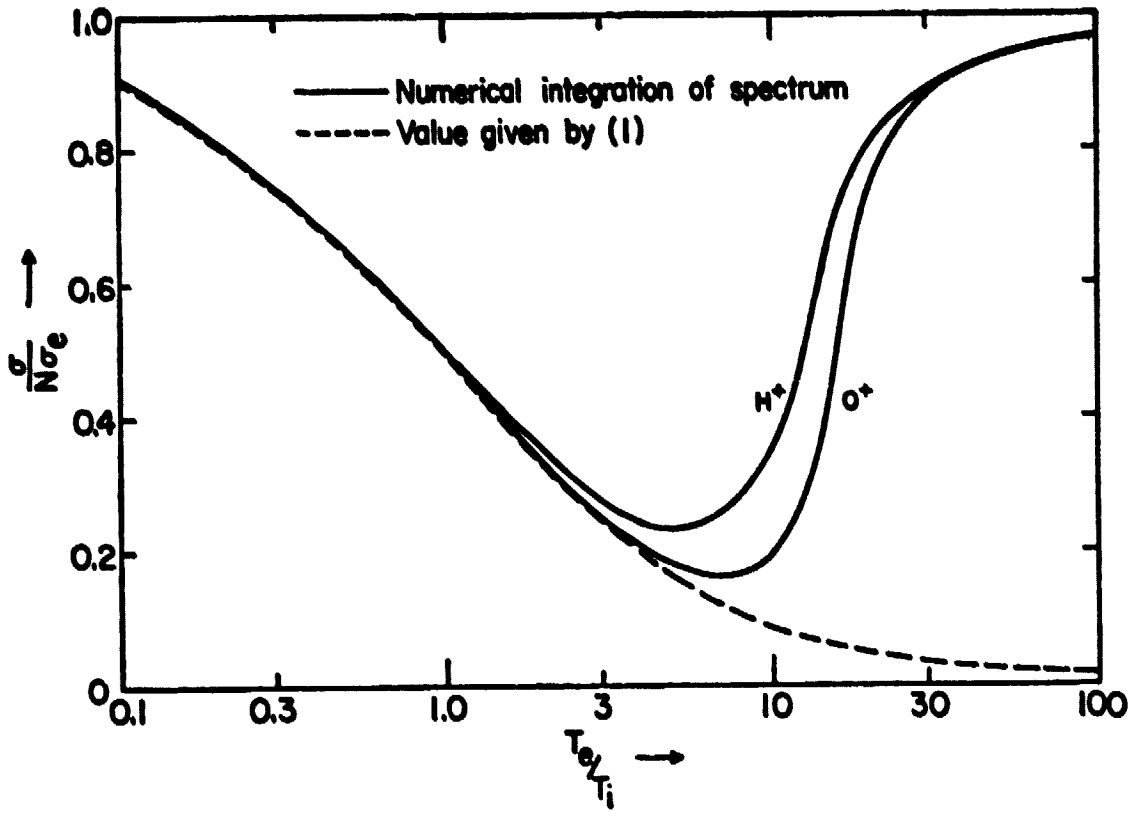

Figure 4.1 Total scattering cross sections as a function of T_e/T_i for $\alpha \to 0$ [after *Moorcroft*, 1963].

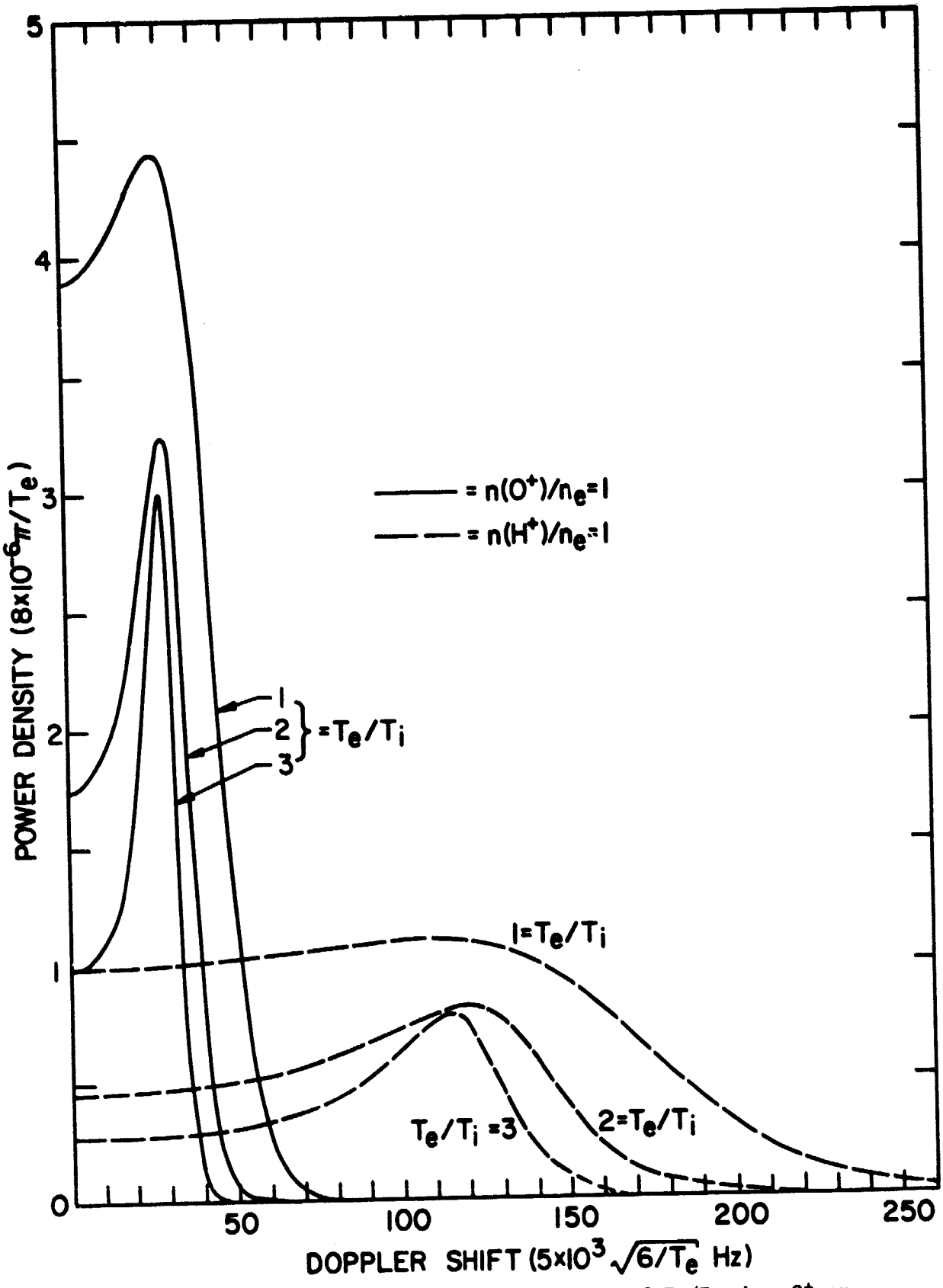

Figure 4.2 Scatter spectra for different values of T_e/T_i when O^+ or H^+ is the scattering ion.

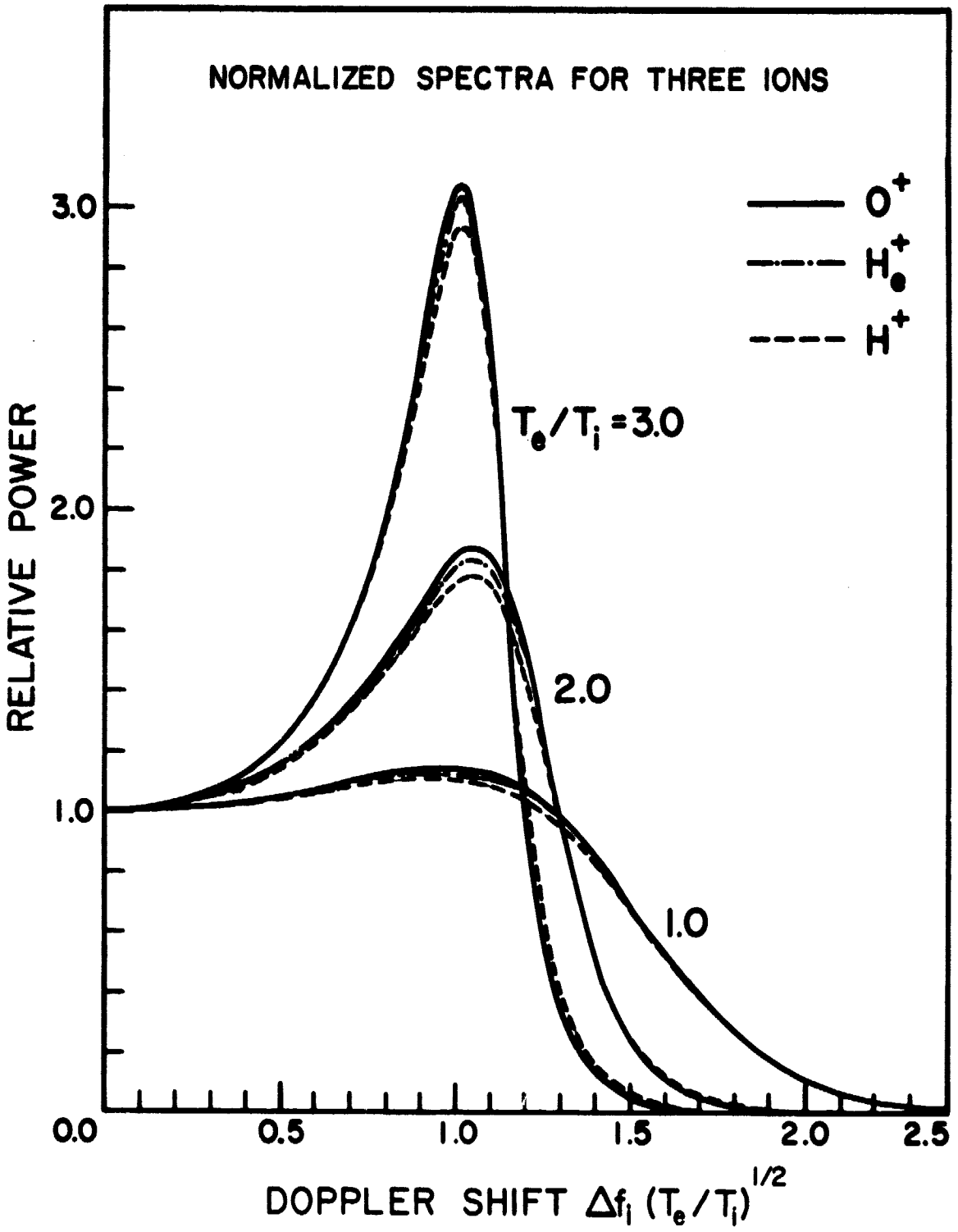

Figure 4.3 Spectrum shapes for the ionic component for three ions for three values of T_e/T_i. These spectra have been plotted against a frequency scale normalized with respect to the ion mass and electron temperature so that they may be compared directly [after *Moorcroft*, 1964]. It can be seen that the shapes are almost identical in all cases.

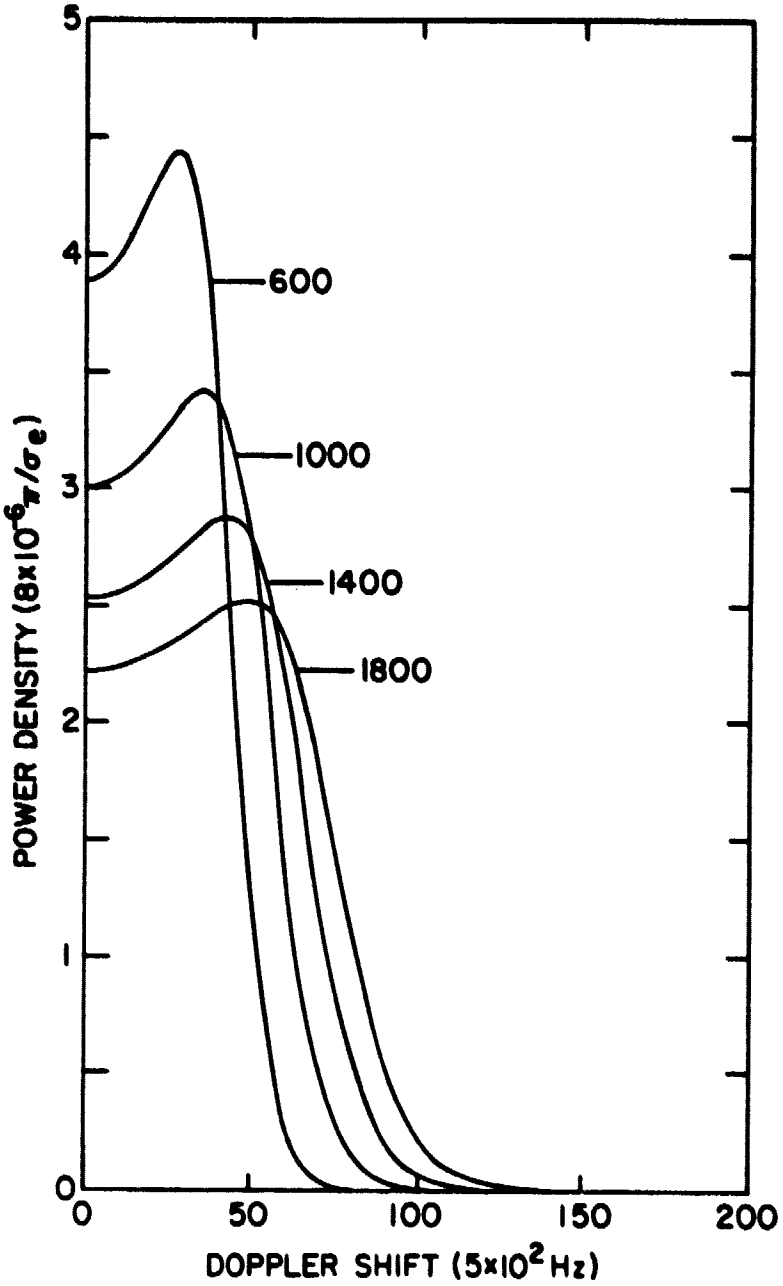

Figure 4.4 Scatter spectra for different values of T_i where $T_e/T_i = 1$.

width of the spectrum increases as T_i increases. This characteristic can be used to calculate T_i from experimental data.

When only one type of ion is present and $T_e = T_i$ the calculation of T_i, T_e and n_e is straightforward. n_e can be found from the power scattered per unit volume σ. T_i can be calculated from the width of the spectrum (Δf). T_e is equal to T_i. Generally in the topside ionosphere the ions are hotter than the electrons. The quantities σ and Δf are then functions of the temperature ratio T_e/T_i. However, the height of the peak of the spectrum relative to the spectrum value at zero Doppler shift, $R = \max\{S(\omega)\}/S(0)$, is a function only of the temperature ratio. So, if R is measured then T_e/T_i can be found which in turn can be used in the calculation of T_i and N_e. Figure 4.5 shows the dependence of R on T_e/T_i for O^+ and $T(O^+) = 1000$ K.

4.3.2 *Spectra for a mixture of* H^+ *and* O^+ *with a single ion temperature.* The interpretation of the scattering from an ionized gas is considerably more complicated when two types of ions are present than when only one kind is present. The discussion in this section is related to a mixture of H^+ and O^+. This is appropriate for the topside atmosphere since densities of other ions are very small compared to the combined densities of H^+ and O^+.

Moorcroft [1964] has calculated the spectrum for the case where the mass of one ion is four times the mass of the other ion. This could apply to mixtures of O^+ and He^+ ions or mixtures of H^+ and He^+ ions. Although this analysis may be useful where the He^+ density reaches its maximum value, generally the He^+ density is much too small to have any appreciable effect on the incoherent-scatter spectrum. The effect of He^+ will therefore be ignored and the mixture of H^+ and O^+ ions will be studied in detail.

While the shapes of spectra for two different ions are similar for a given temperature ratio, the shape of spectra for a mixture of the two ions

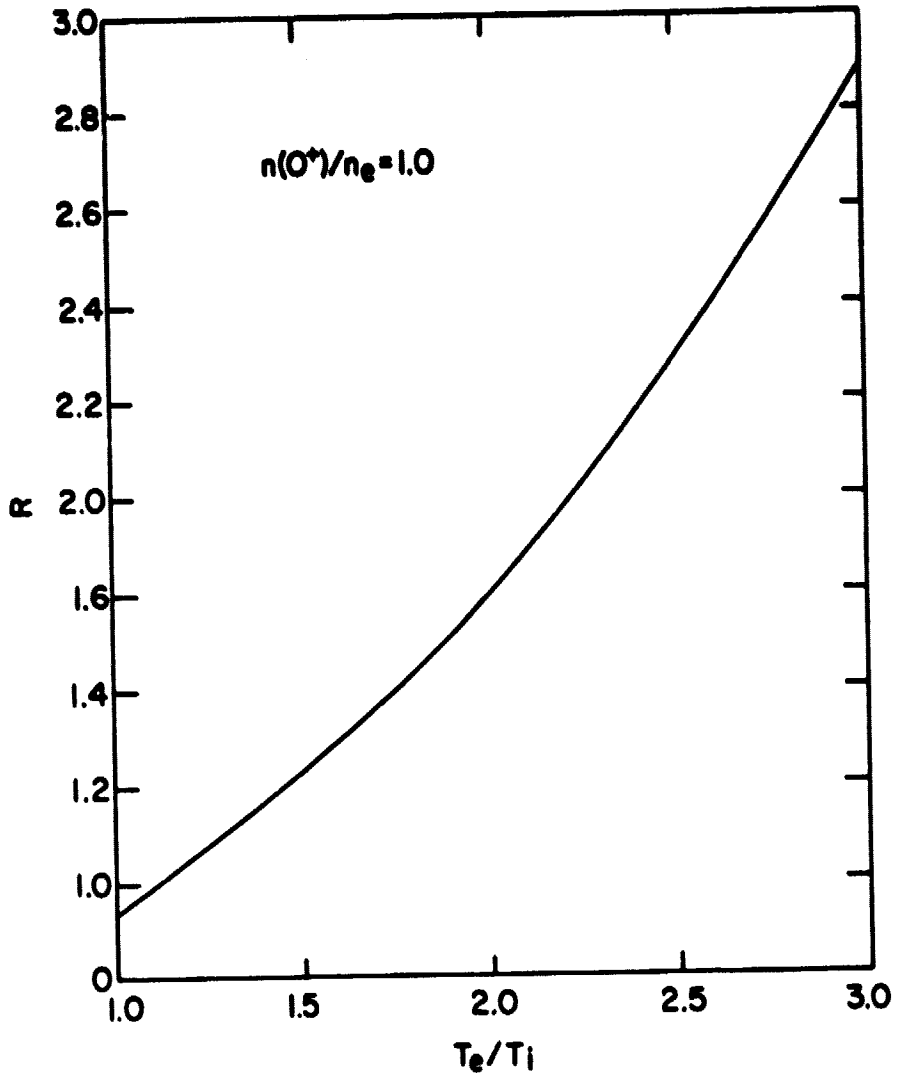

Figure 4.5 Spectrum peak-to-center ratio R as a function of T_e/T_i for O^+ when T_i = 1000 K.

is quite different from those of either ion alone. This is evident in Figure 4.6 where spectra are shown for various mixtures of O^+ and H^+ for a temperature ratio of 2.0. This figure also indicates that the peak-to-center ratio R is now a function of $n(O^+)/n_e$ as well as of T_e/T_i which complicates the calculation of T_e/T_i. The R dependencies must be represented by a whole family of curves rather than a single line as in Figure 4.5. Figure 4.7 shows R as a function of $n(O^+)/n_e$ and T_e/T_i for mixtures of O^+ and H^+.

The appearance of a double hump feature in Figure 4.6 is the result of the Doppler frequency separation of the O^+ peak and the H^+ peak. The peak of the H^+ part of the spectrum doesn't show clearly as a peak until $n(O^+)/n_e$ is 0.4 or less. Likewise, the O^+ peak doesn't become a peak until $n(O^+)/n_e$ is 0.6 or greater. Thus, when $n(O^+)/n_e$ is greater than 0.4 and less than 0.6 there is no peak in the spectrum and the maximum value of the spectrum occurs at zero Doppler shift. This makes the determination of T_e/T_i or $n(O^+)/n_e$ from measurements of R impossible since T_e/T_i and $n(O^+)/n_e$ can take on many values for a single value of R. Thus, an extra parameter is needed in order to determine T_e/T_i and $n(O^+)/n_e$ when $n(O^+)/n_e$ is in the range between 0.4 and 0.6. When $n(O^+)/n_e$ is between 0.6 and 1.0 and between 0.0 and 0.2, R changes rapidly as $n(O^+)/n_e$ changes.

In contrast to R, $f_{\frac{1}{2}}$ (see Figure 4.8) the width of the spectrum at half maximum, changes much more rapidly when $n(O^+)/n_e$ is between 0.2 and 0.6 than when $n(O^+)/n_e$ is between 0.0 and 0.2 and between 0.6 and 1.0. When $n(O^+)/n_e$ is between 0.8 and 1.0, $f_{\frac{1}{2}}$ is almost constant and changes only slightly from one value of T_e/T_i to another. This makes the determination of $n(O^+)/n_e$ and T_e/T_i from $f_{\frac{1}{2}}$ measurements difficult when $n(O^+)/n_e$ is between 0.8 and 1.0., with the result that the error in $n(O^+)n_e$ and T_e/T_i would be much larger.

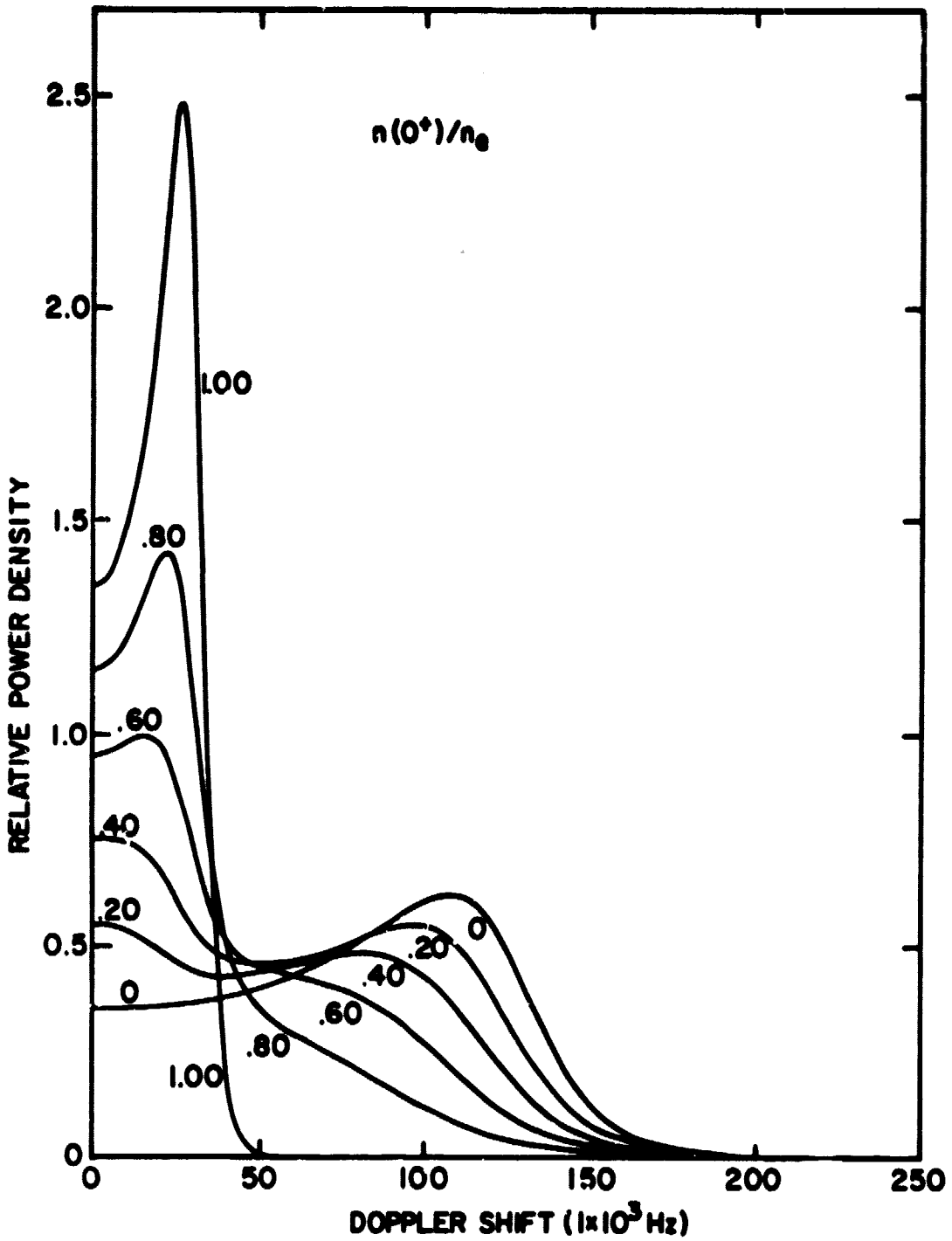

Figure 4.6 Scatter spectra for a mixture of O^+ and H^+ where $T_e/T_i = 2$.

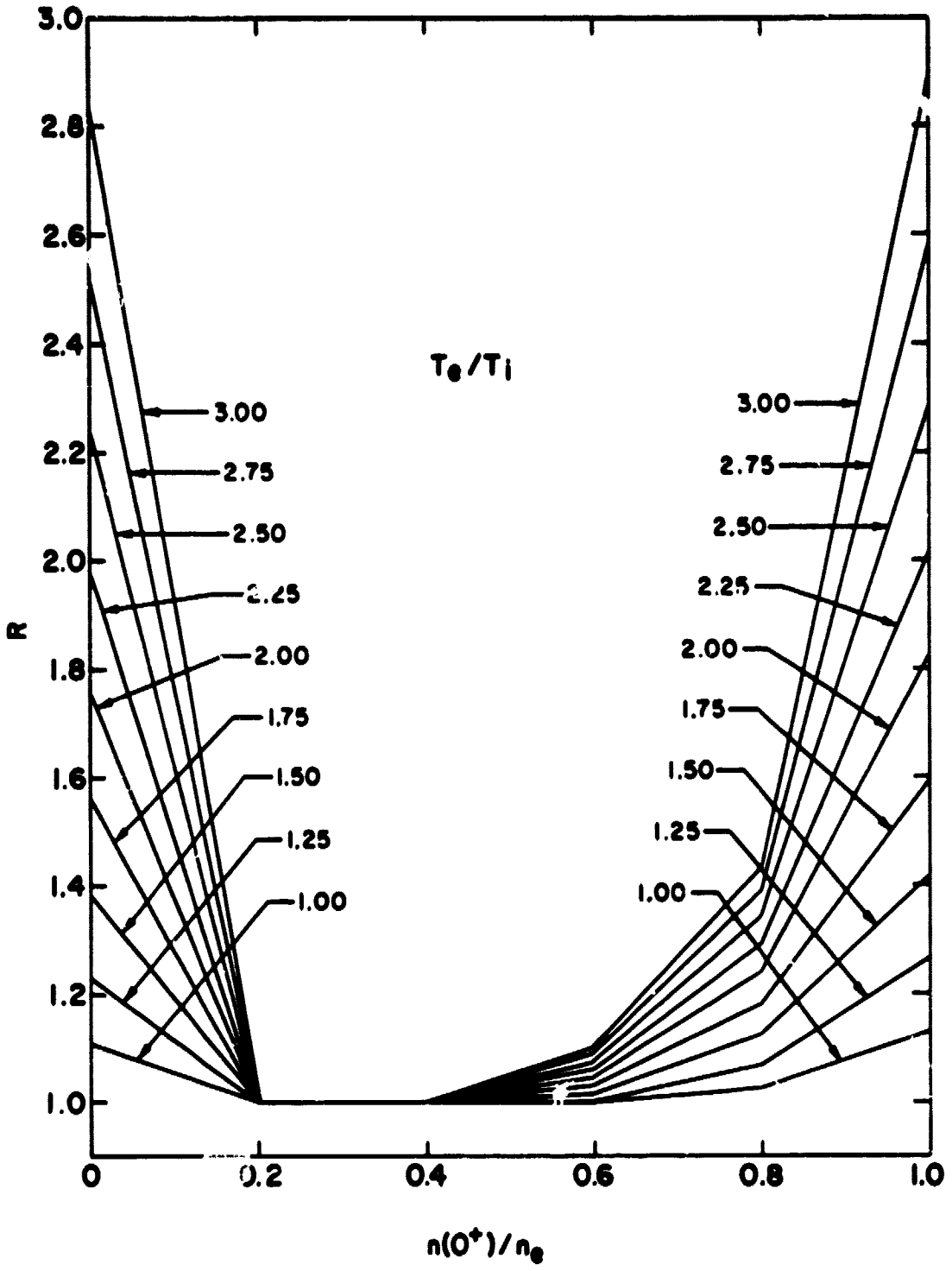

Figure 4.7 Spectrum peak-to-center ratio R as a function of T_e/T_i and $n(O^+)/n_e$ where Ti = 1000 K.

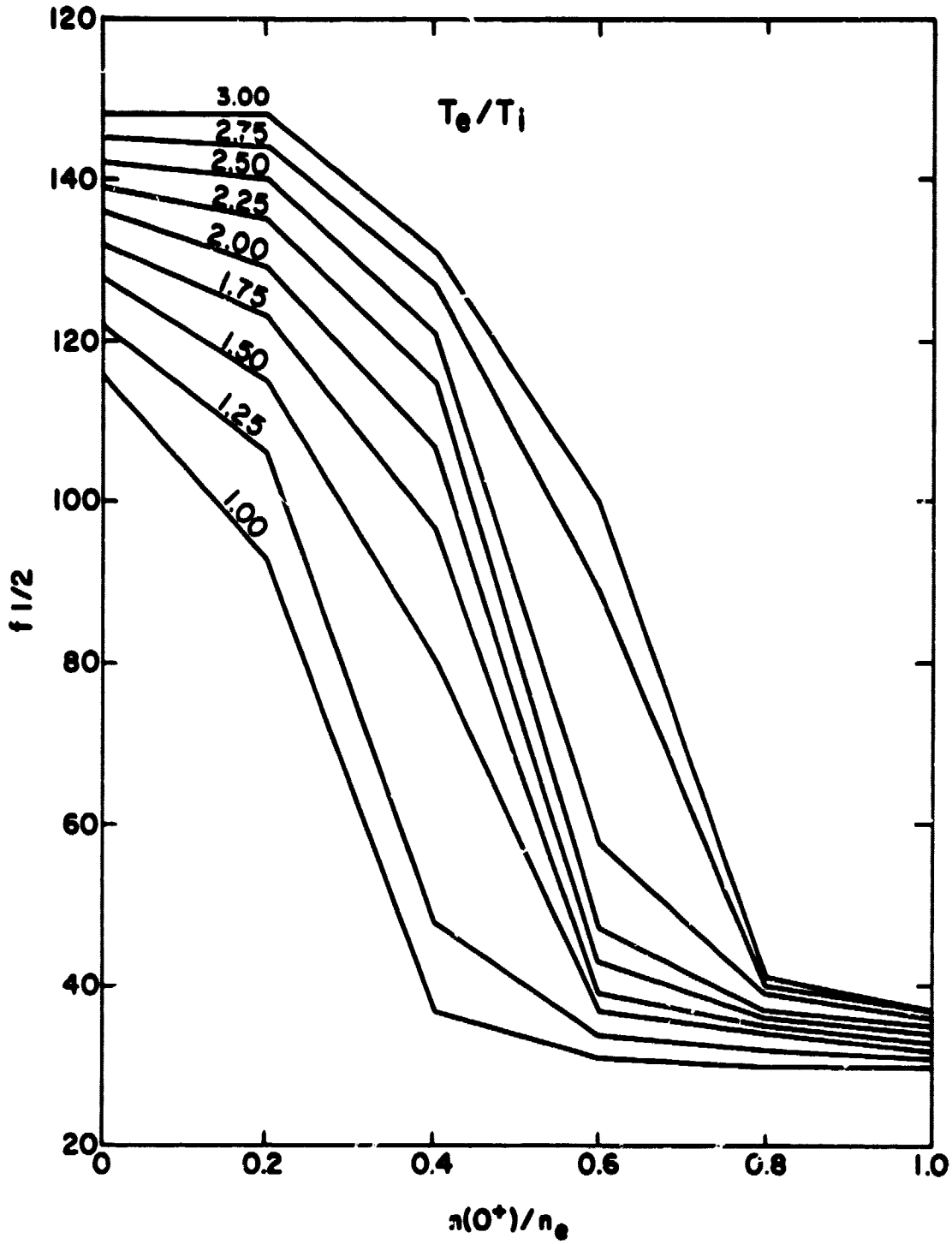

Figure 4.8 Width of the spectrum at half its maximum value ($f_{\frac{1}{2}}$) as a function of T_e/T_i and $n(O^+)/n_e$ where T_i = 1000 K.

One quantity which changes only slightly as the composition is varied is σ/n_e where σ is power scattered per unit volume [*Moorcroft*, 1964]. σ is a function of T_e/T_i which is shown in Figure 4.9. The change in σ/n_e is sufficiently small as the composition varies that it can be either ignored or obtained by a simple interpolation between the curves of Figure 4.9. Since very little error is introduced by ignoring the dependence of σ on composition, σ is assumed hereafter, to be a function only of n_e and T_e/T_i.

Generally, the determination of the temperatures and densities of the electrons and ions requires at least the measurement of four parameters of the spectrum. So, it is clear that measurement of $f_{\frac{1}{2}}$, R, and σ alone is insufficient to determine any of the temperatures or densities. However, prior knowledge of any one of T_e, T_i, T_e/T_i, $n(0^+)/n_e$ or n_e is sufficient to determine all the rest.

Sometimes, for example, an independent measurement of the electron density is available. Then the ratio σ/n_e via Figure 4.9 will give T_e/T_i which combines with R via Figure 4.7 to give $n(0^+)/n_e$. Finally, since $f_{\frac{1}{2}}$ depends on $T_i^{\frac{1}{2}}$, T_e/T_i and $n(0^+)/n_e$ combine via Figure 4.8 to give T_i.

An assumption about either T_e/T_i or $n(0^+)/n_e$ will likewise enable all the other quantities to be determined. When T_i is known it is necessary to make an initial assumption above either $n(0^+)/n_e$ or T_e/T_i to get the other quantity from either Figure 4.7 or 4.8. If the value of $n(0^+)/n_e$ is assumed initially and Figure 4.8 is used to reduce T_e/T_i, then this value of T_e/T_i can be used in Figure 4.7 to determine $n(0^+)/n_e$. This iterative procedure is continued until $n(0^+)/n_e$ and T_e/T_i converge.

One point which has been ignored in the above discussion is the fact that two values of $n(0^+)/n_e$ are possible for a single value of R and T_e/T_i as shown in Figure 4.7. However, this ambiguity can be removed by additional

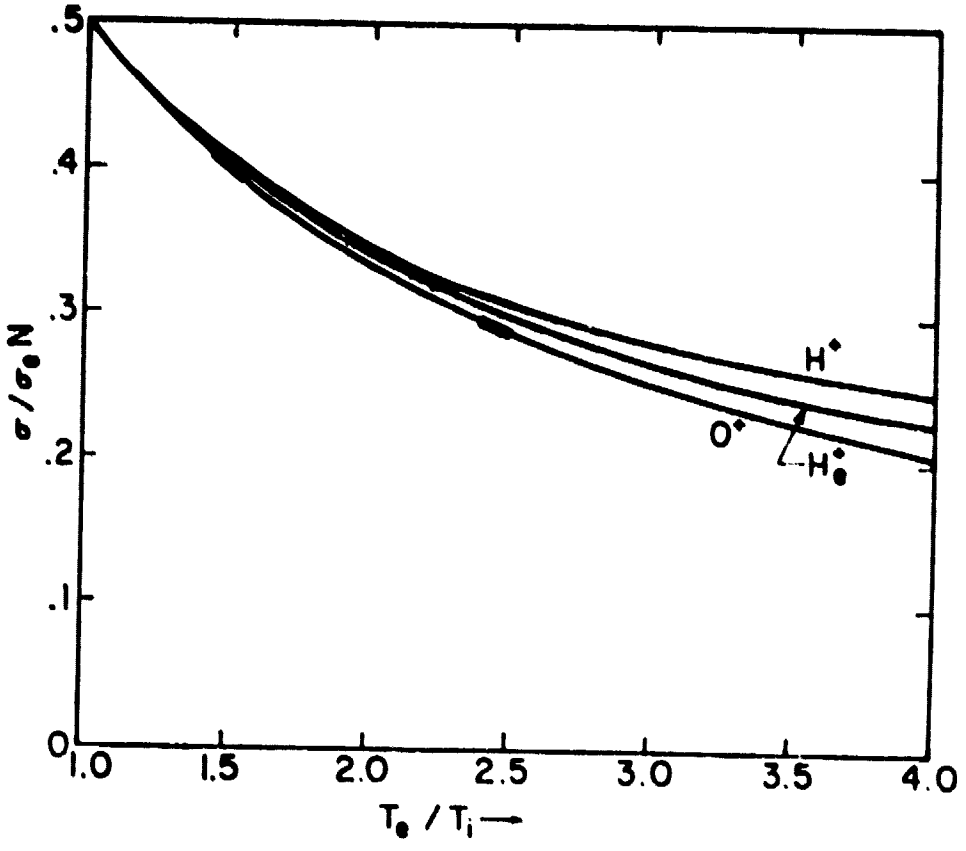

Figure 4.9 σ/N as a function of T_e/T_i for O^+, He^+ and H^+ [after *Moorcroft*, 1964].

information concerning the structure of the upper atmosphere. At lower altitudes it is known that the amount of H^+ is very small. As the investigation is extended upward from the F_1 layer only one of the two possible sets of values for $n(O^+)/n_e$ gives a continuous variation of $n(O^+)/n_e$ with height.

If information about n_e, T_e/T_i, T_e or T_i is not available and if one is to deduce information about temperatures and composition from scattering measurements alone, then another independent measurement on the spectrum is necessary. A survey of the shape of spectra in Figure 4.6 shows that the tail of the spectrum becomes more extended as $n(O^+)/n_e$ decreases. It appears that the measurement of the slope of the tail of the spectrum will yield information on $n(O^+)/n_e$ and T_e/T_i. The choice for this new parameter is the slope of the spectrum at the point where the power spectral density falls to one-half its central value and it will be called $S_{\frac{1}{2}}$. In order to keep it independent of the scales of power density and Doppler shift, $S_{\frac{1}{2}}$ can be measured on a semilogarithmic plot of the spectrum in which the central value of the power spectral density is normalized to zero. Because of this normalization, $S_{\frac{1}{2}}$ is then expressed as the number of decibels of change over a frequency interval corresponding to the Doppler shift to a point - 3 dB from the central value of the spectrum. $S_{\frac{1}{2}}$ is independent of the electron and ion temperatures and is a function only of T_e/T_i and $n(O^+)/n_e$.

4.3.3 *Spectra for a mixture of* H^+ *and* O^+ *with different ion temperatures.* The influence of differing ion temperatures on the spectrum has been ignored in the previous discussion. The ion temperature also has been assumed to be the same for all the ions present. This assumption is valid at lower heights where the ions, electrons, and neutrals all have the same temperature. When T_e/T_i is found to be equal to one using the analysis of the

previous section one can safely assume that the ions have a single temperature. But as T_e/T_i increases above one then the possibility that the ions have separate temperatures must be investigated because H^+ and O^+ ions are heated at different rates by the thermal electrons. In this section the effect of separate ion temperatures on spectra for a mixture of H^+ and O^+ are investigated in detail.

In general the parameters, R, f_{l_2}, σ, and S_{l_2} are functions of each ion temperature. In any of these parameters are functions of T_i then it is a function of both the hydrogen ion temperature ($T(H^+)$) and the oxygen ion temperature ($T(O^+)$). The only parameter which was a function of T_i was f_{l_2}. Therefore, one expects f_{l_2} to be a function of both $T(O^+)$ and $T(H^+)$. The other parameters may also be functions of $T(H^+)$ even though they were not functions of T_i. This will be discussed later in this section.

Instead of dealing with both $T(O^+)$ and $T(H^+)$ the ratio $T(H^+)/T(O^+)$ and $T(O^+)$ will be used. This simplifies some of the numerical calculations which will be carried out later on. In Figure 4.10 the spectra for values of $n(O^+)/n_e$ equal to 0.0 to 1.0 are shown for different values of the ratio $T(H^+)/T(O^+)$. In this figure the ratio T_e/T_i is taken as 2.0. Notice in this figure that a point near the peak due to H^+ ions the curves converge to a single value. For all values of $n(O^+)/n_e$ the power at zero Doppler frequency is greater for larger values of $T(H^+)/T(O^+)$. Also the power decreases less rapidly after the H^+ peak for larger values of $T(H^+)/T(O^+)$. The shape of the spectrum is different for each value of $n(O^+)/n_e$ and $T(H^+)/T(O^+)$. There are points where the spectra intersect which provide a way of calculating $n(O^+)/n_e$. The ratio $T(H^+)/T(O^+)$ can be calculated from places where the spectra differ. Unfortunately most of these parameters also depend on other quantities such as $T(O^+)$, $T_e/T(O^+)$, and $n(O^+)/n_e$. It is very difficult to

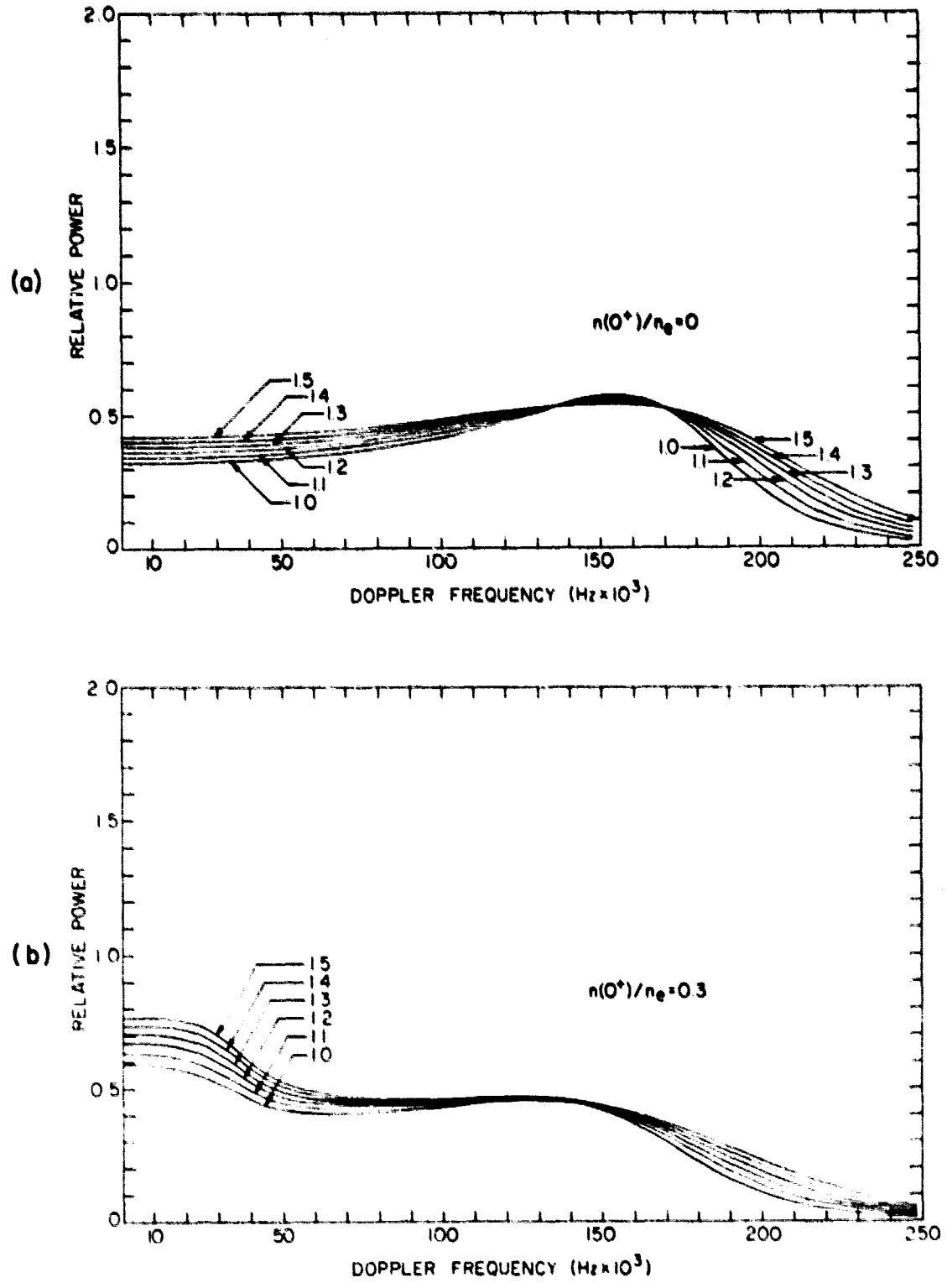

Figure 4.10 Spectra for different values of $n(O^+)/n_e$ and different values of $T(H^+)/T(O^+)$ where $T_e/T(O^+) = 2$. (a)- $n(O^+)/n_e = 0$, (b)- $n(O^+)/n_e = 0.3$, (c)- $n(O^+)/n_e = 0.6$, (d)- $n(O^+)/n_e = 0.9$.

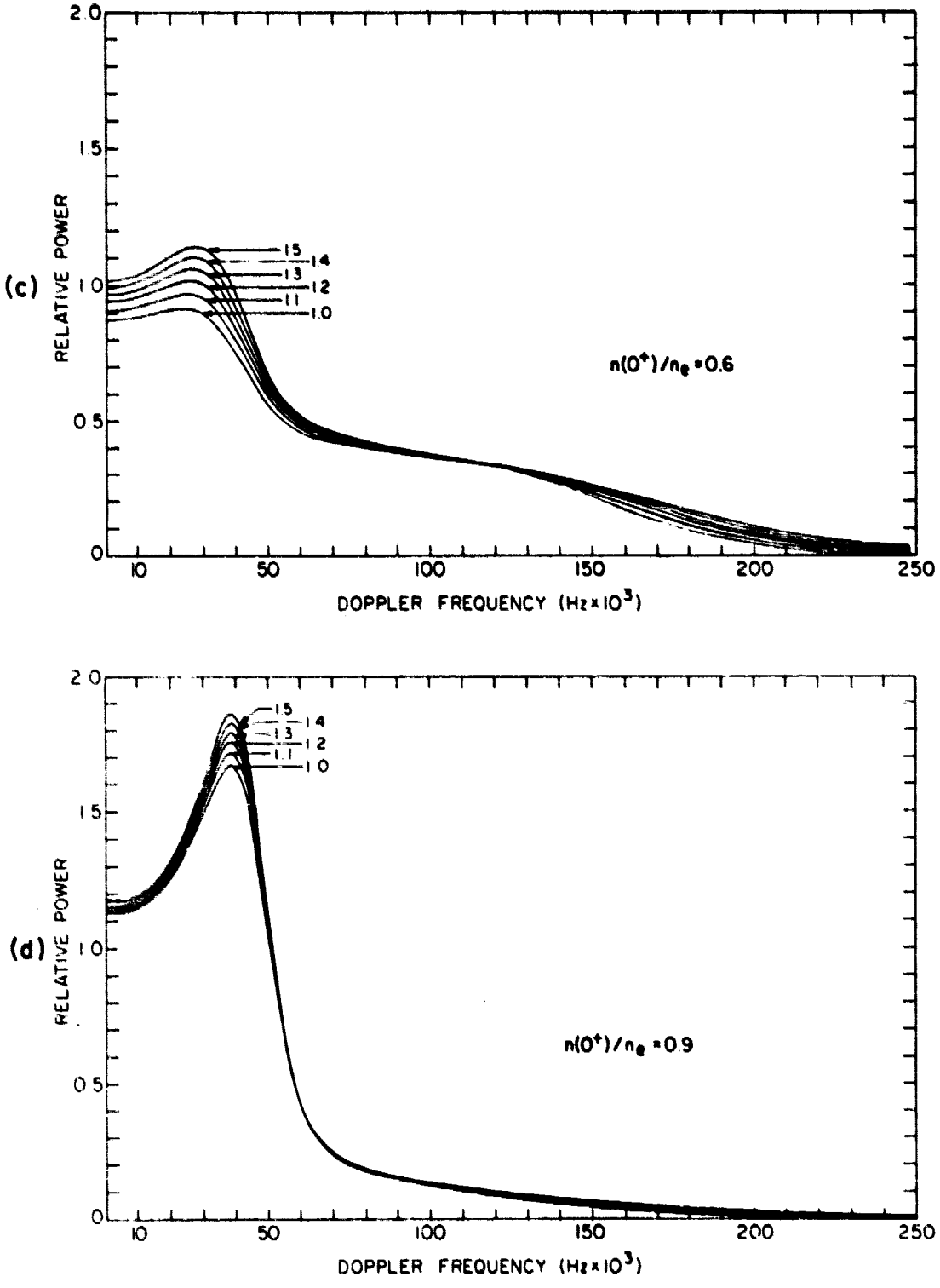

Figure 4.10 Continued.

find parameters of the power spectra which only depend on one quantity such as $n(O^+)/n_e$. This makes the determination of $T(O^+)$, $T_e/T(O^+)$, $T(H^+)/T(O^+)$, and $n(O^+)/n_e$ very complicated. Sometimes the solution is ambiguous due to two or more ways of matching theoretical results with experimental data.

The parameter $f_{\frac{1}{2}}$, which was a function of T_i, is a function of both $T(O^+)$ and $T(H^+)/T(O^+)$. As can be seen from Figure 4.10, $f_{\frac{1}{2}}$ increases as $T(H^+)/T(O^+)$ increases. Another parameter which increases with $T(H^+)/T(O^+)$ is σ. For larger values of $T(H^+)/T(O^+)$ amplitude of the spectrum at frequencies near zero Doppler shift is also larger. Earlier it was found that as $T_e/T(O^+)$ increases, σ decreases, so $T(H^+)/T(O^+)$ has the opposite effect on σ as does $T_e/T(O^+)$.

The effect of $T(H^+)/T(O^+)$ on R is not readily apparent from Figure 4.10. Both the spectrum maximum and the spectrum at zero Doppler shift changes as $T(H^+)/T(O^+)$ changes. If one compares the values of R for $n(O^+)/n_e$ = -/8 at different values of $T(H^+)/T(O^+)$ one can get the relation for the dependence of R on $T(H^+)/T(O^+)$ at $T(H^+)/T(O^+) = 1$, $R_{1.0} = S_1/S_0$ and at $T(H^+)/T(O^+) = 1.5$, $R_{1.5} = (S_1 + \Delta S)/(S_0 + \Delta S)$ so

$$R_{1.5}/R_{1.0} \approx 1 - \Delta S \ \frac{S_1 - S_0}{S_1 S_0}$$

Thus, as $T(H^+)/T(O^+)$ increases from 1.0 to 1.5, R decreases slightly.

4.4 *Characteristics of Theoretical Autocorrelation Functions*

Although the analysis of various parameters of the incoherent-scatter power spectrum is very useful in determining temperatures and densities of electrons and ions, this analysis cannot be directly applied to experimental data. Instead, the autocorrelation function (ACF) or the Fourier transform of the power spectrum is available. To get the experimental power spectrum,

the inverse Fourier transform of the experimental ACF has to be calculated. This leads to larger errors in the determination of temperatures and densities of electrons and ions. Fortunately, analysis of theoretical ACF's can be performed to determine temperatures and densities of electrons and ions. The method of this analysis is discussed in the following subsections.

The ACF like the power spectrum depends on $T(O^+)$, $T_e/T(O^+)$, $T(H^+)/T(O^+)$ $n(O^+)/n_e$. By identifying certain characteristics of the ACF one can understand how the ACF can be used to deduce $T(O^+)$, $T_e/T(O^+)$, $T(H^+)/T(O^+)$ and $n(O^+)/n_e$. Some of these quantities affect the ACF significantly. Others have a slight effect on the ACF. Parameters which are derived from the ACF are discussed in the following subsections. These parameters can be used to determine the temperatures and densities of electrons and ions. In Chapter 5 analysis of the theoretical ACF will be applied to experimental ACF's to calculate the temperatures and densities of electron and ions.

4.4.1 *ACF for a single ion.* The analysis of the ACF when a single ion is present will serve as a basis for the more complicated case of a mixture of ions which will be discussed later. The calculation of the ACF has been performed numerically using Simpson's rule for integration. The time delay step size has been chosen to be at least as short as time delay of experimental ACF's. The general features of the ACF are illustrated in Figure 4.11, which shows ACF's for scatter from ionized gases where the ion present is oxygen or hydrogen and for electron-ion temperature ratios of 1.0, 1.4, and 2.4. All the ACF's have been normalized to one at zero time delay. The position of the first minimum of the ACF, τ_1, is smaller for H^+ than for O^+, and is nearly inversely proportional to the square root of the ion mass. Since the shape of the ACF is of particular interest, the abscissa can be divided by the square root of the ion atomic mass shown in Figure 4.12. It is clear

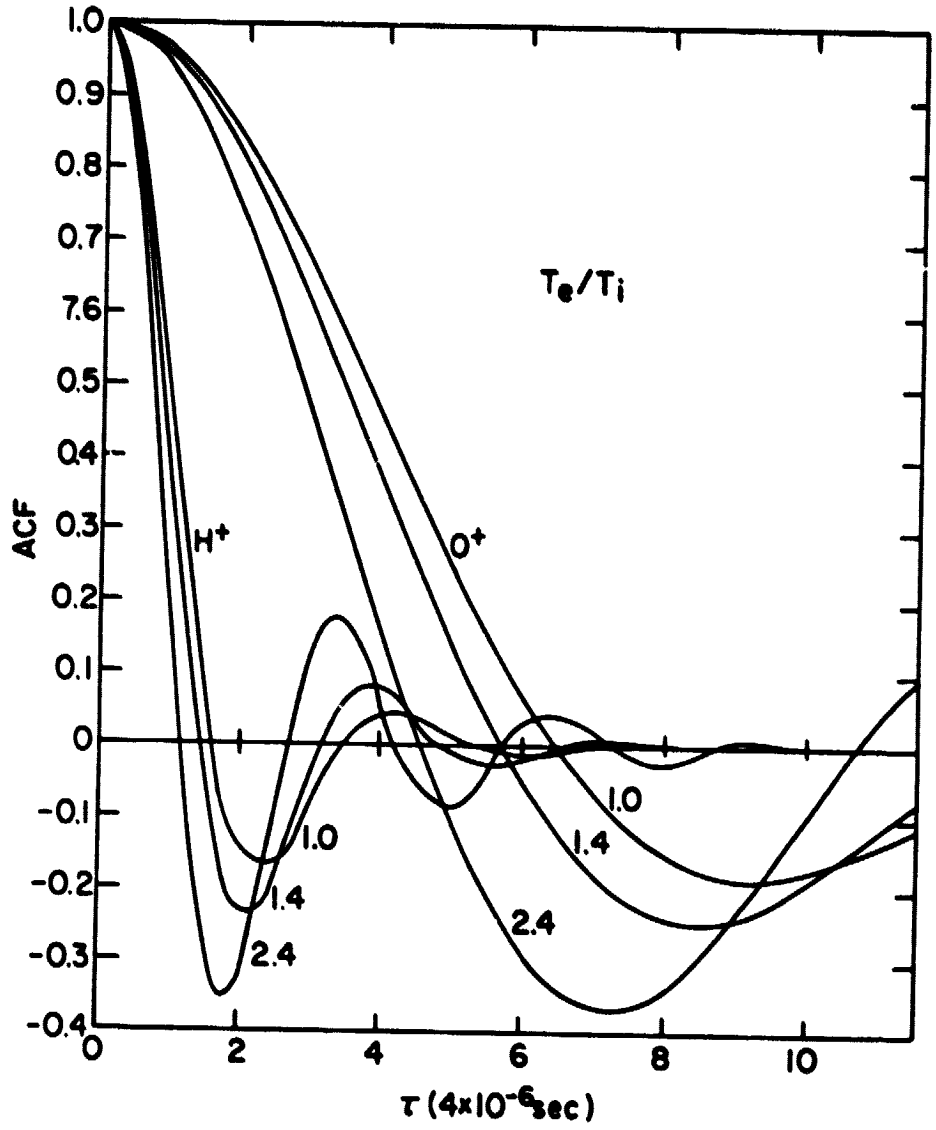

Figure 4.11 ACFs for O^+ and H^+ for T_e/T_i = 1.0, 1.6, and 2.4.

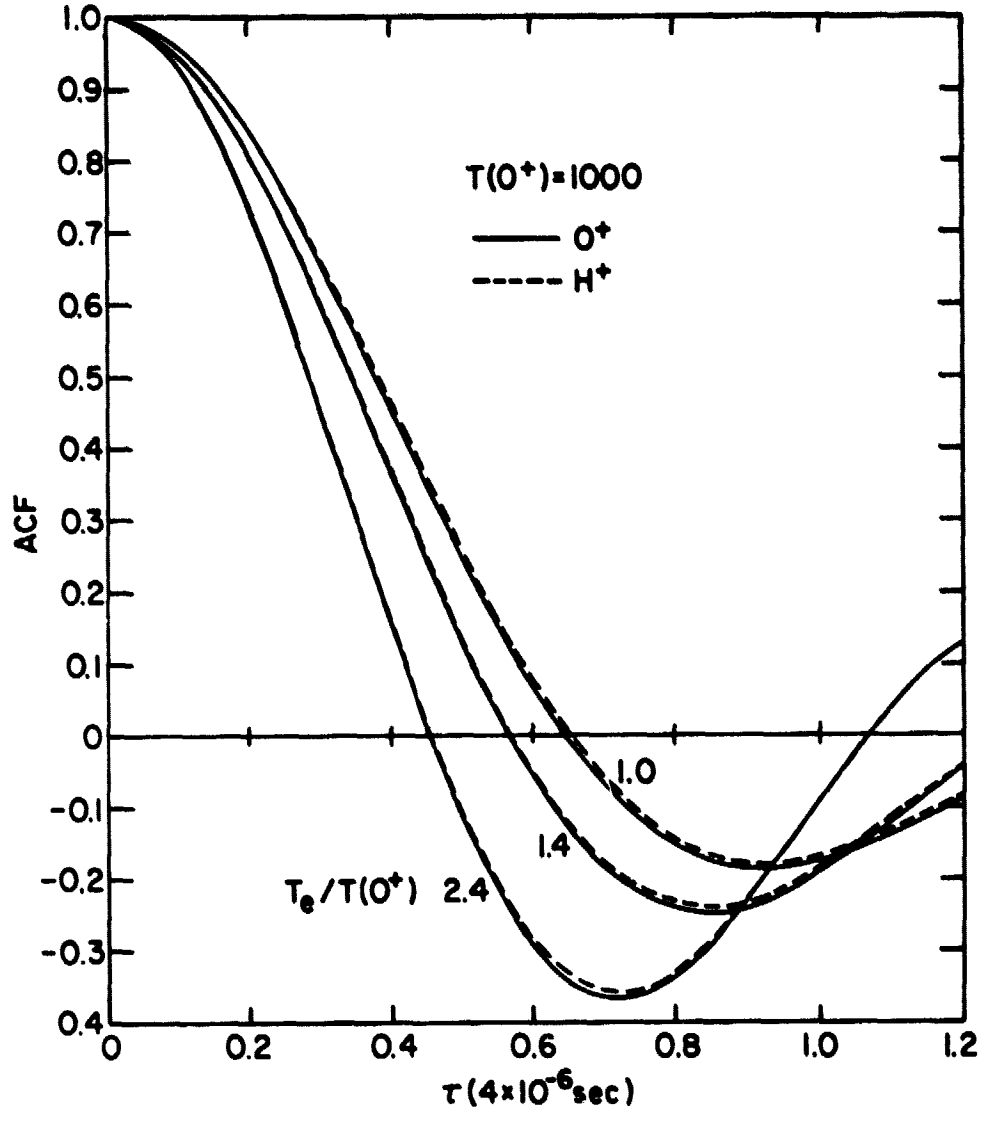

Figure 4.12 ACF's for O^+ and H^+ for T_e/T_i = 1.0, 1.4, and 2.4 with abscissa normalized by the atomic mass of the ion present (A_i).

from this figure that the shape of the ACF is only slightly dependent on the mass of the ion present in the gas. If there were no contribution to the spectrum due to electrons in equation (4.2) then the shape of the spectrum and the ACF could be independent of the ion mass.

Figure 4.11 also shows that the depth of the first minimum of the ACF, AMIN, is strongly dependent of the electron-to-ion temperature ratio. This characteristic of the ACF is due to the dependence of peak-to-center ratio R of the spectrum on T_e/T_i. As R increases for increasing T_e/T_i so does the depth of the first minimum of the ACF. To confirm the relationship between R and AMIN one would except that they do not depend on the ion temperature. Analysis of Figure 4.13, which shows ACF's for different values of T_i, indicates that the AMIN does not depend on T_i even though the position of AMIN does. Thus, if only one type of ion is present in the gas the electron-to-ion temperature ratio could be determined from AMIN.

Another feature of the ACF which is shown in Figure 4.13 is the dependence of the first zero crossing of the ACF (τ_0) on the ion temperature. As the ion temperature increases, τ_0 decreases. This is opposite to the dependence of $f_{\frac{1}{2}}$ on T_i which was discussed in Section 4.2. It was found that $f_{\frac{1}{2}}$ depends on $T_i^{\frac{1}{2}}$. Here, the dependence of τ_0 on T_i is $\tau_0 \propto T_i^{-\frac{1}{2}}$. The first zero crossing doesn't depend on T_i alone, as can be seen from Figure 4.11 which shows ACFs for different values of T_e/T_i. It is evident from this figure that τ_0 also depends heavily on T_e/T_i. As T_e/T_i increases, τ_0 decreases. So, the functional dependence of τ_0 is complicated since it both depends on T_i and T_e/T_i.

When only one type of ion is present one can use the dependencies of σ, τ_0, and AMIN on T_i, T_e/T_i, and n_e to deduce these quantities. These

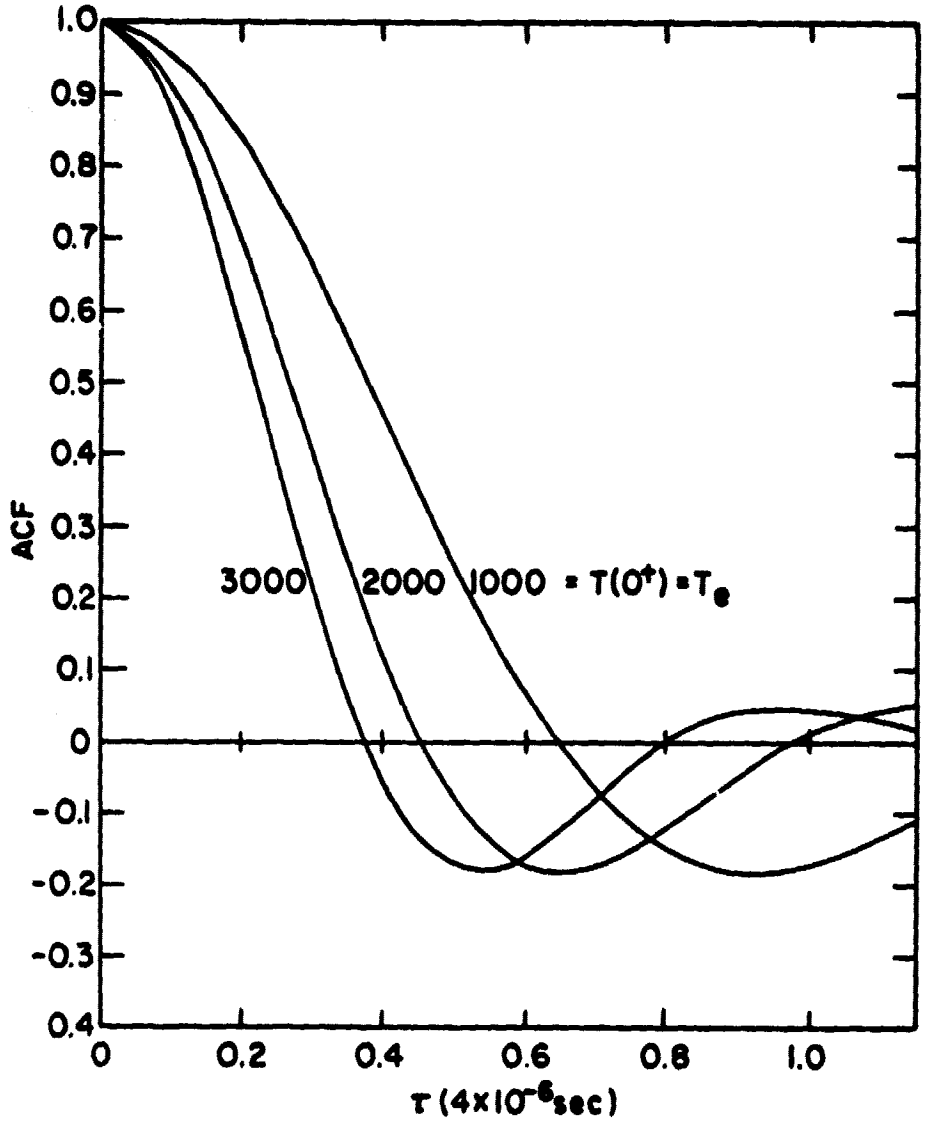

Figure 4.13 ACF's for O^+ for different values of T_i with $T_e = T_i$.

various dependencies are illustrated in Figures 4.14 and 4.15 for the ions O^+ and H^+. In Figure 4.14 the ACF at its first minimum, AMIN, is shown as a function of T_e/T_i for temperature ratios from 1.0 to 2.4, the appropriate range of T_e/T_i for the upper atmosphere. Since the ion mass has a slight effect on the shape of the ACF (see Figure 4.12) AMIN depends just slightly on the ion mass. The effect of T_i on AMIN is slight and can be ignored compared to the dependence of AMIN on T_e/T_i. It is even less significant than the effect of changes in the ion mass. Thus, the functional form of AMIN can be expressed in terms of T_e/T_i alone.

Both τ_0 and σ depend on T_e/T_i but T_e/T_i can be determined from AMIN. Thus, one can find T_i from τ_0 and n_e from σ by using T_e/T_i from AMIN. Although σ is only slightly dependent on the ion mass, τ_0 is strongly affected by the ion mass. Therefore, no further complications are introduced by the ion mass when using σ to find n_e. But, τ_0 cannot be used alone to find T_i. Either some information about the ion present in the gas must be available or τ_0 must be normalized with respect to some other parameter. Sometimes the ion present in the gas is known. For example, at altitudes near the F_2 peak in the electron density it is known that the ionic composition is almost exclusively O^+. At other altitudes the knowledge of the ion present is less certain. In fact, at most altitudes there is a mixture of ions with no one ion more than 90 percent of the total ion density.

Suppose there is only one ion present and it is not known. τ_0 must then be normalized with respect to some other parameter. A suitable parameter to use is $\bar{\tau}_0$; which is a value of τ_0 at a fixed ion temperature of 1000 K. This ion temperature is chosen because the ion temperatures in the topside ionosphere are near 1000 K. In Figure 4.15 the normalized τ_0' is shown as a function of T_e/T_i for O^+ and H^+. Although τ_0' depends slightly on the ion mass

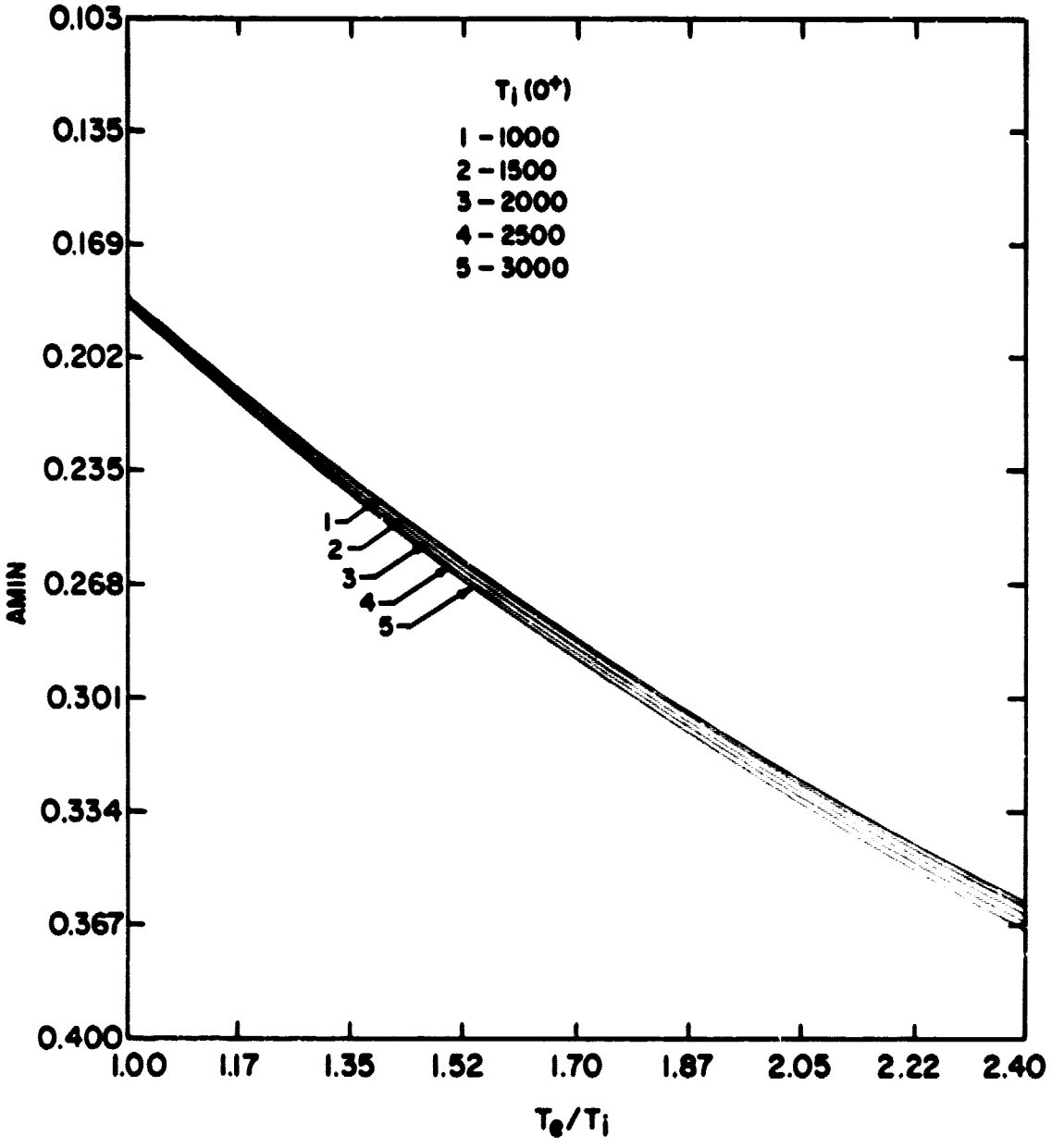

Figure 4.14 The first minimum of the ACF is called AMN. It is shown for O^+ as a function of $T_e/T_i(O^+)$ and $T_i(O^+)$.

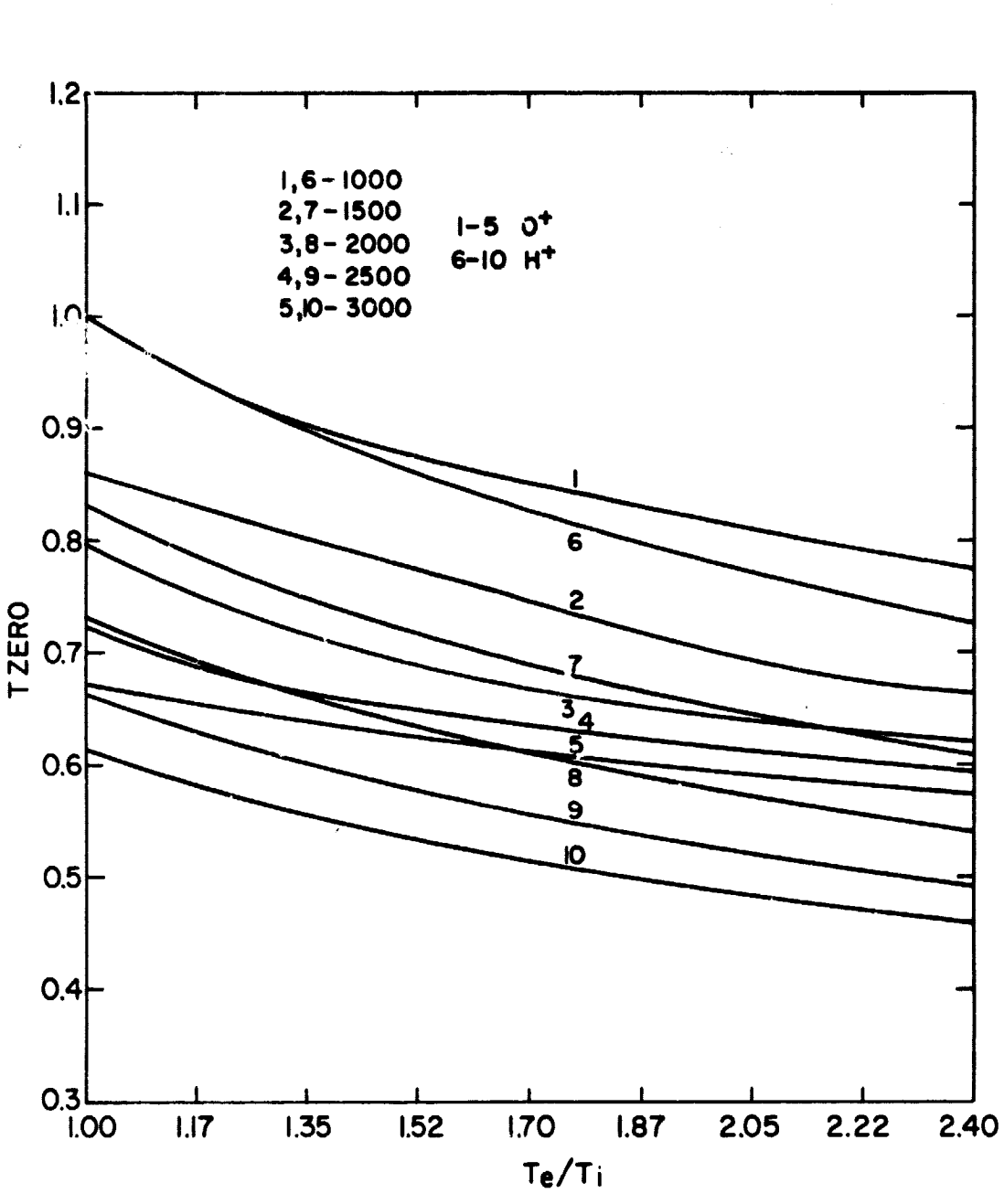

Figure 4.15 The first zero of the ACF normalized with respect to the time delay at ACF = ½ is called TZERO. It is shown for O^+ and H^+ as a function of T_e/T_i and $T(O^+)$.

one can determine T_i fairly accurately if T_e/T_i is known from analysis of σ.

If only one type of ion is present and if AMIN, τ_0', and σ can be measured then it is possible to determine T_e, T_i and n_e using the curves of Figures 4.14, 4.15 and 4.9. However if not all these scattering quantities can be measured, it may be necessary to make some assumptions about the temperatures, or perhaps measure n_e in another way. In Figure 4.16 the various combinations of measurements and assumptions are shown by a schematic diagram.

The case where not all of σ, AMIN, and τ_0' can be measured can be considered with the aid of Figure 4.16. Of the three quantities, the most difficult to measure is AMIN. Examination of Figure 4.16 shows that the measurement of τ_0' and σ must be supplemented by a measurement or an assumed value of one of the other quantities before anything can be deduced. Any of T_i, T_e, T_e/T_i, or n_e will suffice. At certain times, the temperature ratio in the topside ionosphere can be accurately estimated. For example, $T_e/T_i = 1$ at night; also, the ion temperature could be obtained from rocket measurements if an isothermal atmosphere is assumed. Either of these assumptions would be sufficient to deduce both temperatures and the electron density from measurements of σ and τ_0'. For example, values of the electron density from topside sounders could be combined with σ to give T_e/T_i. This value of T_e/T_i along with analysis of τ_0' would give T_i and T_e.

Two quantities which are necessary for the determination of temperatures and the electron density are τ_0' and σ. Without them it is not possible to determine temperatures and the electron density. Early measurement of *Bowles* [1962] only contained measurements of σ. In that case, assumptions about T_e/T_i will give n_e from σ; or an independent measurement of n_e will give T_e/T_i. When only τ_0' is measured, one of T_i, T_e, or T_e/T_i must be obtained

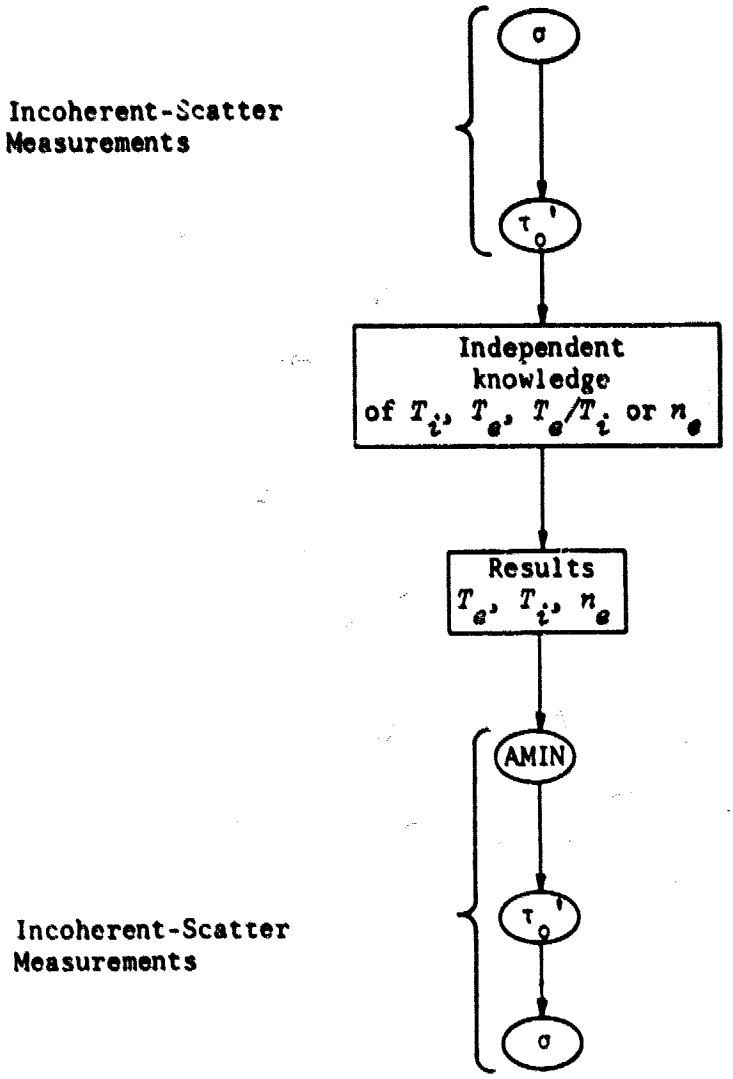

Figure 4.16 Schematic diagram of interrelations between scattering observations and characteristics of an ionized gas when only one type of ion is present.

by independent measurement or assumption and then the others can be obtained from τ_0'.

4.4.2 *ACF for a mixture of two ions at a single ion temperature.* The interpretation of the scattering from an ionized gas is considerably more complicated when two types of ions are present than when only one kind is present. The discussion in this section is related to a mixture of H^+ and O^+, the ions present in the topside ionosphere.

While the shape of the ACF for two different ions are similar for a given temperature ratio, the shape of the ACF for a mixture of the two ions is quite different from those of either ion alone. This is evident in Figure 4.17 which shows ACFs for various mixtures of O^+ and H^+ for a temperature ratio of 1.4 and an oxygen ion temperature of 1000 K. This figure also indicates that the depth of first minimum of the ACF, AMIN, is now a function of $n(O^+)/n_e$ as well as of T_e/T_i. This complicates the calculation of T_e/T_i and $n(O^+)/n_e$. The functional form of AMIN can be represented by a whole family of curves rather than a single line as in Figure 4.14. Figure 4.18 shows AMIN as a function of $n(O^+)/n_e$ and T_e/T_i for mixtures of O^+ and H^+.

There are a number of characteristics in Figure 4.18 which either hinder or aid the determination of T_e/T_i and $n(O^+)/n_e$. One characteristic which aids the determination of T_e/T_i and $n(O^+)/n_e$ is the fact that at either small or large values of $n(O^+)/n_e$, T_e/T_i can be determined fairly accurately if $n(O^+)/n_e$ is known from other measurements. In opposite sense if T_e/T_i is known, Figure 4.17 will give $n(O^+)/n_e$ if it is small or large.

One characteristic which hinders the determination of T_e/T_i and $n(O^+)/n_e$ is the fact the curve of one value of T_e/T_i either crosses the other curves of constant T_e/T_i or becomes almost equal to the curves of constant T_e/T_i at a point in the range between $n(O^+)/n_e$ equal to 50 and 70 percent.

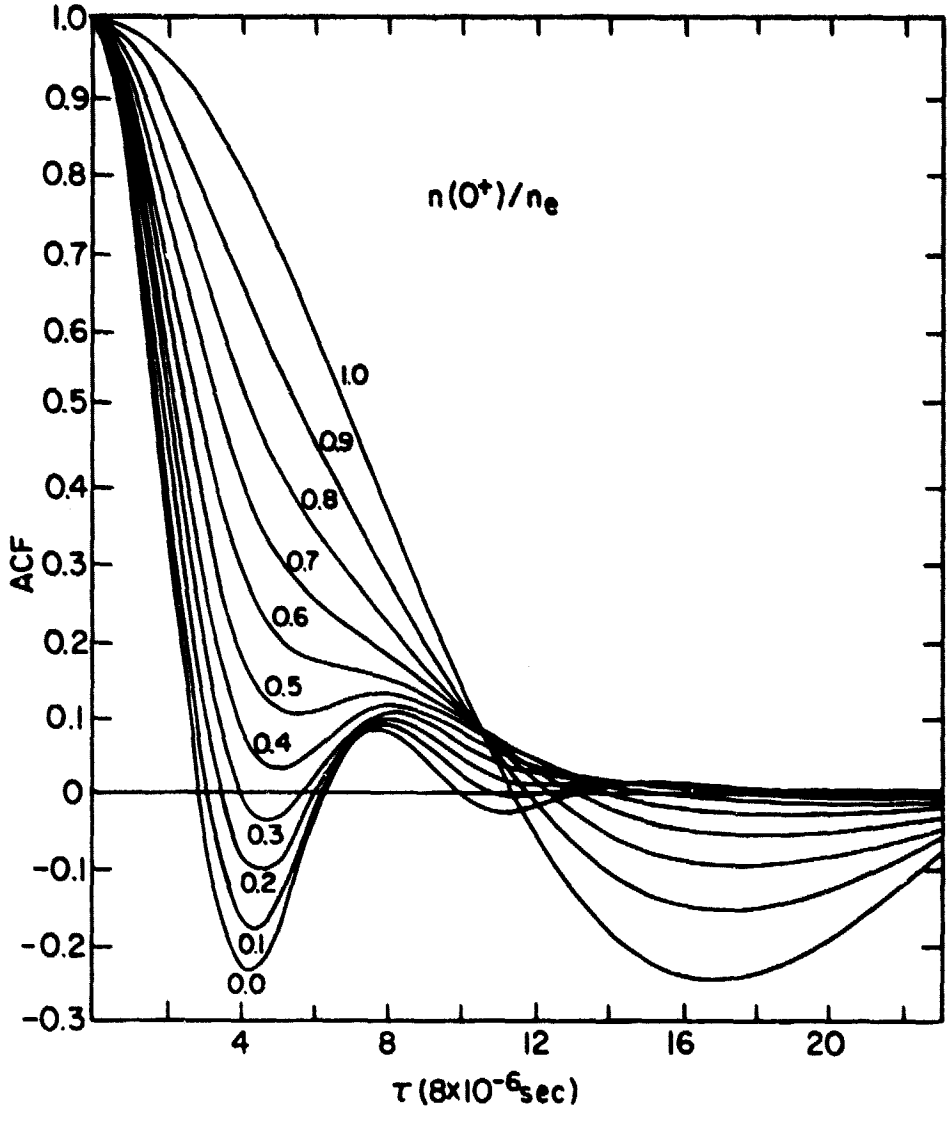

Figure 4.17 ACF's for mixtures of O^+ and H^+ for T_e/T_i = 1.4 and T_i = 1000 K.

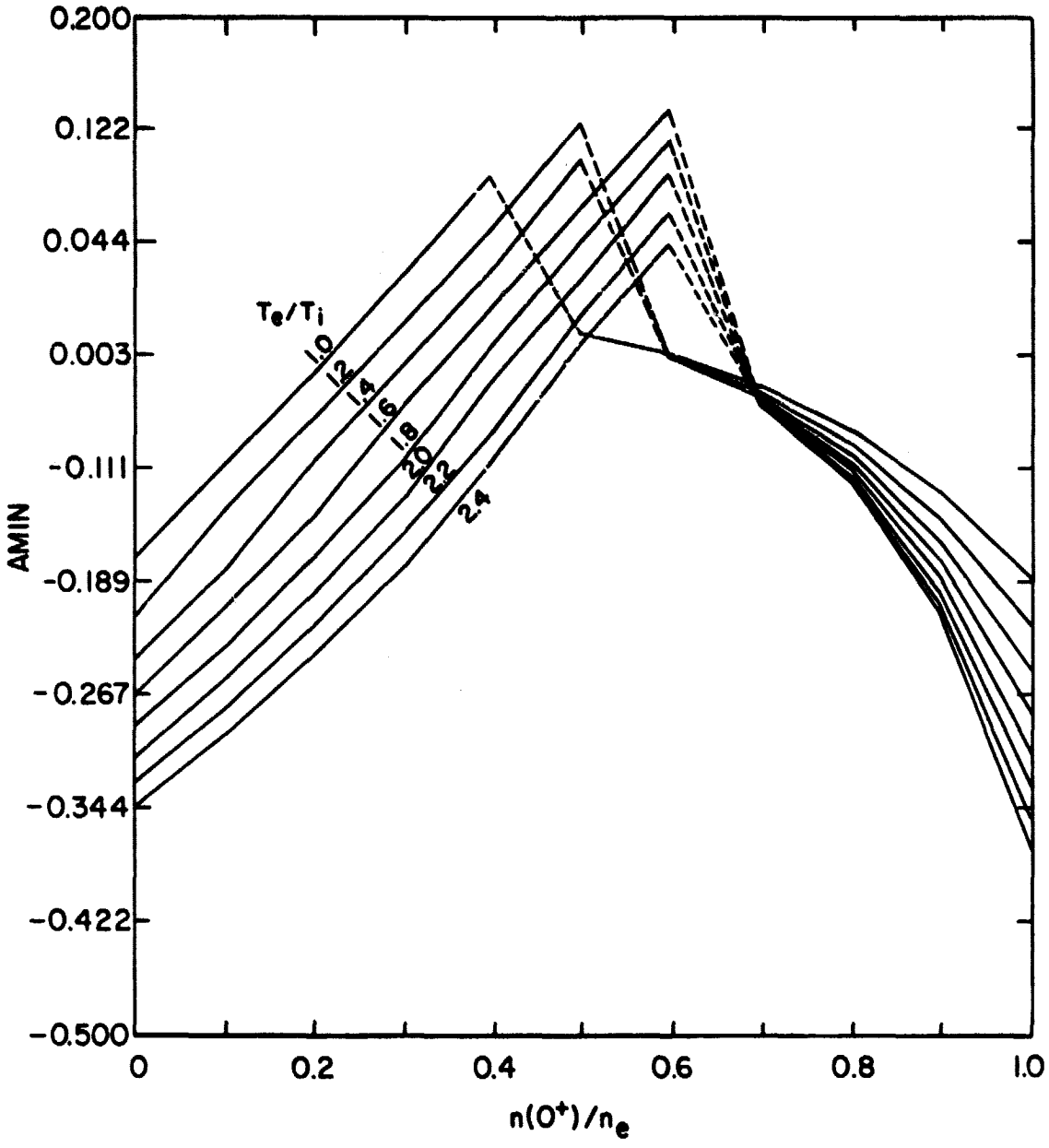

Figure 4.18 AMIN as a function of $n(O^+)/n_e$ and T_e/T_i for T_i = 1000 K. The dotted lines indicate discontinuities in AMIN.

In fact the curve for $T_e/T_i = 1.0$ crosses all the other curves twice between $n(0^+)/n_e$ equal .4 and .7. This characteristic means that 2 values of T_e/T_i can be deduced from AMIN at these points of crossing. Also, AMIN cannot be used to find $n(0^+)/n_e$ or T_e/T_i when $n(0^+)/n_e$ is between .4 and .7 since the curves cross and reach a maximum. This implies, with the use of Fig. 4.18, that when AMIN is greater than -.1 some other parameter must be used to find $n(0^+)/n_e$ and T_e/T_i.

Another characteristic in Figure 4.18 is the similarity of values of AMIN for $n(0^+)/n_e$ near 0.0 or 1.0. This means two values of $n(0^+)/n_e$ can be determined from a single AMIN using one value of T_e/T_i. Usually this is not a problem, since the dominate ion is often known in a particular altitude region and $n(0^+)/n_e$ can be assumed to be smoothly varying with altitude. Also, the ACF is quite different for $n(0^+)/n_e$ near 0.0 and 1.0 (see Figure 4.17).

An important parameter of the ACF which depends on $n(0^+)/n_e$, T_e/T_i, and T_i is the time delay at the point where the ACF is one half (THALF). Figure 4.19 shows the dependencies of THALF on $n(0^+)/n_e$, T_e/T_i, and T_i. The dependence of THALF on $n(0^+)n_e$ is more pronounced with THALF much less for $n(0^+)n_e$ equal to 0 than 1.0. THALF depends on T_i more than it depends on T_e/T_i. Yet, the dependence of THALF on T_e/T_i is significant and cannot be ignored. Since THALF depends on all the quantities that need to be deduced, one must combine measurement of THALF with measurement of at least two other parameters such as AMIN, to find $n(0^+)n_e$, T_e/T_i, and T_i.

Another important parameter of the ACF is the time delay at the first zero of the ACF (TZERO). TZERO depends on T_i, T_e/T_i, and $n(0^+)/n_e$ as shown in Figure 4.20. In this figure, TZERO has been normalized by THALF. Henceforth, the normalized TZERO will be referred to as TZERO.

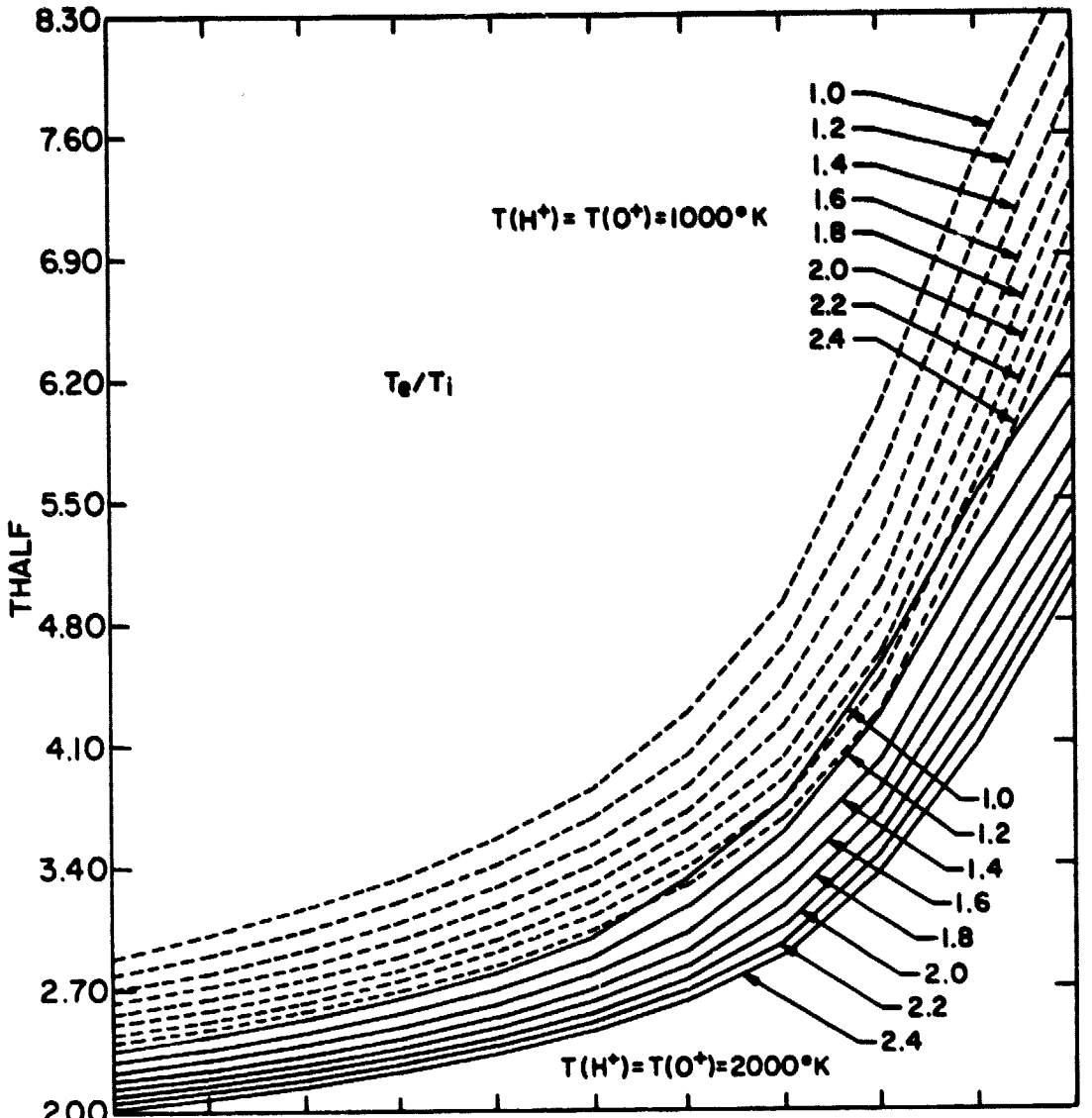

Figure 4.19 The time delay at ACF = ½ is called THALF. It is shown as a function of $n(O^+)/n_e$, T_e/T_i and T_i.

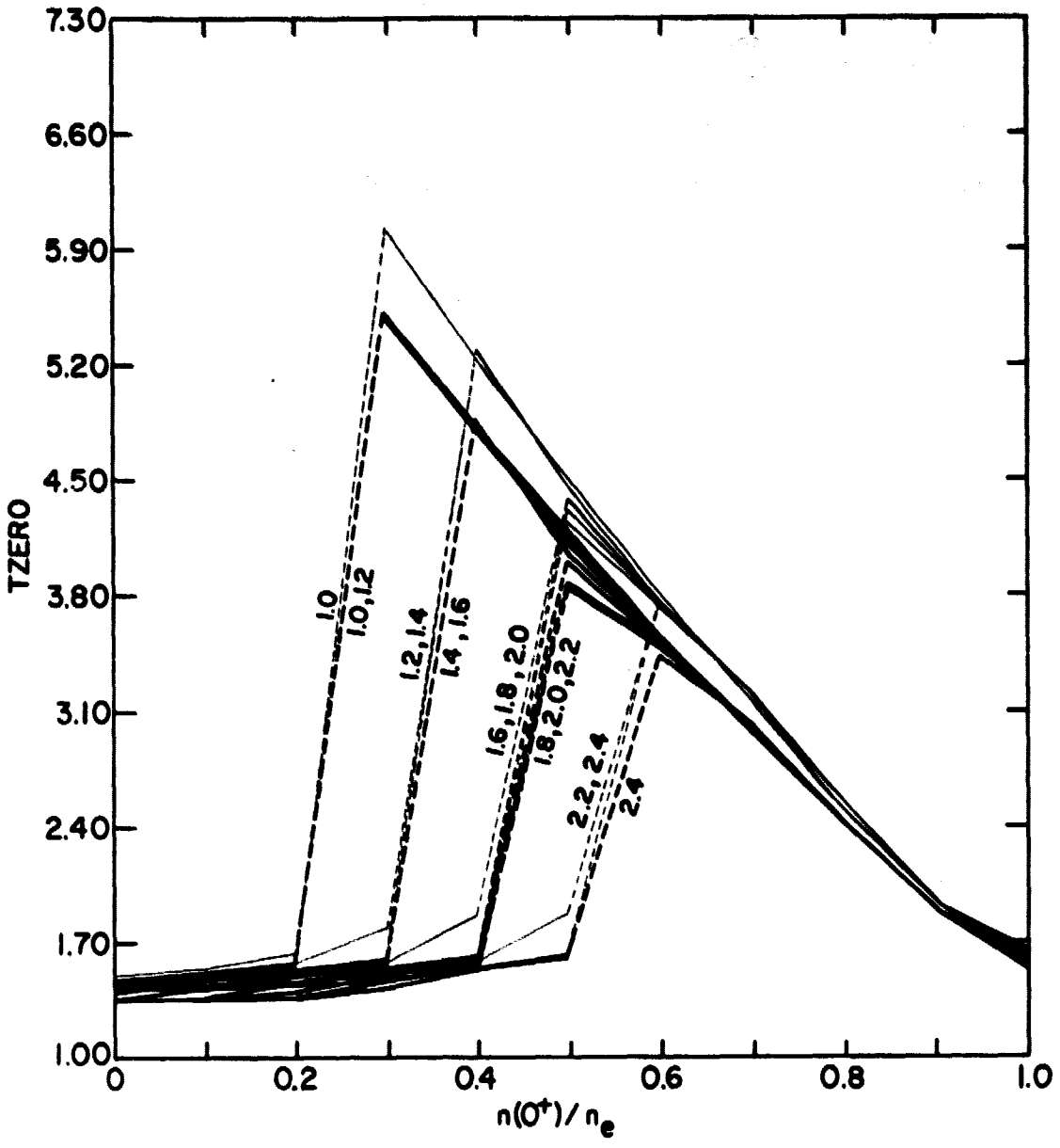

Figure 4.20 TZERO as a function of $n(O^+)/n_e$, T_e/T_i, and T_i. The thin lines are for T_i = 1000 K. The thick lines are for T_i = 2000 K. The dotted lines indicate discontinuities in TZERO.

In Figure 4.20, the dependence of TZERO on $n(O^+)/n_e$ is noticed as the strongest dependence and the dependence of TZERO on T_i as the next strongest. The dependence of TZERO on T_e/T_i is very slight when $n(O^+)/n_e$ is greater than 0.60 and less than 0.20. When $n(O^+)/n_e$ is between 0.2 and 0.6 there is some separation between the curves for different values of T_e/T_i. The curves are discontinuous when $n(O^+)/n_e$ is between 0.2 and 0.6. The reason for this has to do with the disappearance of the minimum of the ACF due to H^+ ions as $n(O^+)/n_e$ increases. The minimum becomes less in magnitude as $n(O^+)/n_e$ increases and increases above zero. Then the minimum due to H^+ disappears altogether and the first minimum is due to O^+. The minimum changes discontinuously when this occurs. The place where the curves become discontinuous depends on the ratio T_e/T_i as well as on $n(O^+)/n_e$. Since the respective step sizes for $n(O^+)/n_e$ and T_e/T_i were 0.1 and 0.2 when these calculations were made, the resolution of the curves in the range of $n(O^+)/n_e$ between 0.2 and 0.6 is not very good. The resolution could be improved with smaller step sizes for either $n(O^+)/n_e$, or T_e/T_i, or both.

In Figure 4.21, TZERO is shown for $n(O^+)/n_e$ in the range 0.2 to 0.6 with step sizes of 0.04 for $n(O^+)/n_e$. This figure shows that the curves have better resolution when the step size for $n(O^+)/n_e$ is smaller. Although Figures 4.20 and 4.21 could theoretically determine $n(O^+)/n_e$ very accurately when TZERO has a discontinuity in its experimental measurement, this is dependent on the accurate measurement of T_e/T_i and T_i. Even though T_i and T_e/T_i are not accurate, Figure 4.20 still could be used to get a fairly accurate value of $n(O^+)/n_e$ if TZERO is greater than 2. When TZERO is less than 2 and a discontinuity has just occurred $n(O^+)/n_e$ is between 0 and .54. If TZERO is less than 2 and $n(O^+)/n_e$ is near 1 then TZERO can again be used to find $n(O^+)n_e$

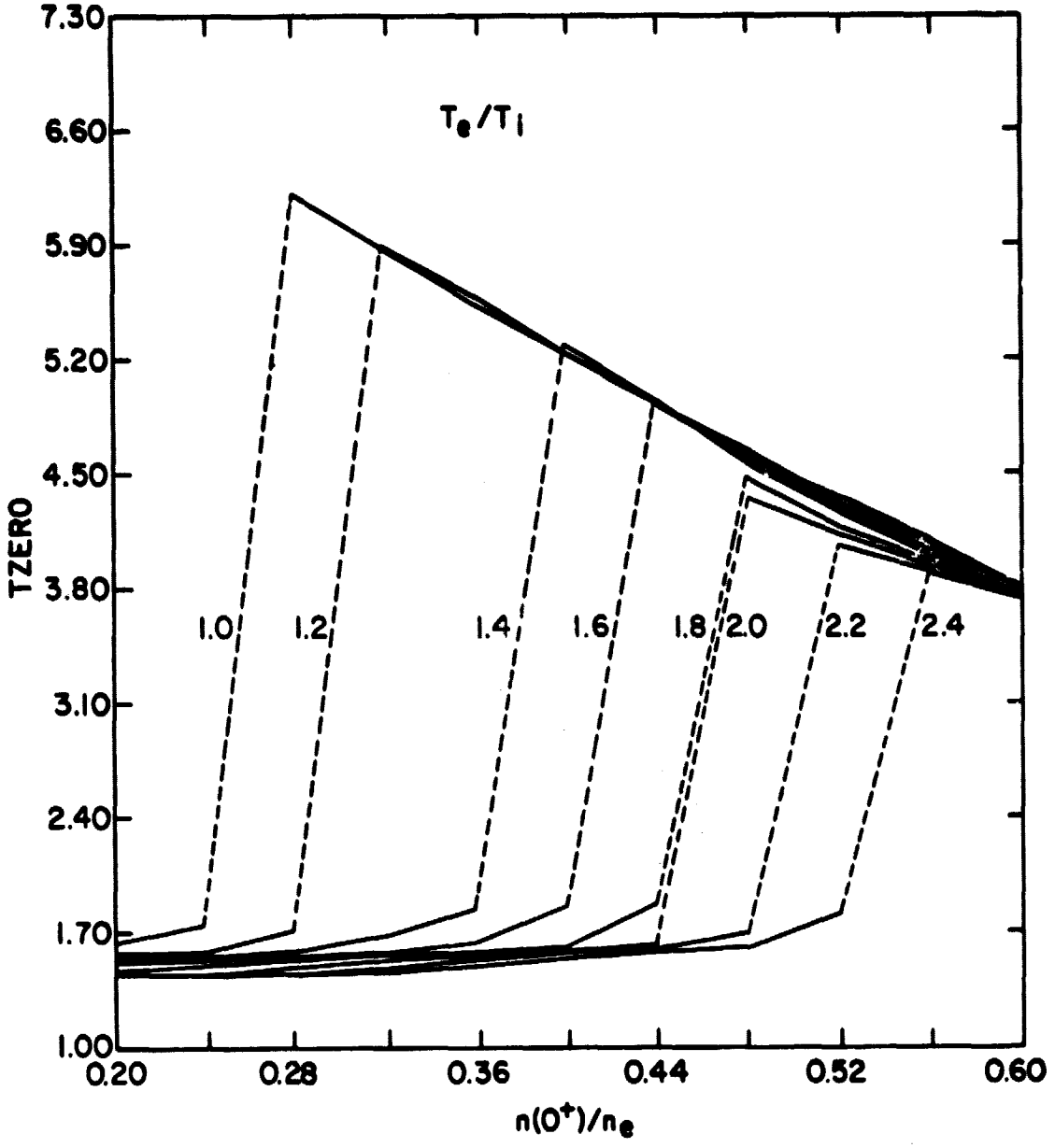

Figure 4.21 TZERO as a function of $n(O^+)/n_e$, T_e/T_i, and T_i where TZERO is calculated at intervals of 0.04 for $n(O^+)/n_e$.

If a single ion temperature is used for both ions and there is a mixture of O^+ and H^+ then the parameters TZERO, THALF, and AMIN (Figures 4.18-4.21) can be used to find $n(O^+)/n_e$, T_i, and T_e/T_i, and σ can be used to find n_e. If σ is not measured, n_e cannot be found. If measurement of one of the other parameters is not possible then the independent knowledge of one of T_e/T_i, T_i, or $n(O^+)/n_e$ must be had in order to determine the rest of these quantities.

4.4.3 *ACF for a mixture of* O^+ *and* H^+ *with different ion temperatures.* This section covers the special case of deducing all the possible quantities of a mixture of O^+ and H^+ from theoretical parameters of the ACF. That is, $n(O^+)/n_e$, $T(O^+)$, $T(H^+)/T(O^+)$, $T_e/T(H^+)$ and n_e can all be calculated with suitable parameters of the ACF. This is possible theoretically since the power spectrum and in turn the ACF depend on all these quantities. The dependence of the ACF on $T(O^+)$ if $T_i = T(H^+) = T(O^+)$ has been shown previously in Figure 4.13. The dependence of the ACF on T_e/T_i and $n(O^+)/n_e$ has been shown in Figures 4.11 and 4.17 respectively. The dependence of the ACF on $T(H^+)/T(O^+)$ is shown in Figure 4.22 for the cases $n(O^+)/n_e = 0.4$ and 0.9 with $T_e/T(H^+)$ equal to 1.4. These are only two of the many possible cases. Other cases will be discussed and illustrated in this section.

The dependence of the ACF on $T(H^+)/T(O^+)$ as shown in Figure 4.22 is weak but still strong enough to permit determination of $T(H^+)/T(O^+)$. The parameters THALF, AMIN and TZERO which depend on $n(O^+)/n_e$, T_e/T_i, and T_i may now depend on $T(H^+)/T(O^+)$ also. From Figure 4.22 one notices that THALF depends on $T(H^+)/T(O^+)$. Since THALF also depends on $n(O^+)/n_e$, T_e/T_i, and T_i it is hard to represent all the dependencies of THALF on a single graph. THALF is shown in Figure 4.19 as a function of $n(O^+)/n_e$, T_e/T_i, and T_i; in Figure 4.23 THALF is shown as a function of $n(O^+)/n_e$, $T(H^+)/T(O^+)$, and $T(O^+)$ with

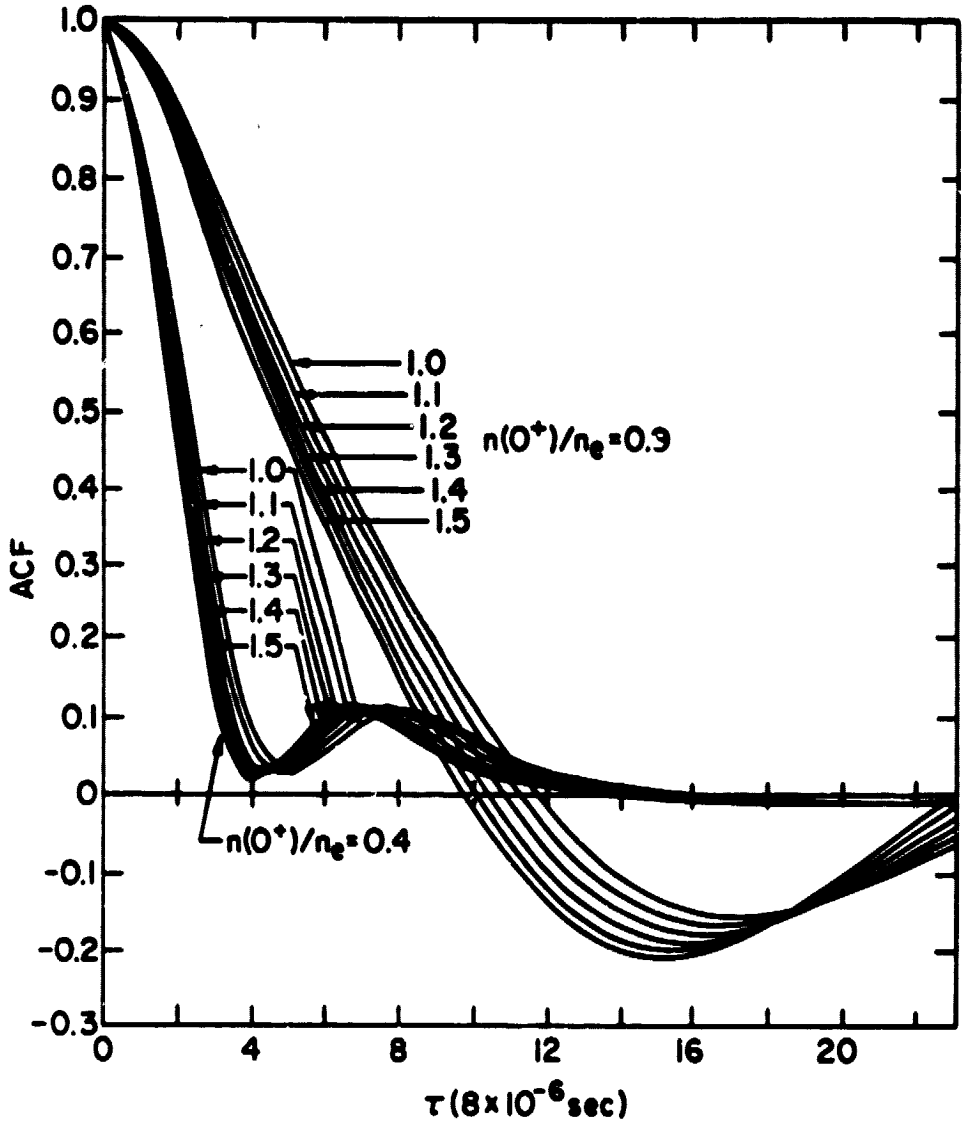

Figure 4.22 The dependence of the ACF on $T(H^+)/T(O^+)$.

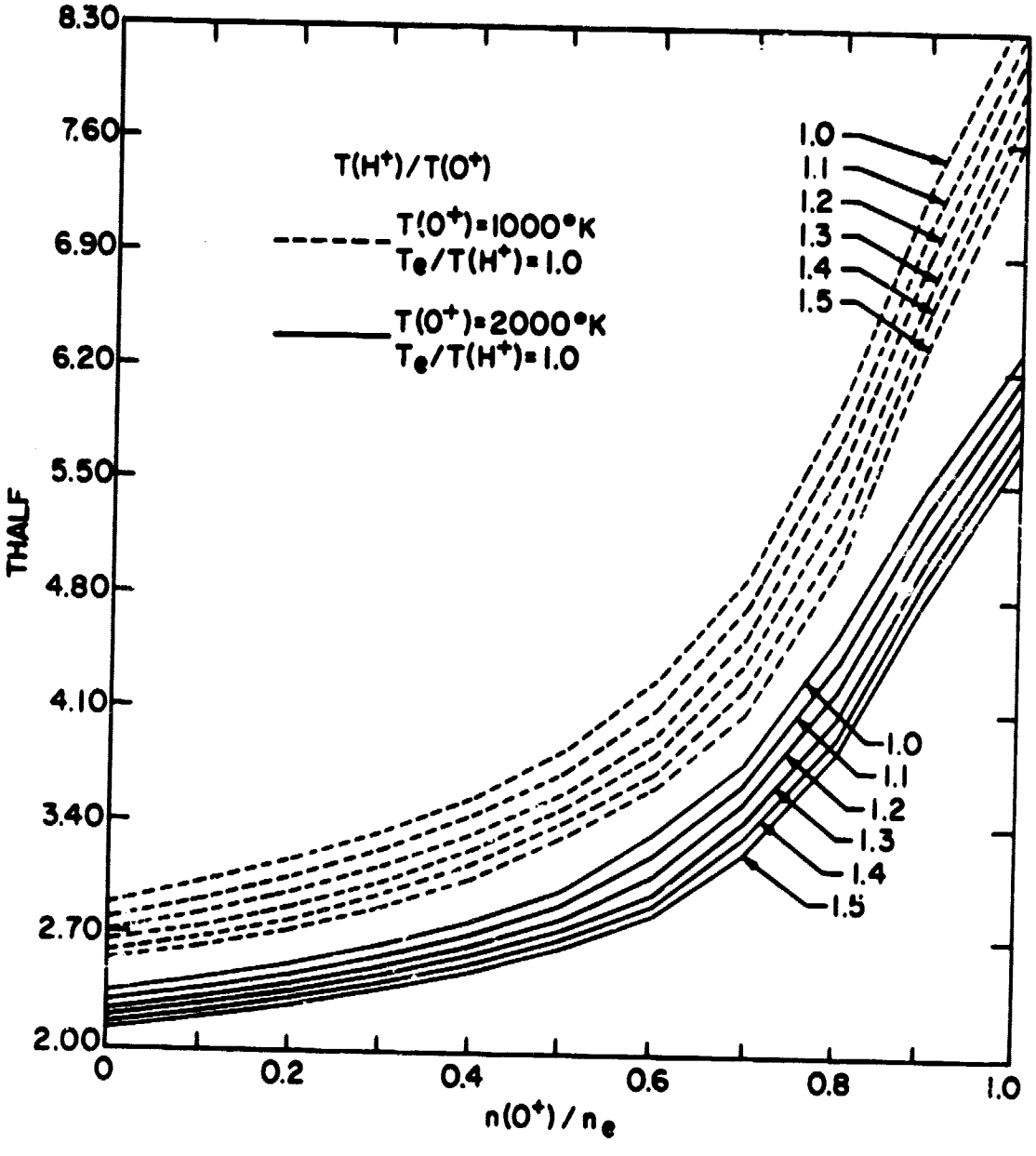

Figure 4.23 THALF as a function of $n(O^+)/n_e$, $T(H^+)/T(O^+)$ with $T_e/T(H^+) = 1.0$.

$T_e/T(H^+)$ = 1.0. Examination of Figure 4.23 shows that the dependence of THALF on $T(H^+)/T(O^+)$ weakens as $T(O^+)$ increases since the curves are closer together for the case where $T(O^+)$ = 2000 K case than for the 1000 K case. Even though the dependence of the ACF and THALF on $T(H^+)/T(O^+)$ (Figures 4.22 and 4.23) indicates that it is theoretically possible to deduce ratios of $T(H^+)/T(O^+)$ if the other quantities that the ACF and THALF depend on are known.

The parameter TZERO which depends on $n(O^+)/n_e$ and T_i does not depend on $T(H^+)/T(O^+)$ in any significant way when $n(O^+)/n_e$ is greater than 0.6. The only places where THALF depends on $T(H^+)/T(O^+)$ are at the discontinuities. Since THALF does not depend on $T(H^+)/T(O^+)$ for most of the range of $n(O^+)/n_e$, the dependence of THALF on $T(H^+)/T(O^+)$ will be ignored, just as the dependence of THALF on T_e/T_i is ignored for most of the range of $n(O^+)/n_e$.

Another parameter which depends on $T(H^+)/T(O^+)$ is AMIN. In Figure 4.24 AMIN is shown as a function of $T(H^+)/T(O^+)$ and $n(O^+)/n_e$ for $T_e/T(H^+)$ = 1.0 and $T(O^+)$ = 1000 K. Fortunately, the dependence of AMIN on $T(O^+)$ is very slight; so this figure can be used for all values of $T(O^+)$. The dependence of AMIN on $T(H^+)/T(O^+)$ is strongest for values of $n(O^+)/n_e$ near 1.0. When $n(O^+)/n_e$ decreases below 0.5 there are values of AMIN which give 2 values of $T(H^+)/T(O^+)$. This is because the curves cross one another. Thus, other parameters must be used to deduce $T(H^+)/T(O^+)$ when $n(O^+)/n_e$ is less than 0.5. The dependence of AMIN on $T(H^+)/T(O^+)$ is also somewhat similar to the dependence of AMIN on $T_e/T(H^+)$ as shown in Figure 4.18. This could cause a problem with ambiguous solutions, i.e. two sets of values for $T_e/T(H^+)$ and $T(H^+)/T(O^+)$ could give the same AMIN. This problem can be eliminated if another parameter can be found which depends on $T_e/T(H^+)$ and $T(H^+)/T(O^+)$ in much different ways than AMIN does.

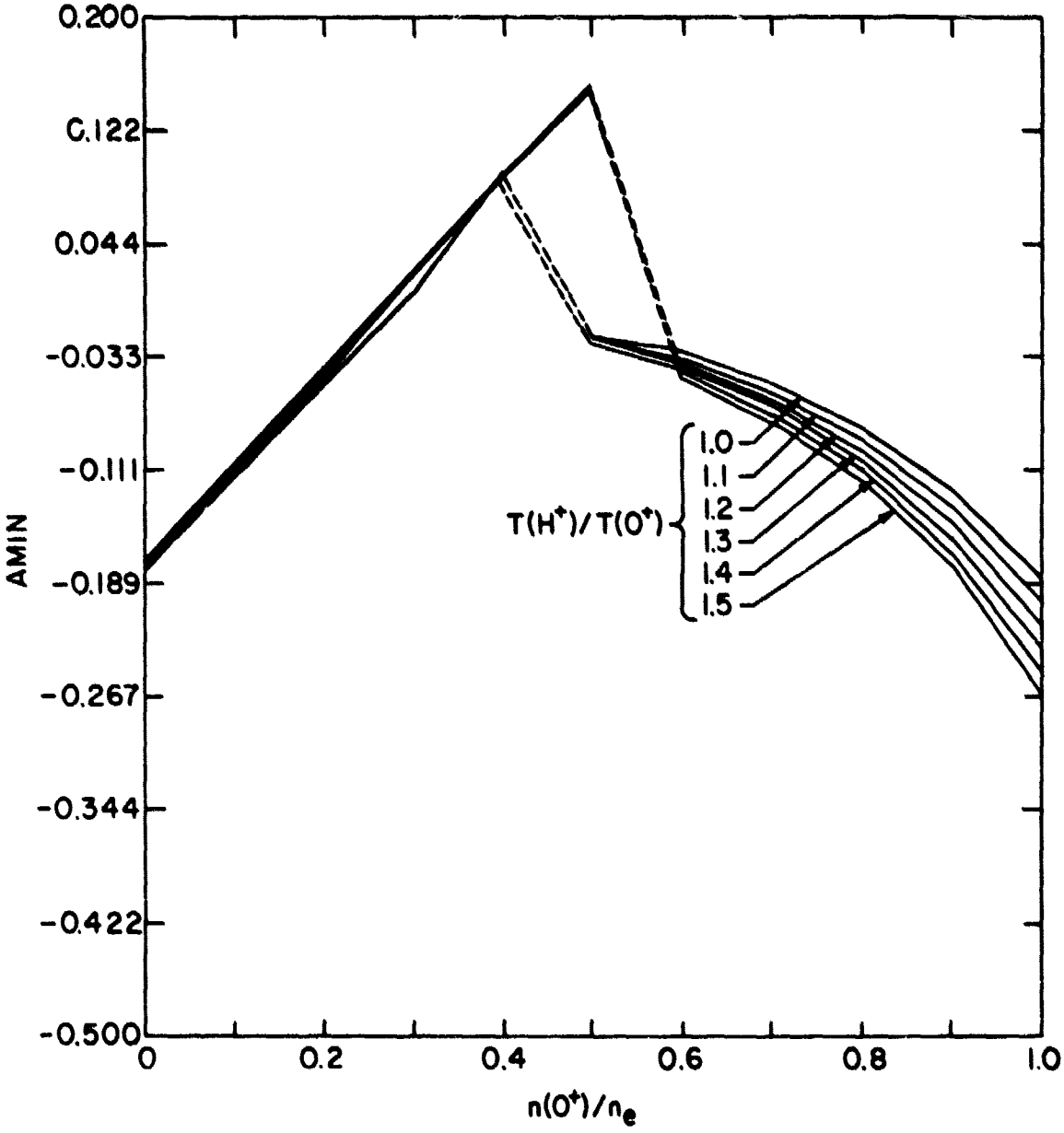

Figure 4.24 AMIN as a function of $n(O^+)/n_e$ and $T(H^+)/T(O^+)$ with $T_e/T(H^+) = 1.0$.

A parameter which depends on $T(H^+)/T(O^+)$ is ADHALF, which is the derivative of ACF at τ = THALF. ADHALF also depends on some of the other quantities. In Figure 4.25 ADHALF is shown as a function of $n(O^+)/n_e$ and $T(H^+)/T(O^+)$ with $T_e/T(H^+)$ = 1.0 and $T(O^+)$ = 1000 K. The dependence of ADHALF on $T(H^+)/T(O^+)$ is slight compared to the dependence on $n(O^+)/n_e$. Usually $n(O^+)/n_e$ is determined quite accurately from TZERO, so the dependence of ADHALF on $T(H^+)/T(O^+)$ can be used to determine $T(H^+)/T(O^+)$. This is not very easy because ADHALF also depends on $T_e/T(H^+)$. Although the dependence of ADHALF of $T_e/T(H^+)$ is not similar to the dependence on $T(H^+)/T(O^+)$, as in the case of AMIN, it is close enough to cause some problems with ambiguous results. Usually this can be overcome with some assumptions based on physical reasoning. For example the quantities $T_e/T(H^+)$ and $T(H^+)/T(O^+)$ are expected to vary smoothly with altitude. Since many altitudes are observed, results that are discontinuous will be rejected.

There are many other parameters of the ACF which depend on the quantities $T(O^+)$, $n(O^+)/n_e$, $T_e/T(H^+)$, and $T(H^+)/T(O^+)$. Parameters such as the time delay at the first minimum of the ACF (TMIN) and the derivative of the ACF at the first zero (A_0) could be used to reduce these quantities. Like the other parameters discussed previously, TMIN and A_0 have complicated dependencies. They will not be discussed here but they may be used if another parameter is not useful in reducing the ion and electron temperatures.

4.4.4 *Summary*. There are five quantities to be determined from analysis of the ACF - n_e, $n(O^+)/n_e$, $T(O^+)$, $T_e/T(H^+)$, and $T(H^+)/T(O^+)$. The only quantity which is easy to determine is $n(O^+)/n_e$ if it is greater than 0.5. It can be determined quite accurately from TZERO. The quantity n_e can be determined to within a factor of 2 from σ. If $T_e/T(H^+)$ is known, then n_e can be determined much more accurately. The $T(O^+)$, $T_e/T(H^+)$, and $T(H^+)/T(O^+)$ are

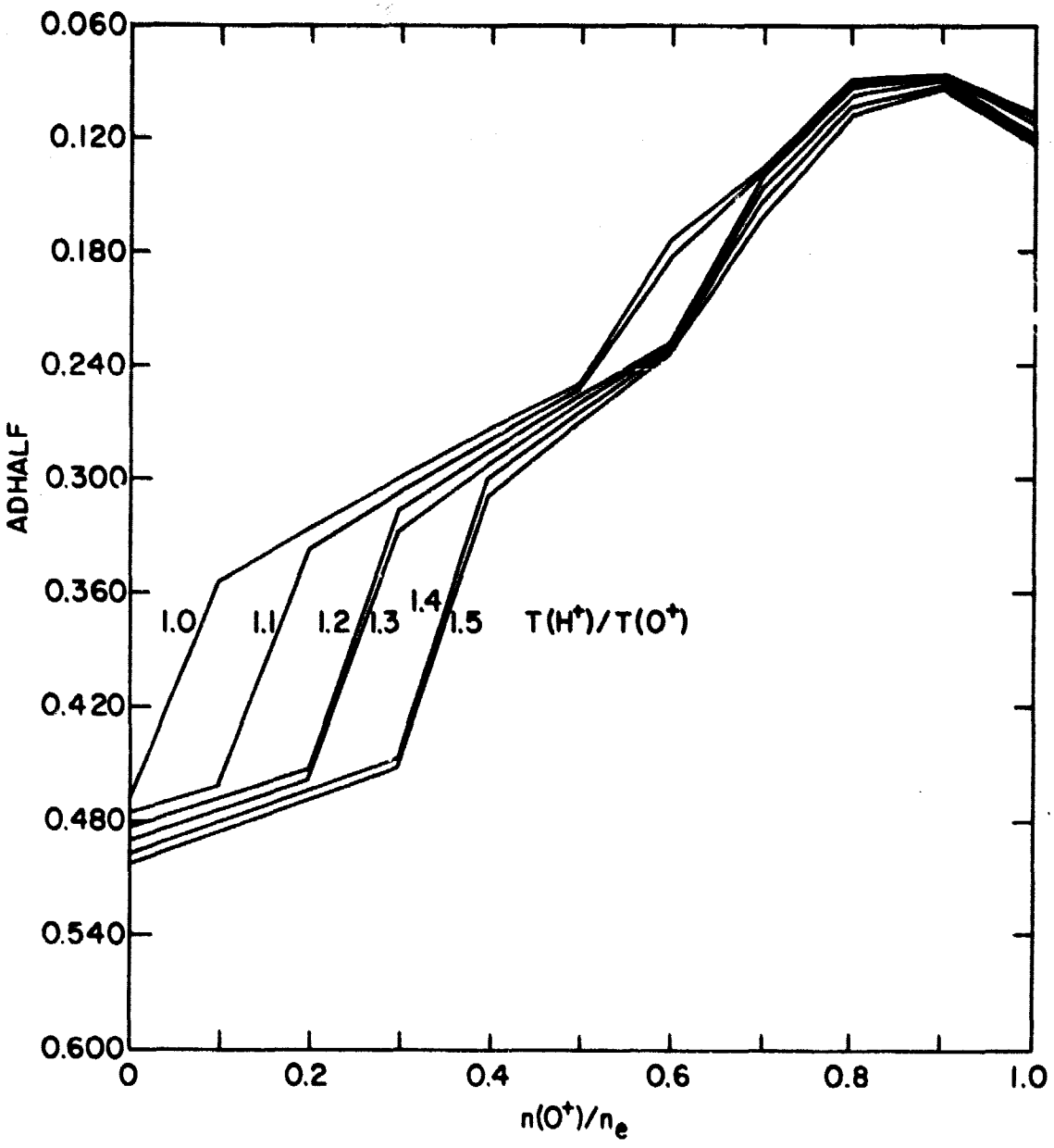

Figure 4.25 ADHALF as a function of $n(O^+)/n_e$ and $T(H^+)/T(O^+)$ with $T_e/T(H^+) = 1.0$.

much more difficult to determine because the ACF parameters depend on all these quantities. If either $T_e/T(H^+)$ or $T(H^+)/T(O^+)$ is known then the task of finding the other quantities is made easier because one dependence is removed. If all the quantities are unknown then the ACF parameters in conjunction with physical assumptions have to be used to reduce these quantities. Sometimes even this doesn't work, in which case the data is rejected either because of an experimental failure causing the problem or the occurrence of other physical events which are not of interest in this study. It was found that useful information can be reduced from almost all of the data.

5. METHOD OF ANALYSIS AND EXPERIMENTAL RESULTS

5.1 *Introduction*

The preceding chapter dealt with different parameters that can be derived from theoretical incoherent-scatter autocorrelation functions and spectra. In this chapter the method of fitting these theoretical parameters to the corresponding experimental parameters will be described. From this one can deduce electron, O^+ and H^+ ion temperatures, and the relative concentrations of O^+ and H^+ ions. The only ions present in the scattering medium are assumed to be H^+ and O^+.

The radar signals from the Arecibo, Puerto Rico facility are in the form of long (2000 μs, 300 km) and short (300 μs, 45 km) pulses transmitted alternately in order to obtain both adequate sensitivity at the highest altitudes and sufficient height resolution for the lower altitudes in the *F* region. The short pulse provides 48 km resolution over the range 230 to 902 km while the long pulse provides 108 resolution over the range 340 to 1850 km. That is, the short pulse samples the ACF every 48 km and these ACF's are averaged over 45 km. The long pulse samples the ACF every 108 km and these ACF's are averaged over 300 km.

The basic design of the Arecibo facility has been described previously by *Gordon* [1964]. The transmitter operates at 430 MHz with a peak power of 2.5 MW. For this work the beam was directed at the zenith. The received 430-MHz signal is processed by converting it to an IF of 30 MHz and passing this through a 125 kHz wide filter and then converting to a second IF of 62.5 MHz which was finally sampled and applied to a digital autocorrelation [*Hagen and Hsu*, 1974]. The hardware correlator has been described by *Hagen and Farley* [1973]. This hardware correlator forms the autocorrelation functions in real time.

The autocorrelation functions are sets of 24 points for each of the 15 altitudes sampled. The time spacing between adjacent points is 8 μs. This data is stored on magnetic tape so that additional processing can be done at a later time. The ACF's on tape are 12 minute averaged ACF's. That is, every 12 minutes the integrated ACF's for both the short and long pulses are written on magnetic tape.

5.2 *Methods of analysis of the ACF*

Two methods of analysis of the ACF are described in this section. The first method is the method of fitting ACF parameters using Newton's method of solving nonlinear equations. The second method is the method of fitting the ACF's using nonlinear least squares analysis; in the second method the entire ACF is used.

5.2.1 *Fitting ACF parameters.* Information about the temperature and composition of the charge particles of the *F* region can be obtained by matching experimental ACF parameters with theoretically generated ACF parameters. The parameters THALF, TZERO, AMIN, and $\left.\frac{\partial ACF}{\partial t}\right|_{THALF}$ = ADHALF are first calculated from the experimental ACF. Then these values can be compared with values calculated from theoretically generated ACF's which has been discussed previously in Chapter 4. As discussed in Chapter 4, these parameters are not simple functions of $T(O^+)$, $T(H^+)/T(O^+)$, $T_e/T(O^+)$, and $n(O^+)/n_e$. So in order to derive temperatures and composition from THALF, TZERO, AMIN, and ADHALF one must first make a initial assumption about the temperatures and composition. Then $n(O^+)/n_e$ is calculated from TZERO. This value of $n(O^+)/n_e$ is then used to calculate $T_e/T(O^+)$ from AMIN. These values of $T_e/T(O^+)$ and $n(O^+)/n_e$ are then used to calculate $T(O^+)$ from THALF. $T(H^+)/T(O^+)$ is then calculated from ADHALF using the previously calculated values of $T(O^+)$, $T_e/T(O^+)$ and $n(O^+)/n_e$. This procedure is repeated with these new

values to solve for $n(O^+)/n_e$, $T_e/T(O^+)$, $T(O^+)$, and $T(H^+)/T(O^+)$ until they converge. This procedure is illustrated in Figure 5.1. This is the general method for solving for $n(O^+)/n_e$, $T_e/T(O^+)$, $T(O^+)$ and $T(H^+)/T(O^+)$. Sometimes this method has to be altered due to problems in the data.

The numerical method used in deducing the ion and electron temperatures and number densities was Newton's method for solving nonlinear equations. The equation that was solved is

$$f(x) = y_e - y_t\ (x) = 0 \tag{5.1}$$

where y_e is the experimental ACF parameter, y_t is the theoretical ACF parameter and x is the physical quantity one is trying to find. The solution for x using Newton's method is found by generating successive approximations from the iteration

$$x_{i+1} = x_i - f(x_i)/f'(x_i) = g(x_i) \tag{5.2}$$

where $f'(x_i)$ is the derivative of $y_t(x)$.

The expected error in x is

$$x_{k+1} - x = \tfrac{1}{2}\, g''(\eta_k)(x_k - x)^2 \tag{5.3}$$

where η_k is between x_k and x.

One of the main problems is the obvious fact that when $n(O^+)/n_e = 1.0$ no information about the H^+ temperature can be deduced from the ACF. Even though $n(O^+)/n_e$ is not often 1.0 it is close enough to 1.0 at altitudes around F_2 layer peak so that H^+ temperatures are almost impossible to deduce from the ACF alone. In this case the H^+ temperature can be derived from the shape of the O^+ and electron temperature profiles using results from therma' processes analysis i.e. the O^+ and electron temperature profiles can have different shapes depending on whether the H^+ temperature is equal to or separate from the O^+ temperature. This will be discussed in more detail in

1. Assume Initial Values

2. Calculate $n(O^+)/n_e$ from TZERO

3. Calculate $T_e/T(H^+)$ from AMIN

4. Calculate $T(O^+)$ from THALF

5. Calculate $T(H^+)/T(O^+)$ from ADHALF

6. Repeat 2-5 until all values converge

Figure 5.1 Schematic diagram of the procedure for finding $T(O^+)$, $T(H^+)$, T_e, and $n(O^+)/n_e$.

Section 5.4.

The deduction of $n(O^+)/n_e$ from TZERO is sometimes ambiguous due to the discontinuity in the theoretical value of TZERO at different values of $n(O^+)/n_e$ for different $T_e/T(O^+)$. This was discussed in Chapter 4. Even though the experimental data of TZERO has discontinuities also, it is difficult to match the theroetical TZERO with the experimental TZERO at the altitudes where the discontinuity takes place. There are two possible solutions to this problem: the first is to try to fit theoretical and experimental values of TZERO but working from the other side of the discontinuity; the second is to find another parameter from the ACF which depends on $n(O^+)/n_e$ in a different way than TZERO does. This will be discussed in detail later in Section 5.4.

The parameter used to calculate $T(O^+)$ is THALF. THALF depends on $T(O^+)$ in a simple way but THALF also depends on $n(O^+)/n_e$, $T(H^+)/T(O^+)$, and $T_e/T(O^+)$. This complicates matters a little but if $n(O^+)/n_e$ is known $T(O^+)$ can be calculated with reasonable accuracy (200 K or 20%) since the dependence of THALF on $T(O^+)$ is stronger than the dependence of THALF on $T_e/T(H^+)$. The calculation of $T(O^+)$ will be discussed in Section 5.5.

Solving for $T_e/T(O^+)$ is simplified if one first ignores the dependence of AMIN on $T(H^+)/T(O^+)$. Then AMIN only depends on $T_e/T(O^+)$ and $n(O^+)/n_e$; it doesn't depend on $T(O^+)$. Now if $n(O^+)/n_e$ is assumed to be known as it was for finding $T(O^+)$ from THALF then $T_e/T(O^+)$ can be found to within 20%. This accuracy can be improved and this will be discussed in more detail in Section 5.5.

There are two more quantities which need to be found n_e and $T(H^+)/T(O^+)$. The electron density n_e can be found quite easily if the total scattered power is known. Data from Arecibo gives the scattered power very accurately

and thus the electron density can be calculated quite accurately. The determination of $T(H^+)/T(O^+)$ is not so precise. This is because the ACF depends on $T(H^+)/T(O^+)$ only weakly. Yet there is a definite dependence in the shape of the ACF. Some of the parameters of the ACF do depend on $T(H^+)/T(O^+)$ and these will give approximately values for $T(H^+)/T(O^+)$. Extensive analysis of the ACF which will be discussed in Section 5.5 give better accuracy for $T(H^+)/T(O^+)$.

5.2.2 *Fitting ACF's.* Experimental ACF's can be matched with theoretical ACF's using the usual least square criterion. The 24 experimental points ξ_n are each weighted by the reciprocal of its expected variance ρ_n. The physical quantity x is found from locating the minimum of

$$f(x) = \sum_{n=1}^{24} [(\xi_n - \theta_n(x))/\rho_n]^2 \tag{5.4}$$

where θ is the theoretical ACF. The condition for the minimum is simply

$$\partial f/\partial x = 0 \tag{5.5}$$

Since the theoretical ACF's are not simple functions of x, numerical techniques are used to find the best fit. The solution for x using nonlinear least squares analysis is found by first numerically differentiating $f(x)$. Then successive approximations are generated by using

$$x^{k+1} = x^k - f(x^k)/f'(x^k) \tag{5.6}$$

If x represents a set of physical quantities then the second term on the right side of equation (5.6) is the solution to the matrix equation

$$A\vec{\delta x}^k = B \tag{5.7}$$

where $A_{ij} = (\partial f/\partial x_i)(\partial f/\partial x_j)$

$B_i = (\partial f/\partial x_i)f$

Equation (5.6) then becomes

$$\vec{x}^{k+1} = \vec{x}^{k} + \vec{x}^{k} \tag{5.8}$$

The variance of the final fitted quantities is given by

$$\text{variance } (x_i) = A_{ii}^{-1} \tag{5.9}$$

The matrix is inverted in the course of solving equation (5.7).

The physical quantities which can be used for $\vec{x}$ are $T(O^+)$, $T_e/T(O^+)$, $T(H^+)/T(O^+)$, and $n(O^+)/n_e$. So matrix A is a 4 x 4 matrix. Particular care must be used in inverting this matrix because some of the elements of A are very small compared to other elements. This gives a determinant of A which is close to zero. If the determinant of A is in fact zero then the inverse of A does not exist and matrix equation (5.7) has no unique solution. If the determinant of A is close to zero then the solution of matrix equation (5.7) is very difficult using nonlinear least squares analysis. In this case, Newton's method can be used to fit the theoretical ACF to the experimental ACF.

By fitting the entire theoretical ACF to the experimental ACF better accuracy can be achieved when deducing the ratio $T(H^+)/T(O^+)$ and also when deducing $T(O^+)$ and $T_e/T(O^+)$. The ratio $n(O^+)/n_e$ is not deduced by this method because it can be deduced accurately from TZERO.

The method of fitting the entire ACF is a more accurate method of deducing the physical quantities than fitting parameters of the ACF. The reason is that much more information is available in the ACF than in the ACF parameters discussed in Chapter 4. All the physical quantities could be deduced by this method but $n(O^+)/n_e$ and sometimes the other quantities are calculated by fitting ACF parameters because fitting the entire ACF is computationally slower and requires much more computer resources. The ratio $n(O^+)/n_e$

and some of the other quantities are deduced by fitting ACF parameters whenever the accuracy is good.

5.3 *Ion and Electron Number Densities*

The determination of $n(O^+)/n_e$ and n_e will give the ion and electron number densities since $n(O^+) + n(H^+) = n_e$ in the topside ionosphere. From TZERO one can calculate $n(O^+)/n_e$ if $T(O^+)$ is known. Even if $T(O^+)$ is not known, $n(O^+)/n_e$ can be estimated from assuming a typical value for $T(O^+)$. For example, if one assumes that $T(O^+)$ is 1000 K throughout the topside ionosphere, one gets what is shown in Figure 5.2 for $n(O^+)/n_e$ profiles. Also, shown in Figure 5.2 is the $n(O^+)/n_e$ profile for $T(O^+) = 2000$ K. Comparison between the $T(O^+) = 1000$ K and $T(O^+) = 2000$ K profile for $n(O^+)/n_e$ shows that error is not too large in the measurement of $n(O^+)/n_e$ if $T(O^+)$ is not known. Thus, reasonable estimates of $n(O^+)/n_e$ can be made even if $T(O^+)$ is not known.

Profiles of $n(O^+)/n_e$ can also be calculated using different assumptions on T_e/T_i. This is shown in Figure 5.3 with T_e/T_i equal to 1.0 and 2.0. As one can obviously see from this figure the effect of T_e/T_i on $n(O^+)n_e$ is very small except when $n(O^+)/n_e$ is around 0.5. When $n(O^+)/n_e$ is greater than 0.6 the dependence of $n(O^+)/n_e$ on T_e/T_i can be ignored. The reason for disagreement in $n(O^+)/n_e$ measurements around 0.5 is due to the discontinuity in theoretical values of TZERO near $n(O^+)/n_e = 0.5$.

Another parameter which has very little effect on $n(O^+)n_e$ is $T(H^+)/T(O^+)$. It is fortunate that T_e/T_i and $T(H^+)/T(O^+)$ have very little influence on measurements of $n(O^+)/n_e$ because other parameters of the ACF depend on $n(O^+)/n_e$ besides $T_e/T(O^+)$, $T(O^+)$, and $T(H^+)/T(O^+)$. Thus if the dependence of $n(O^+)/n_e$ can be eliminated from the other parameters of the ACF then better measurements of $T_e/T(O^+)$, $T(O^+)$, and $T(H^+)/T(O^+)$ can be made.

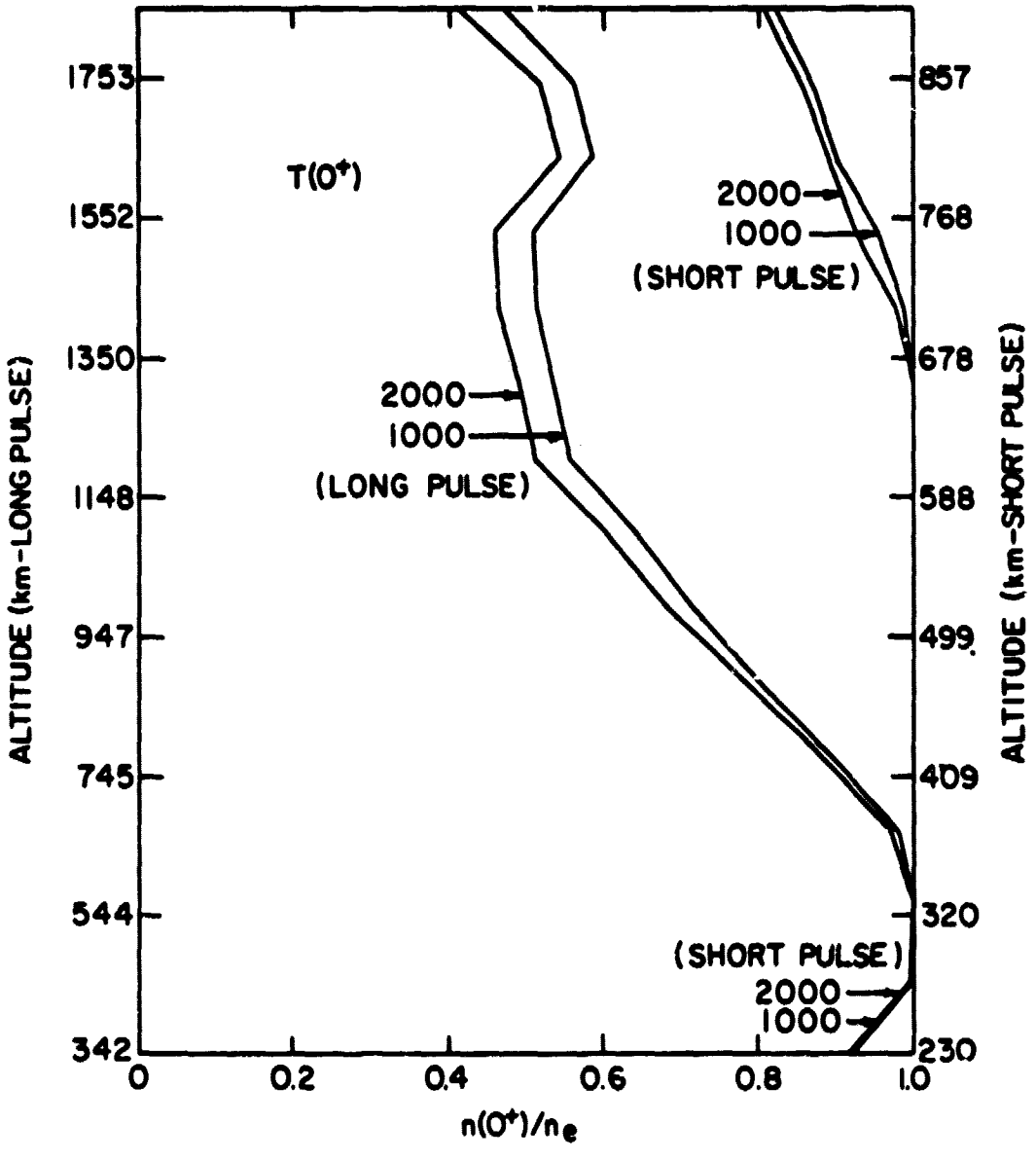

Figure 5.2 Profiles of $n(O^+)/n_e$ for T_i = 1000, 2000 K.

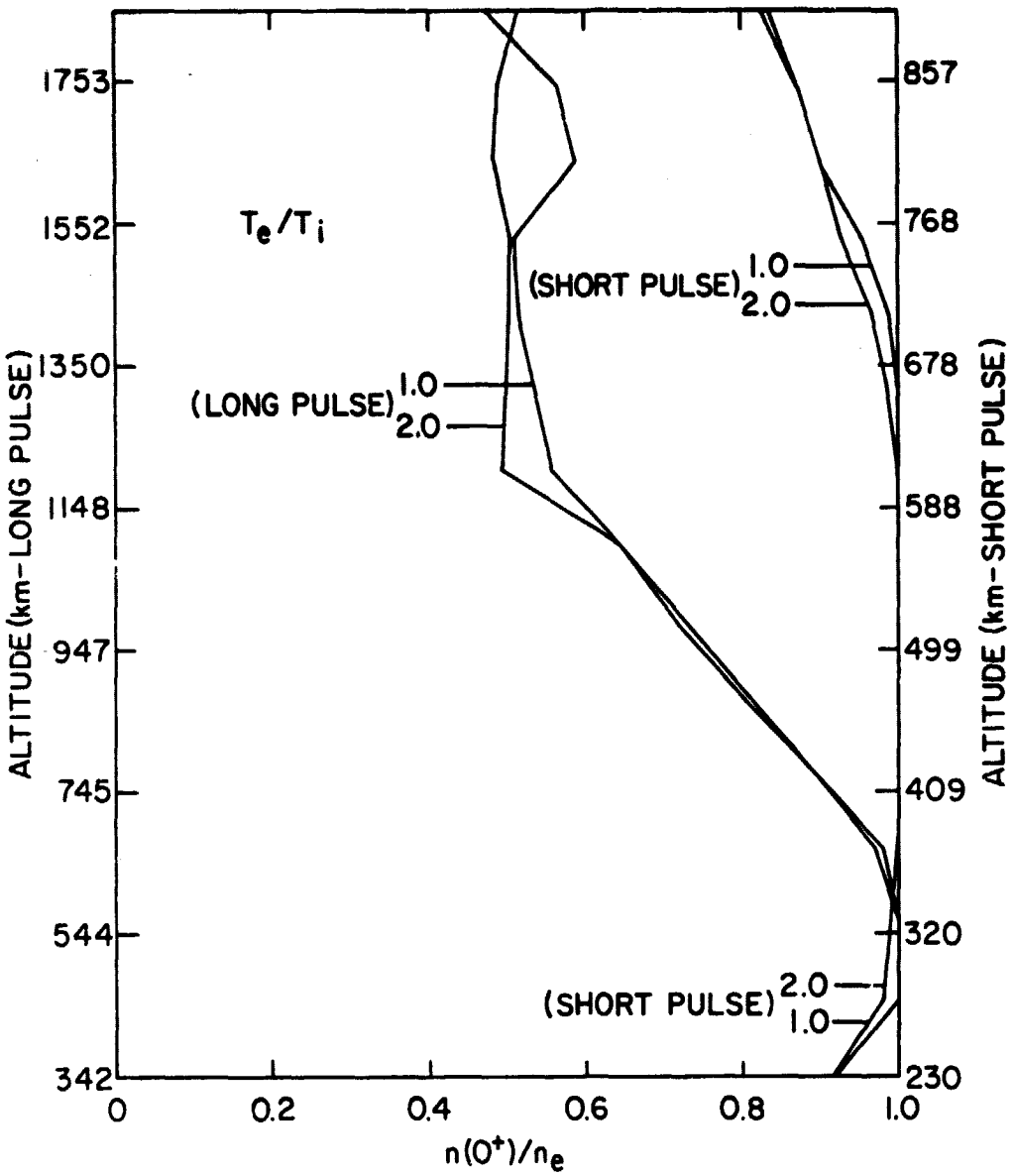

Figure 5.3 Profiles of $n(O^+)/n_e$ for different values of T_e/T_i with T_i = 1000 K.

Usually the ratio $n(O^+)/n_e$ is found from TZERO which has been described previously. If $n(O^+)/n_e$ is less than .55 $n(O^+)/n_e$ is found from the time delay at ACF = 1/2 (THALF). THALF is dependent on $T_e/T(O^+)$, $T(H^+)/T(O^+)$, and $T(O^+)$ besides being dependent on $n(O^+)/n_e$, so the determination of $n(O^+)/n_e$ is much more complicated than previously. If $T(O^+)$, $T_e/T(O^+)$, or $T(H^+)/T(O^+)$ are not known then one must assume values for them. This leads to errors in the calculation of $n(O^+)/n_e$. These errors can be reduced if $T(O^+)$, $T_e/T(O^+)$, or $T(H^+)/T(O^+)$ are calculated separately. For example, $T(O^+)$ is calculated when $n(O^+)/n_e$ is greater then .55. If $T(O^+)$ is assumed to be constant with increasing altitude, then $n(O^+)/n_e$ is found with better accuracy where also $T_e/T(O^+) = T(H^+)/T(O^+) = 1$.

The determination of n_e is a bit more difficult than finding $n(O^+)/n_e$. This is because n_e is found from measurements of σ which depends on the electron to ion temperature ratio. The parameter σ also depends on the electron Debye length to wavelength ratio,

$$\alpha = 4\pi D_e/\lambda \tag{5.10}$$

where D_e is the electron Debye length given in equations 4.1 and λ is the transmitted radio wavelength. The dependence of σ on T_e/T_i and α can be expressed as [*Moorcroft*, 1963]

$$\sigma = n_e\sigma_e/(1 + \alpha^2)(1 + T_e/T_i + \alpha^2) \tag{5.11}$$

where σ_e is Thomson scattering cross section given in equation (4.7). Usually in the F region α is very small so σ only depends on n_e and T_e/T_i. In the topside ionosphere the electron to ion temperature ratio is generally between one and three; therefore the electron density can be found within a factor of 2 since the measurements of σ are quite accurate.

The measured power depends on many experimental factors besides depending on n_e and T_e/T_i. If all these factors are known the electron number density can easily be found, but usually ionosonde data are used to find the peak electron number density. (An ionosonde is a radio wave vertical sounder which sweeps in frequency from about 1 to 25 MHz.) This is then used to find the electron number density at the altitude where the peak power occurs. At other altitudes the electron number density can be found by normalizing the power by the peak power and multiplying this by the peak electron number density found by ionosonde data. In Figure 5.4 are shown some electron number density profiles where α is assumed to be zero and T_e/T_i is set equal to one. These profiles give an indication of variation of the electron number density during a winter day (Feb. 10, 1972). Notice that the peak electron number density increases before dawn and reaches a maximum in the late afternoon. After this the electron number density profiles decrease slowly during the night. The proportion of the O^+ and H^+ ions also varies during the day. This is shown in Figure 5.5 where the temperature of electrons, the O^+ and H^+ ions is equal to 1000 K. In Figure 5.5 there are two set of profiles - one for the daytime and one for the nighttime. The daytime profile indicates that O^+ is the major ion at all altitudes in the altitude region observed. The nighttime profile indicates that H^+ becomes the predominate ion around 750 km, that is, at 750 km the transition between O^+ and H^+ as the major ion takes place. Below 750 km at night O^+ ions are formed through a rapid charge exchange with H^+ ions with the reaction

$$H^+ + O \rightleftarrows O^+ + H + \Delta E$$

The source of H^+ ions is the inward flow of H^+ ions from high altitudes. During the night H^+ ions diffuse inward which results in the maintainance of

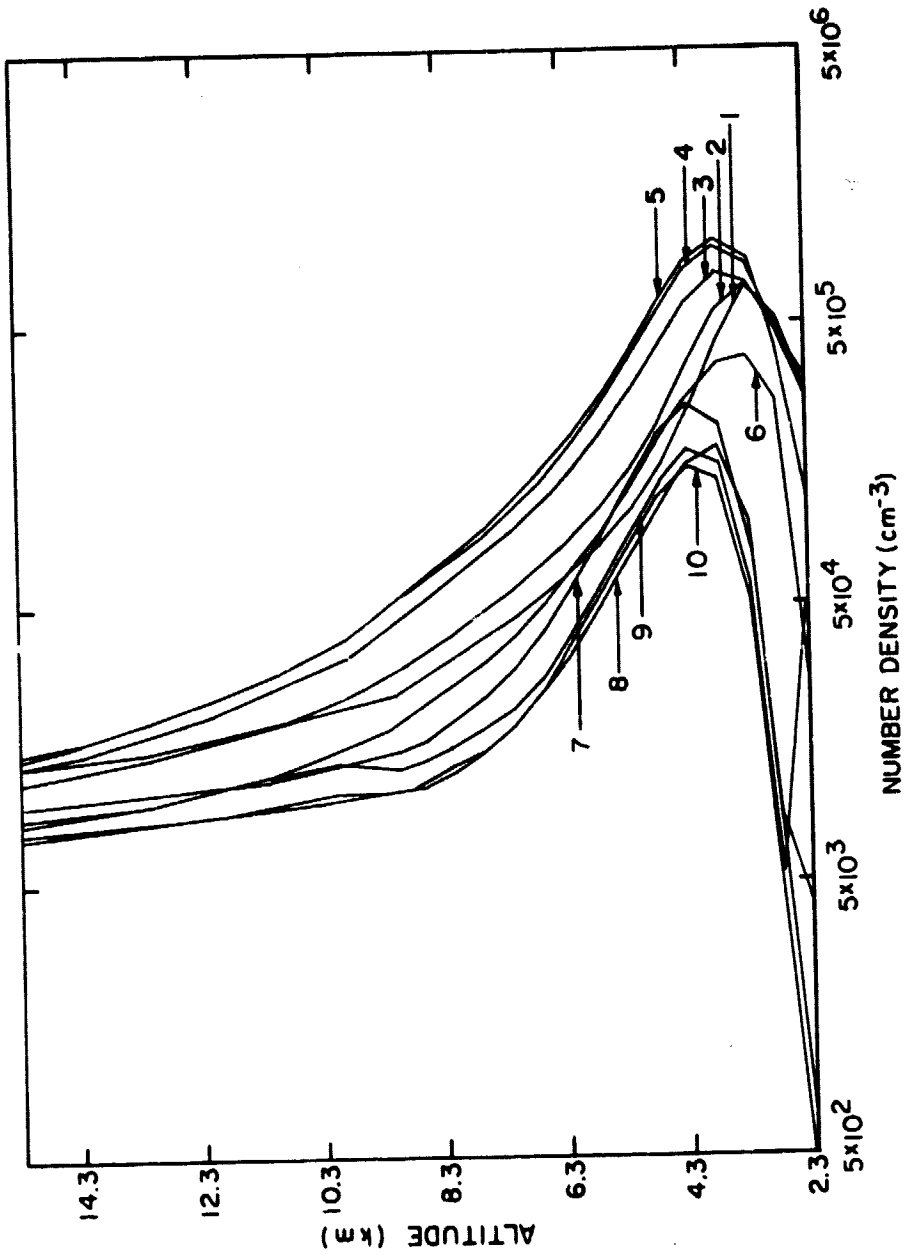

Figure 5.4 Profiles of n_e for Feb. 10, 1972 from 9:07 AM to 3:36 AM in 1 hr. 56 min. periods. Each curve represents data averaged over 12 minutes. Curve 1 is data for 9:07; curve 2 is 1 hr. and 56 min. later, etc.

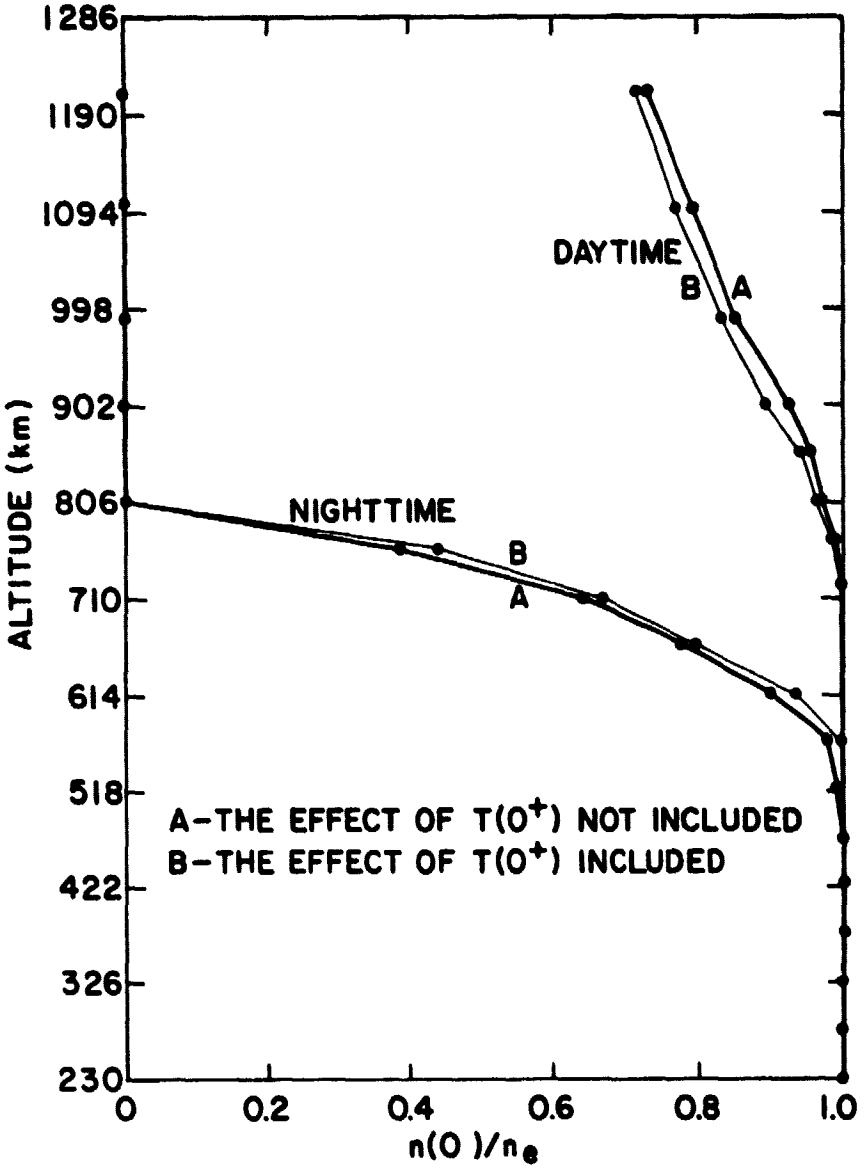

Figure 5.5 Nighttime and daytime profiles of $n(O^+)/n_e$ for Feb. 10, 1972. There are profiles where the effect of the ion temperature is included (A) and profiles where the effect of the ion temperature is not included (B).

substantial ion densities in the *F* region. During the day inward diffusion of H^+ is not important due to the large photoionization rate of O. In fact, during the day there is either a slight outward flow of O^+ ions or diffusive equilibrium exists. This is the reason why O^+ is the predominate ion from 230 to 1200 km during the day.

Also in Figure 5.5 the effect of the ion temperature is included in the calculation of nighttime and daytime profiles of $n(O^+)/n_e$. As mentioned previously, TZERO depends slightly on T_i. So T_i and $n(O^+)/n_e$ are calculated from THALF and TZERO respectively. THALF also depends on T_e/T_i which can be calculated from AMIN. The profiles of $n(O^+)/n_e$ where the effect of T_e is included should be more accurate because the effect of all the physical quantities are included. The profiles of Figure 5.5 are almost the same except that the transition between H^+ and O^+ occurs at a slightly higher altitude in the profile where the effect of $T(O^+)$ is included. The difference in the profiles of Figure 5.5 indicates that the errors in $n(O^+)/n_e$ are less than 5 percent.

The effect of T_e/T_i on electron number densities is shown in Figure 5.6 for daytime profiles of n_e. Profile 1 is for the case where T_e/T_i is assumed to be one. The other profiles include the effect of T_e/T_i where T_e/T_i is calculated from AMIN or from fitting the ACF. The difference between profile 1 and profile 2 or 3 is greatest around the peak of the electron density profile. This is because the ratio T_e/T_i is closer to two at altitudes near the peak. At other altitudes the effect of T_e/T_i is reduced either because n_e is much less than its value at the peak or T_e/T_i is near 1.0. Also shown in Figure 5.6 is a electron number density profile where T_e/T_i has been calculated from nonlinear regression analysis. This method is described in Section 5.2.2 and is the method where the experimental ACF's are fitted to

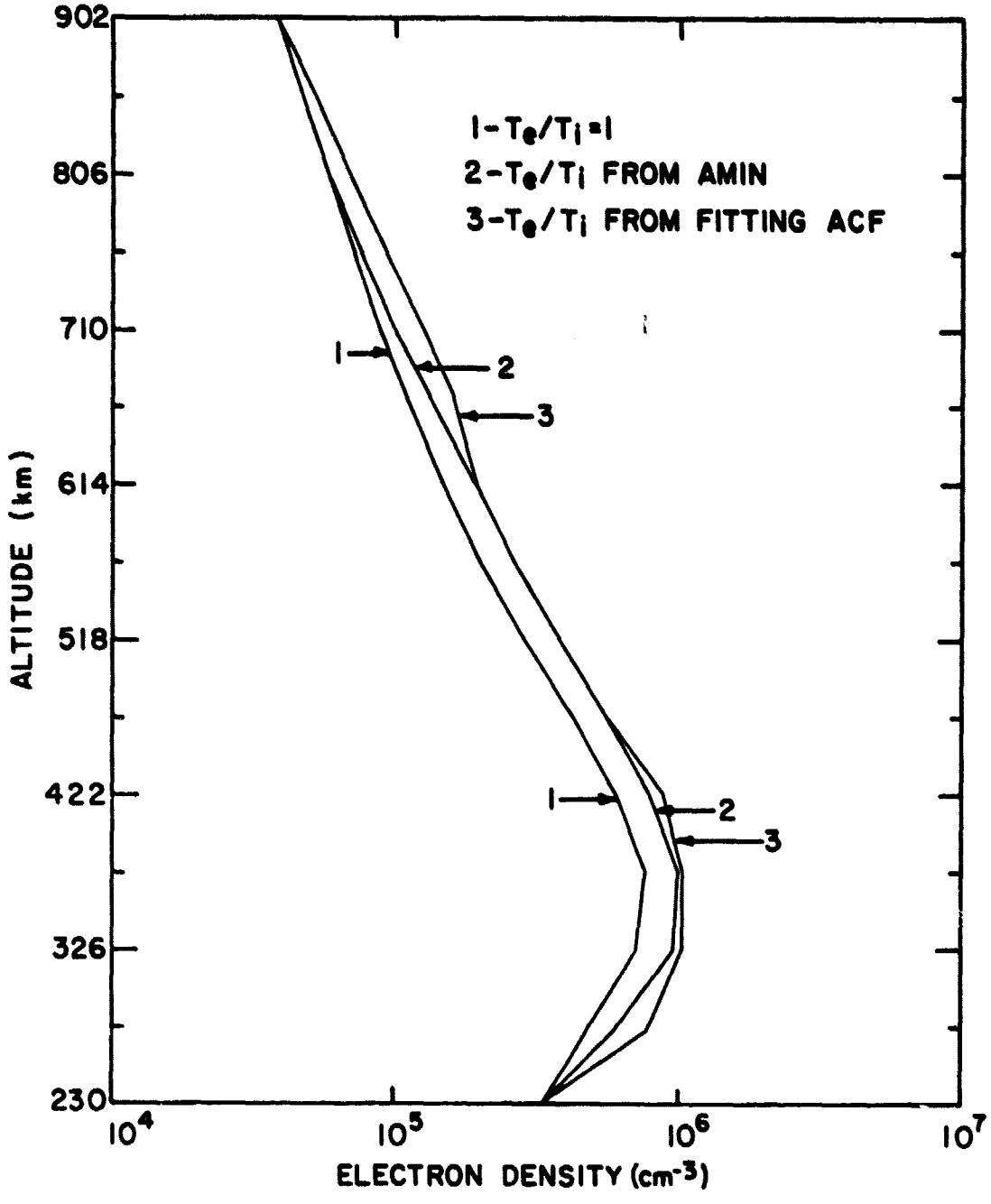

Figure 5.6 Profiles of n_e for Feb. 10, 1972 from 9:07 to 9:17 AM for long pulse data where the effect of T_e/T_i is shown.

theoretically generated ACFs. A library of theroetical ACFs is created for various values of T_i and T_e/T_i and the experimental ACFs are fitted using nonlinear least squares method. The values of T_i and T_e/T_i corresponding to the best fit to the theoretical ACF are found from this method. The value of T_e/T_i is then used in the calculation of electron density profile 3 given in Figure 5.6. This electron density profile is very similar to profile 2 which indicates that the errors of electron density measurements are small. Although the profiles given Figures 5.6 agree fairly closely, above 806 km there is a problem because the measured total scattered power is much smaller than it is around 400 km. Even though one expects the total scattered power to be less because of smaller electron densities, the reduced total scattered power causes larger uncertainities in the measurement of T_e/T_i. Thus, electron densities are less accurate. This can be overcome by longer pulses which were used.

The electron density profile for long pulse signals is shown in Figure 5.7. There are three profiles shown which have been calculated using the three methods used for Figure 5.6. Profile 1 is the case $T_e/T_i = 1$. In profile 2 T_e/T_i is calculated from AMIN. By fitting experimental and theoretical ACF's one gets T_e/T_i used in profile 3. The largest difference between the profiles occurs below 666 km where T_e/T_i is close to 2. Above 666 km the profiles are approximately equal. Profiles 2 and 3 are about equal from 342 to 1206 km. This indicates the accuracy in values of T_e/T_i is good because two different methods of finding T_e/T_i give approximately the same results.

The expected error of the electron densities given in Figure 5.6 and Figure 5.7 depends on the accuracy by which T_e/T_i can be measured. The error of T_e/T_i will be discussed later in Section 5.4. The error of the

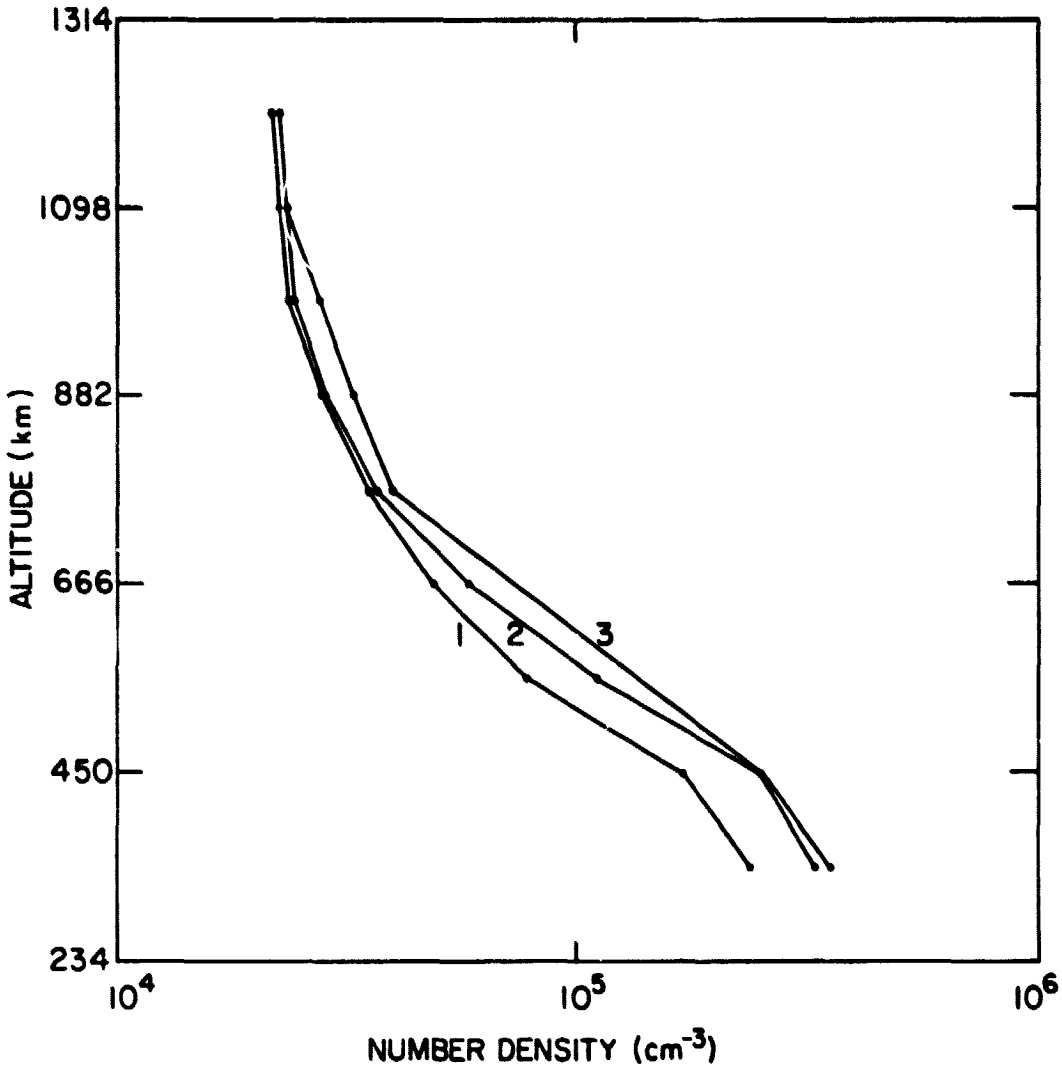

Figure 5.7 Profiles of n_e for Feb. 10, 1972 from 9:07 to 9:17 AM for long pulse data where the effect of T_e/T_i is shown.

electron density also depends on the error in the measurement of the total scattered power which depends on the number of correlated samples taken. As more samples are taken the error in total scattered power decreases. Usually enough samples are taken so that the error in the power is very small (less than 10^{-4}). Therefore, the error of the electron density only depends on the error of T_e/T_i. Typical values for the error of T_e/T_i are less than 25 percent. So the error of the electron density is less than 25 percent.

5.4 *Ion and Electron Temperatures*

While the determination of $n(O^+)/n_e$ and n_e are relatively quite simple, the determination of the ion and electron temperatures is considerably more complicated especially if separate ion temperatures for O^+ and H^+ are calculated. There are a number of parameters of the theoretical ACF which depend on $T_e/T(O^+)$, $T(H^+)/T(O^+)$, and $T(O^+)$. Therefore, one tries to choose parameters which depend on only one or just two of quantities $T_e/T(O^+)$, $T(H^+)/T(O^+)$, and $T(O^+)$.

Fortunately, AMIN depends on $T_e/T(O^+)$ and $T(H^+)/T(O^+)$ and does not depend on $T(O^+)$. AMIN also depends on $n(O^+)/n_e$ which can be calculated from TZERO. When $n(O^+)/n_e$ is between 0.4 and 0.6 temperature ratios deduced from AMIN are unreliable and another parameter of the ACF must be used to deduce temperature ratios. Usually AMIN is very useful in deducing temperature ratios for daytime because only at high altitudes does $n(O^+)/n_e$ drop below 0.6. The ion and electron temperatures discussed in this section apply mostly to daytime results. Daytime is concentrated on because the temperatures during the day are much larger than at night. Also during the day the ion and electron temperatures vary more with altitude than at night.

At nighttime H^+ becomes a dominant ion at much lower altitudes; so $n(O^+)/n_e$ drops below 0.6 at lower altitudes than during the day. At night

the ion and electron temperatures seem to be fairly constant with altitude. In Figure 5.8 ion and electron temperatures are shown for nighttime on Feb. 10, 1972 where a single ion temperature is assumed. This night was characterized by low magnetic activity. The temperatures were calculated from comparing theoretical and experimental values of AMIN and THALF. The electron and ion temperature profiles shown are almost identical at all altitudes. They can be considered the same since experimental errors are greater than the difference between the electron and ion temperatures.

In Figure 5.9 ion and electron temperature profiles are shown for Feb. 10, 1972 from 9:07 to 9:19. These profiles were calculated from AMIN and THALF using the method described in Section 5.2.1 where a single ion temperature was used. Notice that the electron temperature profile is significantly greater than the ion temperature profile. The ion temperature seems to stay relatively constant up to about 500 km. Then the ion temperature increases steeply up to about 700 km. Above 700 km the ion temperature increases more slowly but there is a definite temperature gradient. The electron temperature increases rapidly from 230 to about 400 km. Above 400 km the gradient of the electron temperature gradually decreases until the gradient of the electron temperature is about 1 K/km at 1000 km.

The ion and electron temperatures can also be calculated by fitting the experimental ACF to a theroetical ACF. A library of theoretical ACF's used in this analysis is given in Appendix D along with the computer program which created the library. In this analysis the ratio $n(O^+)/n_e$ is first calculated by matching theoretical and experimental values of TZERO. Then the experimental ACF is fitted to a theoretical ACF by minimizing the square of the difference of the two ACF's. The results of this analysis are shown in Figure 5.10, 5.11, 5.12, 5.13, and 5.14.

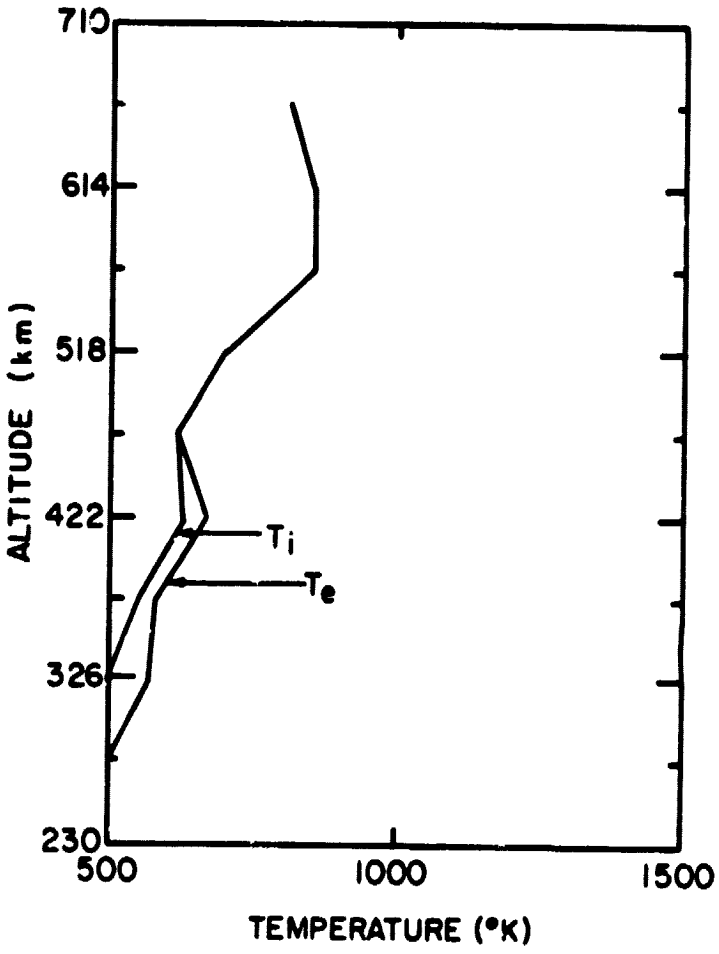

Figure 5.8 T_e and T_i for the night of Feb. 10, 1972 at 2:00 AM.

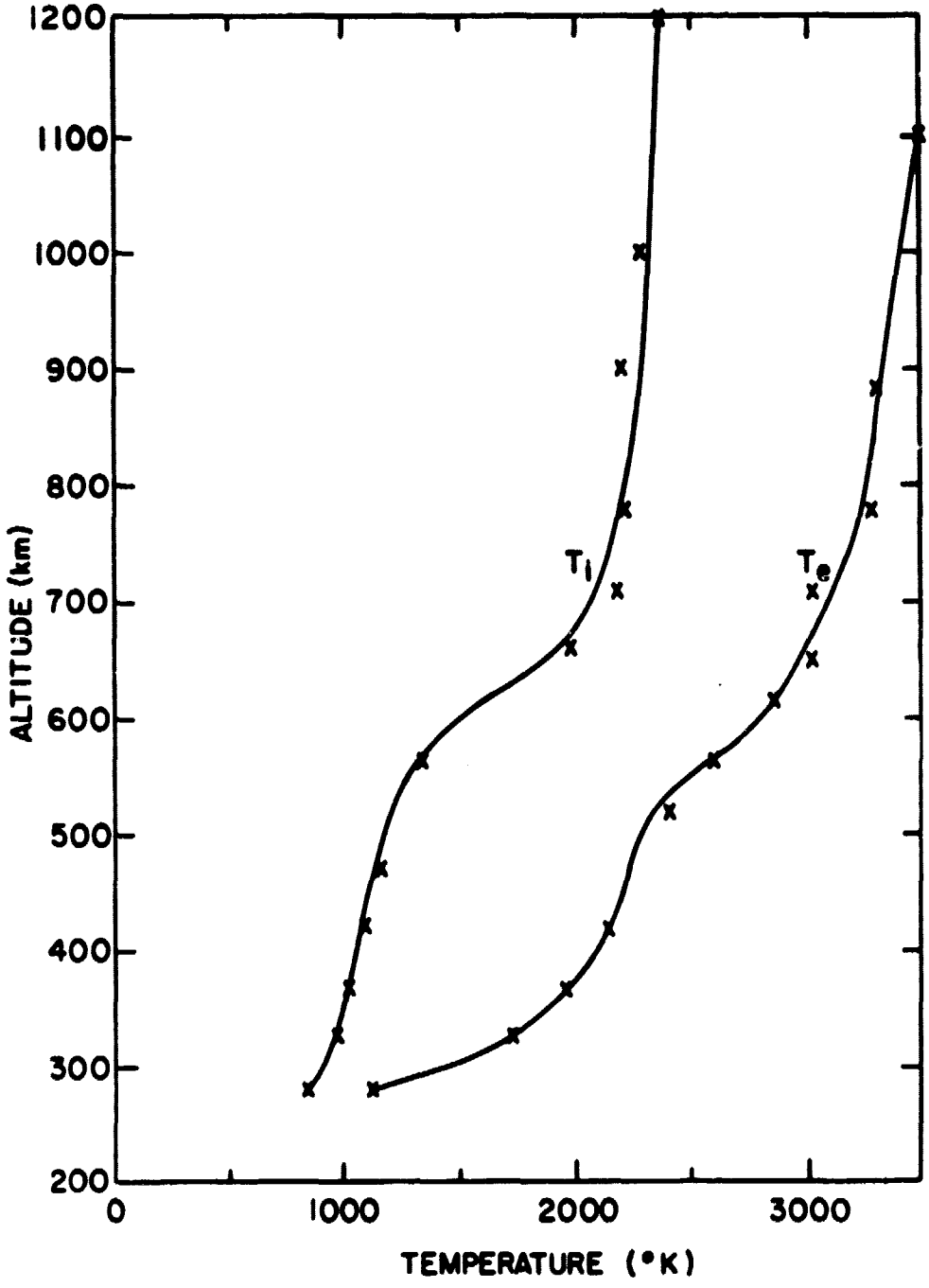

Figure 5.9 $T(O^+)$ and T_e for Feb. 10, 1972 from 9:07 to 9:17 AM where AMIN and THALF of the ACF is used to calculate $T(O^+)$ and T_e.

In Figure 5.10 profiles of $T(O^+)$ and T_e are shown for Feb. 10, 1972 from 9:07 to 9:29 AM. This figure is for two consecutive 12-minute time periods. The circles represent data for the first time period. The data for the second time period are given by X's. Data from both long and short pulses are given. The data above 900 km are not very accurate (±200 K) due to the lack of an extensive library of ACF's for ion temperatures greater than 2000 K. The accuracy of the profiles below 900 km is approximately ±50 K. The accuracy of the profiles below 900 km is much better because of the extensive library of theoretical ACF's from $T(O^+)$ = 800 to 2000 K. Also, one can see that the accuracy below 900 km is good because of the close agreement of data of the two time periods.

Comparison of the results of the methods of fitting ACF parameters (Figure 5.9) and fitting the entire ACF (Figure 5.10) indicates a close agreement of the profiles of $T(O^+)$ and T_e. Therefore, the results for $T(O^+)$ and T_e are very reliable.

When $n(O^+)/n_e$ is approximately 1.0, $T(H^+)$ is very difficult to deduce from experimental data. $T(H^+)$ can be found from analysis of the profiles of $T(O^+)$ and T_e. Profiles of $T(O^+)$ depend on $T(H^+)$ because $T(O^+)$ has a different shape for different circumstances. For example if a single ion temperature is used then $T(O^+)$ becomes equal to the neutral temperature at a higher altitude than that when each ion has different temperatures. Inspection of Figure 5.10 indicates that $T(O^+)$ approaches a neutral temperature of 1000 K at about 500 km. If $T(O^+)$ were equal to $T(H^+)$, $T(O^+)$ would approach 1000 K at about 600 km or higher. So one can conclude $T(H^+)$ must be significantly larger than $T(O^+)$ in altitude region from 500 to 600 km because a larger $T(H^+)$ increases $T(O^+)$.

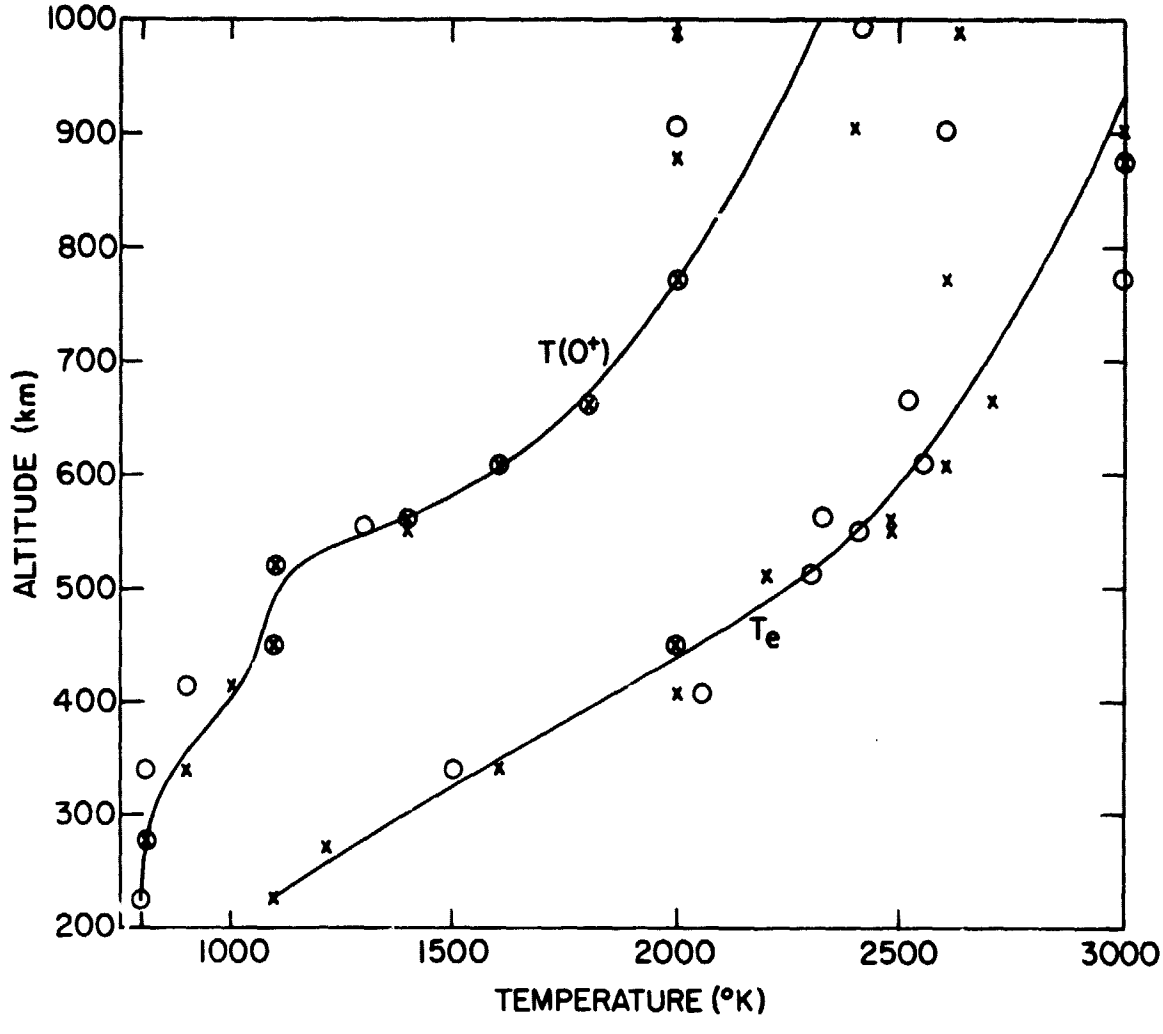

Figure 5.10 $T(O^+)$ and T_e for Feb. 10, 1972 from 9:07 to 9:29 AM where fitting the experimental ACF to theoretical ACF's is used to find $T(O^+)$ and T_e. Data for two consecutive time periods are shown. Circles are for 9:07 to 9:19 ×'s are for 9:19 to 9:29.

In Figure 5.11 the ratio $T(H^+)/T(O^+)$ is shown for Feb. 10, 1972 from 9:07 to 9:27 AM. The circles are for the first time period, X's are for the second. Both long pulse and short pulse data are shown in this figure. The lower altitudes don't have data points for the first time period because $n(O^+)/n_e$ was nearly 1.0 at these altitudes during this time. During the next time period $n(O^+)/n_e$ was slightly below 1.0 which allowed the calculation of $T(H^+)/T(O^+)$. Figure 5.11 shows that $T(H^+)/T(O^+)$ has a maximum near 550 km of about 1.45 and drops off to 1.0 at low and high altitudes. $T(H^+)/T(O^+)$ is very large from 300 to 700 km. The fact that $T(H^+)/T(O^+)$ has these large values indicates that much more heat is being transferred to H^+ from the electron than to O^+. The theory of thermal processes with regard to ion and electron temperatures is discussed in Chapter 6.

In Figure 5.12 the profile of $n(O^+)/n_e$ for Feb. 24, 1972 is shown. This figure includes both long pulse and short pulse data from 7:57 to 8:24 AM where $n(O^+)/n_e$ is calculated from TZERO. The circles represent data for 7:57 to 8:10. The X's represent data for 8:10 to 8:24. The morning of Feb. 24, 1972 was characterized by disturbed magnetic activity. From 300 to 600 km $n(O^+)/n_e$ is nearly equal to 1.0. Long pulse data (300 km altitude sample) give values slightly less than 1.0 at 342, 450, and 558 km which allows the calculation of $T(H^+)/T(O^+)$ at these altitudes.

The profiles of $T(O^+)$ and T_e for same data given in Figure 5.12 are shown in Figure 5.13. Above 900 km the accuracy of the profiles is approximately ±300 K. This is due to the lack of an extensive library of theoretical ACF's for $T(O^+)$ greater than 2000 K. Below 900 km the error in the profiles is less (±100 K) than above 900 km but the error is larger than in Figure 5.10. This is because the data in Figure 5.12 are earlier in the morning than Figure 5.10. At night the ion and electron temperature is approximately

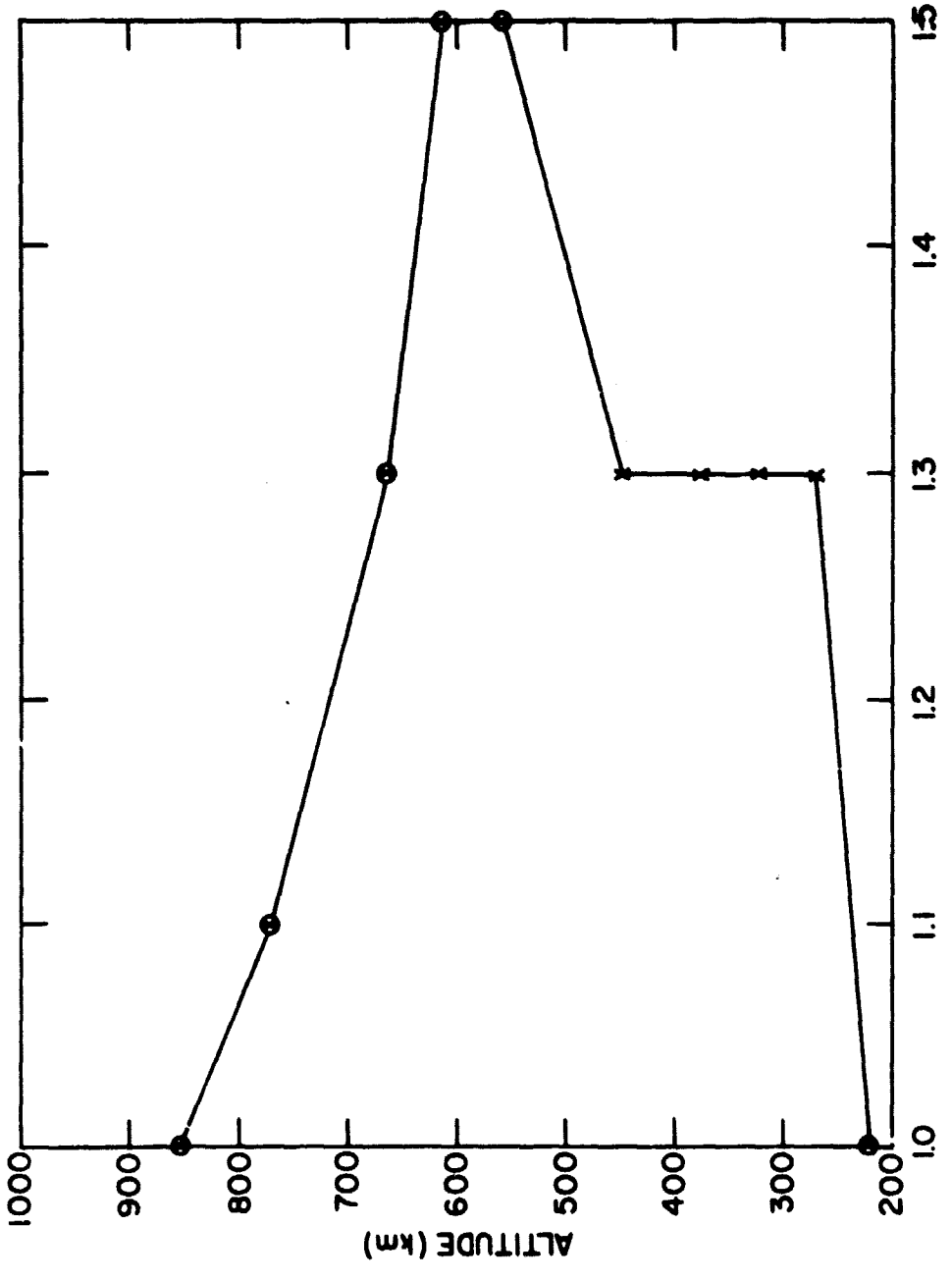

Figure 5.11 Profiles of the ratio $T(H^+)/T(O^+)$ for Feb. 10, 1972 from 9:07 to 9:29 AM where fitting the experimental ACF to theoretical ACF's is used to find $T(H^+)/T(O^+)$. Data for two consecutive time periods are shown. Circles and x's are the same as in Figure 5.10.

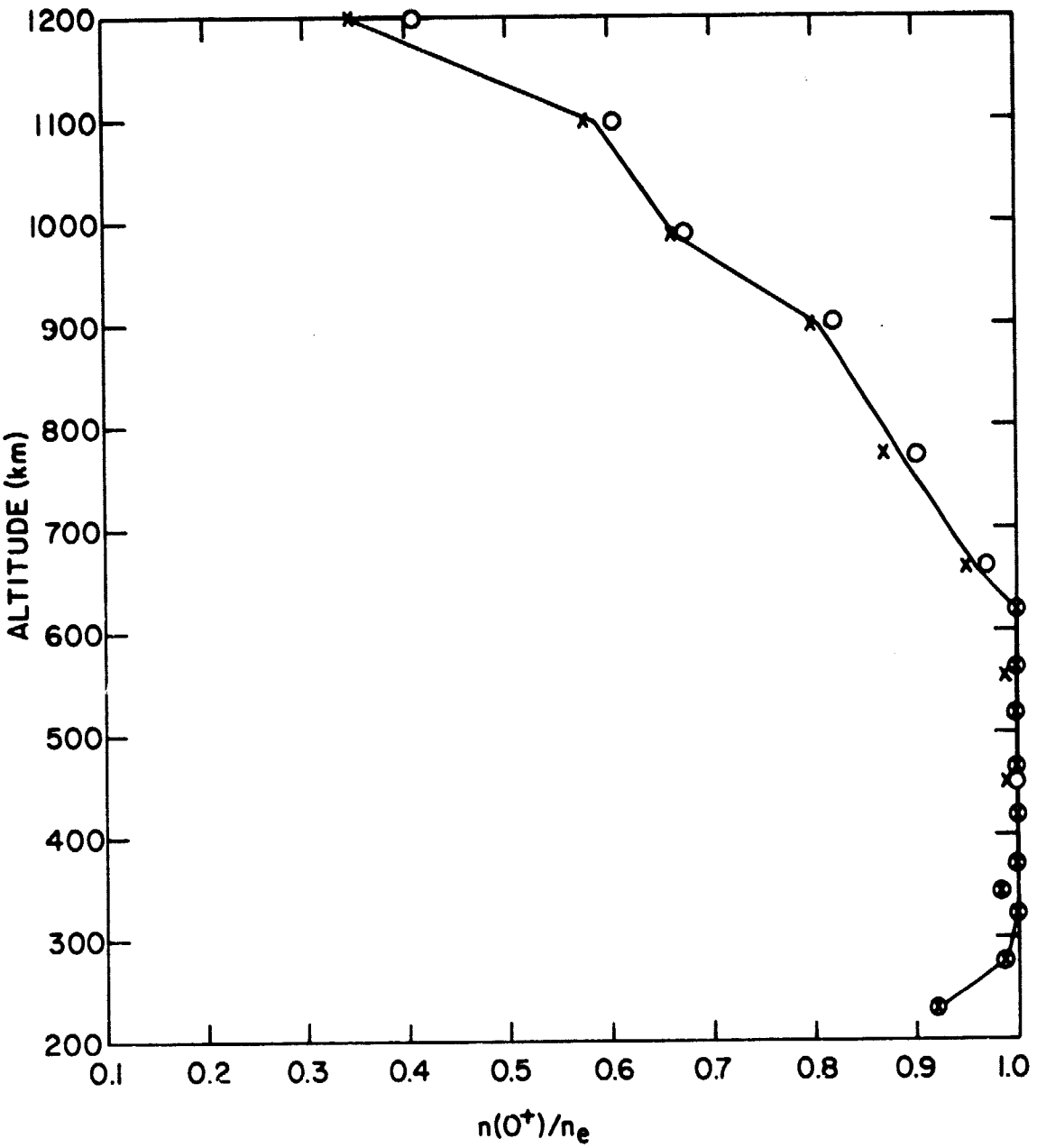

Figure 5.12 Profile of $n(O^+)/n_e$ for Feb. 24, 1972 from 7:57 to 8:24 AM. Data represents two consecutive time periods. Circles are for 7:57 to 8:10. ×'s are for 8:10 to 8:24.

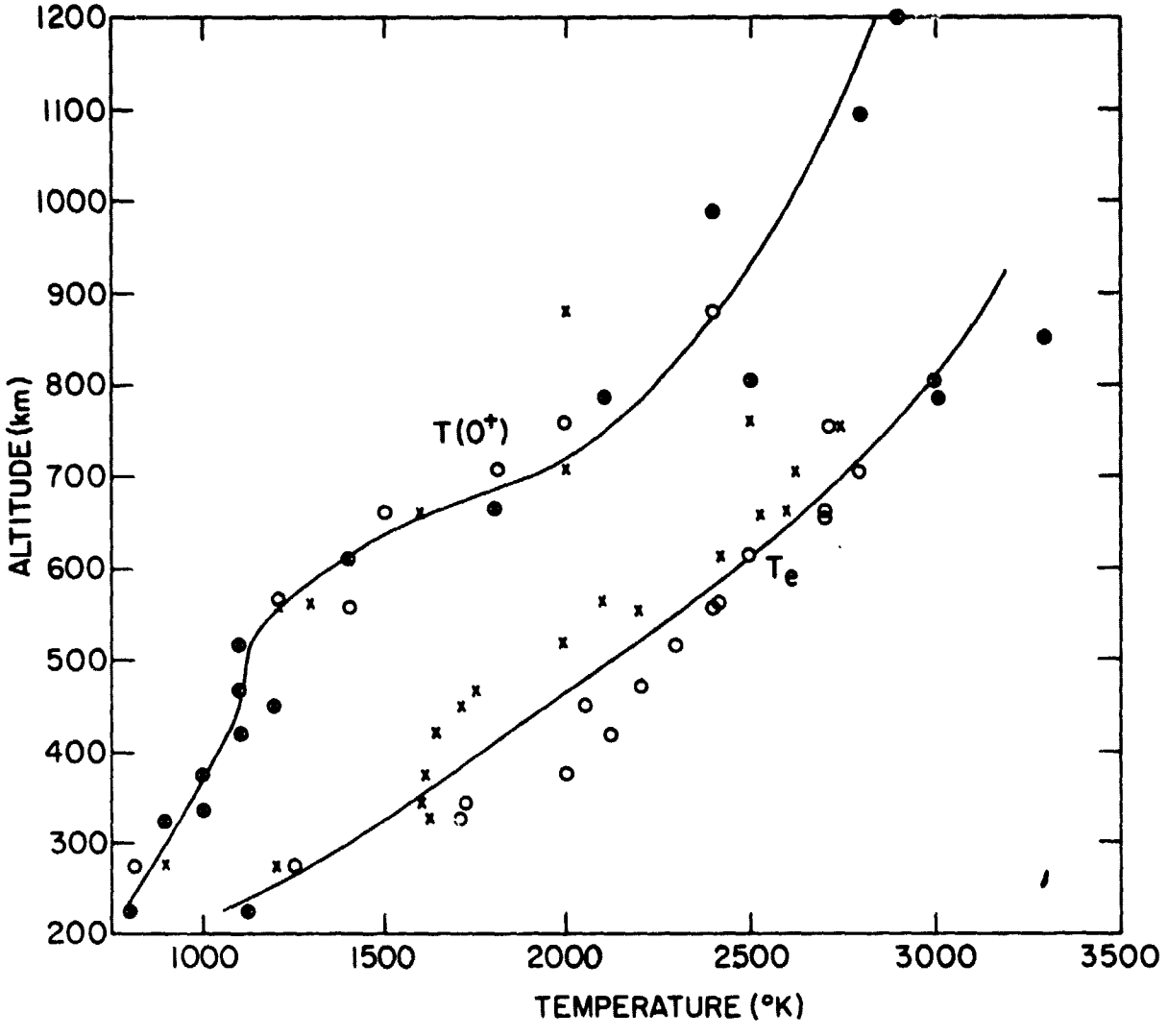

Figure 5.13 $T(O^+)$ and T_e for Feb. 24, 1972 from 7:57 to 8:24 AM. Data represents two consecutive time periods. Circles and ×'s are the same as in Figure 5.12.

constant with altitude and much less than during the day (see Figure 5.8). So, at dawn the ion and electron temperatures must change as a result of solar radiation creating photoelectrons which in turn heat the ambient electrons. One can expect rapid changes immediately after dawn with more gradual or slower changes into the morning. Therefore, the heat transferred to the electron and ions could be changing more at 8:00 AM than at 9:00 AM. Even though the changes are slight this probably is the reason why the errors of Figure 5.13 are larger than those of Figure 5.10.

Although the errors of Figure 5.13 are larger than those of Figure 5.10, Figure 5.13 still gives a good picture of the profiles of $T(O^+)$ and T_e. In fact the profiles of Figure 5.13 are similar to the profiles of Figure 5.10. $T(O^+)$ in both Figures 5.10 and 5.13 is approximately 1000 K up to 500 km. From 500 km to 700 km $T(O^+)$ increases rapidly to 2000 K. Above 700 km the gradient of $T(O^+)$ decreases gradually until it is about 1 K/km at 1200 km. T_e in both Figures 5.10 and 5.13 starts at 1000 K at 230 km and increases steadily to 2500 K at 600 km. At 900 km T_e is approximately equal to 3000 K in both Figures 5.10 and 5.13.

In Figure 5.14 the ratio $T(H^+)/T(O^+)$ is shown for the same data used for Figures 5.12 and 5.13. The maximum of $T(H^+)/T(O^+)$ occurs at about 550 km and is approximately 1.4. There are substantially large values of $T(H^+)/T(O^+)$ from 450 to 770 km. As in Figure 5.11, $T(H^+)/T(O^+)$ again falls off to 1.0 at low and high altitudes.

5.5 *Summary*

The results given in this chapter apply to data taken at the Arecibo Observatory in Puerto Rico. There are two methods used to reduce the data: 1) fitting the parameters of the ACF and 2) fitting the entire ACF. These methods are described in Section 5.2. There are five physical quantities

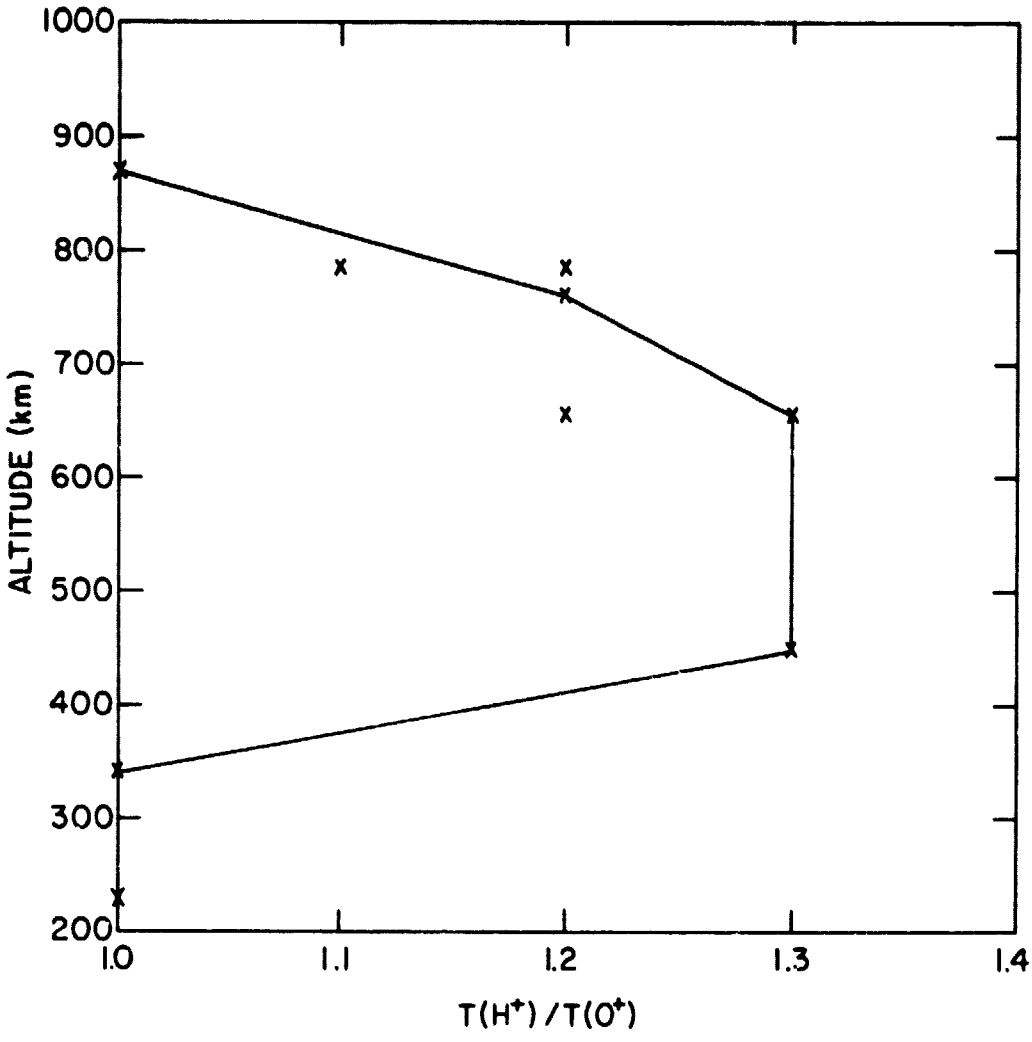

Figure 5.14 $T(H^+)/T(O^+)$ for Feb. 24, 1972 from 7:57 to 8:24 AM. Data represents two consecutive time periods.

which can be reduced from this analysis. They are n_e, $n(O^+)$, $T(O^+)$, $T(H^+)$, and T_e where n_e is assumed to equal $n(O^+)$ plus $n(H^+)$. The quantities n_e and $T(O^+)$ can be found directly from this analysis. The other quantities are found by first computing $n(O^+)/n_e$, $T(H^+)/T(O^+)$, and $T_e/T(O^+)$.

In Section 5.3 the results of n_e and $n(O^+)/n_e$ are discussed and it was determined that n_e and $n(O^+)/n_e$ can be found very accurately. Figures 5.2 and 5.3 show that $n(O^+)/n_e$ could be computed to within ±.05 even if $T(O^+)$ is not known. If $T(O^+)$ is known then $n(O^+)/n_e$ could be calculated with errors less than .01. The determination n_e is less accurate than the determination of $n(O^+)/n_e$ because n_e depends on an accurate measurement of $T_e/T(O^+)$. In the topside ionosphere $T_e/T(O^+)$ is generally between one and three, so n_e can be found within a factor of 2. Usually $T_e/T(O^+)$ is calculated to within ±.1 or less so n_e can be computed with a relative error less than 4 percent.

In Section 5.4 results of ion and electron temperatures are discussed. It was determined the profiles of $T(O^+)$ and T_e were reliable and fairly accurate because of the general agreement of the profiles for both methods used (see Figures 5.9 and 5.10). Using a library of theoretical ACF's and fitting the experimental ACF to the best theoretical ACF it was determined that $T(O^+)$ and T_e could be calculated to within ±100 K (Figures 5.10 and 5.13). The fact that the results of one 12-minute time period are almost exactly the same as the results of the next 12-minute time period (Figures 5.10 and 5.13) indicates that the accuracy of these results is very good. The general agreement between Figures 5.10 and 5.13 and between Figures 5.11 and 5.14 suggests that these results are typical of morning data because two different days are represented. These days include both quiet (Feb. 10, 1972) and disturbed (Feb. 24, 1972) magnetic activity.

Figures 5.11 and 5.14 show the ratio $T(H^+)/T(O^+)$ can have significantly large values in the altitude region between 350 and 700 km. This means that $T(H^+)$ can be significantly larger than $T(O^+)$ in this altitude region with the maximum difference occurring near 550 km. Although the accuracy of the values of $T(H^+)/T(O^+)$ given in Figures 5.11 and 5.14 isn't too good it is certain that $T(H^+)$ is larger that $T(O^+)$ in the altitude region between 350 and 700 km. The larger values of $T(H^+)$ has an effect on the $T(O^+)$ profile because $T(O^+)$ approaches the neutral temperature at 500 km rather than at 600 km. Analysis of the ion and electron temperatures based on the energy balance equations is given in Chapter 6.

6. ION AND ELECTRON TEMPERATURES FROM THE ENERGY BALANCE EQUATIONS

6.1 *Introduction*

During the past 15 years some progress has been made in describing the ion temperature and electron temperature structure in different regions of the magnetosphere. By equating the electron-ion heating rate with the loss of energy of the ions to neutrals, *Hanson* [1963] was the first to show that the oxygen ion temperature profile depends heavily on the altitude. His results show that the ion temperature increases gradually from the neutral gas temperature at 300 km towards the electron temperature above 800 km. *Dalgarno et al.* [1963] investigated the effect of solar ultraviolet radiation on the rate of heating of the ambient electrons and found that the electron temperature reaches a maximum temperature near 200 km at noon in a quiet ionosphere. *Geisler and Bowhill* [1965] developed a theory of nonlocal heating of the topside ionosphere and the protonosphere by photoelectrons which escape the F_2 layer. They found that the electron temperature has a steep temperature gradient at altitudes less than 1000 km for sunspot maximum conditions. The effect of oxygen cooling on ionospheric electron temperature has been reported by *Dalgarno et al.* [1968] who found that the inclusion of electron cooling by excitation of the fine-structure levels of atomic oxygen removes the discrepancy between Thomson scatter data and theoretically predicted electron temperatures above 320 km. The influence of the ion thermal conductivity has been studied by *Banks* [1967b] and *Sanatani and Hanson* [1970]. Their calculations of the ion temperature resulted in an ion temperature significantly less than the electron temperature at high altitudes. In the studies by *Banks* [1967b] and *Sanatani and Hanson* [1970] the electron temperature was assumed to be constant above a certain altitude.

Theoretical profiles of temperature for different model neutral atmospheres and different ion and electron density models are computed from the basic steady state energy balance equations for ions and electrons described in chapter three. In the following sections results of these calculations are discussed. Also, in this chapter the effect of photoelectron heating on electron temperatures will be examined. The importance of thermal conduction in both the electron and ion energy balance equations will be studied too. Other topics studied in this chapter are the effect of temperature gradients at the upper boundary and the effect of various elastic and nonelastic energy transfer processes on electron and ion temperatures.

6.2 *Numerical Methods*

The electron, O^+, and H^+ energy balance equations are coupled differential equations which are second order in z (height). These equations cannot be solved analytically, so numerical methods must be used to find the solution. In order to find the suitable method among the possible methods available, one employs a trial and error procedure. A method which works on one equation under certain conditions may not work on the other equations. For example, a triple diagonal mesh method (which will be explained later) is effective in solving the ion energy balance equation, but not the electron energy balance equation. Thus, one must search for the best method to numerically solve each energy balance equation.

6.2.1 *The triple diagonal mesh method.* The numerical method known as the triple diagonal mesh method is used to solve the ion energy balance equation when thermal conduction is included as an energy transfer term. It was used by *Banks* [1967b] to solve for the ion temperature profile under restrictive conditions. In the following analysis, a modification of the basic

procedure of *Banks* [1967b] is used.

Banks [1967b] assumed a single ion temperature and an electron temperature that was constant with altitude. Also, he assumed a zero temperature gradient as the upper boundary condition. These assumptions are modified in this study so that the O^+ and H^+ ion temperature profiles can be found. An electron temperature profile from the electron energy balance equation is used. Also, the upper boundary condition is modified so that a variable temperature gradient can be used.

The steady-state ion energy balance equation is

$$-\sin^2 I \frac{\partial}{\partial z} K_i \frac{\partial T_i}{\partial z} = P(e\text{-}i) - L(i\text{-}n) - C(i\text{-}j) \tag{6.1}$$

where I is the magnetic dip angle, K_i is the ion thermal conductivity, $P(e\text{-}i)$ is the energy transfer between electrons and ions, $L(i\text{-}n)$ is energy transfer between ions and neutrals, $C(i\text{-}j)$ is the energy transfer between one ion and other ion species, i is a subscript for the ion species (O^+ or H^+), and j is a subscript denoting the other ion species.

The ion thermal conductivity K_i for a single ion gas is

$$K_i = 4.6 \times 10^4 (T_i^5/A_i)^{1/2} / [1 + 3.22 \times 10^4 (T_i^2/n_i) \Sigma n_n \bar{Q}_D] \text{ eV cm}^{-1} \text{ sec}^{-1} \text{ K}^{-1} \tag{6.2}$$

Substituting $\theta = T_i^{7/2}$ in the energy balance equation gives

$$\frac{\partial^2 \theta}{\partial z^2} = f_1(z,\theta) \tag{6.3}$$

where $f_1(z,\theta) = -7 \, (P(e\text{-}i) - L(i\text{-}n) - C(i\text{-}j))/(2F_i \sin^2 I)$

and $F_i = 4.6 \times 10^4/A_i^{1/2} \, [1 + 3.22 \times 10^4 (T_i^2/n_i) \Sigma n_n \bar{Q}_D]$

If one assumes that

$$\theta(z) = g(z) + \Delta(z) \tag{6.4}$$

where $g(z)$ is known from a previous iteration or initial conditions and $\Delta(z)$ is a difference quantity, equation (6.3) can be put in a numerically solvable form after linearization of $f_1(z,\theta)$. Linearization of $f_1(z,\theta)$ gives

$$f_1(z,\theta) = f_2(z,g) + f_3(z,g) \tag{6.5}$$

where $f_2(z,g)$ and $f_3(z,g)$ are function which depend on the energy production and loss rates and factors of the order of Δ^2 and higher are neglected. Using and (6.5) with (6.3) one gets

$$\frac{\partial^2 \Delta}{\partial z^2} = f_2(z,g) + f_3(z,g)\Delta - \frac{\partial^2 g}{\partial z^2} \tag{6.6}$$

Applying central difference formulas to (6.5) results in

$$\Delta_{j+1} + B_j \Delta_j + \Delta_{j-1} = D_j \tag{6.7}$$

where $B_j = -2 - f_3(z,g)\ \delta^2$

$$D_j = f_2(z,g)\ \delta^2 - (g_{j+1} - 2g_j + g_{j-1})$$

δ is the altitude step size (5 km), and the j's refer to integration steps extending from $j = 0$ to a maximum value, $j$max.

Since (6.3) is a second order differential equation one needs two boundary conditions. The first boundary condition is that the ion temperature is equal to the neutral temperature at an altitude of 200 km. This gives $\Delta_0 = 0$. The second boundary condition is that the ion temperature profile has a temperature gradient at an altitude of 1200 km of $\partial T_i/\partial z\big|_{1200}$. Typical experimental values of $\partial T_i/\partial z\big|_{1200}$ lie between 0 and 2 K/km. This gives

$$\Delta_{j\max+1} = \Delta_{j\max} + 7/2 \quad g_{j\max}^{5/7}\ \partial T_i/\partial z\big|_{1200} \tag{6.8}$$

Since (6.7) is in the triple diagonal form, the solutions for the Δ_j are found by first calcuiating mesh coefficients K_j and L_j for $j = 0$ to $j$max according to

$$K_1 = \frac{D_1 - \Delta_0}{B_1} \qquad L_1 = \frac{1}{B_1} \tag{6.9}$$

$$K_j = \frac{D_j - K_{j-1}}{B_j - L_{j-1}} \qquad L_j = \frac{1}{B_j - L_{j-1}}$$

Then one works downward from $j = j$max to $j = 1$ using the relation

$$\Delta_{j-1} = K_{j-1} - L_{j-1}\,\Delta_j \tag{6.10}$$

with

$$\Delta_{j\max+1} = \frac{(g_{j\max} - g_{j\max+1} + K_{j\max} + 17.5\,\partial T_i/\partial z\,\big|\,1200\,g_{j\max}^{5/7})}{(1 + L_{j\max})} \tag{6.11}$$

The iterative solutions for θ (and T_i) are found by using equations (6.7) - (6.11) to find Δ_j which is added to the previous value of g_j. The initial function g is found from the temperature profile which neglects the thermal conduction effects. The iteration process is continued until all the Δ_j's are essentially zero. The final function g is the equivalent to θ which gives the steady-state ion temperature profile. The convergence of the iteration process is rapid with the ratio $\left|\Delta_j/g_j\right|$ for all the j's reaching 10^{-4} after four repetitions of the process.

The profiles for each ion temperature are found by solving for $T(H^+)$ using the triple diagonal mesh method where $T(O^+)$ is set equal to the ion temperature where a single ion temperature is assumed. Then, the triple diagonal mesh method is used again with $T(H^+)$ given from the previous step to solve for $T(O^+)$. The procedure is continued until there is no change in either the $T(O^+)$ or the $T(H^+)$ profile. It generally takes four repetitions

of this iteration process to get convergence of both O^+ and H^+ temperature profiles.

6.2.2 *Modified Newton's method.* A modified Newton's method is used to solve for the ion temperature profiles when thermal conduction effects are ignored. Thus, the ion temperature is calculated using a formula of the form

$$x_{i+1} = x_i - \alpha f(x_i)/f'(x_i)$$

where x is the ion temperature, α is a modification factor, $f(x)$ is the right side of equation (6.1), and $f'(x)$ is the derivative of $f(x)$ with respect to x.

To find the O^+ and H^+ temperature profiles, it is first necessary to find the single-ion temperature profile. Next, the H^+ temperature profile is found, followed by the O^+ temperature profile. Finally, the process of finding the H^+ temperature profile and then the O^+ temperature profile is repeated until the respective profiles converge.

6.2.3 *Integration of the energy balance equation.* The electron energy balance equation is integrated numerically to solve for the electron temperature profile. The integrated steady state energy equation is

$$\sin^2 I \, K_e \frac{dT_e}{dz} = \int_z^\infty (Q - L) \, dz \qquad (6.12)$$

where Q is the heat input through photoelectron heating of electrons, L is the heat lost by Coulomb, elastic, and nonelastic collisions with ions and neutral particles, and K_e is the thermal conductivity of the electron gas given in equation (3.86).

The upper limit of the integral in equation (6.12) is infinity. This is the result of using the assumption of open field lines or flat earth. In other words, the field lines are parallel out to infinity. This is a very good approximation in the altitude region below 1200 km. The integral is

not actually integrated to infinity. The upper boundary condition gives the value of the integral from 1200 km to infinity. This is done by setting the value of the integral from 1200 km to infinity equal to the left side of equation (6.12) where the upper boundary condition is on dT_e/dz.

The lower boundary on T_e is that thermal conduction is unimportant below 200 km. That is, thermal conduction is negligible compared to heating by photoelectrons or cooling by neutral particles.

The electron temperature profile is found by adopting a trial value of T_e at 1200 and integrating equation (6.12) downward in a stepwise fashion (in 5 km steps). The temperature gradient, dT_e/dz, is determined from equation (6.12). The energy equation is used to calculate the second derivitive of T_e, d^2T_e/dz^2, where the value of dT_e/dz from equation (6.12) is used. The electron temperature at the next lowest altitude is found by using a Taylor expansion

$$T_e(z - \Delta z) = T_e(z) - \left.\frac{dT_e}{dz}\right|_z \Delta z - \frac{1}{2}\frac{d^2T_e}{dz^2}\Delta z^2 \qquad (6.13)$$

where $\Delta z = 5$ km. An appropriate value of T_e at the upper boundary will give a profile which satisfies the lower boundary conditions (see Section 6.4). The procedure for finding the electron temperature profile is summarized in Figure 6.1.

6.2.4 *Time relaxation method.* The time relaxation method is sometimes used for investigation of diurnal changes in ion and electron temperatures. It could also be used to calculate steady-state ion and electron temperatures.

The time relaxation method as described by *Da Rosa* [1966] involves solving the energy balance equation which can be written in the form for ions as

1. Input T_e at 1200 km

2. Integrate the heat source, loss terms

3. Find dT_e/dz

4. Find d^2T_e/dz^2

5. $T_e(z - \Delta z) = T_e(z) - \frac{dT_e}{dz}\,\Delta z - \frac{1}{2}\frac{d^2T_e}{dz^2}\,\Delta z^2$

6. Continue 1-5 until lower boundary condition is satisfied

Figure 6.1 Schematic diagram of the procedure for finding the electron temperature profile.

$$\frac{\partial T}{\partial t} = U(z,t,T)\,\frac{\partial^2 T}{\partial z^2} + V(z,t,T)\left(\frac{\partial T}{\partial t}\right)^2 + \omega(z,t,T) \qquad (6.14)$$

where $$U(z,t,T) = \left(\frac{3}{2} n_e k\right)^{-1} \sin^2 I\, K_i$$

$$V(x,t,T) = \left(\frac{3}{2} n_e k\right)^{-1} \frac{5}{2} \sin^2 I\, K_i$$

$$W(z,t,T) = \left(\frac{3}{2} n_e k\right)^{-1} \left(P(e - i) - L(i - n)\right)$$

Central difference formulas can be used to reduce equation (6.14) to

$$\frac{T_{i,j+1} - T_{i,j}}{\Delta t} = U_{i,j}\,\frac{T_{i+1,j} - 2T_{i,j} + T_{i-1,j}}{(\Delta z)^2}$$

$$+ V_{i,j}\,\frac{T_{i+1,j} - T_{i,j}}{\Delta z}^2 + W_{i,j} \qquad (6.15)$$

where i is the subscript for the height step, Δz;

j is the subscript for the time step, Δt;

and $U_{i,j} = U(i\Delta z,\ j\Delta t,\ T_i)$, etc.

The unknown $T_{i,j+1}$ can easily be found since all the other quantities in equation (6.15) are known. The height and time steps have to be chosen carefully so that the solution of the difference equation converges to the solution of the differential equation. Sometimes even if Δz and Δt approach zero there is no convergence (the values of T oscillate wildly with each iteration). The equation is then said to be unstable. The condition of stability as given by *Da Rosa* [1966] is

$$\max\,(U_{i,j})\,\frac{\Delta t}{(\Delta z)^2} < \frac{1}{2} \qquad (6.16)$$

This condition imposes strict restrictions on the steps Δz and Δt, and makes it impossible to solve the physical problem, as verified by the following example: if the electron number density is 10^4 cm^{-3} and the temperature is 1000 K, then with a height step of 20 km, the maximum time step is 0.1 seconds.

Even time intervals of one hour would take far too many iterations and also would render the solution meaningless by the accumulation of truncation and round-off errors.

Different schemes have been formulated to circumvent these difficulties, but care must still be taken in choosing the time step. Methods other than the time relaxation method were found to be easier to apply to this study, and had fewer difficulties.

If one is interested in the thermal response to changing electron number density or varying photoelectron-thermal electron heating one would probably take the extra care in employing the time relaxation method. Fortunately, this study involves the solution of the steady-state ion and electron energy balance equations which can more easily solved by methods described in Sections 6.2.1, 6.2.2, and 6.2.3.

6.3 *The Effect of the Electron and Ion Number Densities on the Electron and Ion Temperature Profiles*

In this section several different models of the electron and ion number density profiles corresponding to different atmospheric conditions will be used to calculate electron and ion temperature profiles. In the two cases considered in this section, parameters other than number densities will be held constant. In the neutral atmospheric model used, the exospheric temperature is equal to 1000 K (*CIRA* [1972]; see Appendix A). Also a thermal-electron heating rate at a solar zenith angle, χ, of 0° from *Mantas* [1973] will be used (see Figure 3.3). The heating rate above 1000 km is assumed to have a constant value set equal to the heating rate at 1000 km.

The electron temperature profile is calculated by integrating the electron energy balance equation which includes thermal conduction. The boundary

condition at 1200 km is that the gradient of the electron temperature is 1 K/km. The lower boundary condition is that thermal conduction is unimportant at the altitude of 120 km. Below 120 km, the electron temperature profile is controlled by energy loss to the neutral gases, so that the electron temperatures are nearly equal to neutral temperatures.

The ion temperature profile is calculated using the triple diagonal mesh method. Thermal conduction is included in the ion energy balance equation. As in the case of the electron temperature profile, the upper boundary is applied at 1200 km and is that the gradient of the temperature is 1 K/km. The lower boundary condition is determined by the fact that thermal conduction is unimportant at altitudes below 200 km. The ion temperature is controlled by energy loss to the neutral gases at altitudes below 200 km. Thus, the ion temperature becomes equal to the neutral temperature near 200 km.

It is necessary to consider two cases depending on the electron and ion number densities. In the first case the effect of the magnitude of the electron number density on the temperature profiles is considered. Electron and ion temperatures (Figure 6.3) have been calculated with the electron number density equal to one, one half, and two times that shown in Figure 6.2. The O^+ plus H^+ number density shown in Figure 6.2 equal the electron number density of Figure 6.2. When the electron density is twice and one half that shown in Figure 6.2 $n(O^+)$ is found by calculating $n(O^+)/n_e$ from Figure 6.2 and multiplying this by twice or one-half n_e. $n(H^+)$ is found by subtracting $n(O^+)$ from n_e.

When the electron number density is smallest, the electron temperature is largest. Also, the separation between the electron and ion temperatures increases as the electron number density decreases. This is the result of

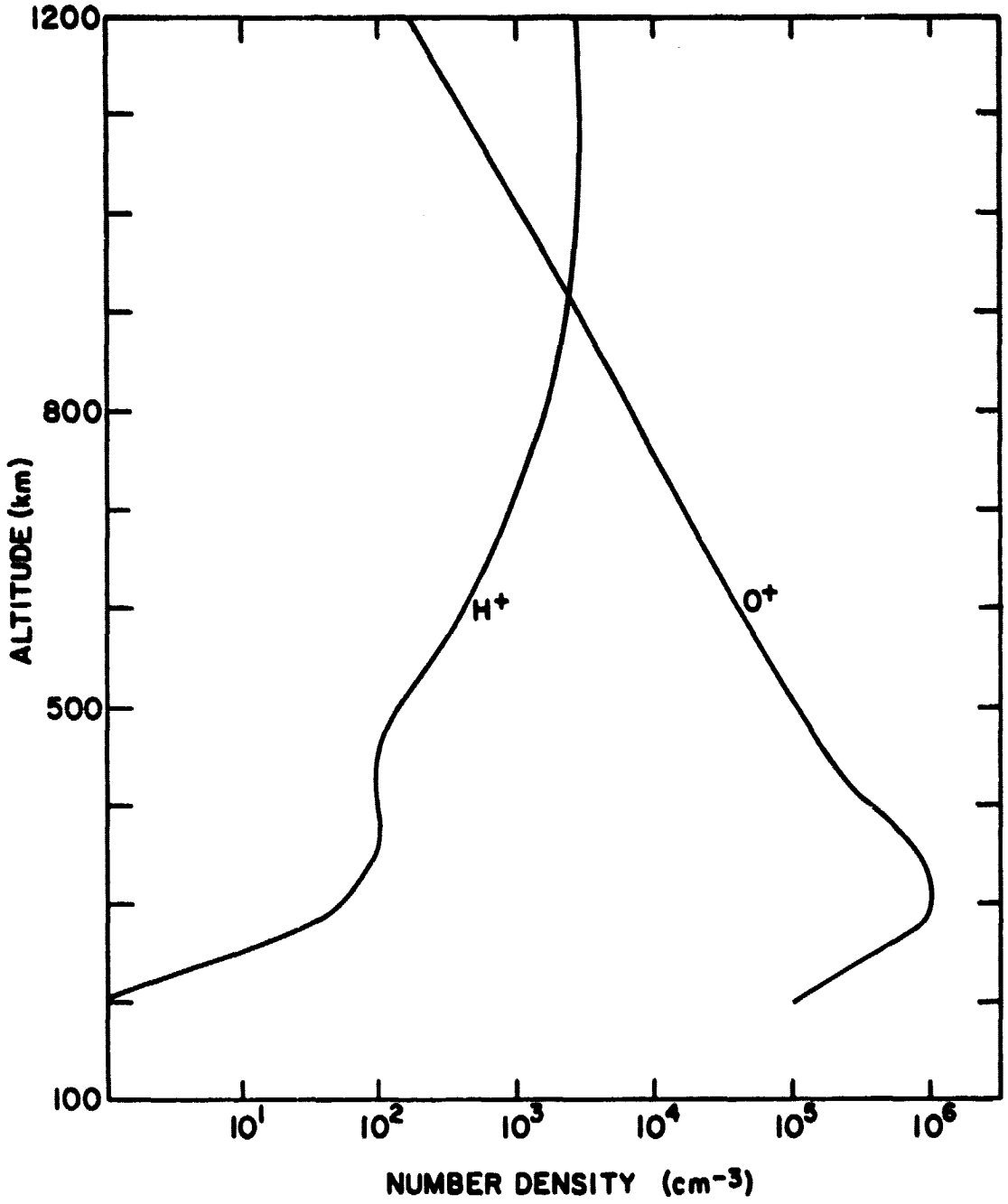

Figure 6.2 Electron, O^+, and H^+ number density profiles used in the calculation of T_i and T_e in Figure 6.3.

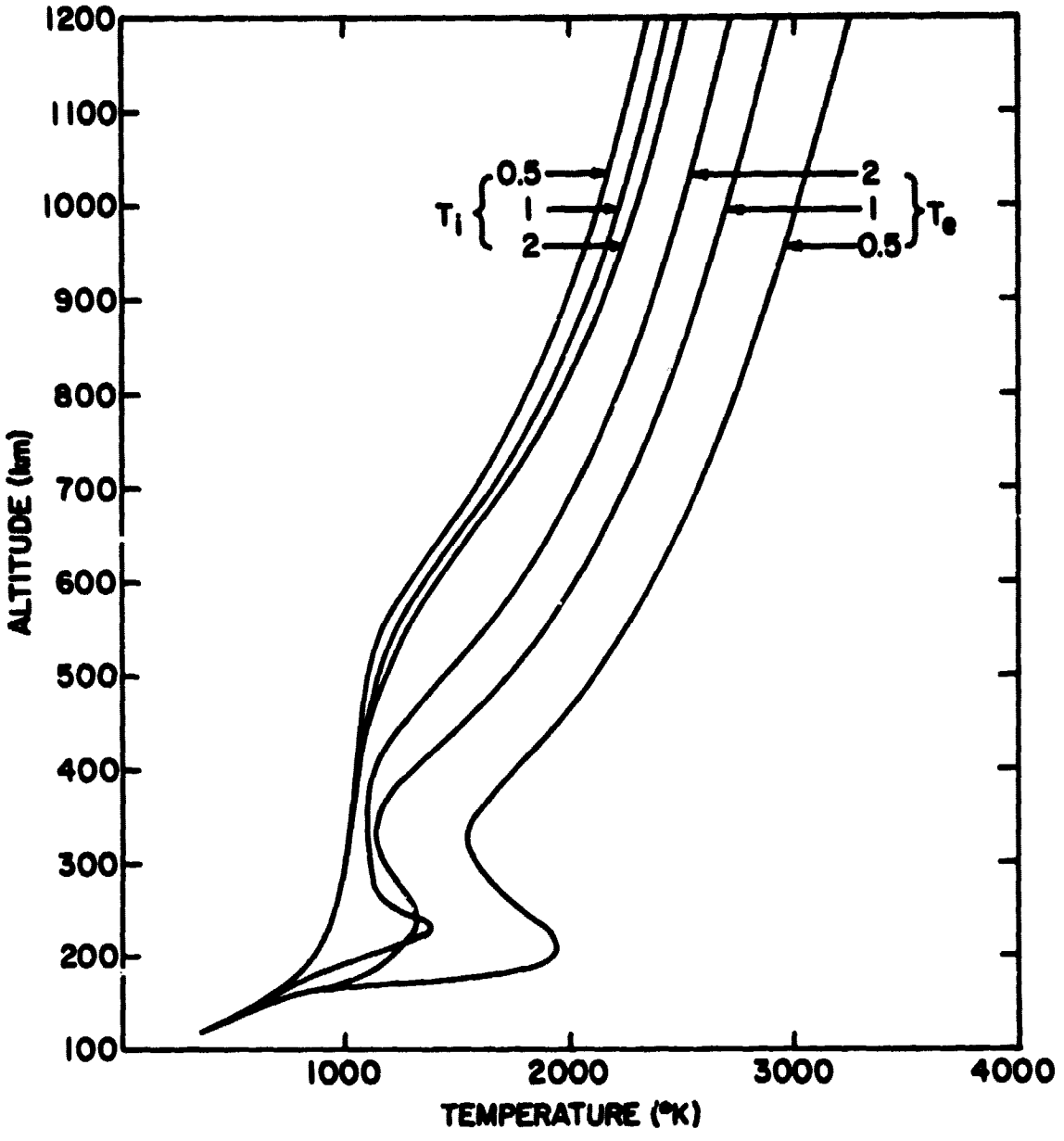

Figure 6.3 T_e and T_i profiles for $\chi = 0°$ and different electron density profiles. 1 refers to the profile in Figure 6.2. 2 refers to 2 times that profile. ½ refers to 0.5 that profile.

two factors. First, the heating of the ions depends on both n_e^2 and $T_e^{-3/2}$; as n_e decreases and T_e increases the heating of the ions remains relatively unchanged. Second, the effect of the electron density on the ion temperature profile is not as great as its effect on the electron temperature profile. While the electron density determines the magnitude by which electron energy is lost to other particles, the electron density is important in both ion energy production and loss.

In the second case the effect of ion number density profiles on electron and ion temperatures is considered (Figure 6.5). In Figure 6.4, the ion number density profiles used to calculate the temperature profiles of Figure 6.5 are shown. Two examples are used to show the effect on electron and ion temperatures when O^+ dominates at all altitudes and when H^+ becomes the predominant ion at a low altitude. These two examples illustrate the effect of Coulomb collisions on electron and ion temperatures.

Since H^+ has a larger energy transfer rate than O^+, the ion temperatures are higher when H^+ is the dominant ion than when O^+ is the dominant ion. This is indeed the case, as is shown in Figure 6.5. Also, since the electron number density is essentially the same at altitudes near 1200 km, the electron temparature profiles A and B are almost identical. Therefore, the species of ion present has very little effect on the electron temperature profile at 1200 km.

Most of the effect of changing the ion density profiles is felt in the ion temperature profiles. Since the ion density profiles change from night to day there will be changes in the ion temperature profiles from this factor alone.

The O^+ ion density is dominant at all altitudes between 200 and 1200 km

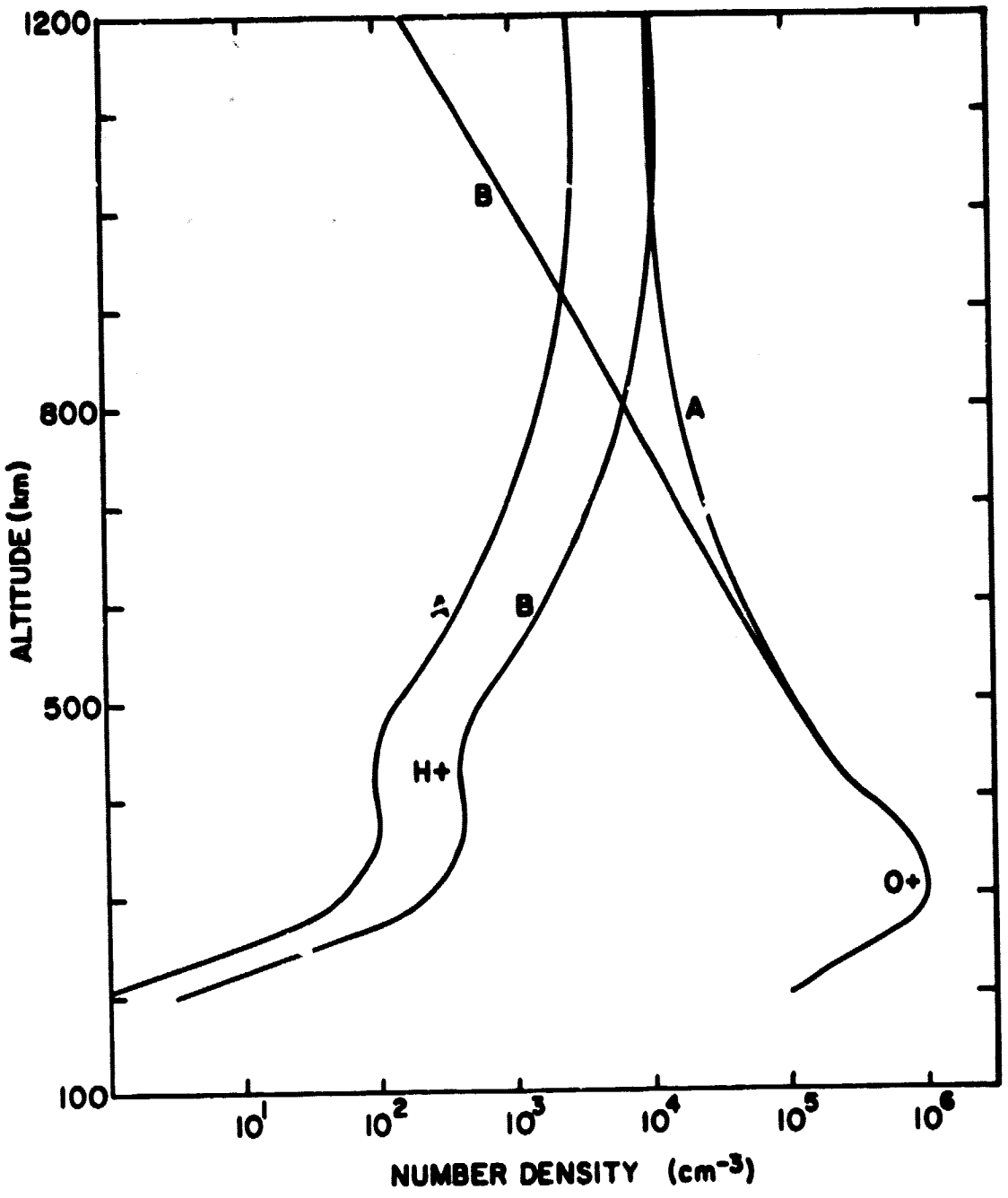

Figure 6.4 Ion number density profiles used in Figure 6.5.

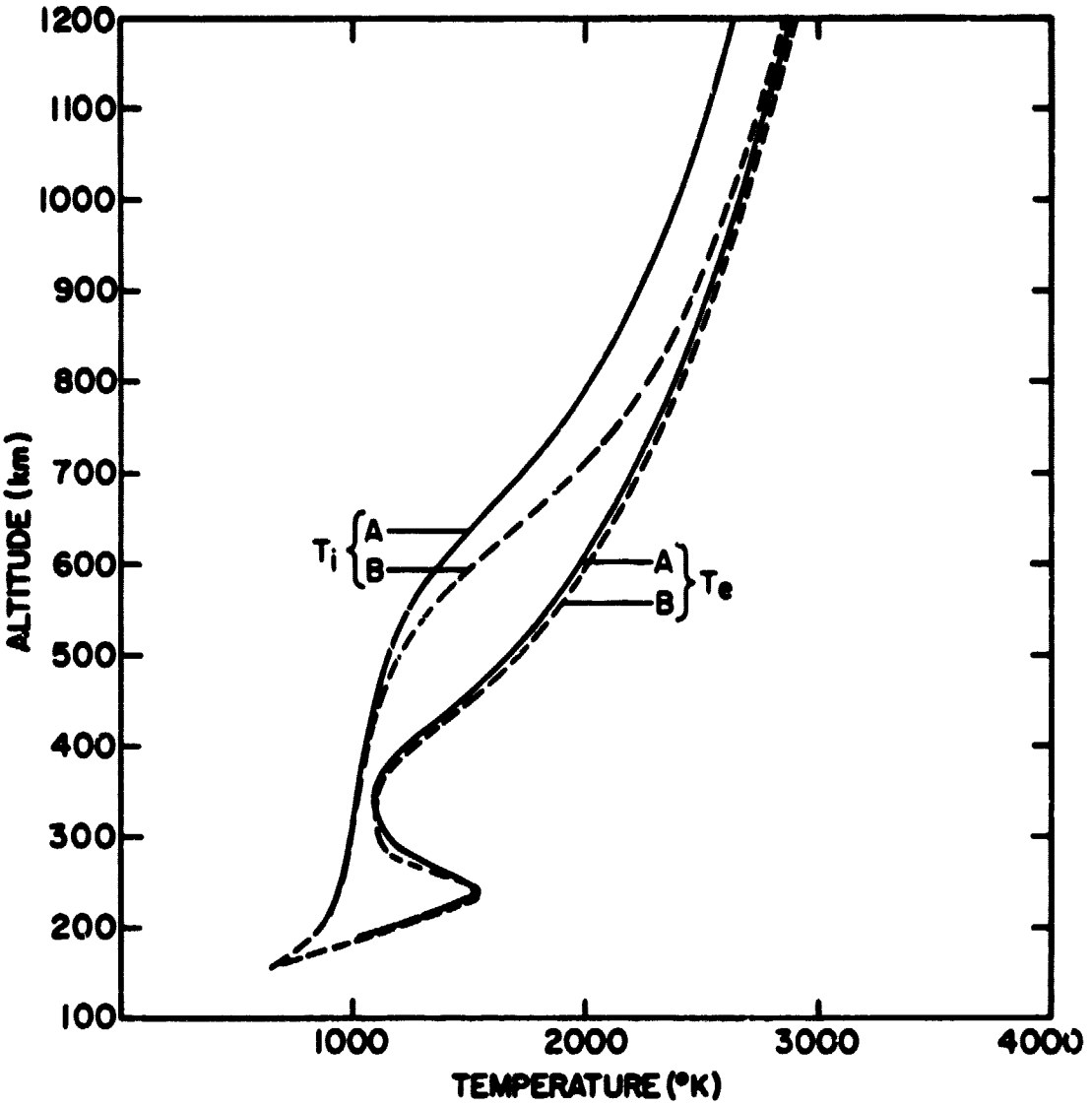

Figure 6.5 Ion and electron temperature profiles for different ion number density profiles. The A and B temperature profiles were calculated using the respective A and B ion density profiles of Figure 6.4.

during the day. This corresponds to profile A in Figure 6.4. At night there is no photoionization source for O^+ ions, but inward flow of H^+ ions and accidentally resonant charge exchange acts as a source of ionization for O^+ ions. Thus, there are substantial O^+ ion densities at night, although H^+ becomes important at lower altitudes. This corresponds to profile B in Figure 6.4. The nighttime profiles of the electron and ion temperatures are discussed in the next section.

6.4 *Changes for the Ion and Electron Temperature Profile from Night to Day*

The electron and ion energy balance equations can be solved for the case where no solar radiation is received. This implies that photoelectrons are no longer being produced. Before dawn and after dusk the ambient electrons can be heated by photoelectrons which originate in the conjugate ionosphere. This occurs if the conjugate ionosphere is still sunlit. During the night there are no photoelectrons, so by neglecting the heating of ambient electrons by photoelectrons, nighttime ion and electron temperature profiles can be calculated. Throughout this section the neutral atmosphere model is CIRA 1972 with T_∞ = 1000 K.

In Figure 6.6, the effect of zero heating of the ambient electrons on the electron temperature profile is shown. This case also uses the ion density profiles shown in Figure 6.4 (profile A). The electron temperature profile has been calculated using thermal conduction in the energy balance equation with upper and lower boundary conditions as discussed in Section 6.3 using the method described in Section 6.2.3. A fixed ion temperature is used. The most significant effect of zero heating of ambient electrons is that the electron temperature profile becomes equal to the ion temperature profile at 400 km and below as shown in Figure 6.6. There is no maximum

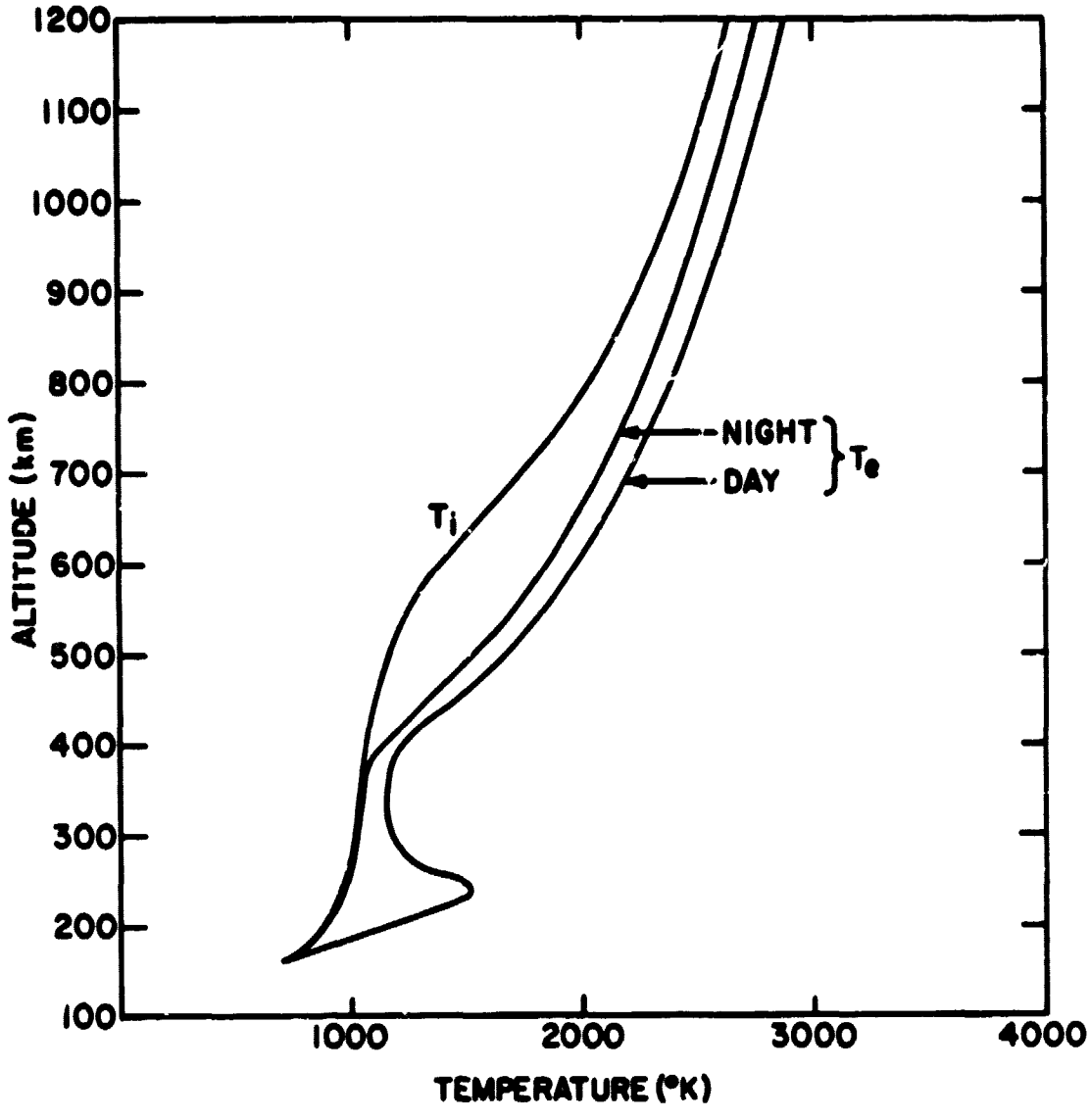

Figure 6.6 Electron temperature profiles for night and day where the upper boundary condition is $\partial T_e/\partial z = 1$ K/km for both night and day. The ion number densities used to calculate T_e are shown in Figure 6.4 A.

of the electron temperature at 250 km, as there is in the daytime electron temperature profile. At higher altitudes the electron temperature is less at night than during the day, but it is still greater than the ion temperature. This is the result of heat flux by thermal conduction from the higher altitudes. The biggest differences between the electron and ion temperatures occur between 500 and 700 km. This is because while ion-neutral energy transfer controls the ion temperature profile at higher altitudes, electron-neutral energy transfer becomes important at a lower altitude than the ion-neutral energy transfer.

The electron temperature profile for the case where the ion densities are given by profile B in Figure 6.4 is shown in Figure 6.7. The lower and upper boundary conditions are the same as the previous example. In this case the ion temperature profile also is calculated using the method described in Section 6.2.1. As in the previous case the electron temperature is equal to the ion temperature below 400 km. The difference between the ion and electron temperatures is largest near 550 km. The ion temperature is still less than the electron temperature up to 1200 km. The electron temperature is equal to the ion temperature only in the region below 400 km.

During the night it is possible that the temperature gradients at the upper boundary may be reduced from those during day. In Figure 6.8 the upper boundary conditions for the ion and electron temperatures are that the temperature gradients are zero and 0.5 K/km respectively. The lower boundary conditions are the same as the previous example and the ion densities are given by profile B in Figure 6.4. The ion and electron temperatures in Figure 6.8 are reduced more than 1000 K at altitudes near 1200 km than those in Figure 6.7. Also, in Figure 6.8 the electron temperature profile is approximately equal to the ion temperature profile at all altitudes. The electron

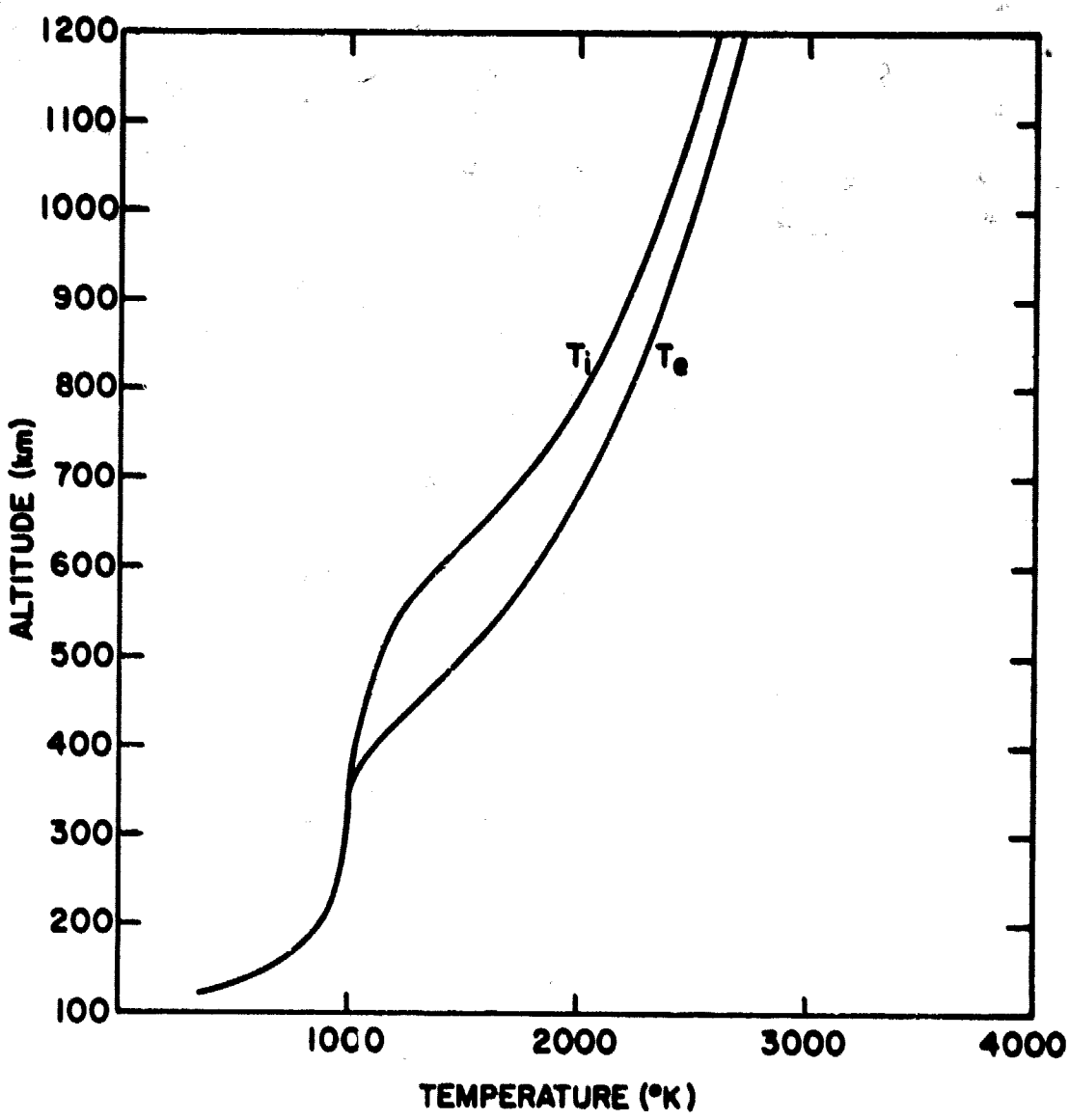

Figure 6.7 Electron temperature profile for night where the upper boundary condition is $\partial T_e/\partial z = 1$ K/km. The ion number densities used to calculate T_e are shown in Figure 6.4 B.

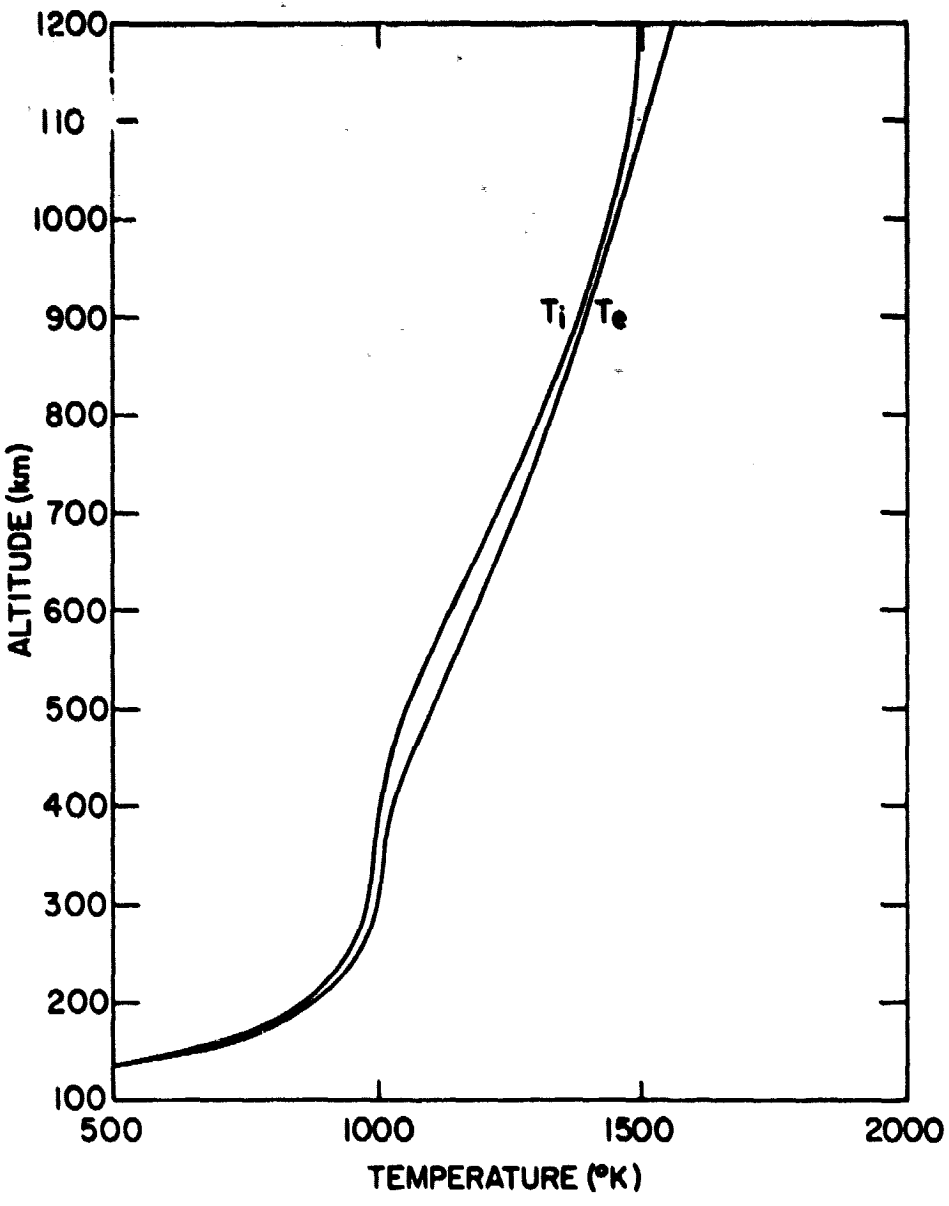

Figure 6.8 Electron and ion temperature profiles for nighttime where the upper boundary conditions are $\partial T_e/\partial z = 0.5$ K/km and $\partial T_e/\partial z = 0$. The ion density profiles are shown in Figure 6.4 B.

and ion temperature profiles increase slowly from 1000 K at 400 km to 1500 K at 1200 km. Therefore, if the temperature gradients at the upper boundary are zero, the electron and ion temperatures increase only 500 K above the neutral temperature (Figure 6.8); whereas, if the temperature gradients at the upper boundary are 1 K/km, the electron and ion temperatures increase more than 1500 K above the neutral temperature (Figure 6.6 and 6.7).

6.5 *The Effect of Inelastic Collisions on the Electron Temperature Profile*

Inelastic collisions of electrons with neutral particles are important as sinks of heat for electrons at altitudes below 400 km. Inelastic collisions were discussed in Section 3.7. Electrons can be cooled through rotational and vibrational excitation of N_2 and O_2. Another important sink of heat for electron is the fine structure excitation of O. These inelastic collisions control the electron temperature profile at the lower altitudes in the *F* region. They gradually become unimportant with increasing altitude due to decreasing neutral densities.

The importance of the various electron heat transfer processes is shown in Figure 6.9. These energy transfer rates were calculated using the *CIRA* [1972] neutral atmosphere model with T_∞ = 1000 K, the ion density profiles given in Figure 6.4 profile A, and the electron and ion temperature profiles given in Figure 6.10 profile B. Curve 1 in Figure 6.9 is the cooling due to electron-ion Coulomb collisions. Curve 2 is the cooling due to electron-neutral elastic collisions. Cooling through vibrational excitation of N_2 and O_2 is shown in curve 3. Cooling through rotational excitation of N_2 and O_2 is shown in curve 4. Curve 5 represents the cooling through fine structure excitation of O. Curve 6 is the heating of thermal electrons by photoelectrons. In curve 7 energy transfer through thermal conduction is shown.

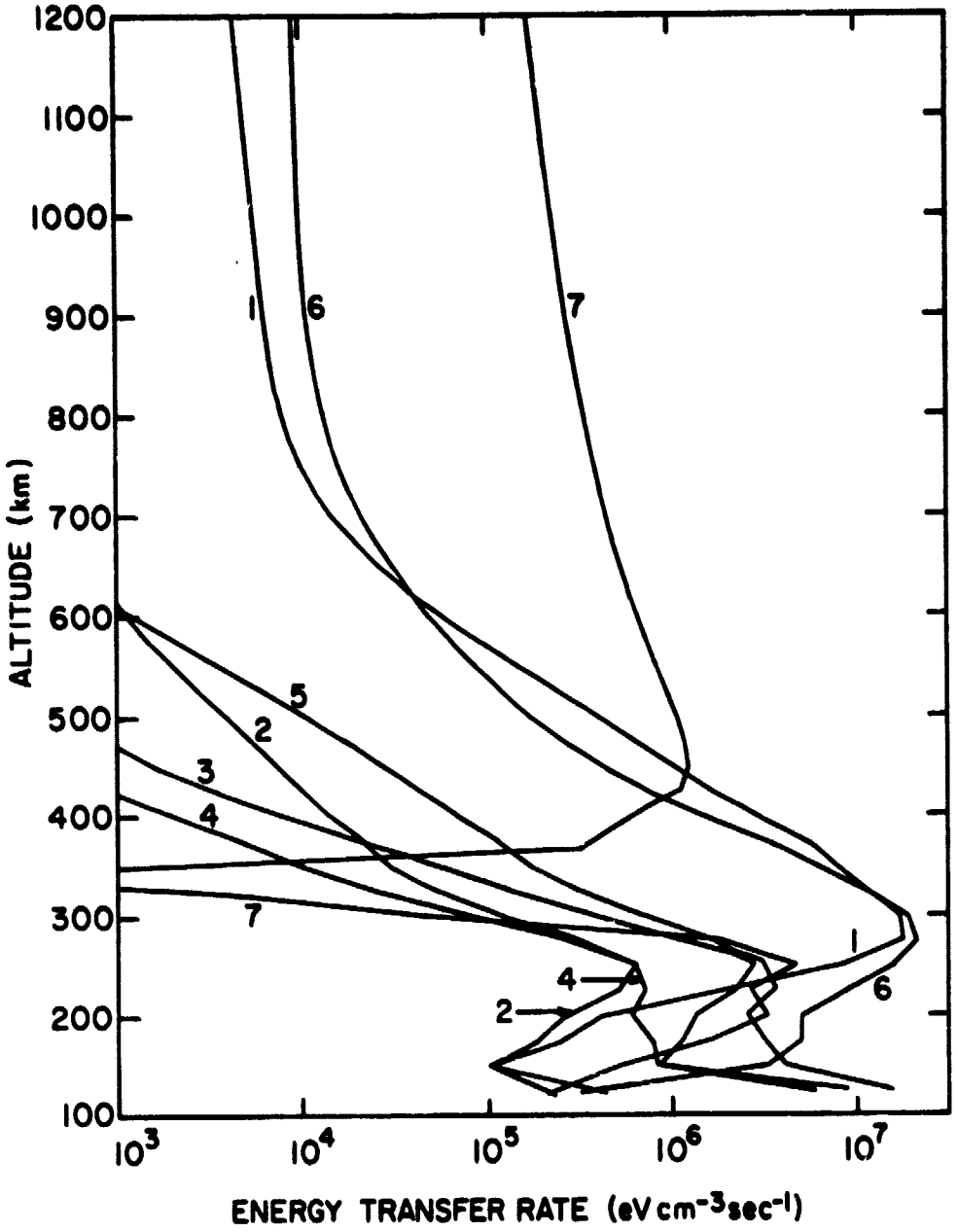

Figure 6.9 Electron energy transfer rates for all the heat transfer processes: 1 - cooling through electron-ion Coulomb collisions, 2 - cooling through electron-neutral elastic collisions, 3 - cooling through vibrational excitation of N_2 and O_2, 4 - cooling through rotational excitation of N_2 and O_2, 5 - cooling through fine structure excitation of O, 6 - heating of thermal electron by photoelectrons, 7 - energy transfer by thermal conduction.

Figure 6.9 illustrates that thermal conduction is the most important energy transfer process at altitudes above 400 km. Photoelectron heating of the ambient electrons and cooling through Coulomb collisions of electrons and ions are the only other significant energy transfer processes above 400 km. Below 400 km there are many important energy transfer processes. Photoelectron heating of the ambient electrons is important below 400 km while cooling through Coulomb collisions loses its importance at altitudes below 250 km. Figure 6.9 shows that elastic collisions are not important at any altitude. Inelastic collisions are important below 250. Cooling through fine-structure excitation of O and through vibrational excitation of N_2 and O_2 are the important inelastic cooling mechanisms.

The importance of inelastic collisions in controlling the electron temperature profile at altitudes below 400 km is illustrated in Figure 6.10. Ion density profiles found using profile A of Figure 6.4, the *CIRA* [1972] neutral atmosphere model with T_∞ = 1000 K, and the thermal-electron heating rate from Figure 3.3 with $\chi = 0°$ were used to calculate the electron temperature profiles shown in Figure 6.10. Inelastic collisions act to reduce the peak in the electron temperature profile near 250 km, as can be seen by the fact that profile B is less than profile A in Figure 6.10. Profile A is the electron temperature profile without including the effect of inelastic collisions in the electron energy equation, whereas profile B does include the effect of inelastic collisions. Thermal conduction is also important in reducing the peak of the electron temperature profile in both profiles A and B. As can be seen from Figure 6.9 photoelectron heating is the important source of heat causing the peak in the electron temperature. Electron-ion Coulomb collisions channel much of this heat away from the electrons at altitudes

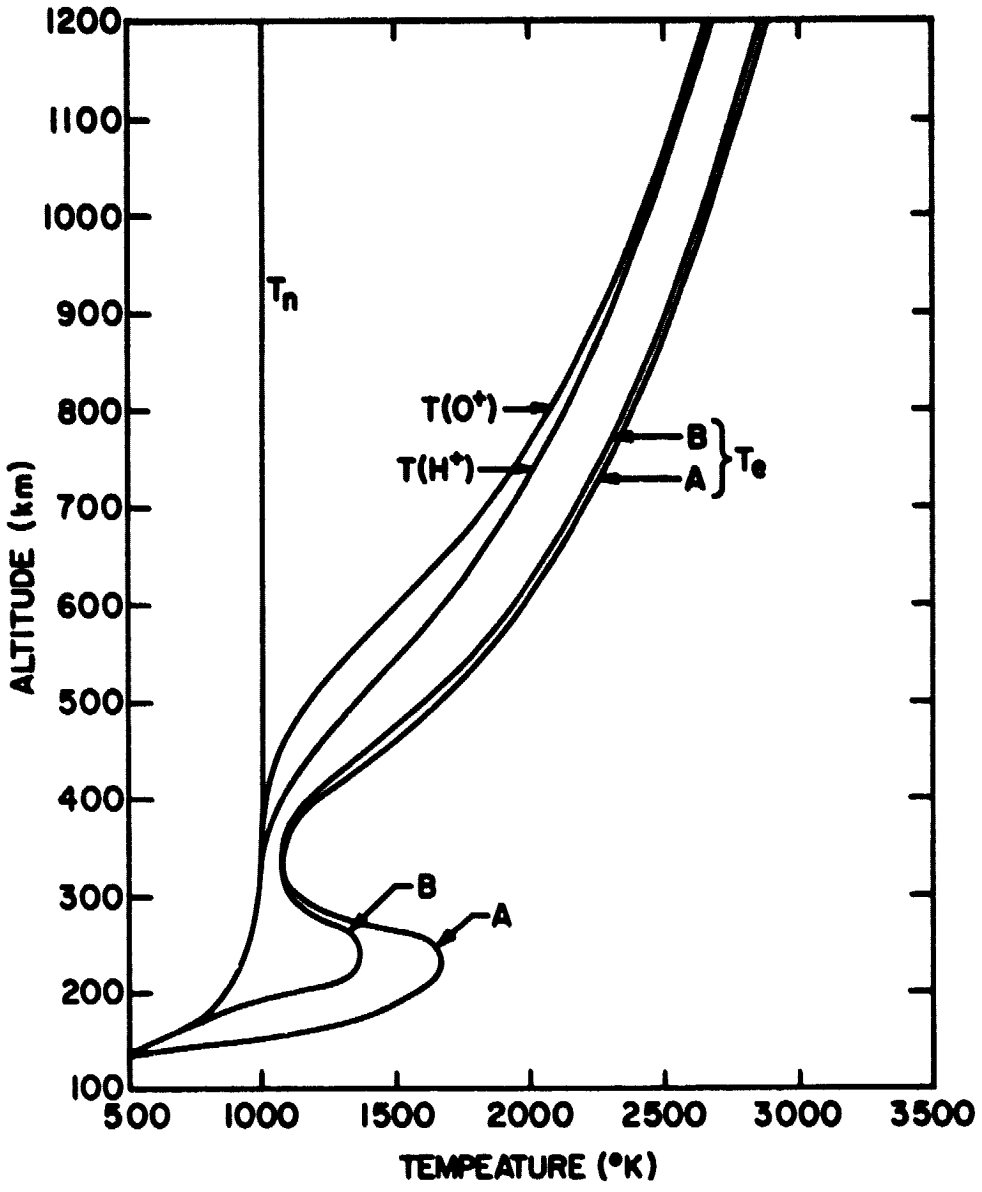

Figure 6.10 Electron temperature profiles for cases where inelastic collisions are not included in the energy balance equation (profile A) and inelastic collisions are included (profile B).

above 300 km. However, below 300 km thermal conduction and inelastic collisions must transfer this excess heat to other altitudes or other particles. Since inelastic collisions are not sufficient to absorb all the heat, there will be temperature gradients. Thus, a small peak in the electron temperature profile occurs.

6.6 *Different Ion Temperatures*

The importance of considering different O^+ and H^+ ion temperatures has been examined by *Banks* [1967a] for the case where thermal conduction is not included in the energy balance equation. He found that H^+ ions can have temperatures 250 K greater than O^+ ions. In this section the separate ion temperatures are calculated with thermal conduction included in the energy balance equations using the method described in Section 6.2.1. Several different cases are considered. Two sets of ion density are considered along with changes in the upper boundary condition.

The lower boundary condition for H^+ and O^+ temperatures is $T_i = T_n$ at 200 km. The electron temperature's lower boundary condition is that thermal conduction is not important at 120 km. The thermal-electron heating rates are from Figure 3.3 with $\chi = 0°$.

In Figures 6.11-6.13 the effect on the ion temperature profiles of changing the upper boundary is shown. The ion number density profiles used are shown in Figure 6.2. The electron temperature profile is held constant in these calculations. In Figure 6.11, $\partial T_j/\partial z = 0$ where j is the subscript for both H^+ and O^+. The H^+ temperature is greater than the O^+ temperature because H^+ has a larger electron-ion heating rate than O^+. The difference between the O^+ and H^+ temperatures is largest near 500 km. This is because ion-neutral cooling is larger for O^+ than H^+. The O^+ temperature is controlled more by ion-neutral cooling at the lower altitudes, so that O^+ temperature

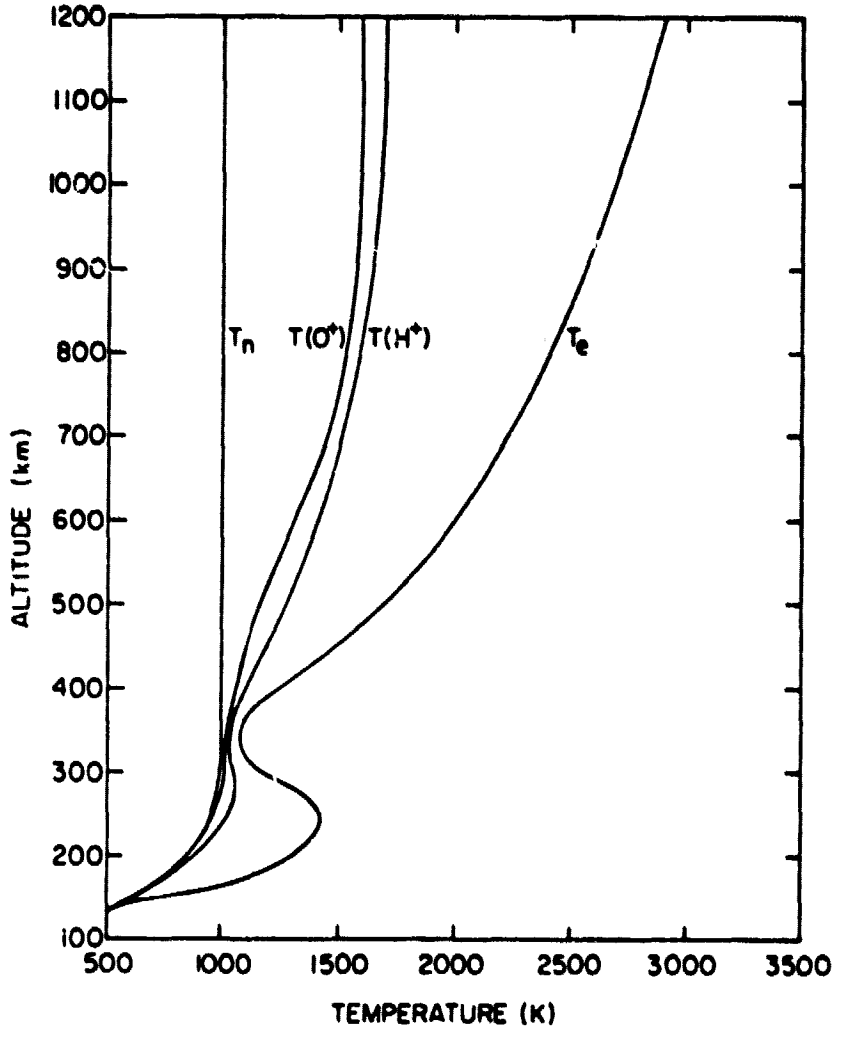

Figure 6.11 Temperature profiles for O^+ and H^+ where the upper boundary condition is $\partial T_i/\partial z = 0$. The ion number densities used to calculate $T(O^+)$ and $T(H^+)$ are shown in Figure 6.2.

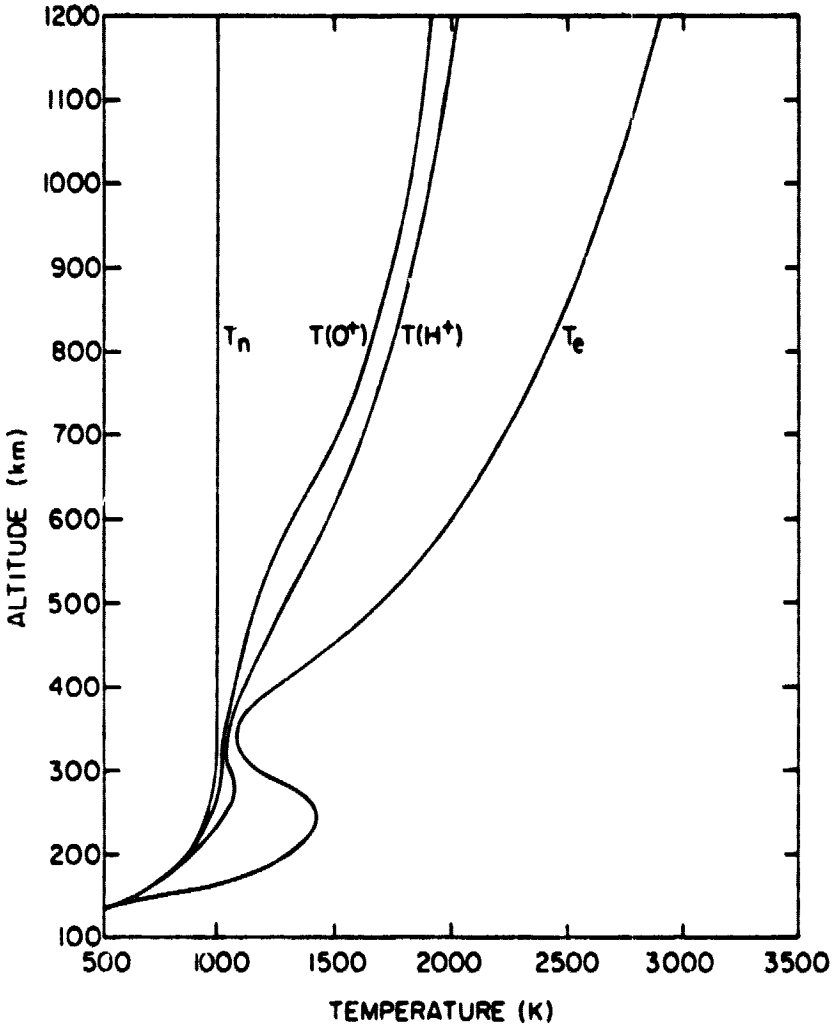

Figure 6.12 Temperature profiles for O^+ and H^+ where the upper boundary condition is $\partial T_i/\partial z$ = 0.5 K/km and the ion number densities are from Figure 6.2.

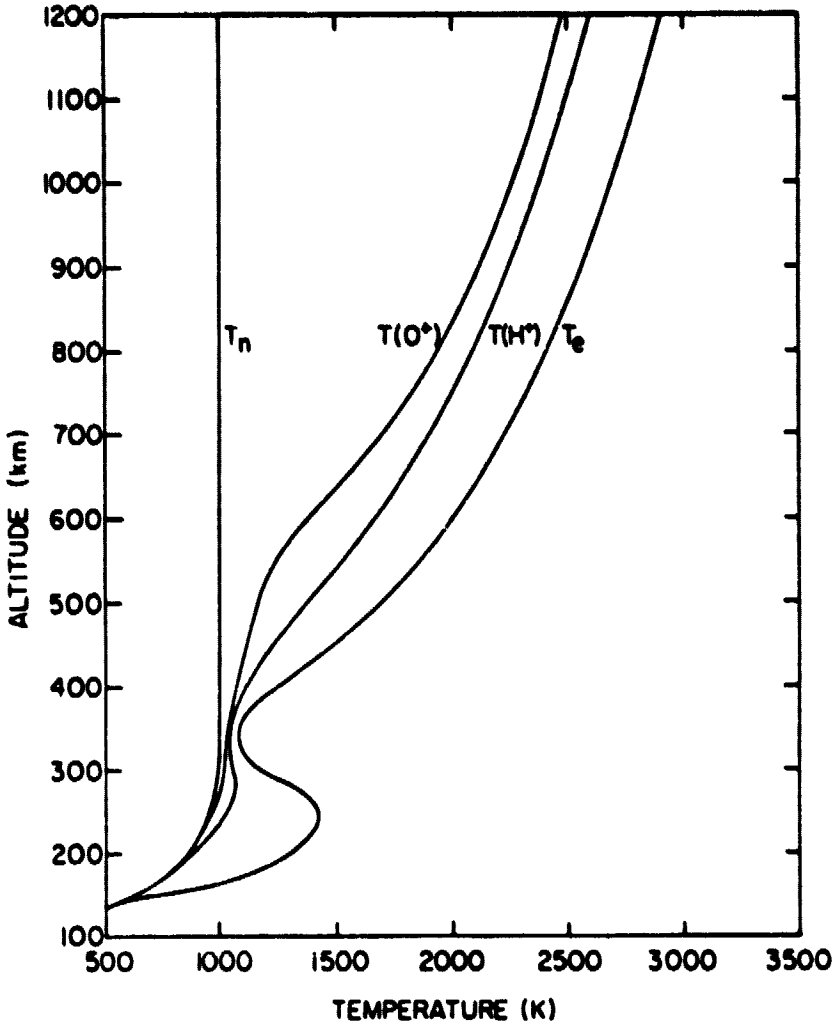

Figure 6.13 Temperature profiles for O^+ and H^+ where the upper boundary condition is $\partial T_i/\partial z = 1.0$ K/km and the ion number densities are from Figure 6.2.

is close to the neutral temperature up to about 500 km.

The ion temperatures are much less than the electron temperature at the higher altitudes in Figure 6.11. There is a gradient in the electron temperature and no gradient in the ion temperature. A large amount of heat is being transferred in the electron gas through conduction, but very little in the ion gas. In fact, the ion temperatures only increase by about 700 K above the neutral temperature, while the electron temperature is more than three times the neutral temperature at 1200 km.

In Figure 6.12 the ion temperature profiles is shown for the case where the upper boundary condition is $\partial T_j/\partial z = 0.5$ K/km. In this case the difference between the O^+ and H^+ temperature profiles is larger than where $\partial T_j/\partial z = 0$. The largest difference occurs at about 500 km. The ion temperature profiles also increase to larger values in Figure 6.12 than in Figure 6.12 than in Figure 6.11. This is because of heat being transferred to lower altitudes through thermal conduction and thereby raising the temperatures. Thus, as the temperature gradients increase more heat is transferred from the high altitudes, and the temperatures increase significantly.

The case where the upper boundary condition is $\partial T_j/\partial z = 1$ K/km is shown in Figure 6.13. In this figure, the difference between the O^+ and H^+ temperature profiles is even larger than the previous two cases. As before, the largest difference occurs near 500 km. There are significant differences even up to 1200 km. Both the O^+ and H^+ temperatures increase to larger values at 1200 km than they do when $\partial T_j/\partial z = 0$ and 0.5 K/km. This is due to more heat being transferred from above the upper boundary to lower altitudes. More heat is transferred to lower altitudes by thermal conduction if temperature gradients are larger because thermal conduction depends on temperature gradients.

Figures 6.11, 6.12, and 6.13 show the effect of different upper boundary conditions on profiles of $T(O^+)$ and $T(H^+)$. These profiles were calculated based on an electron temperature profile which was the same in each figure. This is not a self-consistent calculation because the electron temperature profile is affected by changes in $T(O^+)$ and $T(H^+)$. Figures 6.11, 6.12, and 6.13 still provide useful information on the effect of the upper boundary on ion temperature profiles.

Using Figures 6.11-6.13, H^+-to-O^+ temperature ratios, $T(H^+)/T(O^+)$, can be calculated. These ratios are shown in Figure 6.14. This figure shows that $T(H^+)/T(O^+)$ is largest in the altitude region near 500 km. Curve A represents $T(H^+)/T(O^+)$ for Figure 6.11 where $\partial T_j/\partial z = 0$. Curves B and C are for Figures 6.12 and 6.13, where $\partial T_j/\partial z = 0.5$ and 1.0 K/km respectively. Curve C has the largest values of $T(H^+)/T(O^+)$. The temperature ratio $T(H^+)/T(O^+)$ is large in curve C even at altitudes near 1200 km. $T(H^+)/T(O^+)$ is much smaller at 1200 km in curves B and C. Since curve C represents the case $\partial T_i/\partial z = 1.0$ K/km, this means that more heat can be conducted downward through the H^+ ion gas. Thus the H^+ ion temperature is larger than the O^+ ion temperature. The peak in $T(H^+)/T(O^+)$ is due to the relatively constant temperature gradient of $T(H^+)$ with altitude. The O^+ temperature decreases more rapidly and approaches the neutral temperature at about 500 km.

The ion density was found to be important in controlling the ion and electron temperature in Section 6.3. The ion density is also important in controlling the difference between the H^+ and O^+ ion temperatures. The effect of the ion density profiles A and B of Figure 6.4 on O^+ and H^+ temperature profiles is shown in Figures 6.15 and 6.16 respectively. Also calculated along with O^+ and H^+ temperature profiles is the electron temperature profile.

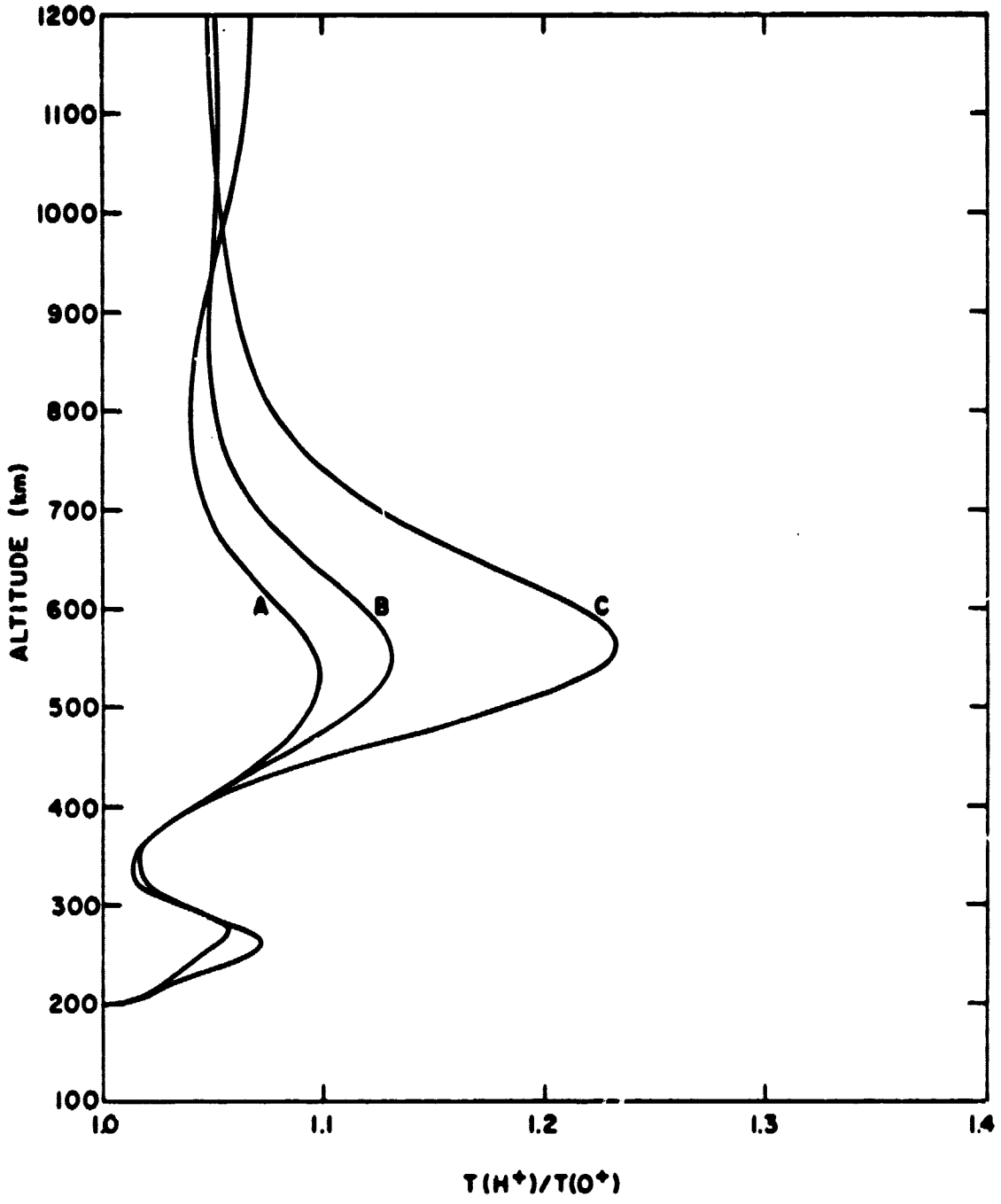

Figure 6.14 Ratios of $T(H^+)/T(O^+)$ for Figures 6.11, 6.12, and 6.13.

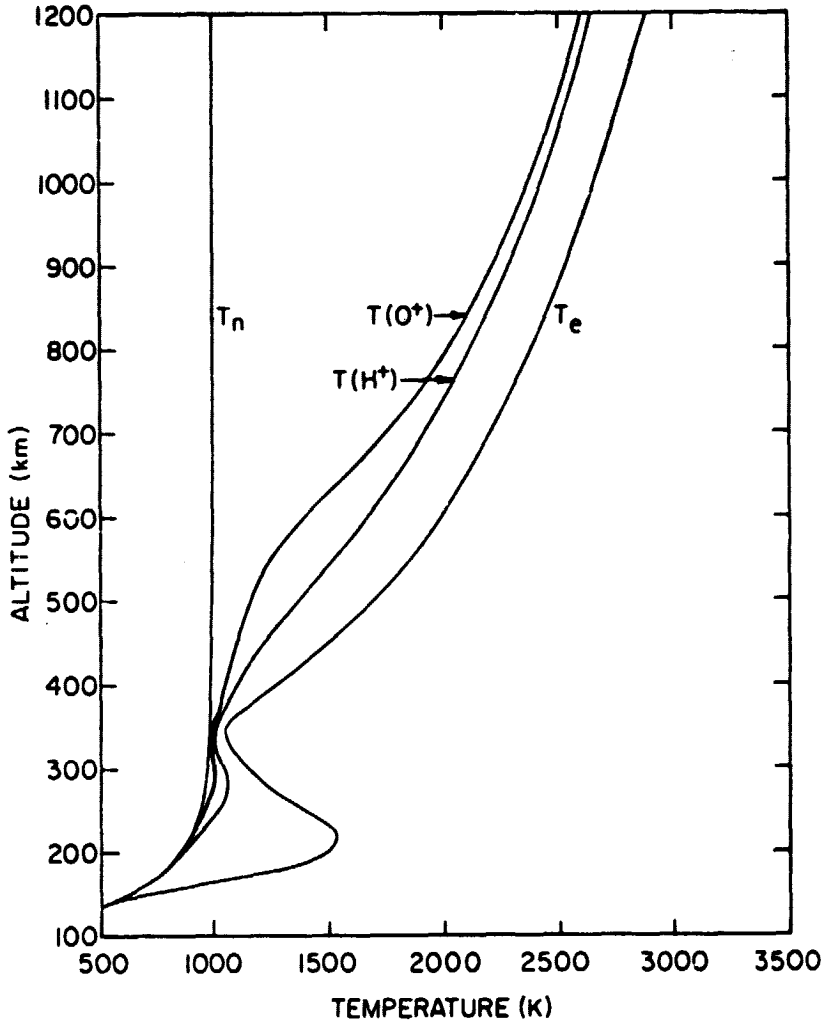

Figure 6.15 $T(O^+)$, $T(H^+)$, and T_e where the upper boundary condition is $\partial T_i/\partial z$ = 1.0 K/km and the ion number densities are from Figure 6.4 A.

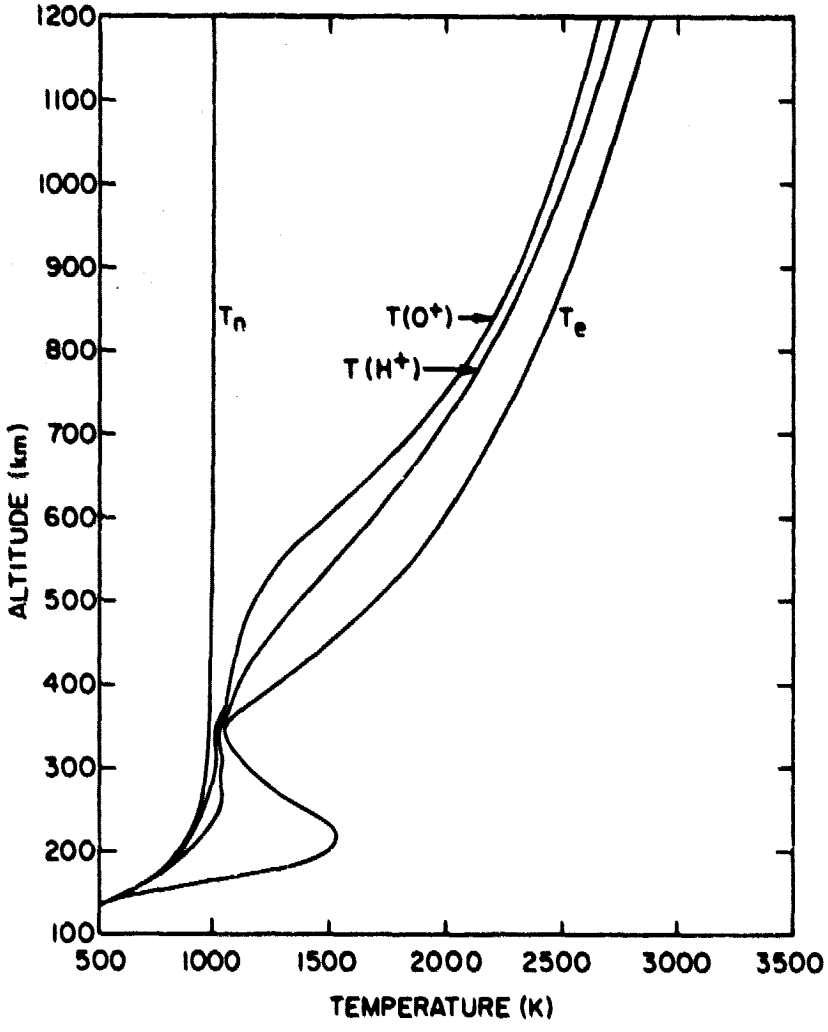

Figure 6.16 $T(O^+)$, $T(H^+)$, and T_e where the upper boundary condition is $\partial T_i/\partial z = 1.0$ K/km and the ion number densities are from Figure 6.4 B.

The upper boundary condition for the ion and electron temperature is that the temperature gradient at 1200 km is 1.0 K/km. The *CIRA* [1972] neutral atmosphere model with T_∞ = 1000 K was used. The thermal-electron heating rates were taken from Figure 3.3 with $\chi = 0°$.

The ion density is important in controlling the magnitude of the difference between H^+ and O^+ temperatures. If H^+ or O^+ densities are large ($\sim 1 \times 10^4$ cm^{-3}) at 1200 km (Figure 6.15 and 6.16) then $T(H^+)/T(O^+)$ is reduced over the case where $n(O^+) = 1 \times 10^3$ cm^{-3} (Figure 6.13). There are still significant values of $T(H^+)/T(O^+)$ in the region near 500 km as shown in Figure 6.15 and 6.16. The magnitude of $T(H^+)/T(O^+)$ in Figure 6.16 is less than that in Figure 6.15 because H^+ densities are greater for Figure 6.16. The larger H^+ densities allow more heat to be transferred to O^+ by Coulomb collisions. Therefore, the H^+ temperatures are reduced and the O^+ temperatures increase.

The importance of the electrons as a heat source for ions is shown in Figure 6.17. In this figure the electron temperature is much greater at altitudes above 500 km than in Figure 6.16. The electron upper boundary condition in Figure 6.16 is $\partial T_e/\partial z\big|_{1200} = 1$ K/km and in Figure 6.17 it is 1.5 K/km. If the temperature gradient is larger, the temperature also are larger.

Since the electron temperatures increase, the H^+ and O^+ temperature also increase. The H^+ temperature increases more than the O^+ temperature because H^+ has a larger electron energy transfer rate than O^+. The difference between H^+ and O^+ temperatures increases greatly from Figures 6.16 to 6.17. Therefore, as the difference between electron and ion temperatures increases, the difference between H^+ and O^+ temperatures also increases.

6.7 *The Effect of the Neutral Atmosphere on Ion and Electron Temperature Profiles*

The neutral atmosphere can be important in determining the ion and elec-

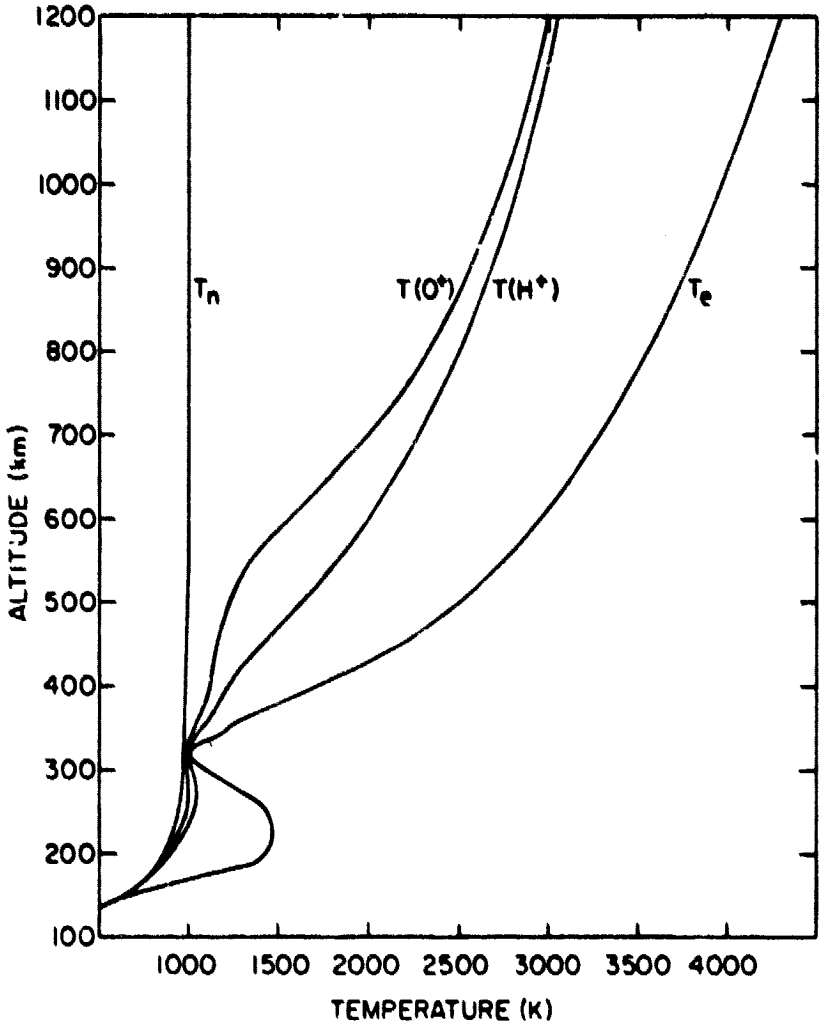

Figure 6.17 $T(O^+)$, $T(H^+)$, and T_e where the upper boundary condition for T_e is $\partial T_e/\partial z = 1.5$ K/km and the ion number densities are from Figure 6.4 B.

tron temperature profiles. In particular, different temperature profiles can result from neutral number densities that differ from one neutral atmosphere model to another. The neutral atmosphere is important at lower altitudes where the major heat losses for ions and electrons are through elastic and inelastic collisions with neutral particles.

In Figures 6.16, 6.18, 6.19, and 6.20, ion and electron temperature profiles are shown for the cases T_∞ = 1000 K, 500 K, 700 K, and 1500 K respectively. The lower boundary conditions is that the electrons O^+ and H^+, and neutral temperatures are equal at 120 km. For each neutral temperature, the upper boundary condition for electrons, O^+, and H^+ temperatures is the gradient of temperature with respect to altitude is 1 K/km. Ion densities used throughout this section are given in Figure 6.6 profile B. The thermal-electron heating rates are from Figure 3.3 with $\chi = 0°$. The electron temperature profile is calculated using the method described in Section 6.2.3 The ion temperature profiles are calculated using the method described in Section 6.2.1.

Comparison between Figures 6.16 and 6.19 indicates that the ion and electron temperatures profiles change very little at the altitudes above 800 km as the neutral temperature changes from 700 K to 1000 K. This is because the dominate heat transfer process above 800 km is thermal conduction. Above 800 km neutral number densities are very small and cooling of ions and electrons is accomplished through thermal conduction of heat to lower altitudes. Since the thermal conductivity is independent of the neutral atmosphere, the ion and electron temperature profiles are independent of the neutral atmosphere above 800 km.

Below 800 km the effect of the neutral atmosphere begins to determine the shape of the ion and electron temperature profiles. For T_∞ = 1000 K, the

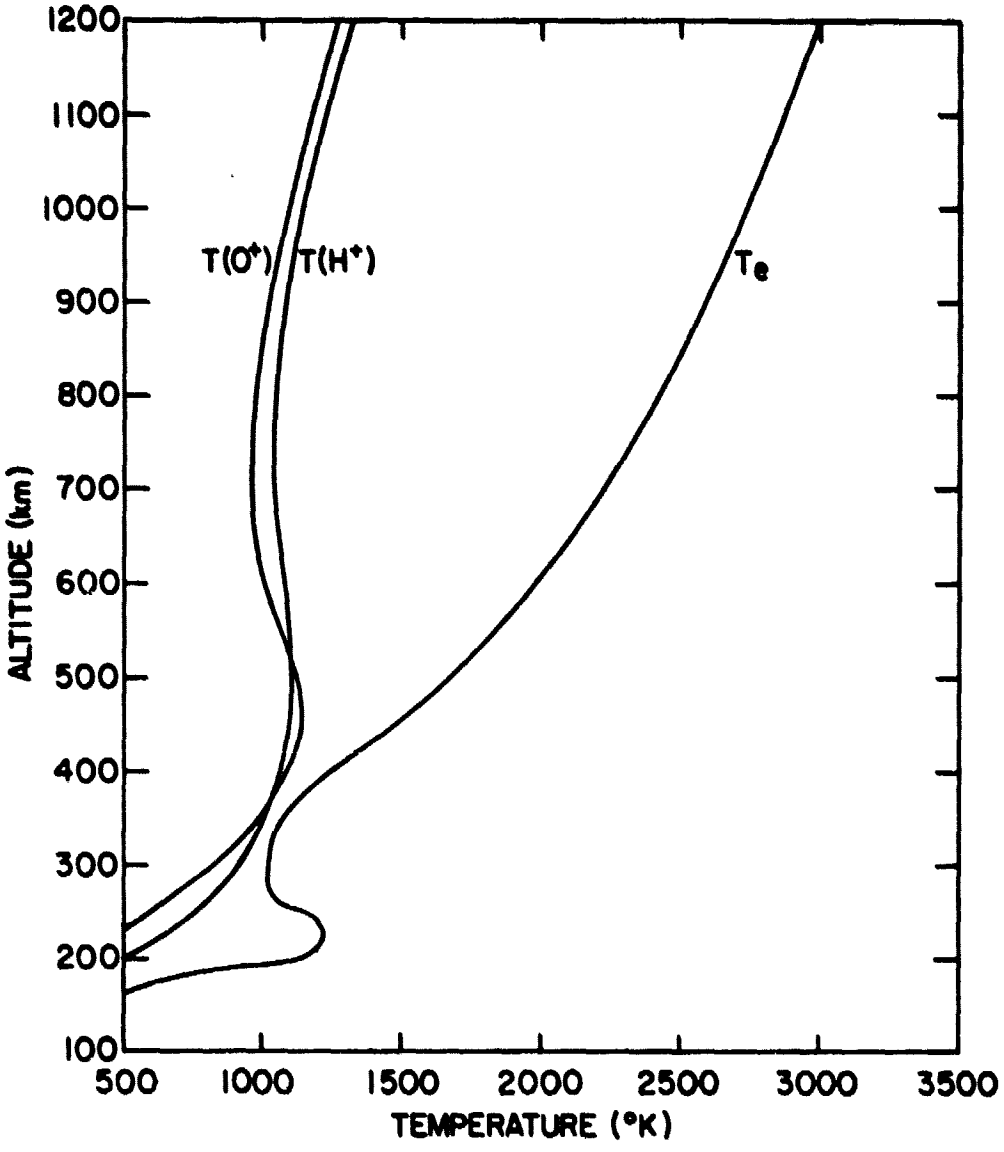

Figure 6.18 $T(O^+)$, $T(H^+)$, and T_e where the upper boundary condition is $\partial T_i/\partial s = 1.0$ K/km and ion number densities are from Figure 6.4 B. The neutral atmosphere model is from *CIRA* [1972] with $T_\infty = 500$ K.

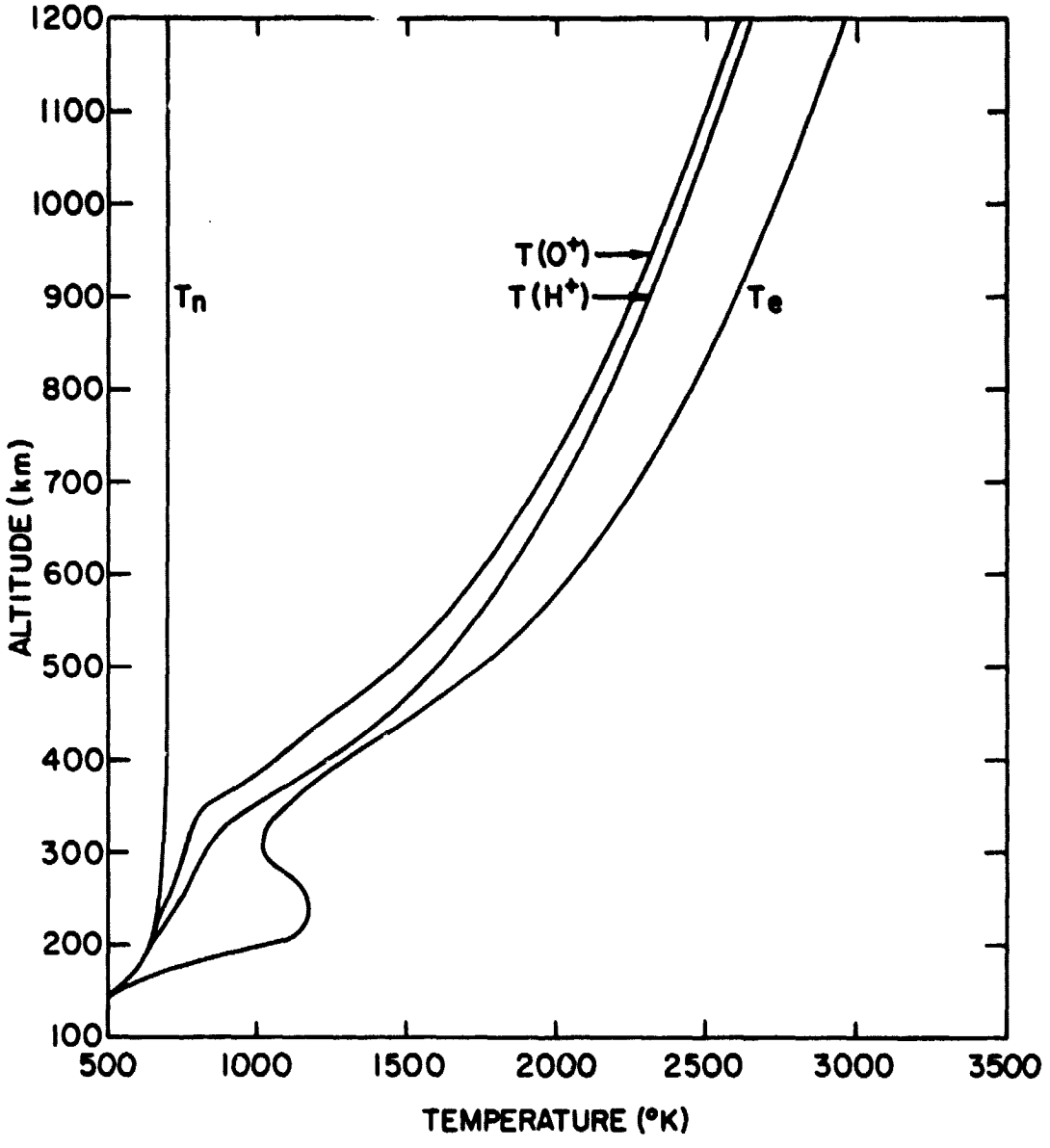

Figure 6.19 $T(O^+)$, $T(H^+)$, and T_e where the upper boundary condition is $\partial T_i/\partial z = 1.0$ K/km and ion number densities are from Figure 6.4 B. The neutral atmosphere model is from *CIRA* [1972] with $T_\infty = 700$ K.

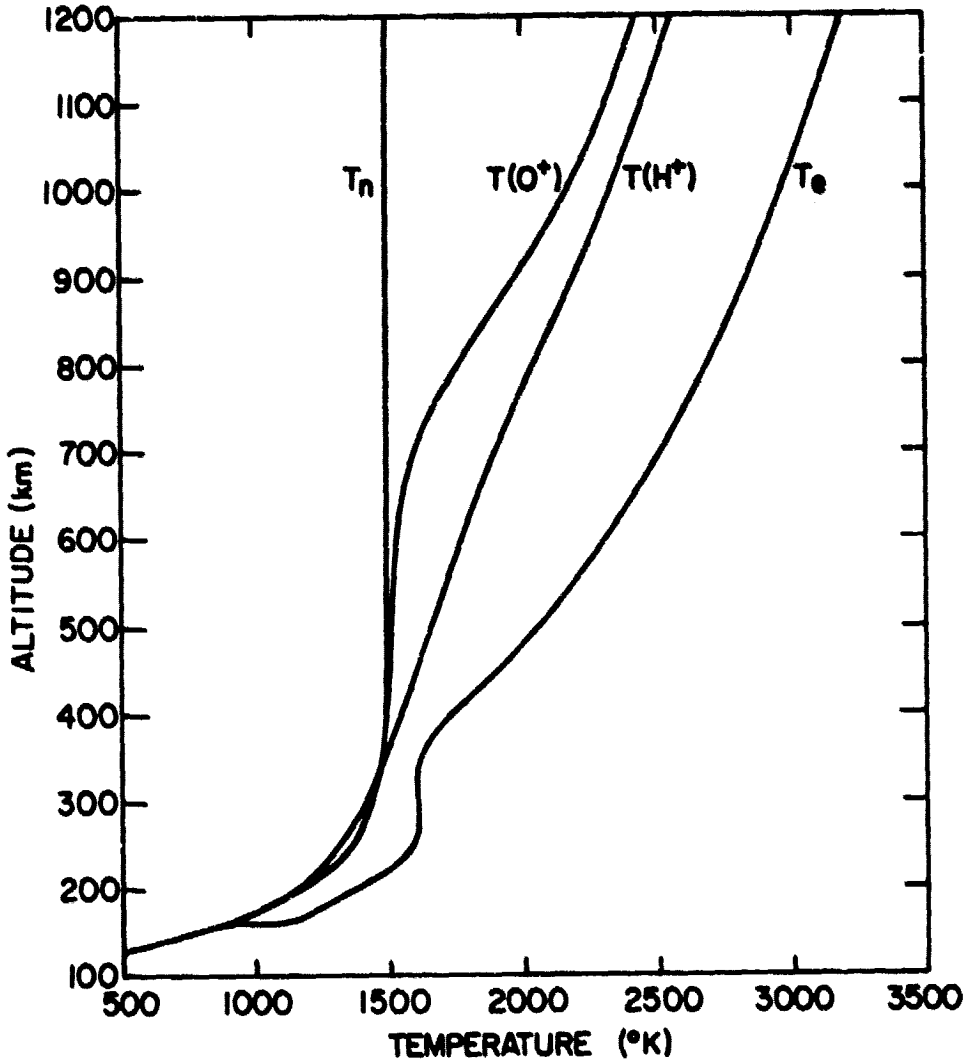

Figure 6.20 $T(O^+)$, $T(H^+)$, and T_e where the upper boundary condition is $\partial T_i/\partial z = 1.0$ K/km and ion number densities are from Figure 6.4 B. The neutral atmosphere model is from *CIRA* [1972] with $T_\infty = 1500$ K.

O^+ ion temperature decreases more rapidly than the H^+ ion temperature, leaving a difference between O^+ and H^+ temperatures. As T_∞ decreases, the difference between O^+ and H^+ temperatures decreases. As the neutral temperature decreases, the neutral number densities also decrease. As a result, the O^+ temperature profile and H^+ temperature profile are much closer to each other for smaller neutral temperatures. Thus, the importance of neutral collisions with ions and electrons is pushed to lower altitudes for smaller nsutral temperatures.

Although the $T(H^+)$ and $T(O^+)$ do not change at altitudes above 800 km when T_∞ = 1000 and 700 K (Figures 6.16 and 6.19), $T(H^+)$ and $T(O^+)$ change when T_∞ = 500 K and 1500 K. In Figure 6.18, (T_∞ = 500 K) and 6.20 (T_∞ = 1500 K) $T(H^+)$ and $T(O^+)$ are much smaller than in Figure 6.19. For T_∞ = 500 K, $T(O^+)$ and $T(H^+)$ are nearly equal from 200 to 1200 km. For T_∞ = 1500 K, $T(O^+)$ and $T(H^+)$ are much different especially near 700 km. When T_∞ = 500 K, $T(O^+)$ and $T(H^+)$ are so close that it is very difficult to distinguish different temperatures. Also when T_∞ = 500 K, $T(O^+)$ is approximately 1000 K from 400 to 1200 km. When T_∞ = 1500 K, $T(O^+)$ is nearly equal to T_n from 200 km to 700 km.

The electron temperature doesn't change drastically as $T(O^+)$ and $T(H^+)$ changes when T_∞ = 500, 700, 1000, or 1500 K. It is approximately the same in for each neutral thermosphere model. This is expected because thermal conduction is more important for electrons than it is for ions.

6.8 *Summary and Comparison with Chapter 5 Results*

In this chapter electron and ion temperatures were found to depend on many factors. The electron number density and the O^+ and H^+ number densities are important (see Figure 6.3 and 6.5). Also, the neutral thermosphere model is an important factor (see Figures 6.16, 6.18, 6.19, and 6.20). The time of day can determine T_e below 500 km (see Figures 6.6, 6.7, and 6.8).

Inelastic collisions have an effect on the T_e profile at altitudes below 400 km (see Figure 6.10). Thermal conductivity and the upper boundary condition are also very important in determining the shape of the T_e, $T(O^+)$, and $T(H^+)$ profiles (see Figure 6.11, 6.12, 6.13, and 6.17).

In Figure 6.9 the importance of the various electron heat transfer processes is shown. Thermal conduction is the most important electron energy transfer process at altitudes above 400 km. Even though the thermal conductivity of O^+ and H^+ is much less than the electron thermal conductivity, the thermal conduction of ions is still important in keeping $T(O^+)$ and $T(H^+)$ significantly below T_e. Since the thermal conductivity of O^+ is smaller than the thermal conductivity of H^+, less heat flows through O^+ than through H^+.

The electron-H^+ energy transfer rate is larger than the electron-O^+ energy transfer rate, and $T(O^+)$ and $T(H^+)$ are weakly coupled. Therefore, $T(H^+)$ is generally larger than $T(O^+)$ (see Figures 6.11, 6.12, 6.13, 6.15, 6.16, 6.17, 6.18, 6.19, and 6.20). Thermal conduction and the upper boundary condition control the magnitude of the difference between $T(H^+)$ and $T(O^+)$. As the ion temperature gradient increases from zero to one K/km the peak difference between $T(H^+)$ and $T(O^+)$. Larger values of T_e result in more heat transferring to H^+ and thus a larger difference between $T(H^+)$ and $T(O^+)$ (see Figure 6.17).

Some of the results of this chapter can be compared with experimental results of Chapter 5. The ion densities are given by experimental results of Figures 5.3, 5.6, 5.7, and 5.12 and by the empirical model of Figure 6.4. Experimental daytime electron temperatures of Figures 5.9, 5.10, and 5.13 can be compared to theoretical electron temperatures of Figures 6.3, 6.5, 6.15, 6.16, and 6.17. Nighttime electron temperatures are shown in Figures 5.8 and

6.8 The O^+ and H^+ temperatures are given by the experimental results of Figures 5.9, 5.10, 5.11, 5.13, and 5.14 and by the theoretical results of Figures 6.15, 6.16 and 6.17.

The ion densities of Figures 5.3, 5.6, 5.7, and 5.12 are consistent with the ion densities shown in profile A of Figure 6.4 because Figure 6.4 is based on experimental results. The magnitude and the location of the peak of the O^+ density are approximately the same in both Figures 5.5 and 6.4. At altitude below 500 km O^+ is the dominant ion. At altitudes near 1200 km $n(O^+)/n_e$ is about 0.5. The agreement between Figures 5.3, 5.6, 5.7, and 5.12 and Figure 6.4 A is good enough so that the ion and electron temperatures based on these figures can be compared. The errors for theoretical ion and electron temperatures due to any disagreement in the ion densities would be less than the differences between profile 1 and 2 of Figure 6.3 which is less than 100 K for T_i and 200 K for T_e. In Figure 6.5 the effect of the ion species on T_e is shown to be unimportant.

The electron temperature profiles in Figures 5.9, 5.10 and 5.13 have a temperature gradient at the upper boundary of about 1.0 to 1.5 K/km. In Figure 6.15 and 6.16 T_e has been calculated based on the assumption that the temperature gradient at the upper boundary is 1.0 K/km. Figure 6.17 shows T_e when the temperature gradient is 1.5 K/km. The values of T_e in Figures 5.10 and 5.13 are somewhat greater than those in Figures 6.15 and 6.16 but less than those in Figure 6.17. This indicates that the theoretical T_e profiles are consistent at the upper boundary with the experimental T_e profile since the experimental temperature gradient is between 1.0 and 1.5 K/km at the upper boundary. The experimental and theoretical T_e profiles don't agree below 400 km. The theory predicts T_e to be approximately equal to $T(H^+)$ and

$T(O^+)$ from 300 to 400 km, and T_e has a relative maximum at about 240 km. However, the experimental T_e profile becomes equal to $T(H^+)$ and $T(O^+)$ below 230 km and T_e has a steep temperature gradient from 300 to 400 km. This region below 400 km needs to be investigated in future research to find the reason for the discrepancy between experimental and theoretical T_e profiles. There are several possible reasons for this discrepancy - 1) the heating of the ambient electrons by photoelectrons is not accurate below 400 km, 2) the electron density model below 400 km is not accurate and actual experimental electron densities should be used instead, and 3) there are other sources of heat for electron which have not yet been identified as important.

In Figure 5.8 nighttime electron and ion temperature profiles are shown. Although the profiles only extend to 650 km one can still compare then with theoretical calculations of T_e and T_i given in Figures 6.6, 6.7, and 6.8. Figures 6.6 and 6.6 don't agree with Figure 5.8 because T_e is significantly greater than T_i from 400 to 650 km in Figures 6.6 and 6.7. However, Figure 6.8 is similar to Figure 5.8. The T_e profile is approximately equal to the T_i profile in both Figures 5.8 and 6.8 and the temperatures are fairly constant with altitude in both figures due to zero or near zero temperature gradients at the upper boundary.

The agreement between experimental and theoretical profiles of $T(O^+)$ and $T(H^+)$ is quite good (see Figures 5.9, 5.10, 5.11, 5.13, 5.14, 6.15, 6.16, and 6.17). Both the experimental and the theoretical profiles of $T(O^+)$ are close to the neutral temperature of 1000 K up to about 500 km where $T(O^+)$ starts to increase rapidly. The temperature gradient at the upper boundary is approximately 1.0 K/km for both experimental and theoretical $T(O^+)$ profiles.

Comparison between experimental and theoretical $T(H^+)$ profiles cannot be made directly because Figure 5.11 and 5.14 give $T(H^+)/T(O^+)$ instead.

Calculation of values of $T(H^+)/T(O^+)$ for Figures 6.15, 6.16, and 6.17 give values of about 1.0 at low and high altitudes which is the same for Figures 5.11 and 5.14. The peak value given by Figures 5.11 and 5.14 is located at 550 km. This is also about the same location of the peak of $T(H^+)/T(O^+)$ calculated from Figures 6.15, 6.16, and 6.17. The values of $T(H^+)/T(O^+)$ at 550 km calculated from Figures 6.15, 6.16, and 6.17 are about 1.3, 1.2, and 1.5 respectively. The maximum of $T(H^+)/T(O^+)$ in Figures 5.11 and 5.14 is about 1.3 and 1.4 which are consistent with those of Figures 6.15 and 6.17.

It is important that the experimental and theoretical ion temperature profiles agree because it means that all the important energy transfer processes are included in the ion energy balance equations. There is no reason to look for additional energy sources or sinks for ions because there is no discrepancy between experimental and theoretical ion temperatures.

The experimental and theoretical electron temperatures agree above 400 km. However, below 400 km there is a discrepancy which needs to be investigated by further research of electron energy transfer processes.

APPENDIX A
CIRA 1972 Neutral Atmospheric Models

EXOSPHERIC TEMPERATURE = 500 K

HEIGHT KM	TEMP K	LOG(N(N2) /M3)	LOG(N(O2) /M3)	LOG(N(O) /M3)	LOG(N(A) /M3)	LOG(N(HE) /M3)
110	216.6	19.206	17.424	17.590	15.989	13.710
112	223.0	18.864	17.263	17.502	15.793	13.690
114	230.4	17.925	17.100	17.415	15.603	13.661
116	244.6	17.791	16.957	17.331	15.420	13.633
118	255.6	17.661	16.812	17.248	15.243	13.606
120	267.1	17.536	16.672	17.169	15.073	13.579
122	279.2	17.416	16.537	17.092	14.909	13.552
124	291.5	17.300	16.408	17.018	14.752	13.527
126	304.0	17.189	16.283	16.947	14.602	13.502
128	316.3	17.083	16.165	16.879	14.458	13.479
130	328.3	16.981	16.051	16.814	14.320	13.457
135	355.9	16.745	15.786	16.664	13.998	13.406
140	378.9	16.531	15.565	16.530	13.704	13.363
145	397.3	16.334	15.323	16.408	13.431	13.325
150	411.9	16.149	15.114	16.296	13.176	13.291
155	423.6	15.973	14.914	16.190	12.928	13.260
160	433.1	15.804	14.723	16.089	12.691	13.231
165	440.9	15.640	14.537	15.992	12.461	13.204
170	447.4	15.480	14.355	15.899	12.236	13.178
175	452.6	15.324	14.177	15.807	12.015	13.153
180	457.7	15.170	14.002	15.717	11.798	13.129
185	461.8	15.019	13.830	15.629	11.584	13.106
190	465.4	14.870	13.660	15.542	11.372	13.083
195	468.5	14.722	13.492	15.457	11.163	13.060
200	471.4	14.576	13.325	15.372	10.956	13.038
210	476.2	14.287	12.996	15.205	10.546	12.995
220	480.1	14.003	12.672	15.042	10.142	12.952
230	483.3	13.722	12.351	14.880	9.743	12.911
240	485.9	13.444	12.035	14.720	9.348	12.870
250	488.1	13.169	11.721	14.562	8.956	12.830
260	489.9	12.896	11.409	14.406	8.568	12.790
270	491.4	12.626	11.100	14.251	8.182	12.751
280	492.7	12.357	10.793	14.096	7.799	12.712
290	493.7	12.089	10.487	13.943	7.418	12.673
300	494.6	11.823	10.184	13.791	7.039	12.635
310	495.4	11.559	9.882	13.640	6.662	12.597
320	496.0	11.295	9.581	13.489	6.287	12.559
330	496.5	11.033	9.281	13.339		12.521
340	496.9	10.772	8.983	13.190		12.484
350	497.3	10.512	8.686	13.041		12.446
360	497.6	10.253	8.391	12.893		12.409
370	497.9	9.995	8.096	12.746		12.372
380	498.2	9.738	7.802	12.599		12.335
390	498.4	9.481	7.509	12.452		12.299

EXOSPHERIC TEMPERATURE = 500 K

HEIGHT KM	TEMP K	LOG(N(N2) /M3)	LOG(N(O2)? /M3)	LOG(N(O) /M3)	LOG(N(A) /M3)	LOG(N(HE) /M3)	LOG(N(H) /M3)
400	498.5	9.226	7.218	12.306		12.262	
420	498.8	8.718	6.637	12.016		12.189	
440	499.1	8.213	6.061	11.728		12.117	
460	499.2	7.712		11.441		12.045	
480	499.4	7.213		11.156		11.974	
500	499.5	6.718		10.873		11.903	12.060
520	499.5	6.225		10.592		11.833	12.042
540	499.6			10.312		11.763	12.024
560	499.7			10.035		11.693	12.007
580	499.7			9.758		11.624	12.789
600	499.8			9.484		11.555	12.772
620	499.8			9.216		11.487	12.754
640	499.8			8.939		11.419	12.737
660	499.8			8.669		11.352	12.720
680	499.9			8.401		11.284	12.703
700	499.9			8.134		11.218	12.687
720	499.9			7.868		11.151	12.670
740	499.9			7.605		11.085	12.653
760	499.9			7.342		11.020	12.637
780	499.9			7.081		10.954	12.620
800	499.9			6.822		10.889	12.604
820	499.9			6.564		10.825	12.588
840	499.9			6.308		10.761	12.571
860	499.9			6.053		10.697	12.555
880	500.0					10.634	12.539
900	500.0					10.570	12.524
920	500.0					10.508	12.508
940	500.0					10.445	12.492
960	500.0					10.383	12.476
980	500.0					10.321	12.461
1000	500.0					10.260	12.445
1020	500.0					10.199	12.407
1100	500.0					9.950	12.360
1150	500.0					9.810	12.332
1200	500.0					9.644	12.295
1250	500.0					9.520	12.259
1300	500.0					9.377	12.223
1350	500.0					9.237	12.188
1400	500.0					9.098	12.153
1450	500.0					8.962	12.118
1500	500.0					8.827	12.084
1600	500.0					8.561	12.018
1700	500.0					8.303	11.952
1800	500.0					8.051	11.889
1900	500.0					7.805	11.827
2000	500.0					7.565	11.767

EXOSPHERIC TEMPERATURE = 700 K

HEIGHT KM	TEMP K	LOG(N(N2) /M3)	LOG(N(O2) /M3)	LOG(N(O) /M3)	G(N(A) /M3)	LOG(N(HE) /M3)
110	229.9	18.206	17.426	17.580	15.998	13.706
112	241.7	18.066	17.270	17.491	15.808	13.675
114	254.7	17.932	17.120	17.405	15.626	13.645
116	269.0	17.802	16.975	17.321	15.452	13.615
118	284.3	17.678	16.837	17.239	15.285	13.586
120	300.5	17.559	16.705	17.161	15.126	13.558
122	317.3	17.446	16.579	17.087	14.975	13.530
124	334.5	17.338	16.459	17.015	14.831	13.504
126	351.9	17.236	16.345	16.947	14.694	13.479
128	369.2	17.139	16.237	16.883	14.564	13.455
130	386.2	17.046	16.134	16.821	14.440	13.433
135	426.3	16.834	15.897	16.682	14.156	13.382
140	462.0	16.644	15.686	16.558	13.900	13.338
145	492.5	16.472	15.494	16.449	13.667	13.300
150	518.2	16.315	15.317	16.349	13.452	13.267
155	539.7	16.168	15.152	16.257	13.250	13.238
160	557.8	16.029	14.995	16.172	13.058	13.211
165	573.2	15.897	14.846	16.091	12.875	13.186
170	586.3	15.769	14.702	16.015	12.697	13.164
175	597.6	15.646	14.562	15.941	12.525	13.142
180	607.5	15.526	14.426	15.869	12.357	13.122
185	616.2	15.410	14.294	15.800	12.193	13.102
190	623.8	15.295	14.163	15.732	12.032	13.083
195	630.7	15.182	14.036	15.666	11.874	13.065
200	636.8	15.072	13.910	15.601	11.718	13.047
210	647.2	14.855	13.663	15.474	11.412	13.012
220	655.8	14.643	13.422	15.350	11.112	12.979
230	662.9	14.436	13.186	15.230	10.818	12.948
240	668.7	14.231	12.953	15.112	10.528	12.917
250	673.5	14.030	12.723	14.995	10.242	12.886
260	677.6	13.831	12.497	14.881	9.960	12.857
270	680.9	13.634	12.272	14.767	9.680	12.828
280	683.7	13.439	12.050	14.655	9.403	12.799
290	686.0	13.246	11.829	14.544	9.128	12.770
300	688.0	13.054	11.610	14.434	8.854	12.742
310	689.6	12.863	11.392	14.324	8.583	12.715
320	691.0	12.674	11.176	14.216	8.313	12.687
330	692.2	12.485	10.960	14.108	8.044	12.660
340	693.2	12.298	10.746	14.000	7.777	12.633
350	694.0	12.111	10.533	13.894	7.511	12.606
360	694.8	11.925	10.321	13.787	7.247	12.579
370	695.4	11.740	10.110	13.681	6.983	12.553
380	695.9	11.556	9.899	13.576	6.720	12.526
390	696.4	11.372	9.690	13.471	6.459	12.500

EXOSPHERIC TEMPERATURE = 700 K

HEIGHT KM	TEMP K	LOG(N(N2) /M3)	LOG(N(O2) /M3)	LOG(N(O) /M3)	LOG(N(A) /M3)	LOG(N(HE) /M3)	LOG(N(H) /M3)
400	696.8	11.189	9.481	13.367	6.198	12.473	
420	697.4	10.826	9.065	13.159		12.421	
440	697.9	10.465	8.653	12.952		12.370	
460	698.3	10.106	8.243	12.747		12.318	
480	698.6	9.749	7.836	12.544		12.267	
500	698.8	9.395	7.431	12.341		12.216	11.55
520	699.0	9.043	7.029	12.140		12.166	11.547
540	699.1	8.693	6.629	11.940		12.116	11.534
560	699.3	8.345	6.232	11.742		12.066	11.521
580	699.4	8.000		11.544		12.017	11.509
600	699.5	7.656		11.348		11.968	11.496
620	699.5	7.314		11.153		11.919	11.484
640	699.6	6.975		10.95		11.870	11.472
660	699.6	6.637		10.76		11.822	11.460
680	699.7	6.301		10.574		11.774	11.448
700	699.7			10.383		11.726	11.435
720	699.7			10.194		11.679	11.424
740	699.8			10.005		11.632	11.412
760	699.8			9.816		11.585	11.400
780	699.8			9.632		11.538	11.388
800	699.8			9.446		11.492	11.376
820	699.9			9.262		11.446	11.365
840	699.9			9.079		11.400	11.353
860	699.9			8.897		11.354	11.342
880	699.9			8.715		11.309	11.330
900	699.9			8.535		11.264	11.319
920	699.9			8.356		11.219	11.308
940	699.9			8.178		11.175	11.296
960	699.9			8.000		11.130	11.285
980	699.9			7.824		11.086	11.274
1000	699.9			7.649		11.042	11.263
1050	699.9			7.215		10.934	11.236
1100	700.0			6.786		10.826	11.209
1150	700.0			6.364		10.721	11.182
1200	700.0					10.616	11.156
1250	700.0					10.513	11.130
1300	700.0					10.412	11.104
1350	700.0					10.312	11.079
1400	700.0					10.213	11.054
1450	700.0					10.115	11.029
1500	700.0					10.018	11.005
1600	700.0					9.829	10.958
1700	700.0					9.644	10.911
1800	700.0					9.464	10.866
1900	700.0					9.289	10.821
2000	700.0					9.117	10.778

EXOSPHERIC TEMPERATURE = 800 K

HEIGHT KM	TEMP K	LOG10(N2) /M3)	LOG10(O2) /M3)	LOG10(O) /M3)	LOG10(A) /M3)	LOG10(HE) /M3)
110	235.1	18.205	17.427	17.576	16.001	13.701
112	248.2	18.067	17.273	17.487	15.814	13.670
114	262.7	17.934	17.126	17.401	15.634	13.639
116	278.5	17.806	16.982	17.317	15.463	13.609
118	295.5	17.684	16.846	17.236	15.300	13.579
120	313.5	17.567	16.716	17.158	15.145	13.550
122	332.2	17.456	16.593	17.084	14.997	13.522
124	351.3	17.351	16.477	17.014	14.858	13.496
126	370.6	17.251	16.366	16.947	14.725	13.471
128	389.9	17.157	16.261	16.883	14.600	13.447
130	408.8	17.067	16.162	16.823	14.481	13.424
135	454.1	16.862	15.934	16.687	14.208	13.373
140	495.1	16.680	15.731	16.566	13.964	13.329
145	531.1	16.516	15.548	16.460	13.742	13.291
150	562.1	16.366	15.380	16.363	13.539	13.258
155	588.6	16.227	15.224	16.275	13.349	13.228
160	611.3	16.096	15.078	16.194	13.171	13.202
165	630.9	15.973	14.938	16.118	13.000	13.178
170	647.8	15.855	14.805	16.045	12.837	13.155
175	662.5	15.741	14.677	15.976	12.679	13.134
180	675.4	15.632	14.553	15.910	12.526	13.115
185	686.9	15.525	14.432	15.846	12.377	13.096
190	697.1	15.420	14.314	15.783	12.231	13.078
195	706.2	15.319	14.198	15.723	12.089	13.061
200	714.4	15.218	14.084	15.664	11.948	13.044
210	728.4	15.023	13.863	15.548	11.673	13.012
220	740.0	14.834	13.647	15.437	11.405	12.982
230	749.5	14.648	13.436	15.329	11.144	12.953
240	757.4	14.467	13.229	15.223	10.887	12.925
250	764.0	14.288	13.026	15.120	10.633	12.897
260	769.5	14.112	12.825	15.018	10.384	12.871
270	774.0	13.938	12.627	14.917	10.137	12.845
280	777.8	13.764	12.431	14.818	9.892	12.819
290	781.0	13.596	12.236	14.720	9.650	12.794
300	783.7	13.427	12.043	14.623	9.410	12.769
310	785.9	13.259	11.852	14.527	9.171	12.744
320	787.8	13.092	11.662	14.431	8.934	12.720
330	789.4	12.927	11.473	14.336	8.698	12.696
340	790.7	12.762	11.285	14.242	8.464	12.672
350	791.9	12.598	11.098	14.148	8.231	12.648
360	792.8	12.435	10.912	14.055	7.998	12.625
370	793.7	12.273	10.727	13.962	7.767	12.601
380	794.4	12.112	10.542	13.869	7.537	12.578
390	795.0	11.951	10.358	13.777	7.308	12.555

EXOSPHERIC TEMPERATURE = 800 K

HEIGHT KM	TEMP K	LOG10(N2) /M3)	LOG10(O2) /M3)	LOG10(O) /M3)	LOG10(A) /M3)	LOG10(HE) /M3)	LOG10(H) /M3)
400	795.6	11.791	10.175	13.686	7.079	12.532	
420	796.5	11.472	9.812	13.504	6.625	12.486	
440	797.1	11.156	9.450	13.323	6.174	12.441	
460	797.6	10.841	9.091	13.143		12.396	
480	798.1	10.529	8.735	12.965		12.351	
500	798.4	10.219	8.381	12.788		12.307	11.108
520	798.6	9.911	8.029	12.612		12.263	11.097
540	798.8	9.605	7.679	12.437		12.219	11.086
560	799.0	9.300	7.331	12.263		12.175	11.075
580	799.1	8.998	6.986	12.090		12.132	11.064
600	799.3	8.697	6.642	11.918		12.089	11.053
620	799.4	8.398	6.301	11.747		12.046	11.042
640	799.4	8.101		11.577		12.004	11.032
660	799.5	7.805		11.409		11.962	11.021
680	799.6	7.512		11.241		11.920	11.010
700	799.6	7.220		11.074		11.878	11.000
720	799.7	6.929		10.908		11.836	10.989
740	799.7	6.640		10.743		11.795	10.979
760	799.7	6.353		10.579		11.754	10.969
780	799.8	6.068		10.416		11.713	10.958
800	799.8			10.254		11.673	10.948
820	799.8			10.093		11.632	10.938
840	799.8			9.932		11.592	10.928
860	799.8			9.773		11.552	10.918
880	799.8			9.614		11.513	10.908
900	799.9			9.457		11.473	10.898
920	799.9			9.300		11.434	10.888
940	799.9			9.144		11.395	10.878
960	799.9			8.989		11.356	10.868
980	799.9			8.835		11.317	10.859
1000	799.9			8.681		11.279	10.849
1050	799.9			8.301		11.184	10.825
1100	799.9			7.926		11.090	10.801
1150	799.9			7.557		10.998	10.778
1200	800.0			7.192		10.906	10.755
1250	800.0			6.832		10.816	10.732
1300	800.0			6.476		10.727	10.710
1350	800.0			6.125		10.640	10.688
1400	800.0					10.553	10.666
1450	800.0					10.468	10.645
1500	800.0					10.383	10.623
1600	800.0					10.217	10.582
1700	800.0					10.056	10.541
1800	800.0					9.898	10.501
1900	800.0					9.745	10.463
2000	800.0					9.594	10.425

EXOSPHERIC TEMPERATURE = 1000 K

HEIGHT KM	TEMP K	LOG(N(N2) /M3)	LOG(N(O2) /M3)	LOG(N(O) /M3)	LOG(N(A) /M3)	LOG(N(ME) /M3)
110	243.5	18.205	17.429	17.570	16.006	13.694
112	256.7	18.068	17.276	17.481	15.822	13.662
114	275.6	17.937	17.130	17.394	15.647	13.630
116	294.0	17.811	16.991	17.311	15.480	13.599
118	313.7	17.692	16.859	17.230	15.322	13.568
120	334.5	17.579	16.733	17.154	15.172	13.539
122	356.2	17.471	16.615	17.081	15.031	13.510
124	378.5	17.370	16.502	17.011	14.897	13.483
126	400.9	17.274	16.396	16.946	14.771	13.458
128	423.3	17.183	16.296	16.884	14.652	13.433
130	445.4	17.098	16.202	16.826	14.539	13.411
135	499.1	16.903	15.986	16.693	14.282	13.359
140	549.0	16.730	15.794	16.577	14.053	13.315
145	594.5	16.575	15.623	16.473	13.848	13.276
150	635.2	16.435	15.467	16.381	13.660	13.242
155	671.3	16.306	15.323	16.297	13.487	13.213
160	703.1	16.187	15.189	16.220	13.325	13.186
165	731.3	16.075	15.064	16.149	13.172	13.162
170	756.2	15.969	14.945	16.082	13.027	13.140
175	778.4	15.868	14.831	16.019	12.888	13.119
180	798.1	15.770	14.721	15.959	12.755	13.100
185	815.9	15.677	14.616	15.901	12.625	13.082
190	831.9	15.586	14.514	15.846	12.500	13.065
195	846.3	15.498	14.414	15.793	12.377	13.049
200	859.3	15.413	14.317	15.741	12.258	13.034
210	882.0	15.247	14.129	15.641	12.026	13.005
220	900.7	15.087	13.948	15.546	11.802	12.977
230	916.4	14.932	13.772	15.454	11.585	12.952
240	929.4	14.781	13.601	15.366	11.372	12.927
250	940.2	14.634	13.434	15.279	11.164	12.904
260	949.3	14.490	13.269	15.195	10.960	12.881
270	956.8	14.347	13.107	15.112	10.759	12.859
280	963.1	14.207	12.947	15.031	10.560	12.838
290	968.4	14.069	12.790	14.951	10.364	12.817
300	972.8	13.932	12.633	14.872	10.169	12.796
310	976.5	13.796	12.479	14.794	9.976	12.776
320	979.7	13.661	12.325	14.716	9.785	12.756
330	982.3	13.528	12.173	14.639	9.595	12.737
340	984.6	13.395	12.021	14.563	9.406	12.717
350	986.5	13.263	11.871	14.488	9.219	12.698
360	988.1	13.132	11.721	14.412	9.032	12.679
370	989.5	13.002	11.572	14.338	8.846	12.660
380	990.7	12.872	11.424	14.263	8.661	12.641
390	991.7	12.743	11.277	14.189	8.477	12.623

EXOSPHERIC TEMPERATURE = 1000 K

HEIGHT KM	TEMP K	LOG(N(N2) /M3)	LOG(N(O2) /M3)	LOG(N(O) /M3)	LOG(N(A) /M3)	LOG(N(ME) /M3)	LOG(N(H) /M3)
400	992.6	12.614	11.130	14.116	8.294	12.604	
420	994.1	12.359	10.838	13.969	7.930	12.567	
440	995.2	12.105	10.548	13.824	7.569	12.531	
460	996.1	11.853	10.261	13.680	7.210	12.495	
480	996.8	11.603	9.975	13.538	6.853	12.459	
500	997.3	11.355	9.692	13.396	6.499	12.423	10.438
520	997.7	11.108	9.410	13.255	6.147	12.388	10.428
540	998.1	10.863	9.130	13.115		12.353	10.420
560	998.4	10.619	8.851	12.975		12.318	10.411
580	998.6	10.377	8.575	12.837		12.283	10.402
600	998.8	10.137	8.300	12.699		12.249	10.393
620	998.9	9.897	8.027	12.563		12.214	10.384
640	999.1	9.659	7.755	12.427		12.180	10.376
660	999.2	9.423	7.485	12.292		12.147	10.367
680	999.3	9.188	7.216	12.157		12.113	10.359
700	999.4	8.954	6.949	12.024		12.080	10.350
720	999.4	8.722	6.684	11.891		12.046	10.342
740	999.5	8.491	6.420	11.759		12.013	10.334
760	999.5	8.261	6.157	11.628		11.981	10.325
780	999.6	8.032		11.498		11.948	10.317
800	999.6	7.805		11.368		11.915	10.309
820	999.7	7.579		11.239		11.883	10.301
840	999.7	7.355		11.111		11.851	10.293
860	999.7	7.131		10.983		11.819	10.285
880	999.8	6.909		10.856		11.787	10.277
900	999.8	6.688		10.730		11.756	10.269
920	999.8	6.469		10.604		11.724	10.261
940	999.8	6.250		10.480		11.693	10.253
960	999.8	6.033		10.356		11.662	10.245
980	999.8			10.232		11.631	10.237
1000	999.9			10.109		11.601	10.229
1050	999.9			9.805		11.525	10.210
1100	999.9			9.506		11.450	10.191
1150	999.9			9.210		11.375	10.173
1200	999.9			8.918		11.302	10.154
1250	999.9			8.630		11.230	10.136
1300	999.9			8.345		11.159	10.118
1350	1000.0			8.065		11.089	10.101
1400	1000.0			7.788		11.020	10.083
1450	1000.0			7.514		10.951	10.066
1500	1000.0			7.244		10.884	10.049
1600	1000.0			6.715		10.751	10.016
1700	1000.0			6.198		10.622	9.983
1800	1000.0					10.496	9.951
1900	1000.0					10.373	9.920
2000	1000.0					10.253	9.890

EXOSPHERIC TEMPERATURE = 1500 K

HEIGHT KM	TEMP K	LOG(N(N2) /M3)	LOG(N(O2) /M3)	LOG(N(O) /M3)	LOG(N(A) /M3)	LOG(N(HE) /M3)
110	257.6	18.204	17.431	17.561	16.014	13.682
112	276.4	18.070	17.282	17.471	15.836	13.649
114	297.2	17.941	17.140	17.384	15.666	13.615
116	319.9	17.819	17.005	17.301	15.506	13.583
118	344.2	17.704	16.878	17.221	15.355	13.551
120	370.0	17.595	16.758	17.146	15.213	13.521
122	396.7	17.493	16.645	17.074	15.080	13.491
124	424.2	17.397	16.539	17.007	14.955	13.464
126	451.8	17.306	16.440	16.943	14.838	13.438
128	479.5	17.221	16.347	16.884	14.728	13.413
130	507.0	17.141	16.258	16.827	14.624	13.390
135	574.7	16.959	16.058	16.700	14.387	13.338
140	640.2	16.799	15.882	16.589	14.179	13.293
145	702.7	16.656	15.725	16.490	13.993	13.253
150	761.7	16.528	15.583	16.401	13.824	13.218
155	817.1	16.410	15.454	16.321	13.670	13.187
160	868.7	16.303	15.334	16.248	13.528	13.159
165	916.8	16.203	15.224	16.181	13.396	13.134
170	961.4	16.110	15.120	16.119	13.272	13.110
175	1002.7	16.022	15.023	16.061	13.155	13.089
180	1041.1	15.940	14.931	16.007	13.044	13.070
185	1076.7	15.861	14.843	15.956	12.938	13.051
190	1109.6	15.786	14.759	15.908	12.836	13.034
195	1140.1	15.714	14.679	15.862	12.739	13.019
200	1168.3	15.645	14.601	15.818	12.645	13.004
210	1218.6	15.514	14.454	15.735	12.466	12.976
220	1261.4	15.391	14.315	15.658	12.296	12.951
230	1297.8	15.274	14.184	15.586	12.135	12.929
240	1328.5	15.162	14.057	15.518	11.980	12.908
250	1354.4	15.054	13.936	15.453	11.830	12.889
260	1376.2	14.950	13.818	15.390	11.685	12.870
270	1394.4	14.849	13.703	15.330	11.543	12.853
280	1409.7	14.750	13.591	15.272	11.404	12.837
290	1422.6	14.654	13.481	15.215	11.268	12.821
300	1433.4	14.559	13.373	15.159	11.133	12.806
310	1442.5	14.465	13.266	15.104	11.001	12.791
320	1450.1	14.373	13.161	15.051	10.870	12.777
330	1456.6	14.281	13.057	14.998	10.741	12.763
340	1462.1	14.191	12.954	14.945	10.613	12.749
350	1466.8	14.101	12.852	14.894	10.486	12.736
360	1470.8	14.013	12.751	14.842	10.360	12.723
370	1474.2	13.924	12.650	14.792	10.234	12.710
380	1477.2	13.837	12.550	14.741	10.110	12.697
390	1479.7	13.750	12.451	14.691	9.986	12.684

EXOSPHERIC TEMPERATURE = 1500 K

HEIGHT KM	TEMP K	LOG(N(N2) /M3)	LOG(N(O2) /M3)	LOG(N(O) /M3)	LOG(N(A) /M3)	LOG(N(HE) /M3)	LOG(N(H) /M3)
400	1481.9	13.663	12.352	14.641	9.863	12.671	
420	1485.5	13.492	12.156	14.543	9.618	12.646	
440	1488.3	13.321	11.962	14.445	9.376	12.621	
460	1490.4	13.153	11.770	14.349	9.136	12.597	
480	1492.0	12.985	11.578	14.253	8.897	12.573	
500	1493.4	12.819	11.389	14.158	8.661	12.549	9.482
520	1494.4	12.654	11.200	14.064	8.426	12.525	9.476
540	1495.3	12.491	11.013	13.970	8.192	12.502	9.470
560	1496.0	12.328	10.827	13.877	7.960	12.478	9.464
580	1496.5	12.166	10.643	13.785	7.730	12.455	9.458
600	1497.0	12.005	10.459	13.693	7.501	12.432	9.452
620	1497.4	11.846	10.277	13.601	7.273	12.409	9.446
640	1497.7	11.687	10.095	13.511	7.047	12.387	9.440
660	1498.0	11.529	9.915	13.421	6.822	12.364	9.434
680	1498.2	11.372	9.736	13.331	6.598	12.342	9.429
700	1498.4	11.216	9.558	13.242	6.376	12.319	9.423
720	1498.6	11.061	9.381	13.153	6.155	12.297	9.417
740	1498.8	10.907	9.205	13.065		12.275	9.412
760	1498.9	10.754	9.030	12.978		12.253	9.406
780	1499.0	10.602	8.856	12.891		12.231	9.401
800	1499.1	10.450	8.683	12.804		12.210	9.395
820	1499.2	10.300	8.511	12.718		12.188	9.390
840	1499.3	10.150	8.340	12.633		12.167	9.384
860	1499.3	10.001	8.170	12.547		12.145	9.379
880	1499.4	9.853	8.000	12.463		12.124	9.374
900	1499.4	9.705	7.832	12.379		12.103	9.368
920	1499.5	9.559	7.665	12.295		12.082	9.363
940	1499.5	9.413	7.498	12.212		12.061	9.358
960	1499.6	9.268	7.333	12.129		12.041	9.353
980	1499.6	9.124	7.168	12.047		12.020	9.347
1000	1499.6	8.981	7.005	11.965		12.000	9.342
1050	1499.7	8.626	6.599	11.762		11.949	9.330
1100	1499.7	8.276	6.200	11.562		11.899	9.317
1150	1499.8	7.931		11.365		11.850	9.304
1200	1499.8	7.590		11.171		11.801	9.292
1250	1499.8	7.254		10.978		11.753	9.280
1300	1499.9	6.922		10.789		11.705	9.268
1350	1499.9	6.594		10.602		11.659	9.256
1400	1499.9	6.271		10.417		11.612	9.245
1450	1499.9			10.235		11.567	9.233
1500	1499.9			10.055		11.522	9.222
1600	1499.9			9.702		11.433	9.200
1700	1500.0			9.357		11.347	9.178
1800	1500.0			9.021		11.263	9.157
1900	1500.0			8.693		11.181	9.136
2000	1500.0			8.373		11.101	9.116

APPENDIX B

Reactions and Reaction Coefficients

$O^+(^4S) + N_2(^1\Sigma) \rightarrow N(^4S) + NO^+(^1\Sigma) + 1.10$ eV $\gamma_1 = 1.2 \times 10^{-12}\ (300/T(N_2))\ cm^3\ sec^{-1}$

$O^+(^4S) + O_2(^3\Sigma) \rightarrow O_2^+(^2\Pi) + O(^3P) + 1.14$ eV $\gamma_2 = 1.2 \times 10^{-11}\ (300/T)^{\frac{1}{2}}\ cm^3\ sec^{-1}$

$He^+(^2S) + N_2 \rightarrow He(^1S) + N(^4S) + N^+(^3P) + 0.28$ eV $\gamma_6 = 10^{-9}\ cm^3\ sec^{-1}$

$He^+(^2S) + N_2 \rightarrow He(^1S) + N_2 + (C^2\Sigma)_{v=3,4}$ $\gamma_6^* = 10^{-9}\ cm^3\ sec^{-1}$

$He^+(^2S) + O_2(^3\Sigma) \rightarrow He(^1S) + O(^3P) + O^+(^4S) + 5.85$ eV $\gamma_{10} = 1.5 \times 10^{-9}\ cm^3\ sec^{-1}$

$He^+(^2S) + O_2(^3\Sigma) \rightarrow He(^1S) + O_2^+\ (^2\Pi) + 12.25$ eV $\gamma_{10}^* = 2 \times 10^{-10}\ cm^3\ sec^{-1}$

$He(^1S) + h\nu(\lambda < 504\text{Å}) \rightarrow He^+\ (^2S) + e$: $I(He) = (8.0 \pm 4.0) \times 10^{-8}\ sec^{-1}$

APPENDIX C

The following is a calculation of the nonanalytic term in the power spectra of incoherent-scatter returns.

$$\int_0^{\omega/\Omega} \exp y^2 \, dy = \int_0^{\omega/\Omega} \left(1 + t^2 + \frac{t^4}{2!} + \ldots\ldots\right) dt$$

$$= \frac{\omega}{\Omega} + \frac{(\omega/\Omega)^3}{3} + \frac{(\omega/\Omega)^5}{5 \cdot 2!} + \frac{(\omega/\Omega)^7}{7 \cdot 3!} + \ldots\ldots$$

$$= \frac{\omega}{\Omega}\left(1 + \frac{(\omega/\Omega)^2}{3} + \frac{(\omega/\Omega)^4}{5 \cdot 2!} + \ldots\ldots\right)$$

$$= \frac{\omega}{\Omega} \, {}_1F_1(1/2;\ 3/2;\ \omega^2/\Omega^2)$$

where ${}_1F_1(1/2;\ 3/2;\ \omega^2/\Omega^2)$ is the degenerate hypergeometric function or Kummei function given in *Abramowitz and Stegun* [1964].

Gradshteyn and Ryzhik [1965] gives an expression for ${}_1F_1$ as

$${}_1F_1(1/2;\ 3/2;\ \omega^2/\Omega^2) = \exp\left(\omega^2/\Omega^2\right) \sum_{k=1}^{\infty} \frac{(k-1)!}{(2k-1)!} \left(-\omega^2/\Omega^2\right)^{k-1}$$

This summation is useful when ω^2/Ω^2 is not large. When ω^2/Ω^2 becomes large the summation will not converge. Therefore, one has to use an asymptotic expansion, which is given by [*Abramowitz and Stegun*, 1964]

$${}_1F_1(1/2;\ 3/2;\ \omega^2/\Omega^2) = \frac{\Omega^2}{2\omega^2} \exp\left(\omega^2/\Omega^2\right) \left(1 + \frac{\Omega^2}{2\omega^2} + 3\left(\frac{\Omega^2}{2\omega^2}\right)^2 + 15\left(\frac{\Omega^2}{2\omega^2}\right)^3 + 105\left(\frac{\Omega^2}{2\omega^2}\right)^4 + \ldots\ldots\right)$$

APPENDIX D
COMPUTER PROGRAMS USED IN THE CALCULATION OF EXPERIMENTAL AND THEORETICAL ELECTRON AND ION TEMPERATURES

In this appendix a list and description of some of computer programs used in Chapters 5 and 6 is given. Programs MAC, NOINE, and ACNAL were used to calculate the experimental electron and ion temperatures and densities given in Chapter 5. The program used to calculate the theoretical electron and ion temperatures is also described and given in this appendix.

The following program calculates a library of theoretical ACF's and stores them on tape. Subroutine DISP calculates the electron and ion dispersion functions. Subroutine CFS calculates the cosine factors for the cosine transform of the power spectrum. Subroutine ACF calculates the autocorrelation function. The power spectrum is calculated and stored in array W. The variables M1, M2, and M3 refer to the masses in kg of O^+, H^+, and the electron respectively while T1, T2, and T3 represent these particles temperatures. Constant factors necessary for the calculation of the power spectrum are given by C, C2, C3, and C4.

The power spectrum is calculated for a range of values of $T(O^+)$, $T_e/T(O^+)$, $T(H^+)/T(O^+)$, and $n(O^+)/n_e$ (B4). After the ACF (A) is calculated it is sent to the printer and stored on magnetic tape for use by other programs.

```
      PROGRAM MAC(INPUT,OUTPUT,TAPE7,AOA,TAPE5=INPUT,PUNCH,TAPE6=AOA)
      COMMON/CFA/CF(24,301)
       DIMENSION W(301),F(301),G(301),A(24)
      DIMENSION H(301)
      DIMENSION X(9)
      REAL   L,K,M2,M3,PO,K1,PI,M1


      PI=3.141592654
      K=1.380622E-23
      PO=8.854185E-12
      M1=2.655913E-26
      M2=1.672614E-27
      M3=9.109558E-31
      L=.69719186
      NACF=0
      E=2.0E11
      C=L**2./(32.*PI**2.*K)
      C2=C*PI
      C3=      (1.6021917E-19)**2/PO/K
      C4=(L/4./PI)**2.
      D4=1.0E3
      TS=8.E-6
      CALL CFS(   D4,TS)
      READ(5,100)ITO
      READ(5,100)ITS
      READ(5,100)IT1
100   FORMAT(I4)
      T1=ITS+FLOAT(ITO-1)*IT1
      REWIND 7
      READ(5,100)IF1
      WRITE(6,109)ITO,ITS,IT1,IF1
109   FORMAT(1X,7HNO. INC,I4,7HST TEMP,I4,8HTEMP INC,I4,8HNO FILES,I4)
      READ(5,100)ITRS
      READ(5,100)ITRI
      READ(5,100)IBS
      READ(5,100)IBI
      WRITE(6,110)ITRS,ITRI,IBS,IBI
110   FORMAT(1X,5HTR ST,I4,6HTR INC,I4,5HB4 ST,I4,6HB4 INC,I4)
      IF(IF1.EQ.0)GO TO 85
      DO 84 IFIL=1,IF1
      DO 84 IFK=1,96
      READ(7)A
84    CONTINUE
85    CONTINUE
      X1=M1/T1
      CALL DISP(X1,D4,F,C)
      DO 19 IT=1,4
      T2=T1+FLOAT(IT-1)*T1/10.0
      X2=M2/T2
      CALL DISP(X2,D4,G,C)
      DO  23 J=1,4
      T3=(ITRS+(J-1)*ITRI)*T1/10.
      X3=M3/T3
      CALL DISP(X3,D4,H,C)
      DO 56 IB=1,6
      B4=(IBS+(IB-1)*IBI)/1000.
      NACF=NACF+1
      WRITE(6,104)T1,T2,T3,B4,NACF
104    FORMAT(1X,3F8.1,F8.2,I5)
       W1=0.0
      DO 30 IK=1,301
34    F1=F(IK)
      F2=G(IK)
      F3=H(IK)
      F8=(1.-B4)*SQRT(C2*X2)*EXP(-C*X2    *W1**2 )
      F5=-F8*W1
       F9=SQRT(C2*X3)*EXP(-C*X3    *W1**2 )
```

```
      F6=-F9*W1
      F7=B4     *SQRT(C2*X1)*EXP(-C*X1    *W1**2 )
      F4=-F7*W1
38      A1=(1.+C4*C3*E*(B4*F1/T1+(1.-B4)*F2/T2))**2 *F9
      A2=C4*C4*(C3*E*(    F4/T1+         F5/T2))**2 *F9
      A3=C4*C4*(C3*E/T3)**2 *(F3**2 +F6**2 )*(F7+F8)
      A4=(1.+C4*C3*E*(F3/T3+F1*B4/T1+F2*(1.-B4)/T2))**2
      A5=C4*C4*(C3*E*(F6/T3+F4    /T1+F5         /T2))**2
      W(IK)=(A1+A2+A3)/(A4+A5)
      W1=W1+D4
70     CONTINUE
      CALL ACF(W,A,D4)
        WRITE(6,103)A
56     CONTINUE
23    CONTINUE
19    CONTINUE
      END




      SUBROUTINE DISP(X1,D4,F,C)
      DIMENSION F(301)
      Z=C*2
        K7=1
      C5=1.0
      DO 77 I=1,301
      W1=FLOAT(I-1)*D4
      IF(W1.NE.0.0)GO TO 82
      F1=1.0
      GO TO 86
82    IF(K7.LT.60)GO TO 85
83    C5=Z*X1*W1*W1
      F1=-1./C5-3./C5**2-15./C5**3-105./C5**4-945./C5**5
      GO TO 86
85    AK1=1.0
      AF2=1.0
      F1=0.0
      G1=0.0
      DO 61 K7=1,61,2
      AK1=(2.0  * FLOAT(K7)-1.0  )*AK1
      F1=AF2/AK1+F1
      AF2=    (W1*W1*Z*X1)*AF2
      AK1=(2.0  * FLOAT(K7)+1.0  )*AK1
      F1=-AF2/AK1+F1
      AF2=    (W1*W1*Z*X1)*AF2
      IF( ABS((F1-G1)/F1).LT.1.0E-8)GO TO 69
       G1=F1
61      CONTINUE
      GO TO 83
69    F1=1.0  -F1*    (W1*W1*Z*X1)
86     F(I)=F1
77     CONTINUE
      RETURN
      END
```

```
      SUBROUTINE CFS(   D4,TS)
      COMMON/CFA/CF(24,301)
      DO 94 I=1,24
      W1=0.0
      CF(I,1)=1.0000000
      H0=FLOAT(I-1)*TS
      DO 97 K9=2,298,2
      W1=W1+D4
      CF(I,K9)=4.*COS(W1*H0)
      W1=W1+D4
      CF(I,K9+1)=2.*COS(W1*H0)
97    CONTINUE
      CF(I,300)=COS((W1+D4)*H0)*4.0
      CF(I,301)=COS((W1+D4*2.)*H0)
94    CONTINUE
      RETURN
      END
      SUBROUTINE ACF(W,A,D4)
      COMMON/CFA/CF(24,301)
      DIMENSION W(301),A(24)
      DO 94  I=1,24
      W1=0.0
      H0=FLOAT(I-1)*8.E-6
      A(I)=W(1)
      DO 97 K9=2,298,2
      A(I)=A(I)+CF(I,K9)*W(K9)+CF(I,K9+1)*W(K9+1)
97     CONTINUE
      A(I)=A(I)+CF(I,300)*W(300)+CF(I,301)*W(301)
      IF(I.NE.1)A(I)=A(I)/A(1)
94    CONTINUE
      RETURN
      END
```

Below is a list of the physical quantities for the library of ACF's. Each file contains 96 ACF's. For files 1.34 $T(H^+)/T(O^+)$ goes from 1.0 to 1.3 in steps of .1. For files 35-37 $T(H^+)/T(O^+)$ equals 1.4-1.7 in steps of .1.

FILE	$n(O^+)/n_e$	$T(O^+)$	$T_e/T(O^+)$
1	0.0 - 0.5	800	1.4 - 1.7
2	0.0 - 0.5	1000	1.4 - 1.7
3	0.0 - 0.5	1200	1.4 - 1.7
4	0.0 - 0.5	1400	1.4 - 1.7
5	0.0 - 0.5	1600	1.4 - 1.7
6	0.0 - 0.5	1800	1.4 - 1.7
7	0.0 - 0.5	2000	1.4 - 1.7
8	.55 - .80	800	1.4 - 1.7
9	.55 - .80	1000	1.4 - 1.7
10	.55 - .80	2000	1.4 - 1.7
11	.55 - .80	2400	1.4 - 1.7
12	.55 - .80	2800	1.4 - 1.7
13	.85 - .975	800	1.4 - 1.7
14	.85 - .975	1000	1.4 - 1.7
15	.85 - .975	1200	1.4 - 1.7
16	.85 - .975	1400	1.4 - 1.7
17	.85 - .975	1600	1.4 - 1.7
18	.85 - .975	1800	1.4 - 1.7
19	.85 - .975	2000	1.4 - 1.7
20	.85 - .975	800	1.8 - 2.1
21	.85 - .975	900	1.8 - 2.1
22	.85 - .975	1000	1.8 - 2.1
23	.85 - .975	1100	1.8 - 2.1
24	.85 - .975	2000	1.0 - 1.3
25	.85 - .975	2500	1.0 - 1.3
26	.85 - .975	3000	1.0 - 1.3
27	0.0 - 0.5	800	1.0 - 1.3
28	0.0 - 0.5	1200	1.0 - 1.3
29	0.0 - 0.5	1600	1.0 - 1.3
30	0.0 - 0.5	2000	1.0 - 1.3
31	.55 - .80	800	1.0 - 1.3
32	.55 - .80	1200	1.0 - 1.3
33	.55 - .80	1600	1.0 - 1.3
34	.55 - .80	2000	1.0 - 1.3
35	.85 - .975	1200	1.5 - 1.8
36	.85 - .975	1400	1.5 - 1.8
37	.85 - .975	1600	1.5 - 1.8
38	1.0	800-1500	1.4 - 2.5

Program NOINE calculates $n(O^+)/n_e$ by fitting theoretical values of TZERO to experimental values of TZERO. This program also calculates T_e/T_i by fitting theoretical values of AMIN to experimental values of TZERO. A library of theoretical ACF's is read from magnetic tape. Experimental ACF's are also read from magnetic tape. Theoretical and experimental values of TZERO are found in subroutine AZH. In subroutine FAMIN theoretical and experimental values of AMIN are found. Subroutine RRAF calculates the array of theoretical values of AMIN. Newton's method (see Section 5.2.1) is used to calculate $n(O^+)/n_e$. This is done in subroutine FINDX. T_e/T_i is also calculated by Newton's method. The program outputs the results of $n(O^+)/n_e$ and T_e/T_i for the 15 altitudes of both short and long pulse data into file XFILE for later use by program ACNAL.

The array AC contains the library of theoretical ACF's. The arrays TZT and AMINT contain the theoretical values of TZERO and AMIN. X(1) represents $n(O^+)/n_e$. X(2) represents T_e/T_i.

```
      PROGRAM NOINE(INPUT,OUTPUT,XFILE,TAPE9=XFILE,TAPE5=INPUT,
     1TAPE6=OUTPUT,TAPE8,ACFF,TAPE7=ACFF)
      DIMENSION AC(24,7,24),ACF(24),REX(24),TZT(6),X(2),SN(16)
      DIMENSION TZ(16),AMIN(16),AMINT(3,12,6),EN(16),TH(16),THT(6)
      DIMENSION ACE(24)
      REWIND 7
      REWIND 8
      READ(5,103)IREC
103   FORMAT(I4)
      IF(IREC.EQ.0)GO TO 231
      DO 230 I=1,IREC
      DO 229 J=1,15
229   READ(8)ACF
      READ(8)SN
230   READ(8)EN
231   CONTINUE
      DO 1 I=1,29
      DO 1 L=1,96
1     READ(7)ACF
      DO 2 I=1,24
2     READ(7)(AC(M,1,I),M=1,24)
      WRITE(6,100)(AC(M,1,1),M=1,5)
      REWIND 7
      DO 201 I=1,6
      DO 201 L=1,96
201   READ(7)ACF
      DO 3 I=1,24
3     READ(7)(AC(M,2,I),M=1,24)
      WRITE(6,100)(AC(M,2,1),M=1,5)
      REWIND 7
      DO 4 I=1,33
      DO 4 L=1,96
4     READ(7)ACF
      DO 5 I=1,24
5     READ(7)(AC(M,3,I),M=1,24)
      WRITE(6,100)(AC(M,3,24),M=1,5)
      REWIND 7
      DO 6 I=1,9
      DO 6 L=1,96
6     READ(7)ACF
      DO 7 I=1,24
7     READ(7)(AC(M,4,I),M=1,24)
      WRITE(6,100)(AC(M,4,1),M=1,5)
      REWIND 7
      DO 8 I=1,23
      DO 8 L=1,96
8     READ(7)ACF
      DO 9 I=1,24
9     READ(7)(AC(M,5,I),M=1,24)
      WRITE(6,100)(AC(M,5,1),M=1,5)
      REWIND 7
      DO 10 I=1,12
      DO 10 L=1,96
10    READ(7)ACF
      DO 11 I=1,24
11    READ(7)(AC(M,6,I),M=1,24)
      WRITE(6,100)(AC(M,6,1),M=1,5)
      REWIND 7
      DO 12 I=1,19
      DO 12 L=1,96
12    READ(7)ACF
      DO 13 I=1,24
13    READ(7)(AC(M,7,I),M=1,24)
      WRITE(6,100)(AC(M,7,1),M=1,5)
      DO 131 I=1,7
      DO 131 J=1,24
131   AC(1,I,J)=1.0
100   FORMAT(1X,12F10.5)
```

```
      CALL RRAF(AMINT,AC)
C     FIND NO+/NE                          READ IN EXP ACF
      DO 70 IFI=1,10
      X(1)=.975
      X(2)=1.4
      DO 67 JH=2,16
      READ(8)ACE
      WRITE(6,109)JH,(ACE(M),M=1,5)
109   FORMAT(I4,2X,5F10.5)
      IF(IFI.EQ.2.AND.JH.GT.11)GO TO 66
101   FORMAT(1X,16F6.2)
      CALL AZH(TZ(JH),TH(JH),ACE)
      CALL FAMIN(AMIN(JH),ACE)
      WRITE(6,100)TZ(JH),TH(JH),AMIN(JH)
      TH(JH)=10.*(TH(JH)-1.3)
      IF(X(1).LT..85)GO TO 51
      DO 20 I=1,6
      DO 19 M=1,24
19    REX(M)=AC(M,6,I)
20    CALL AZH(TZT(I),THA,REX)
      XM1=.975
      XL1=.850
      CALL FINDX(XM1,XL1,X,TZT,TZ(JH))
      IF(X(1).GT.XL1)GO TO 60
      IF(X(1).LT.XL1)X(1)=XL1
C     FIND NO+/NE IF .55<NO+/NE<.80
      DO 21 I=1,6
      DO 22 M=1,24
22    REX(M)=AC(M,4,I)
21    CALL AZH(TZT(I),THA,REX)
51    IF(X(1).LE..526)GO TO 52
      XM1=.80
      XL1=.55
      CALL FINDX(XM1,XL1,X,TZT,TZ(JH))

      IF(X(1).GT..526)GO TO 60
C     FIND NO+/NE IF 0.0<NO+/NE<.5
      DO 24 I=1,6
      DO 23 M=1,24
23    REX(M)=AC(M,2,I)
      CALL AZH(TZT(I),THT(I),REX)
24    THT(I)=10.*(THT(I)-1.3)
52      XL1=0.0
      XM1=.5
      CALL FINDX(XM1,XL1,X,THT,TH(JH))
      IF(X(1).GT..524)X(1)=.524
      IF(X(1).LT.0.0)X(1)=0.0
C     READ IN THE REST OF AMINT FILE
C     FIND TR FROM AMIN
60    IF(X(1).GE..85)IX1=3
      IF(X(1).LT..85.AND.X(1).GT..526)IX1=2
      IF(X(1).LE..526)IX1=1
      IB4=(X(1)-XL1)/(XM1-XL1)/.2+1.49
      IF(IB4.GT.6)IB4=6
      X2=1.75
      IF(X(1).GT..85)X2=2.15
      DO 65 ITER=1,10
      IF(X(2).LT.1.0)X(2)=1.0
      IF(X(2).GT.X2)X(2)=X2
      ITR=(X(2)-1.0)*10.+1.49
      K=1
      IF(ITR.EQ.1)K=-1
      DX2=(AMINT(IX1,ITR,IB4)-AMINT(IX1,ITR-K,IB4))*K*10.
      X(2)=X(2)-(AMINT(IX1,ITR,IB4)-AMIN(JH))/DX2
      IF(ABS(AMINT(IX1,ITR,IB4)-AMIN(JH)).LT..001)GO TO 66
65    CONTINUE
      IF(X(2).LT.1.005)X(2)=1.05
66    WRITE(6,104)X
67     WRITE(9,104)X
```

```
104   FORMAT(F8.5,F8.5)
      READ(8)SN
      READ(8)EN
      WRITE(6,101)SN
70    CONTINUE
      END
      SUBROUTINE RRAF(AMIN,AC)
      DIMENSION AMIN(3,12,6),AC(24,7,24),REX(24)
      DO 641 K=1,3
      DO 62 I=1,4
      DO 62 J=1,6
      K3=(K-1)*2+1
      J3=J+(I-1)*6
      DO 61 M=1,24
61    REX(M)=AC(M,K3,J3)
62     CALL FAMIN(AMIN(K,I,J),REX)
      DO 63 I=5,8
      DO 63 J=1,6
      K3=(K-1)*2+2
      J3=J+(I-5)*6
      DO 621 M=1,24
621   REX(M)=AC(M,K3,J3)
63    CALL FAMIN(AMIN(K,I,J),REX)
641   CONTINUE
      REWIND 7
      DO 632 I=9,12
      DO 632 J=1,6
      J3=J+(I-9)*6
      DO 631 M=1,24
631   REX(M)=AC(M,7,J3)
632   CALL FAMIN(AMIN(3,I,J),REX)
      RETURN
      END
      SUBROUTINE AZH(TZ,TH,R)

      DIMENSION R(24)
      DO 19 I=2,24
      IF(R(I).LT..5)GO TO 20
19    CONTINUE
20    TH=(R(I)-(R(I)-R(I-1))*FLOAT(I)-.5)/(R(I-1)-R(I))
      DO 21 I1=I,24
      IF(R(I1).LT.0.0)GO TO 22
21    CONTINUE
22    TZ=FLOAT(I1)+(R(I1))/(R(I1-1)-R(I1))
      TZ=TZ/TH
      RETURN
      END
      SUBROUTINE FAMIN(AMIN,R)
      DIMENSION R(24)
      DO 1 I=2,23
      IF(R(I).GT.R(I-1))GO TO 2
1     CONTINUE
2     CALL POL3(A1,A2,A3,I,R)
      XA=-A2/2./A1
      AMIN=A1*XA**2+A2*XA+A3
      RETURN
      END
      SUBROUTINE FINDX(XM1,XL1,X,TZT,TZ)
      DIMENSION X(2),TZT(6)
      DO 1 ITER=1,10
       IF(X(1).LT.XL1)X(1)=XL1
       IF(X(1).GT.XM1)X(1)=XM1
      IB4=(X(1)-XL1)/(XM1-XL1)/.2+1.49
      K=1
      IF(IB4.EQ.1)K=-1
      DX=(TZT(IB4)-TZT(IB4-K))*K/(XM1-XL1)/.2
      X3=(TZT(IB4)-TZ)
      X(1)=X(1)-X3/DX
      IF(ABS(X3).LT..01)GO TO 2
```

```
1       CONTINUE
2       CONTINUE
        RETURN
        END
        SUBROUTINE POL3(B0,B1,B2,J,R)
        DIMENSION R(24)
C       SUBROUTINE TO FIT  A THIRD DEGREE POLNOMIAL TO ACF
        J1=J-2
        J2=J-1
        J3=J
        B1=(R(J2)*FLOAT(J3**2-J1**2)+R(J3)*FLOAT(J1**2-J2**2)+R(J1)*FLOAT
       1(J2**2-J3**2))/(FLOAT(J2*(J3**2-J1**2)+J3*(J1**2-J2**2)+J1*(J2**2
       1-J3**2)))
        B0=(R(J1)-R(J3)-B1*FLOAT(J1-J3))/(FLOAT(J1**2-J3**2))
        B2=R(J1)-B0*FLOAT(J1**2)-B1*FLOAT(J1)
        RETURN
        END
```

Program ACNAL calculates $T(O^+)$, $T_e/T(O^+)$, and $T(H^+)/T(O^+)$ where $n(O^+)n_e$ from program NOINE is used. The method used is the method of fitting the theoretical ACF to the experimental ACF by minimizing the square of the difference between the two ACF's.

```
      PROGRAM ACNAL(INPUT,OUTPUT,XFILE,TAPE5=INPUT,TAPE8,
     1TAPE6=OUTPUT,TAPE9=XFILE,XFILE1,TAPE10=XFILE1,ACFF,TAPE7=ACFF)
      COMMON AC(24,3,96)
      DIMENSION X(5),ACF(24),HT(16),HTS(16),EN(16),Y(1)
      DIMENSION TZ(16),TH(16),TZT(4,6),REX(24),SN(16),ACE(24)
      REWIND 7
      REWIND 8
      READ(5,103)IREC
103   FORMAT(I4)
      IF(IREC.EQ.0)GO TO 231
      DO 230 I=1,IREC
      DO 229 J=1,15
      READ(8)ACF
102   FORMAT(1X,12F7.4/1X,12F7.4)
229   CONTINUE
      READ(8)SN
      READ(8)EN
106   FORMAT(1X/1X/1X,1P8E9.1/1X,1P8E9.1/1X,8F6.2/1X,8F6.2)
230   CONTINUE
231   CONTINUE
      XL4=1.0
      XM4=1.3
102   FORMAT(F8.3)
C     READ IN EXP. DATA
      DO 75 IFI=1,2
      DO 72 JH=2,16
      REWIND 7
      READ(8)ACE
C     READ IN X(1),X(2)
      READ(9,104)X(1),X(2)
      WRITE(6,104)X(1),X(2)
      WRITE(6,107)(ACE(M),M=1,5)
107   FORMAT(1X,5F10.5)
104   FORMAT(2F8.5)
      IF(IFI.EQ.2.AND.JH.GT.10)GO TO 72
      IF(X(1).GE..825)IX1=3
      IF(X(1).GT..526.AND.X(1).LT..825)IX1=2
      IF(X(1).LE..526)IX1=1
      GO TO(41,51,61),IX1
41    CONTINUE
      I1=X(1)*10.+1.49
      REWIND 7
      DO 42 I=1,26
      DO 42 L=1,96
42    READ(7)ACF
      DO 43 I=1,3
      DO 43 L=1,96
43    READ(7)(AC(M,I,L),M=1,24)
      CALL COMP(ACE,VAR,I3,I2,I4,I1)
      VAR1=VAR
      X(3)=800.+(I3-1)*400.
      X(2)=1.0+(I2-1)*.1
      X(4)=1.0+(I4-1)*.1
      DO 44 L=1,96
44    READ(7)(AC(M,1,L),M=1,24)
      REWIND 7
      REWIND 7
      DO 441 I=2,3
      DO 441 L=1,96
441   READ(7)(AC(M,I,L),M=1,24)
      CALL COMP(ACE,VAR,I3,I2,I4,I1)
      IF(VAR1.LT.VAR)GO TO 451
      VAR1=VAR
      X(2)=1.4+(I2-1)*.1
      IF(I3.EQ.1)X(2)=1.0+(I2-1)*.1
      X(3)=800.+(I3-2)*200.
      IF(I3.EQ.1)X(3)=2000.
      X(4)=1.0+(I4-1)*.1
```

```
451     DO 46 I=1,3
        DO 46 L=1,96
46      READ(7)(AC(M,I,L),M=1,24)
        CALL COMP(ACE,VAR,I3,I2,I4,I1)
        IF(VAR1.LT.VAR)GO TO 461
        VAR1=VAR
        X(4)=1.0+(I4-1)*.1
        X(2)=1.4+(I2-1)*.1
        X(3)=1200.+(I3-1)*.1
461     DO 47 I=2,3
        DO 47 L=1,96
47      READ(7)(AC(M,I,L),M=1,24)
        CALL COMP(ACE,VAR,I3,I2,I4,I1)
        IF(VAR1.LT.VAR)GO TO 71
        X(4)=1.0+(I4-1)*.1
        X(3)=1600.+(I3-1)*200.
        X(2)=1.4+(I2-1)*200.
        IF(I3.EQ.3)X(3)=1200.
48      GO TO 71
C       READ IN ACF FOR .55<NO+/NE<.85
51      REWIND 7
        I1=(X(1)-.55)*20.+1.49
        DO 511 I=1,7
        DO 511 L=1,96
511     READ(7)ACF
        DO 52 I=1,3
        DO 52 L=1,96
52      READ(7)(AC(M,I,L),M=1,24)
        CALL COMP(ACE,VAR,I3,I2,I4,I1)
        VAR1=VAR
        X(2)=1.4+(I2-1)*.1
        X(3)=600.+(I3-1)*200.
        IF(I3.EQ.3)X(3)=2000.
        X(4)=1.0+(I4-1)*.1

        DO 521 I=1,2
        DO 521 L=1,96
521     READ(7)(AC(M,I,L),M=1,24)
        DO 531 I=1,18
        DO 531 L=1,96
531     READ(7)ACF
        DO  53 L=1,96
53      READ(7)(AC(M,3,L),M=1,24)
        CALL COMP(ACE,VAR,I3,I2,I4,I1)
        IF(VAR1.LT.VAR)GO TO 540
        VAR1=VAR
        X(4)=1.0+(I4-1)*.1
        X(2)=1.4+(I2-1)*.1
        IF(I3.EQ.3)X(2)=1.0+(I2-1)*.1
        X(3)=2400.+(I3-1)*400.
        IF(I3.EQ.3)X(3)=800.
540     DO 541 I=1,3
        DO 541 L=1,96
541     READ(7)(AC(M,I,L),M=1,24)
        CALL COMP(ACE,VAR,I3,I2,I4,I1)
        IF(VAR1.LT.VAR)GO TO 71
        X(4)=1.0+(I4-1)*.1
        X(3)=1200.+(I3-1)*400.
        X(2)=1.0+(I2-1)*.1
55      GO TO 71
61      REWIND 7
        I1=(X(1)-.85)*40.+1.49
        IF(I1.GT.6)I1=6
        IF(I1.LT.1)I1=1
        DO 62 I=1,12
        DO 62 L=1,96
62      READ(7)ACF
        DO 63 I=1,3
        DO 63 L=1,96
```

```
63      READ(7)((AC(M,I,L),M=1,24)
        CALL COMP(ACE,VAR,I3,I2,I4,I1)
        VAR1=VAR
        X(2)=1.4+(I2-1)*.1
        X(4)=1.0+(I4-1)*.1
        X(3)=800.+(I3-1)*200.
        DO 64 I=1,3
        DO 64 L=1,96
64      READ(7)((AC(M,I,L),M=1,24)
        CALL COMP(ACE,VAR,I3,I2,I4,I1)
        IF(VAR1.LT.VAR)GO TO 641
        VAR1=VAR
        X(3)=1400.+(I3-1)*200.
        X(2)=1.4+(I2-1)*.1
        X(4)=1.0+(I4-1)*.1
641     DO 65 I=1,3
        DO 65 L=1,96
65      READ(7)((AC(M,I,L),M=1,24)
        CALL COMP(ACE,VAR,I3,I2,I4,I1)
        IF(VAR1.LT.VAR)GO TO 651
        VAR1=VAR
        X(3)=800.+(I3-2)*100.
        IF(I3.EQ.1)X(3)=2000.
        X(2)=1.8+(I2-1)*.1
        IF(I3.EQ.1)X(2)=1.4+(I2-1)*.1
        X(4)=1.0+(I4-1)*.1
651     DO 66 I=1,3
        DO 66 L=1,96
66      READ(7)((AC(M,I,L),M=1,24)
        CALL COMP(ACE,VAR,I3,I2,I4,I1)
        IF(VAR1.LT.VAR)GO TO 661
        VAR1=VAR
        X(3)=1000.+(I3-1)*100.
        IF(I3.EQ.3)X(3)=2000.

        X(2)=1.8+(I2-1)*.1
        IF(I3.EQ.3)X(2)=1.0+(I2-1)*.1
        X(4)=1.0+(I4-1)*.1
661     DO 67 I=2,3
        DO 67 L=1,96
67      READ(7)((AC(M,I,L),M=1,24)
        CALL COMP(ACE,VAR,I3,I2,I4,I1)
        IF(VAR1.LT.VAR)GO TO 71
        X(3)=2500.+(I3-2)*500.
        IF(I3.EQ.1)X(3)=1000.
        X(2)=1.0+(I2-1)*.1
        IF(I3.EQ.1)X(2)=1.8+(I2-1)*.1
        X(4)=1.0+(I4-1)*.1
71      CONTINUE
        WRITE(6,100)JH,X(1),X(3),X(2),X(4)
100     FORMAT(I4,F8.2,F8.0,2F8.2)
72      WRITE(10,111)(X(IXM),IXM=1,4)
111     FORMAT(F7.4,F7.3,F7.0,F7.3)
        READ(8)SN
        READ(8)EN
        WRITE(6,105)SN
105     FORMAT(1X,16F7.3)
75      CONTINUE
        END
        SUBROUTINE COMP(ACE,VAR,I3,I2,I4,I1)
        COMMON AC(24,3,96)
        DIMENSION ACF(24),ACE(24)
        VAR1=0.
        DO 51 II=1,3
        DO 51 J=1,4
        DO 51 KK=1,4
        L=I1+24*(KK-1)+6*(J-1)
        DO 40 I=1,24
40      ACF(I)=AC(I,II,L)
```

```
32      VAR=0.0
        ACF(1)=1.0
        DO 7 K=2,24
7       VAR=VAR+(ACE(K)-ACF(K))**2
        IF(VAR.GT.VAR1)GO TO 50
        VAR1=VAR
        I2=J
        I3=II
        I4=KK
50      CONTINUE
51      CONTINUE
        VAR=VAR1
        RETURN
        END
```

The following program calculates profiles for $T(O^+)$, $T(H^+)$, and T_e. The triple diagonal mesh method is used to calculate $T(O^+)$ and $T(H^+)$. T_e is calculated by integration of the energy balance equation. Arrays D, T, and S represent T_e, $T(O^+)$, and $T(H^+)$, respectively. The neutral atmosphere model is contained in arrays R, S, and P. Arrays W and Q represent the model used for photoelectron heating of thermal electrons. The ion densities are given in array N.

```
10 FORMAT F5.0,E8.0,F6.0,F6.0,E8.0,F6.0,F6.0,E8.0,F6.0,F6.0,E8.0,F6.0
20 FORMAT F6.0,F7.1,7E9.2
30 DIM D[217],T[201],RS[6,93],K[201],L[201],PS[6,217],N[2,101],S[201]
40 DIM N[110],C[217]
50 LOAD  DATA 17,R
60 GOSUB 1860
70 PRINT "FILE=";17;"TN=";R[1,93]
80 LOAD  DATA 22,N
90 FOR I=17 TO 201 STEP 10
100 L1=I*5+115
110 J=I/2-7.5
120 WRITE (15,20)L1,P[1,I],P[2,I],P[3,I],P[4,I],P[5,I],P[6,I],N[1,J],N[2,J]
130 NEXT I
140 LOAD  DATA 10,D
150 N7=N8=1
160 LOAD  DATA 18+K0,T
170 LOAD  DATA 17+K0,S
180 T9=S[201]↑(2/7)
190 PRINT " T(C+) PROFILE "
200 PRINT " L1  T(H+) T(O+)  TE    B       D       KI       LI    C(O+,H+) PE-I'
210 K[1]=L[1]=0
220 FOR L1=205 TO 1135 STEP 5
230 J=(L1-195)/5
240 I=(L1-115)/5
250 T5=D[I]
260 T7=S[J]↑(0.285714286)
270 T8=T[J]↑(0.285714286)
280 GOSUB 1270
290 GOSUB 450
300 L[J]=1/(B-L[J-1])
310 K[J]=(D-K[J-1])*L[J]
320 IF INT(L1/300)#L1/300 THEN 350
330 WRITE (15,340)L1,T7,T8,T6,2+B,D,K[J],L[J],C1*(T9-T7),S4*(T6-T8)
340 FORMAT F5.0,F6.0,2F5.0,7E9.1
350 NEXT L1
360 GOSUB 1510
370 IF Q<1 THEN 400
380 PRINT Q,L[Q],T[Q]
390 GOTO 210
400 STORE  DATA 18+K0,T
410 GOSUB 1020
420 IF ABS(T9-T[201]↑(2/7))/T9)>5E-04 THEN 160
430 GOSUB 580
440 RETURN
450 REM Q+ HEAT LOSS AND PRODUCTION
460 S1=(6.6*N2+5.8*O2+2.8*H5)*03
470 P6=(0.21*03*SQR(T8+T4))*0
480 R1=(0.4*H*C3)*SQR(T4)
490 S4=4.8*03*E/SQR(T6↑3)*1E+07
500 C1=3.3E+10*H3*03/(16*(T8/16+T7)↑1.5)
510 B=(S4*2+S1*2+P6*2+R1*2+(P6/(T8+T4))*(T8-T4)+C1*2)
520 B=(B+C1*(T8-T7)*3/(T8/16+T7))*0.52/7/T8↑2.5
530 B=-2.25*B*1E-07
540 D=(S1+P6+R1)*(T8-T4)+C1*(T8-T7))
550 D=0.52*25*(D+S4*(T8-T6))*1E-07-T[J+1]+2*T[J]-T[J-1]
560 RETURN
570 REM PRINT TEMPERATURE RESULTS
580 SCALE 100,4500,0,1300
590 XAXIS 100,500,50,4500
600 YAXIS 500,100,10,1200
610 GRID 100,500,50,4500
620 YAXIS 4500,100,1,0,1200
630 LABEL (4,1,1,0,1)
640 FOR L1=100 TO 1200 STEP 100
650 PLOT 300,L1,-1
660 CPLOT 0,-0.5
670 LABEL (4,1.7,1.7,0,1)L1
680 NEXT L1
690 FOR T0=1000 TO 4000 STEP 500
700 PLOT T0,50,-1
710 CPLOT -2.5,0
720 LABEL (4)T0
730 NEXT T0
740 PLOT 3000,7,-1
750 LABEL (4)"TEMPERATURE  K"
760 PLOT 105,500,-1
770 LABEL (4,3,1.7,P[1,3,8/11)" HEIGHT   KM"
780 FOR I=1 TO 89
790 L1=I+100+115
800 PLOT R[1,I],L1,-2
810 NEXT I
820 PLOT R[1,90],120,-2
830 REM
840 FOR I=1 TO 201
850 T7=T[I]↑2/7
860 L1=I*5+95
```

```
870 PLOT T7,L1,-2
880 NEXT I
890 PEN
900 FOR I=1 TO 201
910 L1=I+5+195
920 T7=S[I]+(2.7)
930 PLOT T7,L1,-2
940 NEXT I
950 PEN
960 FOR L1=120 TO 1210 STEP 5
970 I=(L1-115)/5
980 PLOT D[I],L1,-2
990 NEXT L1
1000 PEN
1010 RETURN
1020 REM HERE T(H+) PROFILE IS CALCULATED
1030 LOAD  DATF 17+K0,T
1040 LOAD  DATF 18+K0,S
1050 PRINT " T(H+) PROFILE"
1060 PRINT "  L1   T(H+) T(O+) TE    B         D        KI       LI   C(O+,H+)  PE-)
1070 K[1]=LL[]-0
1080 FOR L1=205 TO 1195 STEP 5
1090  J=(L1-195)/5
1100  I=(L1-115)/5
1110  D=D[I]
1120  T2=T[J]+(.2857/.4286)
1130  T8=S[J]+(.2857/.4286)
1140  A=1.76
1150  B=.1740
1160  L[J]=1.6-LL[I-1]
1170  K[J]=D+K[I-1]+L[J]
1180  IF I<L1-200)# 1300 THEN 1300
1190  PRINT L1,3.60*L,T7,T8,T6,2+B+D+K[J],L[J],L1+(T8-T7),S4+(T6-T7)
1200 NEXT L1
1210 GOSUB 1510
1220 IF U 1 THEN 1.50
1230 PRINT U,L[U],T[U]
1240 GOTO 1070
1250  DATF  DATA 17+.0,T
1260 K1=K[1]
1270 FOR I=2 TO 6
1280 K(I)=K[I],I]
1290 NEXT I
1300 K=K[1,1]
1310 K1=K[,]
1320 K2=K[,2]
1330 K3=K[,3]
1340 K4=K[,4]
1350 K=K[,0]
1360 IF K 0 THEN 1400
1370 K3=K3
1380 K2=K2
1390 GOTO 1460
1400 IF J 2#INT(J/2) THEN 1440
1410 K2=10+(LGT(K[2,J-2]+LGT(K[3,J/2+1]))+2)
1420 K3=10+(LGT(K[1,J-2]+LGT(K[1,J-2+1]))/2)
1430 GOTO 1460
1440 K2=K[2,J-2]
1450 K3=K[1,J-2]
1460 L=0
1470 K2=K2+K
1480 K=K2+K4+1E-04
1490 K=K+43
1500 K1=EN
1510 U=0
1520 K[,201]=1+(1.2*U)+.T[,200]-T[201]+(1200+17.5+N7+T[200])+(5.7+)
1530 K[,1]=K[,201]+L[,201]
1540 FOR I=200 TO 2 STEP -1
1550 K[,I]=K[,I]+L[I]+.I+1
1560 K[I]=K[I]+L[I]
1570 IF ABS(L[I] T[I]  5E-04 THEN 1590
1580 U=I
1590 NEXT I
1600 FOR I=11 TO 300 STEP 50
1610 L1=I+5+195
1620 L2=I+5+245
1630 L3=I+5+295
1640 T1=T[I]+(2.7)
1650 T2=T[I+10]+(2.7)
1660 T3=T[I+20]+(2.7)
1670 T4=T[I+30] T[I+.]
1680 T5=T[I+40]
1690 T6=T[I+50] T[I+.]
1700 T7=T[I+60]+(2.7)
1710 A=(15+16*L1+L[I]) T[I]+11+L2+L[I+10] T[I+10]+T2+L3+T4+T3+L4+T5+T6
1720 NEXT I
1730 END
```

```
1740 REM H+ HEFT LOSS AND PRODUCTION
1750 S2=(3.1*N2+2.8*O2+5.5*H5)*H3
1760 P6=(0.34+H3*SQR(T7))*0
1770 R1=(1.4+H*H3)*SQR(T7+T4)
1780 S4=77+H3*E/SQR(T6↑3)*1E+07
1790 C1=2.3E+10*H3*O2/(16*(T8/16+T7)↑1.5)
1800 B=(S4*2+S2*2+P6*2+R1*2+(P6/T7+R1/(T7+T4))*(T7-T4)+C1*2)
1810 B=(B+C1*(T7-T8)*3/(T8/16+T7))*0.13/7/T7↑2.5
1820 B=-2.25+B*1E-07
1830 D=-(S2+P6+R1)*(1/-T4)+C1*(T7-T8))
1840 D=0.13*25*(D+S4*(T7-T6))*1E-07-T[J+1]+2*T[J]-T[J-1]
1850 RETURN
1860 D1=0.00833
1870 D2=0.01965
1880 D3=0.0279E
1890 K1=8.62E-05
1900 LOAD  DATF 1,W
1910 FOR I=1 TO 178
1920 IF I/2=INT(I/2) THEN 1950
1930 Q[I]=W[I/2+0.51]
1940 GOTO 1960
1950 Q[I]=(W[I/2]+W[I/2+1])/2
1960 NEXT I
1970 FOR I=179 TO 217
1980 Q[I]=0[178]
1990 NEXT I
2000 FOR I=1 TO 89
2010 FOR J=1 TO 6
2020 P[J,I*2-1]=P[J,I]
2030 NEXT J
2040 NEXT I
2050 FOR I=2 TO 176 STEP 2
2060 FOR J=1 TO 6
2070 IF J=1 THEN 2100
2080 P[J,I]=10↑(LGT(P[J,I-1])+LGT(P[J,I+1]))/2)
2090 GOTO 2110
2100 P[J,I]=(P[J,I-1]+P[J,I+1])/2
2110 NEXT J
2120 NEXT I
2130 FOR I=89 TO 93
2140 FOR J=1 TO 6
2150 P[J,I+10-713]=R[J,I]
2160 NEXT J
2170 NEXT I
2180 FOR I=177 TO 207 STEP 10
2190 FOR I1=1 TO I+1
2200 FOR J=1 TO 6
2210 IF J=1 THEN 2240
2220 P[J,I1]=10↑(LGT(P[J,I])-LGT(P[J,I+10]))*(I-I1)/10+LGT(P[J,I]))
2230 GOTO 2250
2240 P[J,I1]=P[J,I]-P[J,I+10])*(I-I1)/10+P[J,I]
2250 NEXT J
2260 NEXT I1
2270 NEXT I
2280 RETURN
2290 FOR N8=1 TO 1.5 STEP 0.5
2300 D8=29*D[217]
2310 D7=D8+200+N8↑3
2320 D6=T9=T[201]↑(2/7)
2330 D5=D[217]=D8
2340 M=L9=L9=N1=0
2350 U=U7-(D-C.45*S-D5↑5)+N8
2360 WRITE (15,2890)200,T[201]↑(2/7),D5,U8
2370 FOR I1=115 TO 100 STEP -5
2380 I=I1-105
2390 I=I1-115
2400 GOSUB 3200
2410 IF J=0 THEN 2440
2420 T7=T4
2430 GOSUB 3040
2440 T7=T[J]↑(2/7)
2450 T=T[J]↑(2/7)
2460 REM
2470 GOSUB 3090
2480 D4=D5
2490 T6=T7
2500 GOSUB 3200
2510 U8=U9+E+5.2
2520 L9=D+5.04
2530 F=(T+T4)*(L9↑2+16)+F.14 *12.5
2540 D5=D[I]=D4-L9+F
2550 IF M=0 THEN 2580
2560 IF I=I1+5 AND ABS(U8-U)<0.1 THEN 2580
2570 IF I=I1+E-F > T6 T4+200 THEN 2800
2580 M=M+1
2590 GOTO 2350
2600 REM
```

```
2610 FOR M=1 TO 20
2620 T6=W5
2630 GOSUB 3220
2640 G=F
2650 FOR M1=1 TO 3
2660 T6=D5+0.44*M1*50*G/ABS(G)
2670 GOSUB 3220
2680 IF F*2<G*2/3 THEN 2710
2690 IF M>2 AND F*G<0 THEN 2780
2700 NEXT M1
2710 IF F<0 THEN 2740
2720 X7=T6
2730 GOTO 2750
2740 X8=T6
2750 D5=D5+(X8-X7)*G ABSG/2
2760 IF X8-X7<5 AND F*G<0 THEN 2780
2770 NEXT M
2780 D(I)=D5
2790 GOTO 2870
2800 IF D5>D8+100 THEN 2920
2810 IF D5>T7-10 THEN 2860
2820 T6=(D(I+1)+T7)/2
2830 GOSUB 3220
2840 IF C4>Q(I)*E-F THEN 2920
2850 GOTO 2580
2860 U8=U9=U8+F*5/2
2870 IF INT((L1)/300)*(L1)/300 THEN 2900
2880 WRITE (15,2890)L1,T7,D(I),C4,F,F1+F2,F3+F4,Q(I)*E,L9,K9,M
2890 FORMAT F5.0,F6.0,F5.0,E9.1,4E9.1,F7.1,F7.2,F4.0
2900 NEXT L1
2910 GOTO 3000
2920 WRITE (15,2890)L1,T7,T6,W1*3.22*T6↑2,F,F1+F2,F3+F4,Q(I)*E,L9,K9
2930 IF D5<T7 THEN 2960
2940 D7=D8
2950 GOTO 2970
2960 D6=D8
2970 D8=(D6+D7)/2
2980 IF ABS(D6-D7)<1E-02 THEN 3020
2990 GOTO 2930
3000 WRITE (15,3010)L1,T7,T0,T6,M
3010 FORMAT F5.0,3F6.0,F4.0
3020 STORE  DATA 19+K0,D
3030 GOSUB 1F0
3040 IF ABS(D(217)-Z9)/Z9<1E-03 THEN 3060
3050 GOTO 2300
3060 K4=K5=1
3070 NEXT N8
3080 STOP
3090 REM CALCULATE ENERGY LOSS  AND PRODUCTION TERMS
3100 S1=4.8*03/1000
3110 S2=.7*H3/1000
3120 S3=1.77E-15*N2
3130 S4=1.21E-14*02
3140 S5=3.74E-11*0
3150 S6=9.43E-12*H
3160 S7=2.47E-13*H5
3170 P1=7E-10*C2
3180 P2=3E-10*H2
3190 V1=06-12*C2
3200 S2=3.43E-07*0*E (5+3*EXP(-D1/K1/T4)+EXP(-D3/K1/T4))
3210 RETURN
3220 P1=1
3230 IF T6>3000 THEN 3250
3240 Q1=(1-EXP(-(T6-199)↑2/9E+04))↑2
3250 V3=1E-07*H2*E*EXP/2.61E-03*(T6-2500))+01
3260 V4=0.89*D3*(EXP(-D2 K1 T6)-EXP(-D2/K1/T4))
3270 V4=V4+0.32*D3*(EXP(-D3 K1 T6)-EXP(-D3/K1/T4))+V4
3280 V4=V4+0.37*D1*(EXP(-D1/K1/T6)-EXP(-D1/K1 T4))
3290 V3=V3*SQR(T6)*V4
3300 V4=(1+3.57E-02*SQRT6)
3310 V4=V4/(3.35E-03*T6
3320 IF V4 0.455 THEN 3340
3330 V4=0.455
3340 V5=1/1.35E-04*T6
3350 IF V5 0.3 THEN 3370
3360 V5=0.3
3370 V2=V2+0.262*07*SQRT
3380 W1=W1+02*2.2*09+0*3.4+H5*5.6
3390 W1=(W1+H+C8*54.)*+1E-12/E
3400 P4=0.45185549*(K/T6↑5)*(1+3.22+T6↑2+W1)
3410 P1=(2*(T6-17)+(T6-T0)*E SQR(T6↑3)
3420 P2=(T6-T4)*E+SQR(T6+(53+07*SQRT6+S4+09+S5+08+S7)
3430 P4=P1+P2+(T6-T4)*E/SQRT6
3440 P=(V1+E+(T6-T4)*SQRT6+V3
3450 (0 )*E F1 F2+ F4
3460 RETURN
```

```
3470 SCALE 0.9,1.7,0,1300
3480 XAXIS 200,0.05,1,1.55
3490 XAXIS 1,100,200,1200
3500 XAXIS 1200,0.05,1,1.55
3510 YAXIS 1.55,100,200,1200
3520 LABEL (*,1,1,0,1)
3530 FOR L1=200 TO 1200 STEP 100
3540 PLOT 1,L1,-1
3550 LPLOT -4.5,-0.3
3560 IF L1<999 THEN 3590
3570 SPLOT -0.5,0
3580 LABEL (*,1.5,1.5,0,1)L1
3590 NEXT L1
3600 FOR I=1 TO 201
3610 PLOT T[I]*(2/7)/SL[I]*(2/7),I*5+195,-2
3620 NEXT I
3630 STOP
```

REFERENCES

Abramowitz, M. and I. A. Stegun [1964], *Handbook of Mathematical Functions* U. S. Government Printing Office, Washington, D.C.

Banks, P. M. (1966a), Collision frequencies and energy transfer for electrons, *Planet. Space Sci. 14*, 1085-1102.

Banks, P. M. (1966b), Collision frequencies and energy tranfer for ions, *Planet. Space Sci. 14*, 1105-1122.

Banks, P. M. (1966c), Charged particle temperature and electron thermal conductivity, *Ann. Geophys. 22*, 577-587.

Banks, P. M. (1967a), Temperature coupling of ions in the ionosphere, *Planet. Space Sci. 15*, 77-93.

Banks, P. M. (1967b), Ion temperatures in the upper atmosphere, *J. Geophys. Res. 72*, 3365-3385.

Banks, P. M. and G. Kockarts [1973], *Aeronomy: Part B*, Academic Press; New York and London.

Banks, P. M., A. F. Nagy, and W. I. Axford [1971], Dynamical Behavior of thermal protons in the mid-latitude ionosphere and magnetosphere, *Planet. Space Sci. 19*, 1053-1058.

Bowhill, S. A. [1962], The formation of the daytime peak of the ionospheric F_2 layer, *J. Atmos. Terr. Phys 24*, 503-519.

Bowles, K. L. [1958], Observations of vertical incidence scatter from the ionosphere at 41 Mc/sec, *Phys. Rev. Lett., Vol. 1., No. 12* H623 1/2-H523 2/2.

Bowles, K. L. [1961], Incoherent scattering by free electrons as a technique for studying the ionosphere and exosphere: Some observations and theoretical considerations, *J. Res., NBS, 65D* 1-14.

Bowles, K. L. [1962], Profiles of electron density over magnetic equator obtained using the incoherent-scatter technique, *NBS Tech. Note 169*, 1-12 National Bureau of Standards, Boulder, Colorado and the Instituto Geofisico del Peru, LIMA.

Brachman, R. T., W. L. Fite, and R. H. Neynaber [1958], Collisions of electrons with hydrogen atoms III, *Phys. Rev. 112*, 1157-1161.

Breigg, E. L. and C. C. Lin [1966], Excitation of the spin multiplets of the ground state of oxygen by slow electrons, *Phys. Rev. 151*, 67-79.

Buneman, O. [1962], Scattering of radiation by the fluctuations in a non-equilibrium plasma, *J. Geophys. Res. 67*, 2050-2053.

Cauffman, D. P. and D. A. Gurnett [1971], Double-probe measurements of convection electric fields with the Injira-5 Satellite, *J. Geophys. Res. 76*, 6014-6027.

Chapman, S. and T. G. Bowling [1970], *Mathematical Theory of Nonuniform Gases*, Cambridge Univ. Press, London and New York.

CIRA [1972], *Cospar International Reference Atmosphere*.

Cohen, R. S., L. Spitzer, and R. Routley [1950], The electrical conductivity of an ionized gas, *Phys. Rev. 80*, 230-238.

Cooper, J. W. and J. B. Martin [1962], Electron photodetachment from ions and elastic collision cross sections for O, C, Cl, and F., *Phys. Rev. 126*, 1482-1488.

Dalgarno, A. and T. P. Degges [1968], Electron cooling in the upper atmosphere, *Planet. Space Sci. 16*, 125-127.

Dalgarno, A. and R. J. W. Henry [1965], Electron temperatures in the *D* region, *Proc. Roy. Soc. A 286*, 521-530.

Dalgarno, A. and R. J. Moffett [1962], Electron cooling in the *D* region, *Planet. Space Sci. 9*, 439-441.

Dalgarno, A., M. B. McElroy, and R. J. Moffett [1963], Electron temperatures in the ionosphere, *Planet. Space Sci. 11*, 463-484.

Dalgarno, A., M. B. McElroy, and J. C. Walker [1967], The diurnal variation of ionospheric temperatures *Planet. Space Sci. 15*, 331-345.

Dalgarno, A., M. B. McElroy, M. H. Rees, and J. C. G. Walker [1968], The effect of oxygen cooling on ionospheric electron temperatures, *Planet. Space Sci. 16*, 1371-1380.

Da Rosa, A. V. [1966], The theoretical time dependent thermal behavior of the ionospheric electron gas, *J. Geophys. Res. 71*, 4107-4120.

Desloge, E. A. [1962], Exchange of energy between gases at different temperatures, *Phys. Fluids 5*, 1223-1225.

Dougherty, J. P. and D. T. Farley [1960], A theory of incoherent scattering of radio waves by a plasma, *Proc. Roy. Soc. A 259*, 79-99.

Drukarev, G. [1946], On the mean energy of electrons released in the ionization of gas, *J. Phys. 10*, 81-84.

Englehardt, A. G., A. V. Phelps, and C. G. Rish [1964], Determination of momentum transfer and inelastic collision cross sections for electrons in nitrogen fusing transport coefficients, *Phys. Rev. 135*, 1566-1574.

Evans, J. V. [1962], Diurnal variation of the temperature of the *F* region, *J. Geophys. Res. 67*, 4914-4920.

Evans, J. V. [1969], Theory and practice of ionospheric study by Thomson scatter radar, *Proc. IEEE 57*, 496-530.

Fejer, J. A. [1960], Scattering of radio waves by an ionized gas in thermal equilibrium, *Can. J. Phys. 38*, 1114-1133.

Fejer, J. A. [1961], Scattering of radiowaves by an ionized gas in thermal equilibrium in the presence of a uniform magnetic field, *Can. J. Phys. 39*, 716-740.

Geisler, J. E. [1967], On the limiting daytime flux of ionization into the protonosphere, *J. Geophys. Res. 72*, 81-84.

Geisler, J. E. and S. A. Bowhill [1965], Exchange of energy between the ionosphere and the protonosphere, *J. Atmos. Terr. Phys. 27*, 1119-1146.

Gleeson L. J. and W. I. Axford [1967], Electron and ion temperature variations in temperate zone sporadic-*E* layers, *Planet. Space Sci. 15*, 123-136.

Gordon, W. E. [1958], Incoherent scattering of radio waves by free electrons with applications to space exploration by radar, *Proc. IRE 46*, 1824-1829.

Gordon, W. E. [1964], Arecibo ionospheric observatory, *Science, 146*, 26-30.

Gradshteyn, I. S. and I. M. Ryshik [1965], *Tables of Integrals, Series, and Products*, Academic Press, New York.

Hagen, J. B. and D. T. Farley [1973], Digital correlation techniques in radio science, *Radio Sci. 8*, 775-784.

Hagen, J. B. and P. Y. Hsu [1974], The structure of the protonosphere above Arecibo, *J. Geophys. Res. 79*, 4269-4275.

Hagfors, T. [1961], Density fluctuations in a plasma in a magnetic field with applications to the ionosphere, *J. Geophys. Res. 66*, 1699-1712.

Hake, R. D. and A. V. Phelps [1967], Momentum transfer and inelastic cross sections for electrons in O_2, CO, and CO_2, *Phys. Rev. 158*, 70-84.

Hall, L. A., K. R. Damon, and H. E. Hinteregger [1963], Solar extreme ultraviolet photonflux measurements in the upper atmosphere of August, 1961, *Space Res. III*, 745-771.

Hall, L. A. and H. E. Hinteregger [1970], Solar radiation in the extreme ultraviolet and its variation with solar rotation, *J. Geophys. Res. 75*, 105-111.

Hall, L. A., W. Schweiger, and H. E. Hinteregger [1965], Improved extreme ultraviolet absorption measurements in the upper atmosphere, *J. Geophys. Res 70*, 105-111.

Hall, L. A., J. E. Higgins, C. W. Chagnon, and H. E. Hinteregger [1969], Solar cycle variation of the extreme ultraviolet radiation, *J. Geophys. Res. 74*, 4181-4183.

Hanson, W. B. [1963], Electron temperatures in the upper atmosphere, *Space Res. III*, 282-302.

Hanson, W. B. and R. Cohen [1968], Photoelectron heating efficiency in the ionosphere, *J. Geophys. Res. 73*, 831-840.

Hanson, W. B. and I. B. Ortenburger [1961], The coupling between the protonosphere and the normal *F* region, *J. Geophys. Res 66*, 1425-1435.

Hanson, W. B., S. Sanatani, L. H. Brace, and J. A. Findlay [1969], Thermal structure of an Alouette II topside profile as deduced from rocket measurements, *J. Geophys. Res. 74*, 2229-2239.

Hasted, J. B. [1964], *Physics of Atomic Collisions* Butterworths, London.

Hinteregger, H. E. [1965], Absolute intensity measurements in the extreme ultraviolet spectrum of solar radiation, *Space Sci. Rev. 4*, 462-497.

Hinteregger, H. E. [1970], The extreme ultraviolet solar spectrum and its variation during the solar cycle, *Ann. Geophys. 216*, 547-554.

Hoffman, J. H. [1967], A mass spectrometric determination of the composition of the nighttime topside ionosphere, *J. Geophys. Res. 72*, 1883-1888.

Hoffman, J. H., W. H. Dodson, C. R. Lippincott, and H. D. Hammack [1974], Initial ion composition results from the Isis 2 satellite, *J. Geophys. Res. 79*, 4246-4251.

Huxley, L. G. H. and R. W. Crompton [1962], The motions of slow electrons in gases, in *Atomic and Molecular Processes*, Academic Press, New York.

Knudsen, W. C. and G. W. Sharp [1966], Ion temperature profile in the topside ionosphere, *J. Geophys. Res. 71*, 4099-4105.

Lane, N. F. and A. Dalgarno [1969], Electron cooling by vibrational excitation of O_2, *J. Geophys. Res. 74*, 3011-3012.

LeDourneuf, M. and R. K. Nesbet [1976], Electron-impact excitation of fine-structure levels of atomic oxygen, *J. Phys. B. 9*, L241-L243.

Mantas, G. P. [1973], Electron collision processes in the ionosphere, *Aeron. Rep. No. 54*, Aeron. Lab., Dep. Elec. Eng., Univ. Ill., Urbana-Champaign.

McClure, J. P., W. B. Hanson, A. F. Nagy, R. J. Cicerone, L. H. Brace, M. Baron, P. Bauer, H. C. Carlson, J. V. Evans, G. N. Taylor, R. F. Woodman [1973], Comparison of T_e and T_i from Ogo 6 and from various incoherent scatter radars, *J. Geophys. Res. 78*, 197-205.

McDaniel, E. W. [1964], *Collision Phenomena in Ionized Gases*, Wiley, New York.

Moorcroft, D. R. [1963], On the power scattered from density fluctuations in a plasma, *J. Geophys. Res. 68*, 4870-4872.

Moorcroft, D. R. [1964], Determination of temperature and ionic coupling by incoherent scatter from the ionosphere and magnetosphere, *J. Geophys. Res. 69*, 955-970.

Nagy, A. F., P. Bauer, and E. G. Fontheim [1968], The nighttime cooling of the protonosphere, *J. Geophys. Res. 73*, 6259-6274.

Nagy, A. F., L. H. Brace, G. R. Caugnan, and M. Kanal [1963], Direct measurements bearing on the extent of thermal nonequilibrium in the ionosphere, *J. Geophys. Res. 68*, 6401-6412.

Nagy, A. F., E. G. Fontheim, R. S. Stolarski, A. E. Butler [1969], Ionospheric electron temperature calculations including protonospheric and conjugate effects, *J. Geophys. Res. 74*, 4667-4676.

Nicolet, M. [1953], The collision frequency of electrons in the ionosphere, *J. Atmos. Terres. Phys. 3*, 200-205.

Pack, J. L. and A. N. Phelps [1961], Drift velocities of slow electrons in helium, neon, argon, hydrogen, and nitrogen, *Phys. Rev. 121*, 798-806.

Pineo, V. C., L. G. Kraft, and H. W. Briscoe [1960], Some characteristics of ionospheric backscatter observed at 440 Mc/s, *J. Geophys. Res. 65*, 2629-2633.

Rees, M. H., R. A. Jones, and J. C. G. Walker [1971], The influence of field-aligned currents on auroral electron temperatures, *Planet. Space Sci. 19*, 313-325.

Rees, M. H., J. C. G. Walker, and A. Dalgarno [1967], Auroral excitation of the forbidden lines of atomic oxygen, *Planet. Space Sci. 15*, 1097-1110.

Renau, J. [1960], Scattering of electromagnetic waves from a nondegenerate ionized gas, *J. Geophys. Res. 65*, 3631-3640.

Rishbeth, H. and D. W. Barron [1960], Equilibrium electron distributions in the ionospheric F_2-layer, *J. Atmos. Terr. Phys. 18*, 234-252.

Rohrbaugh, R. P. and J. S. Nisbet [1973], The effect of energetic oxygen atoms on neutral density models, *J. Geophys. Res. 78*, 6768-6771.

Rycroft, M. J. and S. J. Burnell [1970], Statistical analysis of movements of the ionospheric trough and the plasmapause, *J. Geophys. Res. 75*, 5600-5604.

Salpeter, E. E. [1960a], Electron density fluctuations in a plasma, *Phys. Rev. 120*, 1528-1535.

Salpeter, E. E. [1960b], Scattering of radio waves by electrons above the ionosphere, *J. Geophys. Res. 65*, 1851-1852.

Sanatani, S. and W. B. Hanson [1970], Plasma temperature in the magnetosphere, *J. Geophys. Res. 75*, 769-774.

Schulz, G. J. and J. T. Dowell [1962], Excitation of vibrational and electronic levels in O_2 by electron impact, *Phys. Rev 128*, 174-177.

Schunk, R. W. and P. B. Hays [1971], Photoelectron energy losses to thermal electrons, *Planet. Space Sci. 19*, 113-117.

Smith, P. A. [1968], The determination of vertical distributions of plasma temperatures and composition from satellite measurements, *J. Atmos. Terr. Phys. 30*, 1203-1209.

Smith, K., R. P. McEachron, and P. A. Fraser [1962], Effect of virtual excitation of the 2s state on the elastic scattering of electrons by atomic hydrogen, *Phys. Rev. 125*, 553-557.

Spencer, N. W., L. H. Brace, G. R. Carignan, D. R. Taeusch, and H. Niemann [1965], Electron and molecular nitrogen temperature and density in the thermosphere, *J. Geophys. Res. 70*, 2665-2698.

Spitzer, L. [1962], *Physics of Fully Ionized Gases*, 144, Interscience Publishers.

Stubbe, P. and S. Chandra [1970], The effect of electric fields on the *F*-region behavior as compared with neutral wind effects, *J. Atmos. Terr. Phys. 32*, 1909-1919.

Swartz, W. E. and J. S. Nisbet [1972], Revised calculations of *F* region ambient electron heating by photoelectrons, *J. Geophys. Res. 77*, 6259-6261.

Tambe, B. R. and R. J. W. Henry [1976], Low-energy scattering of electrons by atomic oxygen, *Phys. Rev. A 13*, 224-228.

Walker, J. C. G. [1968], Electron and nitrogen vibrational temperature in the *E*-region of the ionosphere, *Planet. Space Sci. 16*, 321-327.

Walker, J. C. G. [1971], Ionospheric effects of auroral electric field, in *The Radiating Atmosphere*, ed. B. M. McCormack, Reidel Publ. Co., Dordrecht-Holland.